

Geir Hansen

Experimental and theoretical investigation of heat transfer in metallurgical furnace sideling cooling system

Thesis for the degree of Philosophiae Doctor

Trondheim, October 2016

Norwegian University of Science and Technology
Faculty of Engineering
Science and Technology
Department of Energy and Process Engineering



Norwegian University of
Science and Technology

NTNU

Norwegian University of Science and Technology

Thesis for the degree of Philosophiae Doctor

Faculty of Engineering

Science and Technology

Department of Energy and Process Engineering

© Geir Hansen

ISBN 978-82-326-1918-4 (printed version)

ISBN 978-82-326-1919-1 (electronic version)

ISSN 1503-8181

Doctoral theses at NTNU, 2016:290



Printed by Skipnes Kommunikasjon as

Abstract

The purpose of this work was to investigate theoretically and experimentally the heat transfer of a metallurgical furnace side-lining cooling system utilizing evaporation/boiling and condensation of a suitable working fluid. The working temperature range was specified to 400-650°C. The heat flux was specified to 20-30 kW/m² under normal working conditions, under special conditions hot spots with heat fluxes up to 300 kW/m² were to be expected. The heat flux on the cooling panel was specified as unilateral, as it would be in the side-lining of a metallurgical furnace.

The number of working fluid candidates for the temperature range 400-650°C is quite limited. After reviewing literature on working fluids, the following two candidates were selected for further investigation:

- Sulfur
- Potassium

Sulfur was considered as a potential working fluid based on its thermo-physical properties; however, corrosion concern for the heat pipe shell when exposed to boiling sulfur, was a major issue. A corrosion experiment was carried out, in which samples of stainless steels AISI 316L and AISI 304 were submerged in liquid sulfur at 550°C for 100 hours. The experimental results showed that the corrosion was heavy. Without any construction material known to be able to withstand boiling sulfur for years, it was decided not to proceed with the investigation of sulfur as working fluid for the cooling panel.

Potassium was investigated theoretically as a working fluid candidate for a cooling panel utilizing nucleate boiling and for a cooling panel utilizing evaporation from a wick. From the theoretical study it was concluded that the nucleate boiling of potassium in a narrow panel was likely to be periodic, with relatively long waiting times followed by geyser boiling. How the boiling would develop over the required lifetime of the cooling panels (years), with stops and restarts, was also a major concern. A cooling panel utilizing evaporation of potassium from a wick was therefore considered to be the best solution. With regard to construction material both AISI 304 and nickel was reported in heat pipe literature to be compatible with potassium.

A novel hybrid heat pipe design was chosen for the cooling panel. The panel is a hybrid because only the evaporator surface is covered by a wick. The condenser is wickless, and the condensate is flowing back to the evaporator by gravity, like in a thermosyphon. The construction material was chosen to be Nickel 201, due to its high thermal conductivity compared to AISI 304.

A theoretical and experimental wick study was undertaken in order to develop a suitable wick for the hybrid heat pipe evaporator surface. For the experimental hybrid heat pipe the wick was required to manage a lifting height of 150 mm, and be able to withstand hot spot heat flux conditions. Two types of wicks were made and analysed experimentally and theoretically in this study:

- Wicks of sintered nickel powder (Inco 255).
- Wicks of sintered compressed nickel foam plates.

The effective pore radii and the permeabilities of the wicks were determined from rate-of-rise experiments using the model fluid heptane. The porosities of the wicks were measured by use of isopropanol. The experimental results were applied to predict the performance of the wicks in the hybrid heat pipe. The results showed that the performance of the wicks made of sintered nickel powder would be very limited by the vapour static pressure limit. The vapour static pressure limit states that in a closed container (i.e. here the hybrid heat pipe) the capillary pressure produced in the wick can not be higher than the vapour pressure of the working fluid. The wicks produced of compressed nickel foam, having higher effective pore radius and higher permeability than the wicks made of sintered powder, were therefore considered better for the hybrid heat pipe.

A series of 2 layer compressed nickel foam wicks was produced in order to investigate how the effective pore radius, permeability and porosity changed with the degree of compression. The experimental results were reported for the first time. From the maximum capillary rise of heptane in these wicks the contact angle between heptane and the nickel of the wicks was found to be $58,4^{\circ} \pm 8,9\%$.

The final wick for the hybrid heat pipe consisted of 4 layers of compressed nickel foam sintered together. The total thickness was 1,15 mm. From the rate-of-rise experiment the effective pore radius was determined as $1,02 \cdot 10^{-4}$ m (for heptane) and the permeability was $7,30 \cdot 10^{-11}$ m². The contact angle between heptane and the nickel of the wick was estimated to be $60,2^{\circ}$ from the capillary rise in this wick.

The final wick was attached to the evaporator surface of the hybrid heat pipe by electron beam spot welding. The consequence of the welding spots on the performance of the wick was analysed by use of Comsol Multiphysics[®], and the spots were found to cause minor (~1%) reduction of the wicks capacity.

A test rig for the hybrid heat pipe was built, utilizing cartridge heaters for heating of the evaporator and convective cooling by use of nitrogen gas for the condenser. In order to monitor the performance of the hybrid heat pipe it was equipped with thermocouples.

A predictive thermal performance model based on formulas that are reported in the literature was built using Excel and was utilized to produce semi-quantitative estimates of the fluid flow in the hybrid heat pipe.

The experimental results were scattered but indicated that the hybrid heat pipe was able to operate at higher heat fluxes than expected. Specifically, the measured performance could occur if the permeability of the wick was higher than calculated from the rate-of-rise experiment. Increased permeability could have been caused by a small channel in the wick.

Periodic instability of the temperatures in the hybrid heat pipe occurred when heat was supplied to the two lower evaporator sections only. A model of geyser boiling was found to fit the measured instability well.

The thermal expansion of the hybrid heat pipe was analysed by use of Comsol Multiphysics, and showed that structure bending due to unilateral heat flux is a factor to be taken into consideration even when a high thermal conductivity construction material as nickel is used. Thermal expansion has potential to cause thermal contact problems both on the outside of the cooling panel, and between the evaporator wall and the wick. Thermal expansion could have created a high permeability channel in or under the wick in the current study. A robust method for attaching the wick to the evaporator surface is required.

From this study the hybrid heat pipe technology is considered as promising technology for a metallurgical furnace side-lining cooling system.

Revision

Minor misprints corrected, some discussions clarified.

Acknowledgements

On the theoretical side the weekly meetings with my supervisor professor Erling Næss throughout the whole study have constituted the main part, and have been very valuable. In addition I have enjoyed very much the discussions with the students I have co-supervised, in chronological order: Bjarte Ross Idsø, Kolbeinn Jakob Kristjansson, Anders Sandved, Annette Hultin and Dan Adrian Odden.

Many persons have been involved in this work, especially with realization of the experimental parts of it.

Inspiring project meetings with Hilde Løken Larsen and Harald Haaland at Elkem were important milestones in the beginning of the project.

Ove Paulsen and Ove Darell at Sintef Materials and Chemistry provided valuable assistance on sintering, Ørjan Lohne on porosity measurements. Ove Paulsen assisted also on dilatometry. Vegar Øygarden assisted on tape casting and sintering, and also on the thermogravimetric experiment on pure Inco nickel powder in air. Instructions for the use of the other thermogravimetric instruments were provided by Erik Langørgen.

Astrid Salvesen carried out all glass work and cutting of alumina.

Most of the mechanical work related to the test-rig and the high vacuum rig was carried out by Sølve Sterten and Reidar Tellebon. The electrical systems of the rigs were designed by Marius Østnor Døllner and Odin Hoff Gardå. Helge Laukholm, Paul Svendsen, Erik Langørgen, Halvor Flatberg, Halvor Haukvik and Martin Bustadmo did all contribute to various parts of the rigs and experimental work. Most of the machining of the hybrid heat pipe was carried by Øystein Gjervan Hagemo at the fine mechanics workshop at NTNU under leadership of Harald Snekvik. The Electron Beam welding of the heat pipe was carried out by Institute for Energy Technology (IFE). Thanks to Knut Lunde and Jan Arne Johansen at IFE for professional welding and for giving me an introduction to the field of electron beam welding. The wire electric discharge machining of the condenser fins was also carried out at IFE.

Bjarne Salberg and Morten Onsøien assisted in the field of induction welding, Rolf Dahl on high vacuum systems, Ana Maria Martinez, Edel Sheridan and Pei Na Kui on the use of the glove box.

Most of the ordering of parts and materials was carried out by higher executive officer Anita Yttersian at The Department of Energy and Process Engineering, NTNU.

Eugen Uthaug took care of PC maintainance and support throughout this study.

Thanks a lot to everyone for their help.

Trondheim, 23.09.2016. Geir Hansen

List of symbols

Symbol	Description	Unit
a	function, Eq. (3-45).	
A	Area	m ²
A _c	cross sectional area	m ²
c _p	specific heat capacity at constant pressure	J/(kg·K)
c _v	specific heat capacity at constant volume	J/(kg·K)
	velocity of sound	m/s
d	diameter	m
D	diameter	m
\dot{E}	rate of energy transfer	W
f	friction factor	-
g	gravity constant, g=9,81	m/s ²
G	Gibbs free energy	J
h	heat transfer coefficient	W/(m ² ·K)
h _{fg}	latent heat of evaporation	J/kg
H	height	m
I	electric current	A
k	thermal conductivity	W/(m·K)
L	Length	m
M	Merit number, Eq. (2-5)	W/m ²
M	molecular mass	g/mol

m	mass	kg
	factor in fin efficiency equation	-
\dot{m}	mass flow rate	kg/s
n	number of moles	-
P	pressure	Pa
	electric power	W
q	heat flux	W/m ²
\bar{q}	average axial heat flux over cross sectional area	W/m ²
Q	heat flow rate	W
R	thermal resistance	K/W
R	electrical resistance	V/A
	flow resistance, Eq. (4-5)	1/m ²
R''	specific thermal resistance	m ² k/W
R_u	universal gas constant (8,314)	J/(mol·K)
r	radius	m
r_{eff}	effective pore radius	m
t	time	s
T	temperature	K
u	axial velocity	m/s
u_{∞}	axial freestream velocity	m/s
U	Voltage	V
V	volume	m ³
v	specific volume	m ³ /kg

	radial velocity	m/s
W	width	m
wt	mass	kg
x	height	m
z	axial coordinate	m

Greek symbols

α	accomodation coefficient	-
	thermal diffusivity	-
ε	porosity	-
θ	solid-liquid-vapour contact angle	°
κ	permeability	m ²
	ratio of the specific heats, c_p / c_v	-
μ	dynamic viscosity	kg/(m·s)
ν	kinematic viscosity	m ² /s
ρ	density	kg/m ³
σ	surface tension	N/m
δ	thickness	m
Γ	function, Eq. (3-48)	
	evaporation rate	kg/(s·m)
	mass flow rate per unit width of condenser	kg/(s·m)
Δ	difference	

Subscripts

avg	average
b	base
	bubble
c	cross-sectional
cap	capillary
cf	closed form
cp	closed porosity
d _h	hydraulic diameter
eff	effective (pore radius)
evap	evaporation
f	fluid
	fin
ficp	fluid in closed porosity
fric	friction
g	gravity
h	hydraulic
hs	hydrostatic
ig	inert gas
iml	immersion liquid
l	liquid
m	measured
	mean

max	maximum
men	meniscus
NCG	Non-condesable gas
0	uncompressed
op	open porosity
r	radial
sat	saturation
sm	solid material
t	total
v	vapour
wf	working fluid
δ	interface

Superscripts

I	step
n	step

Dimensionless number		
Bo	Bond number	$Bo = D \left[g (\rho_l - \rho_v) / \sigma \right]^{1/2}$
Ja	Jakob number	$Ja = \frac{c_p (T_{surface} - T_{sat})}{h_{fg}}$
Pr	Prandtl number	$Pr = \frac{c_p \mu}{k} = \frac{\nu}{\alpha}$
Re	Reynolds number	$Re = \frac{uL}{\nu}$

Contents

Abstract

Acknowledgements

Table of content

List of symbols

1	Introduction.....	1
1.1	Motivation	1
1.2	Background	1
1.3	Objectives.....	2
2	Review of related theory.....	3
2.1	Cooling concepts	3
2.1.1	Pool boiling.....	5
2.1.2	Flat plate thermosyphon.....	11
2.1.3	Flat plate hybrid heat pipe.....	13
2.2	Working fluids.....	15
2.3	Wicks.....	21
2.3.1	Objectives of the wick study.....	21
2.3.2	Introduction.....	21
2.3.3	Wettability of the wick-fluid system.....	21
2.3.4	Wick pumping capacity	22
3	Hybrid heat pipe.....	25
3.1	Wick studies	25
3.1.1	Wicks subject to different heat fluxes.....	25
3.1.2	A one dimensional (1-D) model	25
3.1.3	A two dimensional (2-D) model	26
3.1.4	Experimental procedures for characterization of wick performance	27
3.1.5	Sintered nickel powder wicks for flat vertical heat pipes	38
3.1.6	Performance of compressed nickel foam wicks for flat vertical heat pipes	70
3.1.7	Conclusions of the wick study	80
3.2	Experimental hybrid heat pipe	81
3.2.1	Heat pipe operation	81
3.2.2	Heat transfer limitations.....	81
3.3	The hybrid heat pipe.....	89
3.4	Design and manufacture.....	89
3.5	Test rig, instrumentation and calibration.....	99
3.6	Instrumentation and calibration.....	101
3.7	Calculation model/Heat flow analysis.....	105
3.8	Thermal resistance network	106
3.8.1	Non-condensable gas	119
3.8.2	A spreadsheet model of the hybrid heat pipe.....	121
3.9	Experimental matrix.....	123
4	Results and discussion for the hybrid heat pipe.....	124
4.1	The non-condensable gas volume of the hybrid heat pipe	125
4.2	The overall energy balance	127

4.3	Spreadsheet model calculations	130
4.4	The wick performance.....	136
4.4.1	Wick failure conditions.....	136
4.4.2	Wick performance with potassium	138
4.4.3	Extrapolated performance data for nickel foam wicks	141
4.5	An evaluation of some operating limits from Chapter 3.2.2.....	142
4.5.1	The startup	142
4.5.2	Nucleate boiling	145
4.6	Potassium as working fluid below 500°C	150
5	Conclusions and recommendations for future work	152
	References.....	154
Appendix A	Heterogeneous boiling.....	159
Appendix B	Corrosion experiment.....	163
Appendix C	Rate-of-rise equations	172
Appendix D	The nickel powder.....	179
Appendix E	Thermophysical data	181
Appendix F	The filling and sealing rig	187
Appendix G	Safety, health and environment.....	197
Appendix H	The nitrogen/water heat exchanger	200
Appendix I	Theory of uncertainty analysis.....	202
Appendix J	Electrical systems for the test rig	213
Appendix K	Paper: Analysis of a vertical flat heat pipe using potassium working fluid and a wick of compressed nickel foam	217

1 Introduction

1.1 Motivation

A concept for reducing the net energy consumption in aluminium electrolysis, and enhance the production yield, was described in a patent by Aune, Johansen & Nos [2]. The first stage of their energy recovery system was heat transfer (cooling) panels located in the walls of the electrolysis cells. The motivation for the present study was to investigate potential working fluids and cooling panel concepts, and provide heat transfer data for cooling panel technology that can operate at the specified temperatures and heat loads, representative for aluminium electrolysis cells.

1.2 Background

Production of aluminium by electrolysis requires large amounts of electric energy; typically around 14 kWh are used for each kg of aluminium produced. The energy efficiency (defined as the ratio of theoretical/actual energy consumption) is usually less than 50%, i.e. around 7 kWh/kg aluminium are lost to the surroundings as heat [3]. Between 40% and 60% of the total heat loss from an electrolysis cell escapes through the top, and about 35% through the side walls [3].

Since heat escapes out of the cells along different paths, it may also be recovered in different ways.

Two main approaches are:

- Heat recovery from the flue gas that escapes from the top of the cells. Typical temperatures of flue gases are 120°C to 150°C. From a heat recovery point of view higher temperatures are desirable, especially if conversion of heat to electric energy is the goal. The gas temperature may be increased by decreasing the gas flow rate. Untreated hot flue gas contains dust and pollutants, and this is another challenge related to recovering heat from the flue gas.
- Heat recovery from the side walls of the electrolysis cells. From the side walls it is possible to recover heat in the temperature range of between 400-650°C, with the appropriate heat recovery system.

In the current study heat recovery/cooling units for the side walls are analysed.

1.3 Objectives

Main (overall) objective:

Identify and analyse a technical solution suitable for aluminium electrolysis cell wall cooling in the temperature range of between 400-650°C.

In order to meet the main objective, the following tasks were identified:

- To identify and evaluate some cooling panel concepts and working fluid candidates for the temperature range 400°C to 650°C.
- Analyse the ability of concepts to handle hot spots and nonuniform heat fluxes.
- Design an experimental apparatus for the selected working fluid and cooling panel concept.
- Construct a test rig, where the heat transfer performance/limitations of the cooling panel model could be validated experimentally. The results of the experiments were to supplement the limited existing body of experimental data.
- Develop a predictive model for the experimental model and verify it against the measurements.

Thesis structure:

Chapter 1 presents the motivation, background and objectives for the study.

Chapter 2 presents literature and important advantages and disadvantages concerning cooling panel concepts, working fluid and wicks. Attention is also given to heat pipe performance limits which were taken into account in the cooling panel concept selection process. The preferred solution is a hybrid heat pipe utilizing potassium working fluid.

Chapter 3 presents the design, analysis and testing of wicks and the experimental hybrid heat pipe. The experiments were carried out in a custom-made test rig.

Chapter 4 presents and compares results of theoretical analysis and the experiments. The potential and limitations of the hybrid heat pipe are analysed from the results.

Chapter 5 presents the conclusions from the study, and recommendations for further work. The hybrid heat pipe utilizing a wick on the evaporator surface and potassium working fluid can be, with some further optimization, a highly effective and reliable heat transfer unit for the operating temperature range 400-650°C.

2 Review of related theory

2.1 Cooling concepts

There are several possible ways to make a cooling system for metallurgical furnace sidelinings. The most significant complicating factor is the working temperature range requirement; up to 650°C.

Convective cooling by use of a gas circulating in a loop recovering heat from all the electrolysis cells is one potential solution [4]. Helium gas has been considered due to its high thermal conductivity and its high specific heat capacity compared to other gases [4]. However, the smaller size of the helium atom makes it very difficult to contain in a cooling circuit. The large volume of gas required in a single loop convective cooling system can also represent a safety problem, as all the gas may be released in case of a leak. The convective gas cooling system would require special flow control installations in order to handle different heat loads in different cells as well as varying heat fluxes. The heat transfer coefficient of the gas system is low compared to liquid based cooling systems, so also its capacity to handle local hot spots. Corrosion problems have to be kept in mind even when the inert gas helium is considered as cooling gas; gas impurities (e.g. H₂O, CO, H₂ and CH₄) have at high temperatures been reported to cause corrosion in helium circuits [5]. The cooling gas can be easily heat exchanged with a secondary fluid for electricity production in a Rankine cycle.

Convective cooling by use of a liquid in a single cooling circuit for all the cells would require a huge volume of liquid, which could represent a safety problem just as for the convective gas systems. In addition, working temperatures up to 650°C eliminate the vast majority of liquids often used for convective cooling at lower temperatures, e.g. oils, Galden[®], etc., among the remaining working fluid candidates are alkali metals and high temperature salts. Compared to salts, the alkali metals have the advantage that they can not dissociate. However, the high reactivity of the alkali metals, especially with water and air, is a major complicating factor related to their use as coolants. In the nuclear industry there has been serious accidents related to the use of alkali metals for convective cooling purposes, for instance the “Monju sodium leak” in Japan and the “Y-12 NaK accident” in the USA. In the Monju accident approximately 1 m³ of sodium compounds were detected under a broken thermocouple well, which was the probable origin of the leak [6]. The heat transfer coefficient of liquid convective systems is generally higher than for gas convective systems. The ability to handle local hot spots is also better than for the gas systems, however, special flow control installations would be necessary also for the liquid convective system in order to handle varying heat fluxes and different heat loads in different cells.

Two-phase cooling systems based on evaporation/boiling and condensation in sealed cooling panels would require a limited amount of working fluid in each panel. Similarly, the amount of working fluid released from a leaking panel would be small compared to the potential leak from a convective cooling system. The heat transfer coefficient of a

two-phase cooling system can be very high. A properly designed two-phase cooling system can handle different heat loads in different cells, heat flux variations, and local hot spots up to a certain limit. A two-phase cooling system can be nearly isothermal because very small temperature differences are required for the evaporation and condensation processes. For temperatures up to 650°C there are few working fluid candidates for two-phase cooling systems, just as for the liquid convective system. A secondary circuit is needed for further utilization of the heat.

It was concluded from an evaluation of the major arguments for and against the gas convective cooling, the liquid convective cooling and the two-phase cooling systems as discussed above that an optimized two-phase cooling system would probably be the best system for the cooling of the walls of the aluminium electrolysis cells. Still, within the two-phase category there are several options with regard to concepts and working fluids, e.g. heat pipe, thermosyphon, etc., and the cooling capacity and robustness of the solution is totally dependent on the choices made.

A "heat pipe cooling plate", where a flat cooling plate is made up of individual cylindrical heat pipes contained between two plates [7] is one potential two-phase solution. A somewhat similar concept utilizing cylindrical thermosyphons (rather than heat pipes) was investigated for use up to 350°C prior to the current project [1]. The potential leak from a heat pipe in a cooling plate is small if the heat pipes are not connected with each other. For heat pipe cooling plates exposed for unilateral and non-uniform heat fluxes there may be challenges related to the heat distribution between the different heat pipes, and around the heat pipes. The resulting temperature gradients can cause harmful thermal deformations and thermal contact problems.

A cooling panel utilizing evaporation and condensation of a working fluid was described by Aune, Johansen & Nos [2]. In their patent a cooling panel in the cell wall is the first stage in the wall heat recovery system; the panel will transport the heat just out of the cell wall, see Figure 2-1. Outside/above the cell wall the heat will be transferred to a cooling circuit. Wall cooling panels for temperatures up to 300°C were developed in a joint project between Elkem, Alcoa, and NTNU [1]. One dr.eng study was carried out as part of the earlier work [8]. The panels were based on synthetic organic heat transfer fluids. The development was successful, but the maximum working temperature was limited to around 300°C due to break down of the organic working fluids at higher temperatures. For temperatures up to circa 650°C the following solutions have been analysed in the current work:

- A flat panel utilizing pool boiling
- Flat plate thermosyphon
- Flat hybrid heat pipe

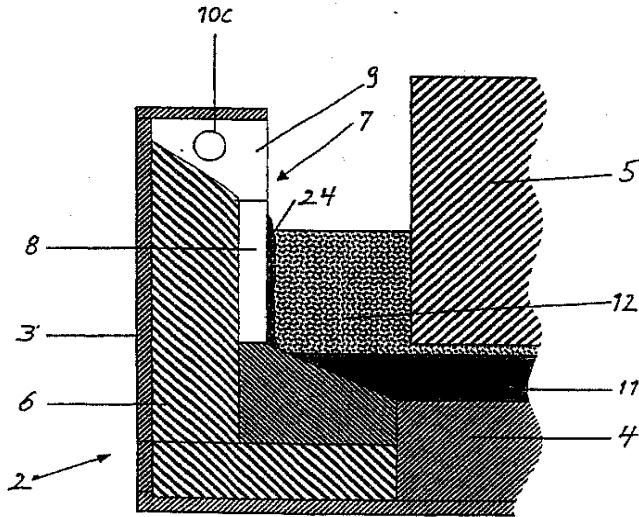


Figure 2-1 From Elkem patent [2]

Table 2-1 Explanation to Figure 2-1

2	Electrolysis cell
3	Steel shell
4	Cathode
5	Anode
6	Insulation
7	Cooling panel
8	Cooling panel evaporator
9	Cooling panel condenser
10C	Cooling circuit
11	Aluminium
12	Electrolyte bath of alumina (Al_2O_3) and cryolite (Na_3AlF_6)
24	Solid electrolyte (side ledge)

2.1.1 Pool boiling

Pool boiling in the cooling panel as shown in Figure 2-2 has several advantages, e.g. a liquid filled evaporator would give very good protection against hot spots, dryout and burnout. A liquid filled panel could alternatively be based on pure liquid convection in the bath and evaporation from the top of the bath, however, due to the geometry of the panel (it should be as thin as possible) a system based on pure liquid convection in the bath and evaporation from the surface of the bath was abandoned (confer discussion in

Chapter 4.5.2). The heterogeneous pool boiling as shown in Figure 2-2 was further analysed.

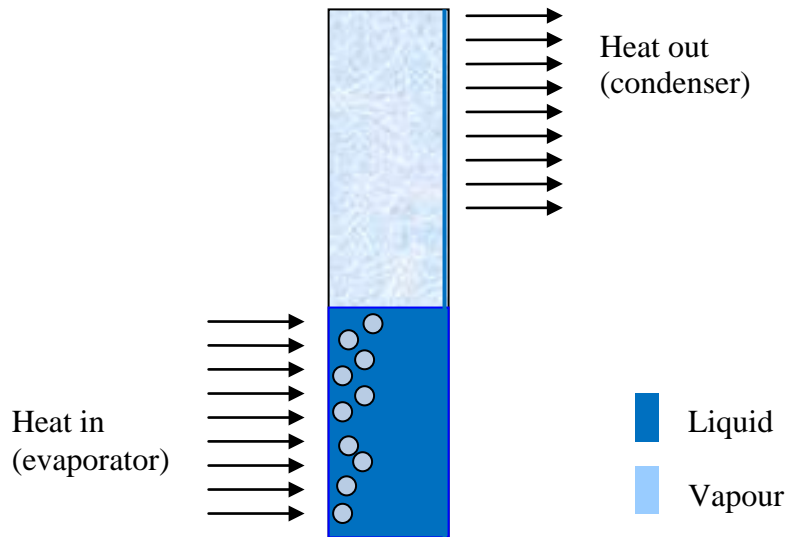


Figure 2-2 Pool boiling.

From a simple pressure balance it can be seen that the pressure inside a vapour bubble in a liquid has to be higher than the pressure of the liquid. For this to be possible the liquid has to be superheated to a temperature corresponding to the vapour pressure inside the bubble. In heterogeneous boiling the bubbles are formed from cavities on the heated surface. In order for the bubbles to start growing and boiling from the cavities a wall superheat is required. The incipient boiling superheat, or wall superheat, is defined as [9]:

$$T_{wall} - T_{sat} \quad (2-1)$$

Neglecting the temperature gradient in the fluid near the surface, the incipient boiling superheat can be estimated as the superheat corresponding to the excess pressure ΔP inside the bubble of radius r . When bubbles grow out of cavities the radius of the cavity mouth is used in the calculation of ΔP . For a pure single component system, a spherical bubble assumption, and by neglecting the effect of curvature on surface tension and vapour pressure one gets [9]:

$$\Delta P = \frac{2\sigma}{r} \quad (2-2)$$

The effect of the interface curvature is to slightly lower the vapour pressure inside the bubble compared to the vapour pressure above a flat interface; an expression for the incipient boiling superheat including the effect of curvature can be found in e.g. Collier and Thome [10]. If inert gas is present in the cavities Equation (2-2) is modified to:

$$\Delta P = \frac{2\sigma}{r} - P_{Inert\ gas} \quad (2-3)$$

$P_{Inert\ gas}$ is here the partial pressure of the inert gas.

The incipient boiling superheats vary a lot from fluid to fluid, so also for the few working fluid candidates for the temperature range 400-650°C.

Alkali metals are known to require high incipient boiling superheats, i.e. for the same cavity size a higher wall superheat for nucleation is required for potassium than for e.g. water [9, 11]. According to Dwyer [9] there are four reasons why liquid metals require higher incipient-boiling-superheats than other fluids:

1. “Liquid metals usually wet solid metal surfaces very well, particularly in the range of temperatures encountered in boiling”.
2. “The alkali metals are very reactive chemically and act to reduce surface oxides of many metals and alloys”.
3. “The solubilities of inert gases in liquid metals increase with an increase in temperature”.
4. “The boiling pressures of liquid metals are generally low with respect to their critical pressures, which means that boiling occurs in that portion of the vapor pressure curve where the slope, dP/dT , is low”.

Dwyer [9] also lists 15 independent variables which may affect the incipient-boiling superheats of liquid metals:

1. Pressure (affects temperature, which, in turn, affects physical properties of liquid and vapor).
2. Partial pressure of inert gas in surface cavities.
3. Heat flux.
4. Flow rate, or Reynolds number.
5. Pressure-temperature history of system.
6. Procedure used to charge the liquid metal to the system (affects amounts of inert gas trapped in surface cavities).
7. Heating method (i.e., direct versus indirect).
8. Inert gas concentration in liquids.
9. Oxygen concentration in liquid.
10. Topography or microstructure, and roughness of the heating surface.
11. Extent of natural circulation (in pool boiling), which is affected by geometry of system.
12. Rate of temperature rise during approach to boiling inception, which depends on experimental method used.
13. High energy nuclear radiation.
14. Operating time on a given system (aging).
15. Manner of controlling the independent variables in approach to boiling state.

Dwyer [9] pointed out that there may be even more factors than the 15 presented above, and considered some of the variables almost impossible to control (for instance cavity size and distribution, and wetting).

The high incipient boiling superheats of alkali metals can cause large temperature fluctuations due to sudden and explosive boiling incipience, as well as unstable boiling. Alkali metal boiling on a wall has been described as “shock boiling”, due to the sudden “explosive” detachment of the bubbles [12]. (Such behaviour was observed in the experimental part of this study for the boiling of potassium, presented in Chapter 4.5.2.) The temperature oscillations caused by boiling cycles are illustrated in principle in Figure 2-3 for a single nucleation site. For alkali metals such oscillations can be large and the waiting periods can be very long (several minutes).

A few experiments reported in the literature indicate that the superheats required for alkali metal boiling may be reduced by special preparation of the heated surface [9]. In such cases boiling nucleation takes place in artificial cavities in the heated surface. From the limited data reported in the literature it is not known how the superheat requirement and boiling stability will develop over time.

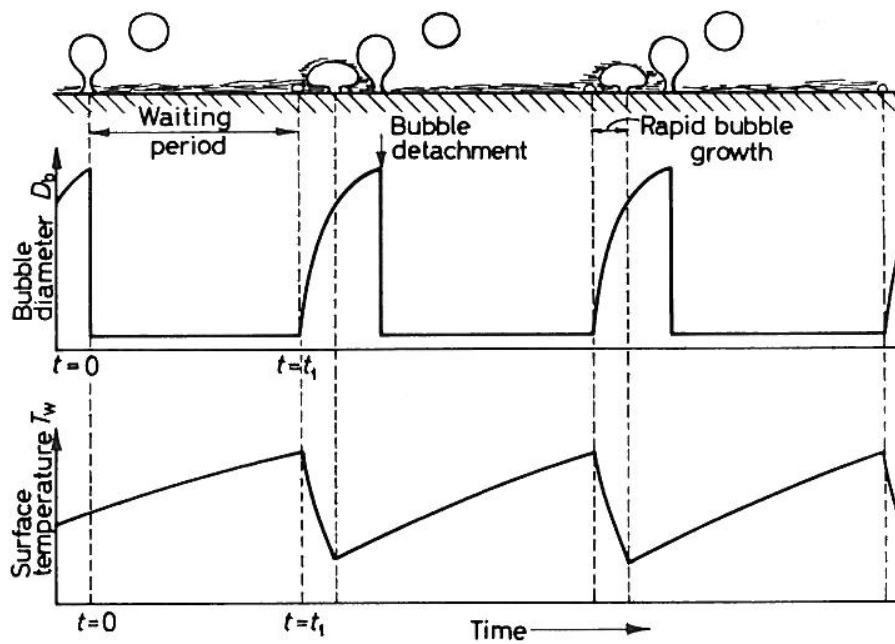


Figure 2-3 Boiling from a single nucleation site [10]

Models for the heating period $t=0$ to $t=t_1$ and for the rapid bubble growth period in Figure 2-3 were developed for the chosen concept and are found in Appendix A.

Homogeneous boiling with potassium working fluid

Homogeneous boiling is described as a process of bubble formation due to clusters of molecules with vapour-like energies coming together to form vapour embryo in bulk liquid [10]. The superheat required for homogenous boiling can be estimated by use of Equation (2-4) [10, 13]:

$$(T_{rg} - T_{rsat}) = 0,905 - T_{rsat} + 0,095T_{rsat}^8 \quad (2-4)$$

Here are:

T_{rg}	The reduced temperature of the liquid, i.e. the absolute temperature of the liquid divided by the critical temperature.
T_{rsat}	The reduced saturation temperature, i.e. the absolute saturation temperature of the liquid divided by the critical temperature.

Equation (2-4) was developed from the van der Waals equation, the Maxwell equal area rule and experimental data for water, some alcohols and some hydrocarbons [13-14]. The validity of Equation (2-4) for potassium is not known. For potassium the critical temperature is $2281 \pm 30K$ [15]. Table 2-2 shows the calculated superheats for potassium at saturation temperatures of interest in this study. Assuming validity of this analysis for potassium, it seems obvious that homogenous boiling of potassium will not take place at these temperatures. Heterogenous boiling requires roughly ~ 10% of the superheats in Table 2-2 and would therefore occur long before the homogenous boiling superheat requirements are obtained, provided that the potassium is receiving heat from a solid surface (e.g. wall, rod, etc.) on which heterogenous boiling can start.

Table 2-2 Superheats required for homogenous boiling

Tsat	$(T_{rg} - T_{rsat})$
[°C]	
400	1391,3
500	1291,3
600	1191,4
700	1091,5

Sulfur considered as a working fluid for a pool boiling solution. Devarakonda and Anderson [16] claimed sulfur as a potential heat pipe working fluid candidate for temperatures above $427^\circ C$. The normal boiling point of pure sulfur, $445^\circ C$, made it to a candidate also for the cooling panels. Unfortunately, the viscosity of pure sulfur is quite high and its temperature variation has a rather peculiar behavior. From the melting point at $119^\circ C$ the viscosity of sulfur increases up to a maximum of about 100 Ns/m^2 at $187^\circ C$, and then decreases again [17]. The peculiar behaviour of the viscosity is shown in Figure 2-4 (Polasek and Stulc [17]).

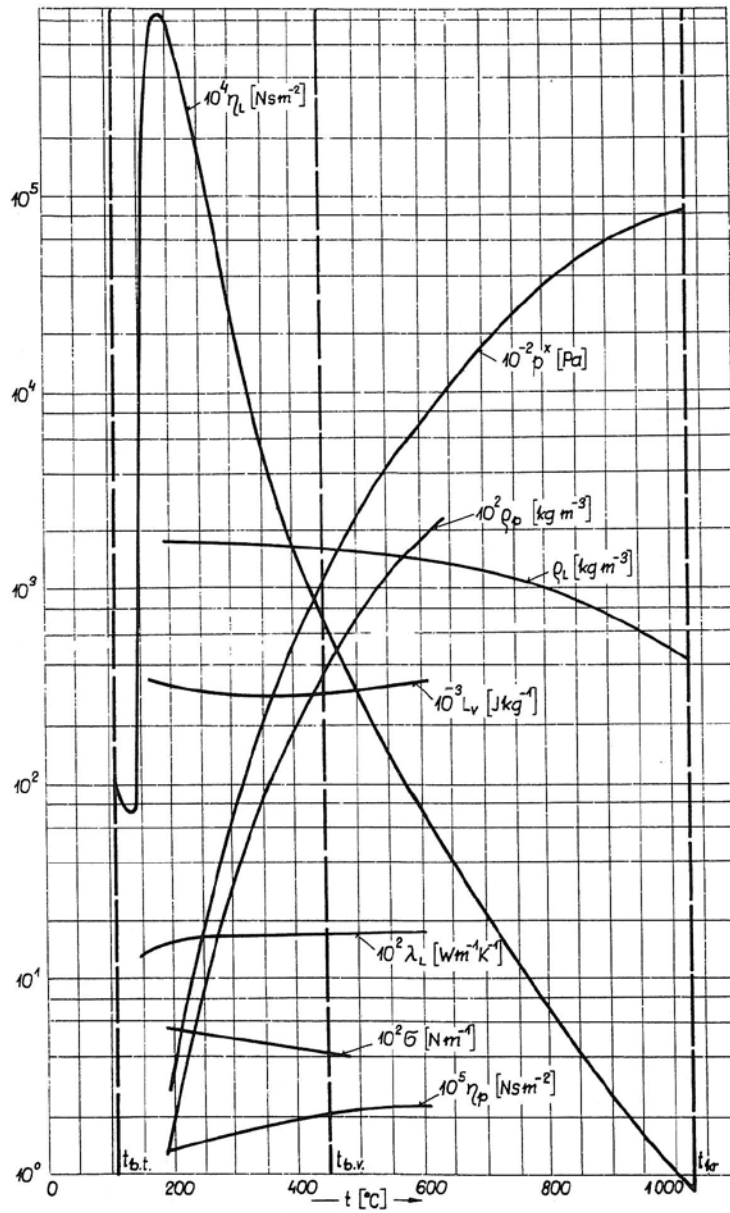


Figure 2-4 Properties of liquid sulfur [17]

Various viscosity reducing additives to sulfur have been suggested in the literature. Addition of halogens, amines or hydrogen sulfides may reduce the viscosity [17]. In 1976 a mixture of sulfur and iodine was proposed as a promising new working fluid for heat pipes [17], where iodine was added to reduce the viscosity. Subsequent studies tested the suitability of the sulfur/iodine mixture as working fluid for thermosyphons [18]. It turned out that the addition of a second component (iodine) did not only bring positive effects, both non-uniform evaporator temperature and reduced condenser temperature have been reported for such zeotropic mixtures, these topics are further addressed in Chapter 2.2. However, at temperatures above 400°C the viscosity of pure sulfur is low enough for use in a cooling panel (thermosyphon).

The corrosiveness of sulfur was another concern. A construction material having longterm compatibility with sulfur is required. Because of great uncertainty related to the corrosiveness of pure sulfur it was decided to do a corrosion experiment with pure sulfur and the most probable construction materials AISI304 and AISI316L. The background for choosing these steels was an experiment where pure sulfur in a heat pipe made of Stainless Steel 304 operating at 350°C was reported to show “No sign of failure” after 1008 hours of operation [19]. This indicated that Stainless Steel 304 could be a suitable construction material also for cooling panels with sulfur. Contrary, Timrot et al. [20] noted that sulfur will react with nickeliferous steels and yield a low melting eutectic of Ni-NiS type. The corrosion experiment with sulfur and the stainless steels 304 and 316L were performed at a temperature of 550°C, as required for the cooling panels. The experiment is described in detail in Appendix B. Conclusion: After 100 hours in sulfur at 550°C both stainless steel samples had been heavily corroded, and due to this sulfur was abandoned as working fluid in the current study.

2.1.2 Flat plate thermosyphon

In a thermosyphon the condenser is placed above the evaporator, so the transport of the condensate to the evaporator is achieved by the gravity force. A flat plate thermosyphon, where the evaporator is cooled by a film of evaporating condensate, was considered as a possible solution here. Challenges related to the flat plate thermosyphon were:

- To have a uniform distribution of the condensate over the evaporator width.
- To cover the whole evaporator plate with a sufficiently thick condensate film to withstand local hot spots (areas of high heat flux).

The flat plate thermosyphons could be divided into two types:

1. Evaporator and condenser on the same side.
2. Evaporator and condenser on opposite sides.

These two types are discussed in the next chapters.

Evaporator and condenser on the same side

When the condenser is on the same side as the evaporator the condensate can simply flow directly down from the condenser to the evaporator surface, as illustrated in Figure 2-5. Such a thermosyphon would require a careful startup as the evaporator and condenser would be initially dry. Ideally heat should from the start just be supplied to the lower part of the evaporator.

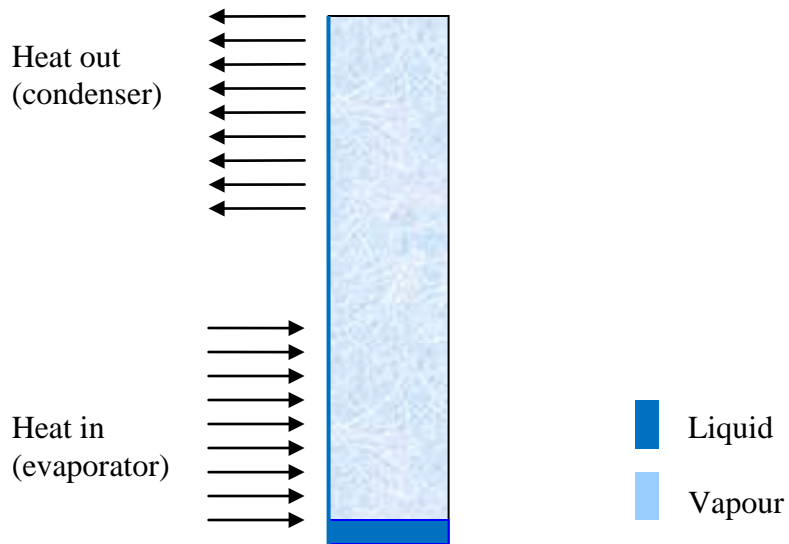


Figure 2-5 Evaporator and condenser on the same side

If the whole panel is out of level there will be some areas of the evaporator which are not covered by condensate film [1], as illustrated in Figure 2-6. This would lead to loss of cooling in this zone. The flat plate thermosyphon with the evaporator and condenser on the same side was therefore considered as not robust enough.

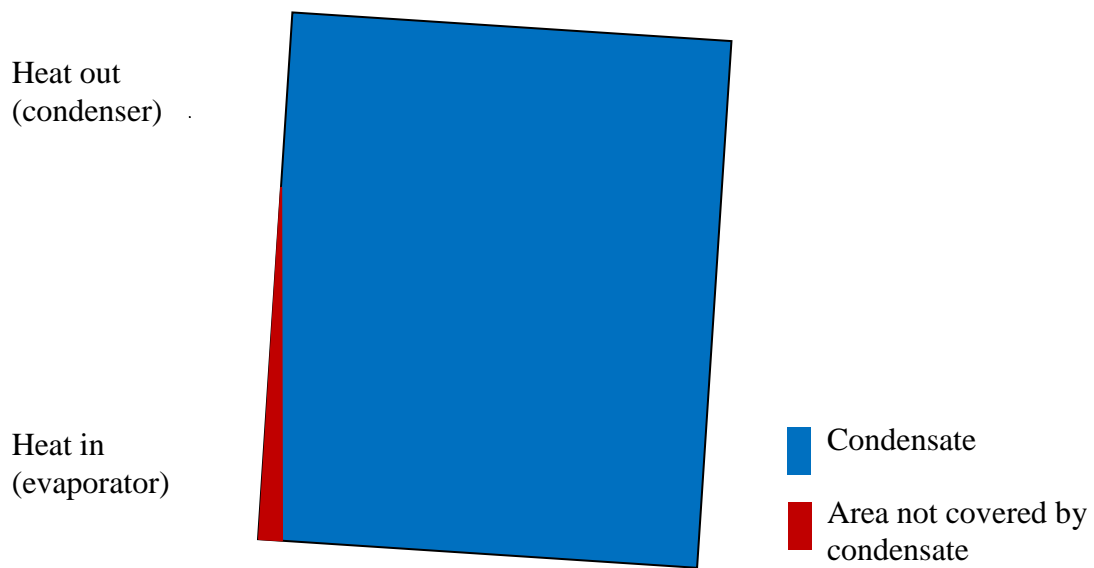


Figure 2-6 A panel out of level

Evaporator and condenser on opposite sides

If the condenser was on the opposite side of the evaporator the condensate had to be transferred from the condenser side to the evaporator side. One way to do this was to use guides to bring the condensate to the top of the evaporator side [1], as illustrated in Figure 2-7. There has to be open space between the guides to allow the vapour from the evaporator to reach the condenser.

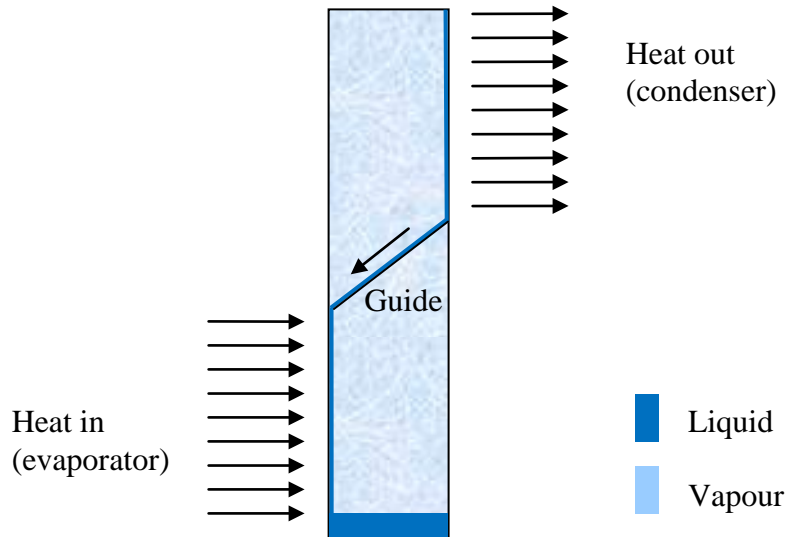


Figure 2-7 A panel with guides for condensate

Still, if the panel is out of level there will also be some areas of the evaporator which are not covered by condensate film. Therefore, this concept was neither considered as robust enough.

2.1.3 Flat plate hybrid heat pipe

The flat plate hybrid heat pipe has a wick on the evaporator surface for working fluid condensate distribution. The advantage of this solution over the wickless solution is that the wick will continue to distribute the working fluid condensate all over the evaporator even when the panel is out of level, if it is properly designed. The wick will also to some extent be able to distribute the condensate such that high heat flux areas will receive more condensate.

If the condensate is supplied to the bottom of the wick it has to be transported up in the wick by the capillary force. This is illustrated in Figure 2-8.

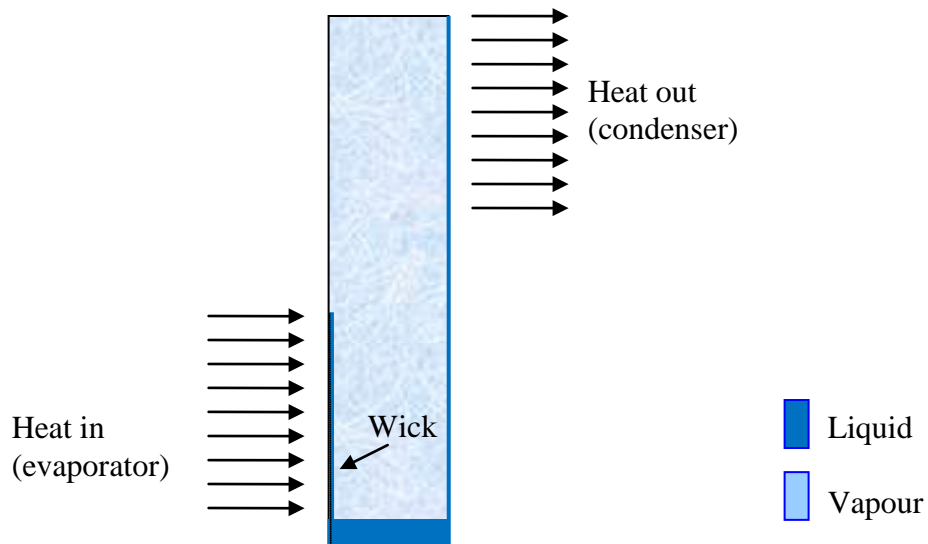


Figure 2-8 A panel with wick for condensate distribution

The heat transport capacity of this panel is very dependent on the capacity of the wick, both with regard to massflow and lifting height of condensate.

If the condensate is supplied to the top of the wick the gravity force will contribute to the vertical distribution as well. This concept in Figure 2-9 is a combination of the concepts in Figure 2-7 and in Figure 2-8.

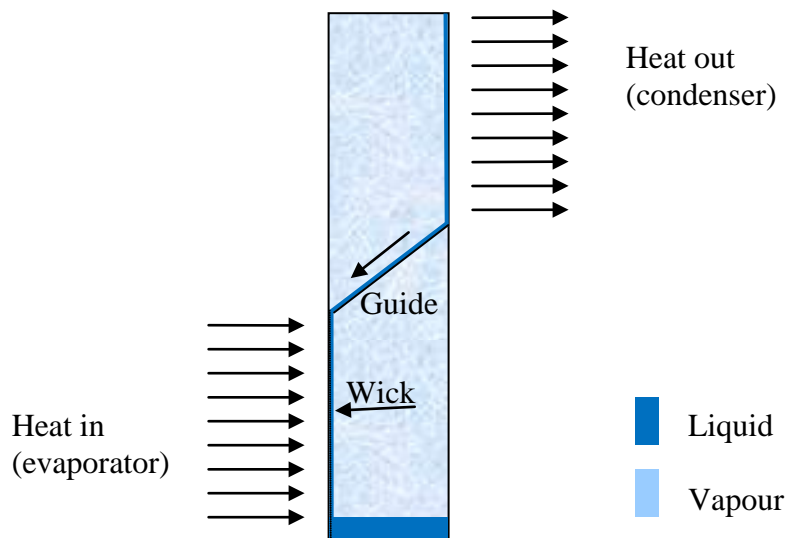


Figure 2-9 A panel with both guides and wick

Conclusion of the cooling concept study

The flat plate hybrid heat pipe will give better condensate distribution over the evaporator surface than the simple wickless flat plate thermosyphon. However, the capacity of the hybrid heat pipe is very dependent on the capacity of the wick. A wick study was therefore carried out in order to determine the capacities of real wicks. The wick study is presented in Chapter 2.3.

2.2 Working fluids

Alkali metals and sulfur were discussed as working fluid candidates for pool boiling in Chapter 2.1, however, in this study a wider literature survey for working fluid candidates for heat pipes and thermosyphons for operating temperatures in the range 400-650°C was carried out.

The requirements for the working fluid candidates were:

- Chemical stability up to at least 700°C.
- Thermophysical data available.
- Vapour pressure of less than 10 bar for temperatures up to 700°C.
- Compatible construction material(s) available.
- Low toxicity.

In the heat pipe literature working fluids are sometimes evaluated by their Merit number, M , defined as [11]:

$$M = \frac{\rho_l \sigma_l h_{fg}}{\mu_l} \quad (2-5)$$

I.e. from the Merit number the following characteristics are seen as advantageous:

- High liquid density; because it reduces the volume flow.
- High liquid surface tension; because it gives high capillary pressure.
- High latent heat of evaporation; because it reduces the mass flow.
- Low liquid dynamic viscosity; because it gives low frictional pressure drop.

In addition, high liquid thermal conductivity is advantageous when heat is to be conducted through a wick filled with working fluid, or through the condensate film.

The Merit numbers for some working fluids are compared in Figure 2-10, however, in the working fluid selection process many additional factors have to be taken into account, e.g. melting point, boiling point, availability, price, etc.

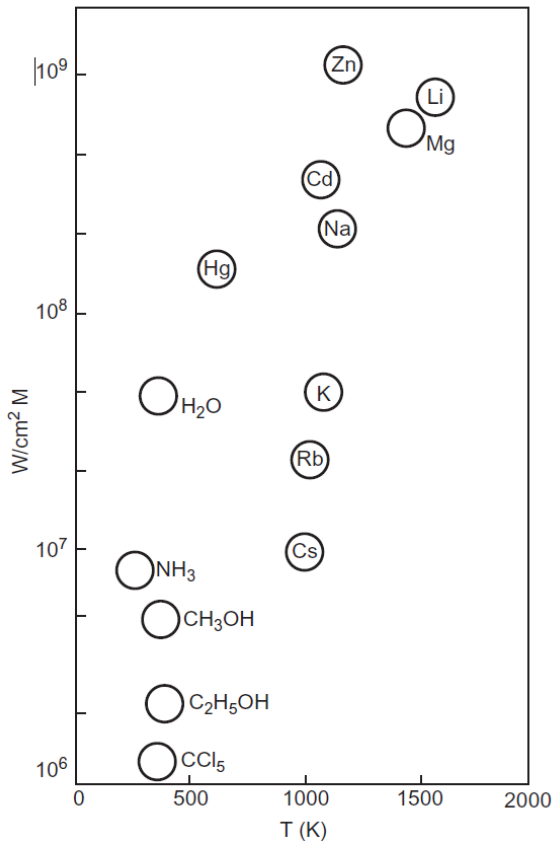


Figure 2-10 Merit number for some working fluids [11]

Both single component and two-component working fluids were considered in the literature study. The number of applicable working fluids for the considered temperature range turned out to be very limited, as discussed in the following paragraphs.

New working fluids

Several new working fluid candidates for temperatures up to around 550°C were discussed by Devarakonda and Anderson [16]. However, it was concluded that none of them were good candidates for this study, and reasons for this were:

- Unknown thermo-chemical stability.
- Lacking or incomplete physical data.
- Unknown compatible construction materials.
- No or limited data on use.

Some arguments for and against the 4 most interesting new working fluids candidates presented by Devarakonda and Anderson [16] are summarized in Table 2-3.

Table 2-3 Pros and cons for some new working fluid candidates [16].

Working fluid candidate	For	Against
Aluminium iodide	Normal boiling point 385°C. Vapour pressure 1.5-10.5 bar for the range 400-600°C. Non-flammable.	No reports on use in heat pipes or thermosyphons. Corrosive.
Antimony tribromide	Normal boiling point 280°C.	Harmful by inhalation and if swallowed. Dangerous for the environment. No known compatible construction material. No reports on use in heat pipes or thermosyphons.
Silicon tetra iodide	Normal boiling point 287.5°C.	Incomplete physical data. No reports on use in heat pipes or thermosyphons.
Titanium tetra iodide	Normal boiling point 377°C.	Corrosive. Causes burns.

None of the listed new working fluid candidates were selected for the current study due to the listed “cons”.

Alkali metals

The alkali metals potassium and sodium are established working fluids for standard high temperature circular tubular heat pipes. Other alkali metals are less used, mainly due to high costs of the alkali metal itself and/or of the compatible envelope material. The useful operating temperature range for potassium has been defined as 500-1000°C, with the lower temperature limit being determined by “the vapour pressure limit” [21]. The vapour pressure limit is further discussed in Chapter 3.2.1. According to Faghri [21], as a rule of thumb, the useful range of a working fluid is above a saturation pressure of 0,1 atm. The useful operating temperature range of sodium has been defined as 600-1200°C [21].

The vapour pressures of potassium and sodium are very low in the temperature range 400-650°C, see Figure 2-11.

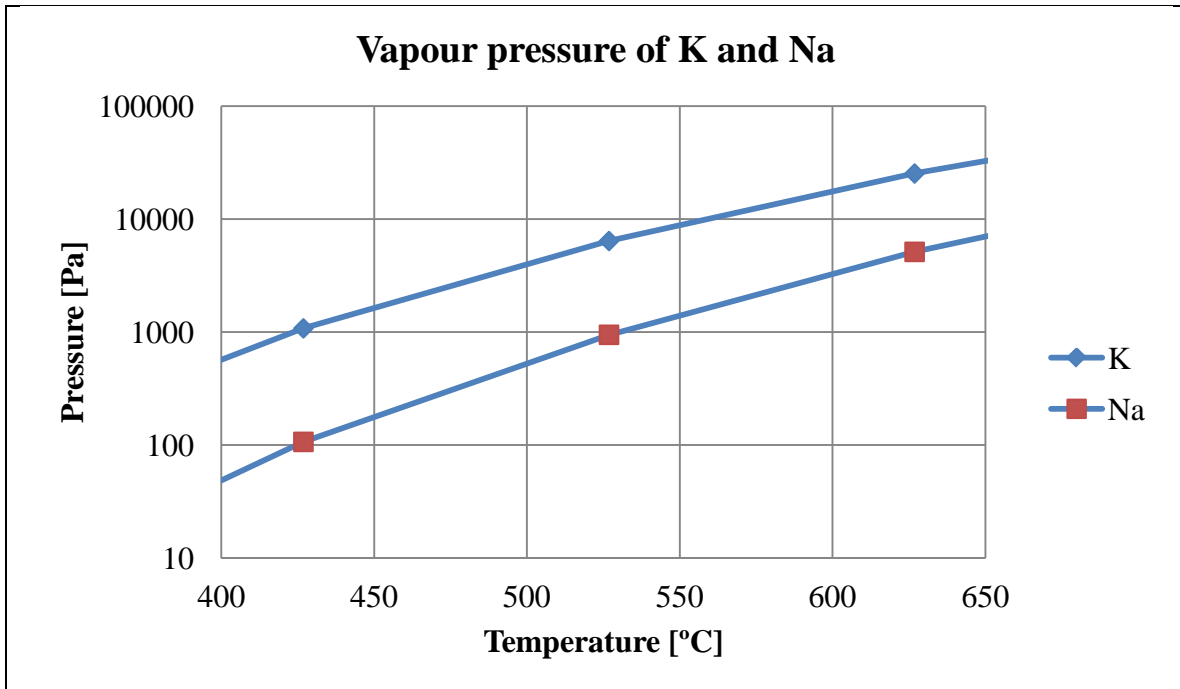


Figure 2-11 The vapour pressure of potassium and sodium [15]

The vapour pressure of the working fluid is important for the performance of the wick (confer Chapter 3.2.2) as well as for the superheat required for the onset of nucleate boiling (confer Chapter 4.5.2). For the performance of the wick in temperature range of this study (400-650°C), potassium was considered as the best working fluid, simply because it has higher vapour pressure than sodium. Still, 400°C is below the useful range defined by Faghri [21], so the usefulness of potassium below 500°C was one issue to investigate in this study.

Potassium dimers and tetramers

Potassium atoms in vapour phase are known to associate into dimer and tetramer molecules to some extent, as shown in Figure 2-12 from Ewing et al. [22]. The working temperature range of interest in this study was 400-650°C. The mass fractions of dimers and tetramers are evidently very small at temperatures below 700°C, and their existence has therefore been neglected in this study. Still the following findings of Ewing et al. [22] are worth mentioning: *“...increasing temperature favors dissociation of each complex molecule while increasing pressure favors its formation. It is interesting that at saturation conditions the effect due to increasing pressure overbalances that due to increasing temperature, and both the dimer content and the apparent tetramer content increase with temperature.”*

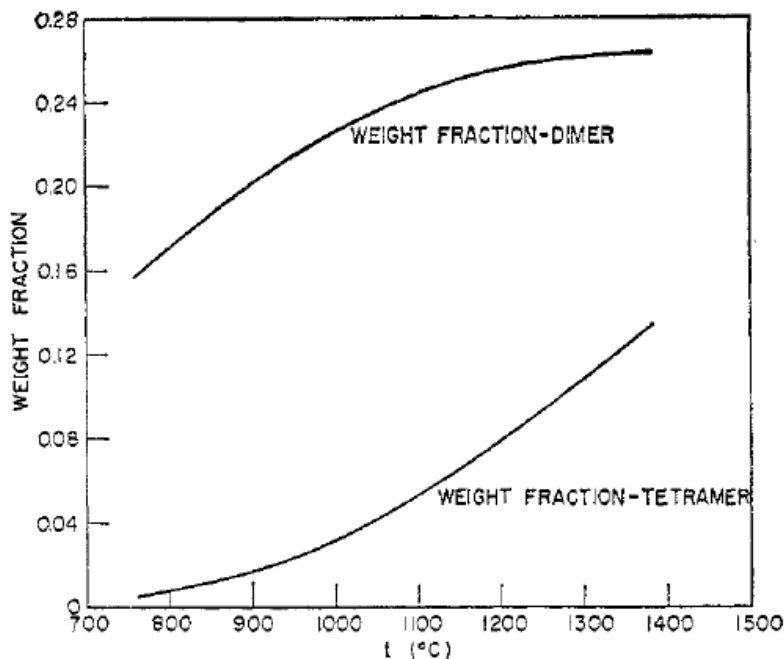


Figure 2-12 Potassium dimers and tetramers [22].

The reactivity of potassium

The reactivity of the alkali metals, especially with water and air, demands special handling procedures [21]. In order to avoid contact with air, pure alkali metals can be handled in high quality gloveboxes filled with argon.

Due to the reactivity it is recommended to carry out testing of heat pipes using alkali metal working fluids in safety chambers, filled with inert gas or vacuumized [21].

The reactivity of alkali metals also limits the number of available construction materials for the cooling panel. Nickel, the low cost AISI304 steel and AISI347 were reported to be compatible with potassium [23].

Mixed working fluids

Working fluids can consist of more than one component. If the mixed working fluid behaves like a single component fluid it is called an azeotropic mixture, i.e. there will be no change in the phase compositions during phase change. To this authors knowledge there exists no azeotropic high temperature working fluid mixtures, but at least two non-azeotropic (zeotropic) high temperature working fluids; NaK and sulfur-iodine.

Non-uniform evaporator temperature

Zeotropic mixtures have been reported to give non-uniform evaporator temperature in heat pipes [24]. They have also been reported to give reduced condenser temperature in thermosyphons [18, 25]. Zeotropic fluids are therefore not ideal working fluids for heat recovery systems where minimum temperature drop is desired.

The mechanisms causing the nonuniform evaporator temperature in a heat pipe have been described by Tarau et al. [24] for an eutectic mixture of potassium and sodium. The non-uniform evaporator temperature was explained by the distillation which took place when the zeotropic fluid evaporated. The evaporation temperature of the liquid in the heat pipe wick increased along the wick length, and approached the evaporation temperature of the least volatile component.

Reduced condenser temperature

The reduced condenser temperature in systems with zeotropic working fluids was observed by Chaffey et al. [18] and Shilovich et al. [25] in experiments with mixtures of sulfur and iodine in thermosyphon tubes. Iodine was in this system the volatile component; it has a boiling point far below the boiling point of sulfur. Both research groups measured considerable lower temperatures on the outside of the condensers than expected from the working pressures (evaporator temperatures and total system pressures). Inside the thermosyphon the temperature was almost constant, but on the outside there was a considerable temperature difference between the evaporator and the condenser part.

The condenser temperature problem was believed to be caused by the zeotropic behavior of the sulfur/iodine mixture. When the mixture evaporated the resulting vapour phase did not have the same concentration of the two components as the liquid phase, which can also be seen from the phase envelope of such mixtures. During the condensation the condensate was enriched with sulfur, and the gas phase was enriched with iodine. The reduced amount of sulfur in the gas phase decreased the partial vapor pressure of sulfur, especially at the condenser wall, which again decreased the condensation temperature of the sulfur. Consequently, for the zeotropic mixture the condensation took place at a lower temperature at the condenser wall than it would for pure sulfur. The total pressure in the condenser was, however, kept high and at the overall system pressure, by the iodine enriched gas phase.

Indications of iodine separation from the sulfur was also visually observed in a quartz tube, according to Ernst [26].

Conclusion of the working fluid study

Fluid cracking, low critical temperatures, material incompatibility, toxicity, non-azeotropic (zeotrope) behavior of mixtures, low vapour pressures and high incipient boiling superheats are among the factors which excluded many working fluid candidates. Utilization of new working fluid candidates has to be preceded by studies of their thermophysical properties as well as compatibility experiments with potential materials for the wick and the envelope. For alkali metals there exist useful data on thermophysical properties and material compatibility. The conclusion of the working fluid study was therefore that the alkali metal potassium was the most suitable working fluid for the cooling panels. However, potassium is not a simple fluid to deal with due to its reactivity with air and moist. It is necessary to handle potassium under an inert gas or in vacuum.

2.3 Wicks

2.3.1 Objectives of the wick study

The objectives were to develop and characterize wicks for use in the hybrid heat pipe using potassium working fluid. Wick characterization experiments were performed using a model fluid; heptane. Utilizing thermophysical data for potassium, the results obtained with heptane were transformed to potassium and the performance with potassium was predicted.

2.3.2 Introduction

Wicks with uniform pore structure are often applied in heat pipes, however, with more advanced wicks the heat pipes could have performed better. Various methods exist for wick performance enhancement, Faghri [21] has briefly reviewed some of them. Wicks with arteries and composite wicks made up of layers with different permeabilities and effective pore radii have been developed [21]. Problems with composite wicks have also been reported [27].

In a patent from 1979 Marcus and Edwards [28] described a heat pipe wick which had graded pore size in the axial direction. Their proposed pore size grading was such that it followed the liquid-vapour pressure difference perfectly everywhere inside the heat pipe. This way the flow resistance in the wick was kept at a minimum. The graded wick described by Marcus and Edwards [28] requires detailed knowledge about the pressure distribution in the heat pipe, both in the liquid and in the vapour phase. The pressure distribution is a function of both heat flux and temperature, so strictly the optimum wick can only be designed for one operating heat flux and temperature.

2.3.3 Wettability of the wick-fluid system

Good wetting of the wick material by the working fluid is vital for the success of the wick. Wetting can be analyzed by use of interfacial (surface) tensions. The surface tension of a solid or liquid, or the interfacial tension between them, is defined as [29]:

$$\sigma = \left(\frac{\partial G}{\partial A} \right)_{T,P} \quad (2-6)$$

where G is Gibbs free energy and A is surface area. Spontaneous wetting requires that the Gibbs free energy is reduced ($\Delta G < 0$), i.e. the surface tension of the unwetted solid surface has to be higher than the solid-liquid interfacial tension plus the liquid-vapour interfacial tension.

The surface energy of a solid surface depends on its structure (crystalline/amorphous) and/or on molecules adsorbed on it. Physically or chemically adsorbed molecules can reverse the wettability of a surface with respect to a fluid. Wettability reversal probably due to adsorption was encountered in this work for the nickel/water system [30]. Hard materials (in pure state) do usually have relatively high surface tensions [29]. Molecules in air and contaminants may therefore easily adsorb to the clean hard solid surfaces, reduce the surface energy, and thereby alter the wettability.

Wettability, expressed by the contact angle between the solid and the liquid, will also be shown (in Chapter 2.3.4) to be a necessary parameter in wick capacity estimates for different working fluids.

2.3.4 Wick pumping capacity

In the hybrid heat pipe the purpose of the wick is to distribute the condensate over the evaporator surface. The ideal wick would:

1. Pump the condensate to the required lifting height.
2. Have sufficient capacity to deal with the highest condensate flow required by the maximum supplied heat flux and hot spots.
3. Have minimum thickness in order to minimize the thermal resistance.

The driving force in the wick is the capillary pressure. The capillary pressure in wicks is usually expressed by the Young-Laplace equation for a circular tube [31]:

$$\Delta P_{cap} = \frac{2 \cdot \sigma \cdot \cos \theta}{r} \quad (2-7)$$

The effective radius (r_{eff}), is introduced to account for the wick structure and the contact angle:

$$\Delta P_{cap} = \frac{2\sigma}{r_{eff}} \quad (2-8)$$

where

$$\cos \theta = \frac{r}{r_{eff}} \quad (2-9)$$

In general, the contact angle will be different for different fluids in contact with the same porous material. The effective pore radius is therefore equal only when the contact angles are equal. From Equation (2-9) the following relation can be derived:

$$\frac{r_{eff, fluid1}}{r_{eff, fluid2}} = \frac{\cos \theta_{fluid2}}{\cos \theta_{fluid1}} \quad (2-10)$$

From Equation (2-7) the relation between the capillary pressures of two different fluids in contact with the same porous material becomes:

$$\Delta P_{cap,fluid2} = \frac{\sigma_{fluid2} \cdot \cos \theta_{fluid2}}{\sigma_{fluid1} \cdot \cos \theta_{fluid1}} \cdot \Delta P_{cap,fluid1} \quad (2-11)$$

In order for the wick to work properly the capillary pressure has to be equal to, or larger than, the hydrostatic pressure plus the frictional pressure drop in the wick. (Momentum changes not being specified by a separate term here). Depending on the wick properties the maximum lifting height is therefore limited by the effective pore radius, the hydrostatic pressure and the flow related friction pressure drop. The hydrostatic pressure of the liquid in the wick is:

$$\Delta P_{hs} = -\rho g x \quad (2-12)$$

”x” is the height of the wetted portion of the wick. The flow-related friction pressure drop in porous structures is given by Darcy’s law [31]:

$$\frac{dP_f}{dx} = -\frac{\mu}{\kappa \rho A_c} \frac{dm}{dt} \quad (2-13)$$

For a uniform heat flux along the wick length (i.e. the evaporation rate per unit height is constant) the mass flow rate of liquid in the wick has a linear profile, see Figure 2-13.

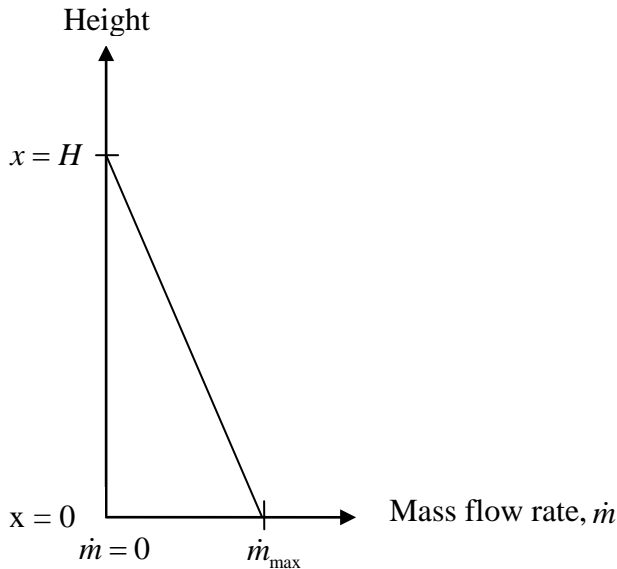


Figure 2-13 The wick mass flow rate for uniform evaporation rate

From Figure 2-13 the wick mass flow rate can be expressed as a function of height (x):

$$\dot{m} = \frac{dm}{dt} = \left(\dot{m}_{\max} - \frac{\dot{m}_{\max}}{H} x \right) \quad (2-14)$$

Equation (2-14) inserted into Darcy's law (Equation (2-13)) and integrated from x=0 to x=H yields

$$\Delta P_f = (P_H - P_0) = -\frac{\mu}{\kappa \rho A_c} \dot{m}_{\max} \left(\frac{H}{2} \right) \quad (2-15)$$

Disregarding momentum changes for the liquid, the pressure balance at the liquid front in the wick is:

$$\Delta P_{cap} + \Delta P_{hs} + \Delta P_f = 0 \quad (2-16)$$

$$\frac{2\sigma}{r_{eff}} - \rho g H - \frac{\mu}{\kappa \rho A_c} \dot{m}_{\max} \left(\frac{H}{2} \right) = 0 \quad (2-17)$$

Equation (2-17) can be solved for the maximum mass flow rate of liquid at the bottom of the wick:

$$\dot{m}_{\max} = \frac{2\kappa \rho A_c}{\mu H} \left(\frac{2\sigma}{r_{eff}} - \rho g H \right) \quad (2-18)$$

The mass flow rate is directly related to the supplied heat through the relation:

$$Q = \dot{m}_{\max} \cdot h_{fg} \quad (2-19)$$

yielding the maximum uniform heat flux that can be applied to the wick:

$$q = \frac{Q}{A_{evap}} \quad (2-20)$$

In order to calculate the wick capacity as defined by Equation (2-18) it is necessary to have knowledge of the permeability and the effective pore radius of the wick. Both the permeability and the effective pore radius depend on the wick production method, and this will be addressed in subsequent chapters.

3 Hybrid heat pipe

3.1 Wick studies

3.1.1 Wicks subject to different heat fluxes

In case of uneven melting furnace sidewall wear or breakup, a heat pipe in the wall of an electrolysis cell can experience different heat fluxes at different heights, as well as concentrated hot spots. It is therefore of interest to examine the ability of wicks to deal with hot spots and varying heat fluxes.

In order to study the effects of nonuniform heat flux the wick-covered evaporator was divided into three sections with individual heat flux control, see Figure 2-14.

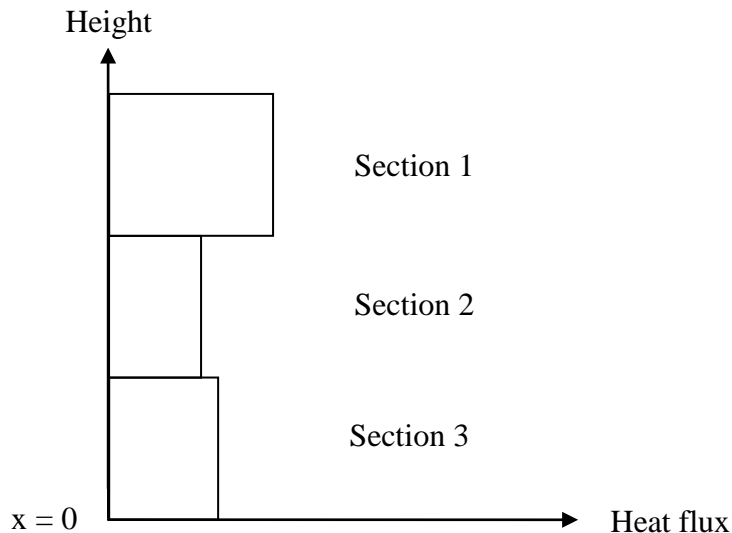


Figure 2-1 Nonuniform heat flux

3.1.2 A one dimensional (1-D) model

Heat flux variations in the vertical direction can be analysed by use of a 1-D model. Odden [32] developed a 1-D model for the pressure drop in a wick exposed to nonuniform heat flux, and compared the two cases in Figure 2-15. The conclusion from his analysis was that a high flux in the upper section (section 1) was most detrimental. Having the highest heat flux in section 1 resulted in the highest total pressure drop, and thereby the lowest wick capacity overall. This finding was reasonable because a high

flux section on the top meant that much liquid had to be transported through the lower sections, which would cause large frictional pressure drop [1].

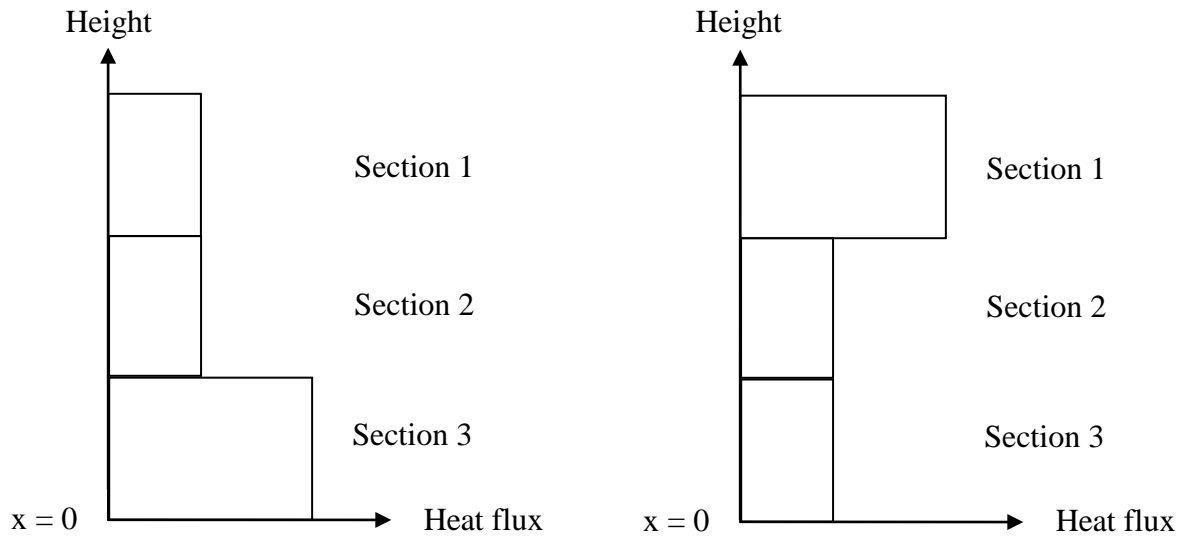


Figure 2-2 High heat flux in lower and higher section respectively.

3.1.3 A two dimensional (2-D) model

Kristjansson [33] developed a numerical 2-D model for the pressure distribution in a uniform wick exposed to a hot spot. He found that the maximum heat flux that the wick could handle decreased when the hot spot was positioned higher up on the wick, which is in accordance with the results from the 1-D model (Chapter 3.1.2). Kristjansson [33] also showed that a hot spot was least detrimental when it was located at the vertical centerline of the wick, where it could have liquid supply from both sides. The most detrimental hot spot position was at one of the upper corners of the wick, see Figure 2-16. Hot spots in the upper corner positions resulted in the longest flow paths for the liquid, and therefore also the highest pressure drops and the lowest average wick capacities. A summary of the theory applied by Kristjansson [33], and more details from his analysis, have been included in [34] enclosed in Appendix K.

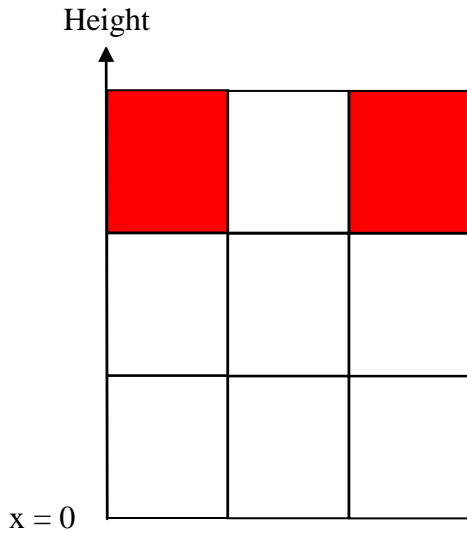


Figure 2-3 The most detrimental hot spot positions.

3.1.4 Experimental procedures for characterization of wick performance

Wick porosity determination

The experimental determination of porosity in this study was based on the procedure described in the international standard ISO 5017:1998(E).

Three different measurements were carried out in the porosity determination:

- m_1 : The mass of the dry sample measured by weighing in air.
- m_2 : The apparent mass of the sample measured when the sample was submerged in an immersion liquid (isopropanol was used in this study).
- m_3 : The mass of the sample soaked with immersion liquid (isopropanol).

The procedure:

First the weight (m_1) of the dry sample was measured. Then the sample was transferred to a vacuum clock and kept under vacuum (less than 20 mbar pressure) for at least 15 minutes. The sample was then flooded with immersion liquid (isopropanol). Thereafter a 30 minutes evacuation of the beaker with the sample still immersed in the liquid. Air was then let slowly into the vacuum clock. After 30 minutes waiting the beaker with the sample was transferred to a scale where the weight (m_2) of the sample was measured while it was still kept submerged. The sample was then taken up of the liquid and kept in

a wet cloth during transfer to another scale where the weight (m_3) of the sample soaked with the liquid was measured.

Three different porosities were defined:

- The apparent (open) porosity, which was due to the open pores of the sample.
- The closed porosity, which was due to the closed pores of the sample.
- The true porosity, which was the sum of the apparent and closed porosities.

In this study it was the apparent (open) porosity which was of interest. The apparent (open) porosity π_a was calculated from:

$$\pi_a = \frac{m_3 - m_1}{m_3 - m_2} \quad (3-1)$$

The masses in Equation (3-1) were defined by the Equations (3-2), (3-3) and (3-4) written by use of the subscripts of Table 3-1:

Table 3-1 Subscripts

sm	solid material
ficp	fluid in closed porosity
op	open porosity
cp	closed porosity
iml	immersion liquid

$$m_1 = \rho_{sm} \cdot V_{sm} + \rho_{ficp} \cdot V_{cp} - \rho_{air} (V_{sm} + V_{cp}) \quad (3-2)$$

$$m_2 = \rho_{sm} \cdot V_{sm} + \rho_{ficp} \cdot V_{cp} - \rho_{iml} (V_{sm} + V_{cp}) \quad (3-3)$$

$$m_3 = \rho_{sm} \cdot V_{sm} + \rho_{ficp} \cdot V_{cp} + \rho_{iml} \cdot V_{op} - \rho_{air} (V_{sm} + V_{cp} + V_{op}) \quad (3-4)$$

The expressions for m_1 , m_2 and m_2 put into Equation (3-1) gives:

$$\pi_a = \frac{\rho_{iml} \cdot V_{op} - \rho_{air} \cdot V_{op}}{\rho_{iml} \cdot V_{op} - \rho_{air} (V_{sm} + V_{cp} + V_{op}) + \rho_{iml} (V_{sm} + V_{cp})} \quad (3-5)$$

Since $\rho_{air} \ll \rho_{iso}$ the expression for the apparent (open) porosity reduces to:

$$\pi_a = \frac{m_3 - m_1}{m_3 - m_2} \approx \frac{\rho_{iml} \cdot V_{op}}{\rho_{iml} \cdot V_{op} + \rho_{iml} (V_{sm} + V_{cp})} = \frac{V_{op}}{V_{op} + (V_{sm} + V_{cp})} \quad (3-6)$$

If there is no closed porosity in the sample Equation (3-6) becomes:

$$\pi_a = \frac{V_{op}}{V_{op} + V_{sm}} \quad (3-7)$$

Equation (3-7) gives a clear volumetric interpretation of the open porosity of the sample, it is the volume of the open pores divided by the total volume of the sample.

Wick permeability and effective pore radius

The rate-of-rise experiment offers simultaneous determination of r_{eff} and κ . The rate-of-rise experiment [31] has some resemblance to the use of the wick in the hybrid heat pipe, in both cases the wick is operating in vertical position.

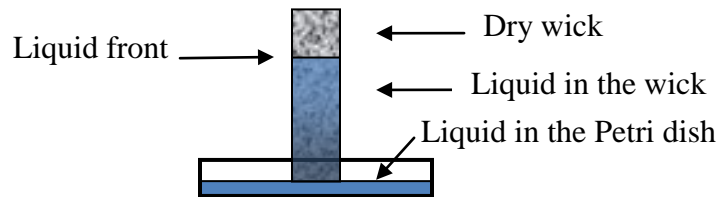


Figure 3-4 Spontaneous rate-of-rise

In the rate-of-rise experiment the spontaneous rate-of-rise of a liquid in a porous wick is measured, as shown in Figure 3-4. The rate-of-rise experiment was earlier considered as not easily repeatable [35] due to factors such as evaporation of liquid from the wick and problems to detect the liquid front. Increased accuracy has recently been achieved by new methods for liquid front detection and data analysis [31]. The new improved approach by Holley & Faghri [31] has been used here, but with somewhat different data analysis.

The rate of rise is calculated from mass and time measurements [31], instead of visual detection of the liquid front. The governing equation for the rate-of-rise test was therefore derived below in terms of mass (m) instead of height (x).

The inertia term is neglected in the derivation of the rate-of-rise test equations. It was shown in the work by Holley and Faghri [31] that the model without the inertia term fit the experimental data very well. The physical justification for neglecting the inertia term is that the rate-of-rise in the wicks is slow.

When the wick is attached to a substrate (e.g. the heat pipe wall) there will be friction between the fluid and the substrate. The relative importance of this friction compared to the total friction obviously depends on the thickness of the wick. In a study with nickel foam from RECEMAT the friction against the substrate was significant for foam thickness below 5 mm [36]. The influence of the substrate can be investigated in very

Careful rate-of-rise experiments. However, for the wicks attached to a substrate in this study the friction against the substrate has been neglected.

Model fluid

Heptane was chosen as model fluid in the rate-of-rise experiments mainly because it wets nickel well and because it is not very volatile at room temperature.

Experimental setup and procedure

The experimental setup for the measurement of the rate-of-rise of liquids in wicks is shown in Figure 2-18. A petri dish containing a model fluid (heptane) is placed on the balance. The mass of the petri dish with the liquid is measured by the balance, a Mettler AT261 Deltarange, connected to the serial (RS232) port of a PC. A LabVIEW program takes care of the data logging of time, mass and temperature. The fastest possible logging rate for the mass measurements is around one measurement per 700ms, due to limitations of the balance and the serial port connection. The datapoints (time, mass) are stored in a file. The temperature of the liquid in the petri-dish is measured by the use of a thin thermocouple, connected to the PC via a USB interface. In order not to disturb the mass measurements the temperature is measured only before and after the rate-of-rise measurements. The wick is hanging above the petri dish, from a wick holder. The arm of the wick holder is going through a narrow gap in the draftshield of the balance, so the wick can be lowered into the liquid, or lifted out of it, without opening the draft shield. As liquid is flowing into the wick the amount of liquid in the petri dish decreases.

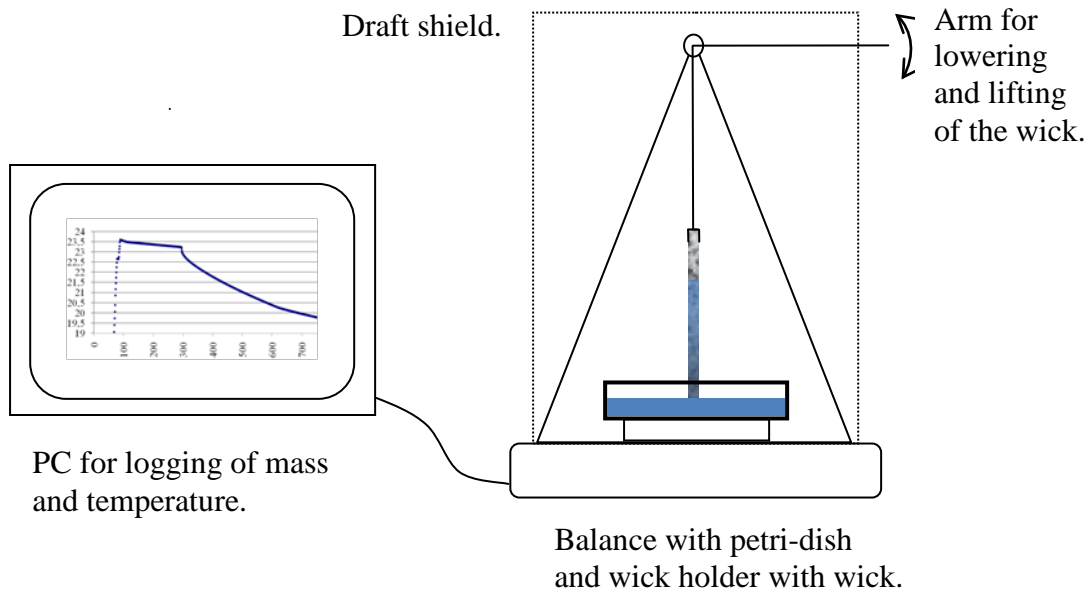


Figure 2-5 The rate-of-rise setup

The procedure for the rate-of-rise experiment is like this:

1. The wick is mounted to the wick holder and held in “lifted” position.
2. The data logging program is started.
3. The petri-dish is filled with heptane.
4. The temperature of the heptane in the petri-dish is measured by submerging the thermocouple tip into the heptane.
5. The draft shield is closed.
6. The mass is recorded for a couple of minutes in order to determine the evaporation rate of heptane from the petri dish.
7. The wick is lowered so that its lower end is just submerged in the heptane, this position is illustrated in Figure 2-18.
8. The maximum wetted height is visually detected, if possible.
9. After the maximum wetted height is reached the recording of the data continues for a couple of minutes. This to determine the evaporation rate from the wick and the petri dish together.
10. The wick is taken up of the liquid.
11. The draft shield is opened and the temperature of the heptane is measured again.

Typical mass versus time recordings

Figure 3-6 shows typical raw data from a rate-of-rise experiment carried out according to the above procedure. Line 1 shows the evaporation rate of the model fluid (heptane) from the petri dish alone. When the wick tip was submerged the heptane started climbing up the wick, fast in the beginning but then slower due to the increase of frictional and gravitational pressure losses. Line 2 shows the evaporation rate of heptane from the petri dish and the wick together, when the heptane reached the maximum “quasi-equilibrium” height in the wick.

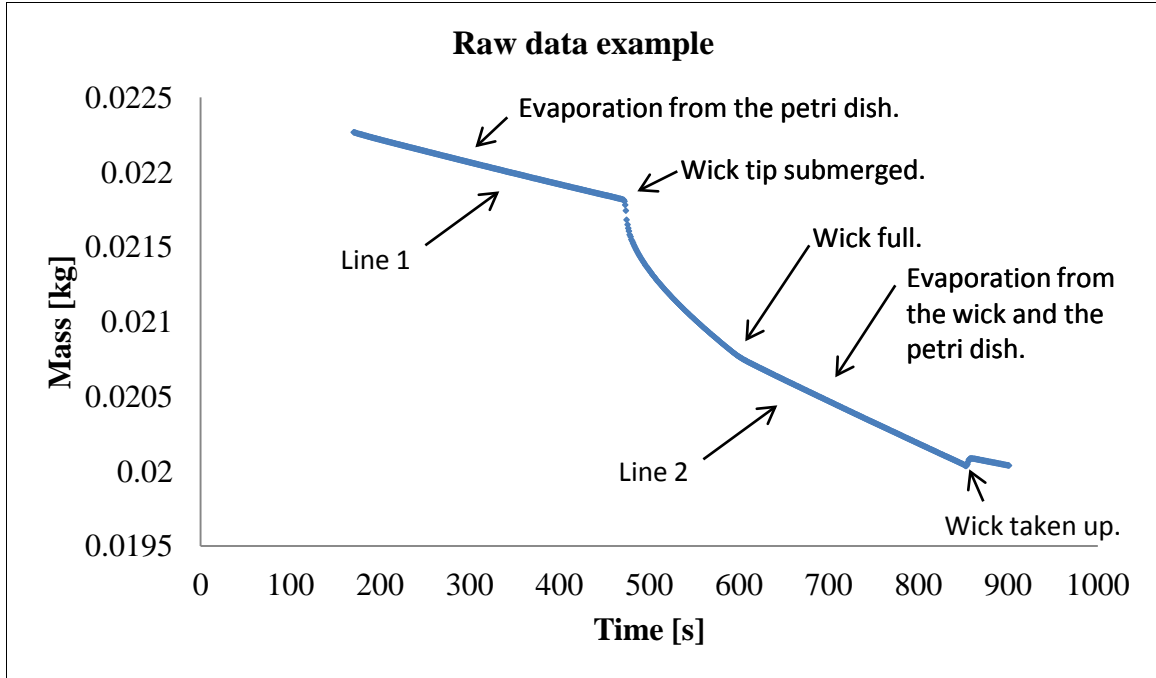


Figure 3-6 Recorded mass-time data during a rate-of-rise experiment

Rate-of-rise test theory with no evaporation from the wick

The capillary pressure is derived from the Young-Laplace equation for a cylindrical tube as in Equation (2-7) and (2-8).

The hydrostatic pressure of the liquid in the wick is; from Equation (2-12):

$$\Delta P_{hs} = -\rho_l g x = -\rho_l g \left(\frac{m_l}{\rho_l A \varepsilon} \right) = -\frac{g m_l}{\varepsilon A} \quad (3-8)$$

where m_l is the mass of liquid in the wick above the liquid bath. The flow related friction pressure drop in the wick is expressed by Darcy's law; Equation (2-13).

The following assumptions are then applied for any particular time [31]:

- The rate of rise is constant, i.e. $u(t) = (dm_l / dt) = \text{constant}$.
- The viscosity, permeability, density and wick cross sectional area are constant.

Darcy's law can then be integrated from the base ($x=0$) of the wick up to the liquid front (at x) yielding

$$\Delta P_f = -\frac{\mu}{\kappa \rho A} \frac{dm_l}{dt} x = -\frac{\mu}{\kappa \rho A} \frac{dm_l}{dt} \left(\frac{m_l}{\rho A \varepsilon} \right) = -\frac{\mu}{\kappa \varepsilon (\rho A)^2} m_l \frac{dm_l}{dt} \quad (3-9)$$

By introducing Equation (2-8), (3-8) and (3-9) in Equation (2-16) one gets

$$m_l \frac{dm_l}{dt} = \frac{\kappa \varepsilon (\rho A)^2}{\mu} \left(\frac{2\sigma}{r_{eff}} - \frac{g}{\varepsilon A} m_l \right) \quad (3-10)$$

This is a first order linear ordinary differential equation. A closed form solution can be obtained by integration, carried out in Appendix C. The final solution solved for time t is [31]:

$$t = - \left(\frac{\varepsilon \mu}{\kappa g^2 \rho^2} \right) \left(\frac{2\sigma}{r_{eff}} \ln \left(1 - \frac{g r_{eff}}{2\sigma \varepsilon A} m_l \right) + \frac{g}{\varepsilon A} m_l \right) \quad (3-11)$$

From Equation (3-11) a set of times can be calculated for each measured mass and for different values of κ and r_{eff} . The calculated times are compared with the measured times, and the set of κ and r_{eff} which gives the overall smallest deviation from the measured times is taken as the values of κ and r_{eff} for the sample. A MATLAB-script performing the calculations and obtaining the best set of κ and r_{eff} was developed in [37].

Rate-of-rise test theory including evaporation from the wick

The analysis leading to Equation (3-11) did not take evaporation of liquid from the wick into account. In experiments with low-volatile fluids or in experiments of short duration the evaporation from the wick may be neglected. The error done by neglecting evaporation will also be relatively small for very thick wicks.

Holley and Faghri [31] presented a solution also for the case where there is a constant evaporation rate Γ per unit height of the wick. The mathematical derivation of the solution is quite laborious, but it is carried out in detail here because only the key equations are presented in the paper by Holley and Faghri [31].

When the evaporation from the wick is taken into account the total mass uptake of the wick is [31]:

$$m = \varepsilon \rho A x + \Gamma \int_0^x t dx \quad (3-12)$$

The time t is a function of height x .

As for the case without evaporation the pressure balance at the liquid front consists of the contributions from capillary pressure, hydrostatic pressure and frictional pressure drop. Following the approach and notations of Holley and Faghri [31] the frictional pressure drop term has to be modified to:

$$\Delta P_f = - \frac{\mu}{\kappa \rho A} \int_0^x \left(\rho A \varepsilon \frac{dx}{dt} + \Gamma (x - \xi) \right) d\xi \quad (3-13)$$

Γ is the constant evaporation rate per unit height. The integration is carried out from $\xi=0$ to $\xi=x$, as illustrated in Figure 3-7. The term (dx/dt) is a constant.

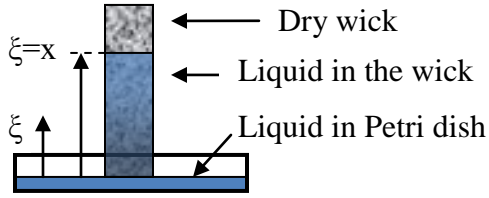


Figure 3-7 The definition of ξ

Equation (3-13) is solved in Appendix C, the result is Equation (3-14):

$$\Delta P_f = -\frac{\mu}{K} \left(\varepsilon x \frac{dx}{dt} + \frac{\Gamma x^2}{2\rho A} \right) \quad (3-14)$$

The pressure balance at the liquid front is still

$$\Delta P_{cap} + \Delta P_{hs} + \Delta P_f = 0 \quad (3-15)$$

Equation (2-8), (3-8) and (3-14) inserted into (3-15) gives Equation (3-16). The derivation can be found in Appendix C.

$$\frac{x \frac{dx}{dt}}{x^2 + \frac{2\rho^2 g A \kappa}{\mu \Gamma} x - \frac{4\sigma \rho A \kappa}{r_{eff} \mu \Gamma}} = -\frac{\Gamma}{2\rho A \varepsilon} \quad (3-16)$$

Equation (3-16) is a first order, linear ordinary differential equation having the following solution [31]:

$$C_1 \ln \left(1 - \frac{x}{C_1} \right) - C_2 \ln \left(1 - \frac{x}{C_2} \right) = -\frac{\Gamma(C_1 - C_2)}{2\varepsilon \rho A} t \quad (3-17)$$

The constants C_1 and C_2 are roots to the quadratic equation (3-18).

$$C^2 + \frac{2\rho^2 g A \kappa}{\mu \Gamma} C - \frac{4\sigma \rho A \kappa}{r_{eff} \mu \Gamma} = 0 \quad (3-18)$$

Equation (3-17) can be solved for time t , and then be used together with measured rate-of-rise data to find the best set of κ and r_{eff} for the actual wick. A MATLAB-script which does this job has been developed [37].

Both MATLAB-scripts, without and with evaporation, calculate the Mean Average Deviation MAD [31] according to Equation (3-19).

$$MAD = \left| \frac{t_m - t_{cf}}{t_{cf}} \right| \quad (3-19)$$

The sum of MAD expresses the total relative deviation between all the measured (t_m) and calculated (t_{cf}) time values for each set (r_{eff}, κ). The set of (r_{eff}, κ) having the smallest sum of MAD is taken as the true (r_{eff}, κ) of the wick. It is important to notice that the MAD is only quantifying the quality of the curve fitting; it is not an expression for the total uncertainty of the experiment.

Alternative data analysis

During this work it was discovered that it was difficult to determine the set of (r_{eff}, κ) having the smallest sum of MAD in the rate-of-rise experiments having short duration. For these experiments an alternative approach based on semi-manual curve fitting in a spreadsheet was used. The approach is described in the publication “Performance of compressed nickel foam wicks for flat heat pipes” [30].

Determination of the evaporation rate from the wick

The evaporation rate from the wick, Γ [kg/(s·m)], was determined from the slopes of the straight line segments 1 and 2 in the rate-of-rise experiment, see Figure 3-6. The slope of line 1 was subtracted from the slope of line 2, and the result then divided by the total wetted height of the wick, as given by Equation (3-20).

$$\Gamma = \left(\left. \frac{dm_l}{dt} \right|_2 - \left. \frac{dm_l}{dt} \right|_1 \right) / H \quad (3-20)$$

Conversion from mass to height in the rate-of-rise experiments

The experimental data acquired in the rate-of-rise experiments were mass uptake versus time. For formulas dealing with height (x) versus time a conversion from mass uptake to height is necessary.

Assuming no evaporation the relation between measured mass uptake and liquid height x in the wick is:

$$x = \frac{m}{\varepsilon \rho A} \quad (3-21)$$

Including evaporation from the wick, the following procedure was developed [37]:

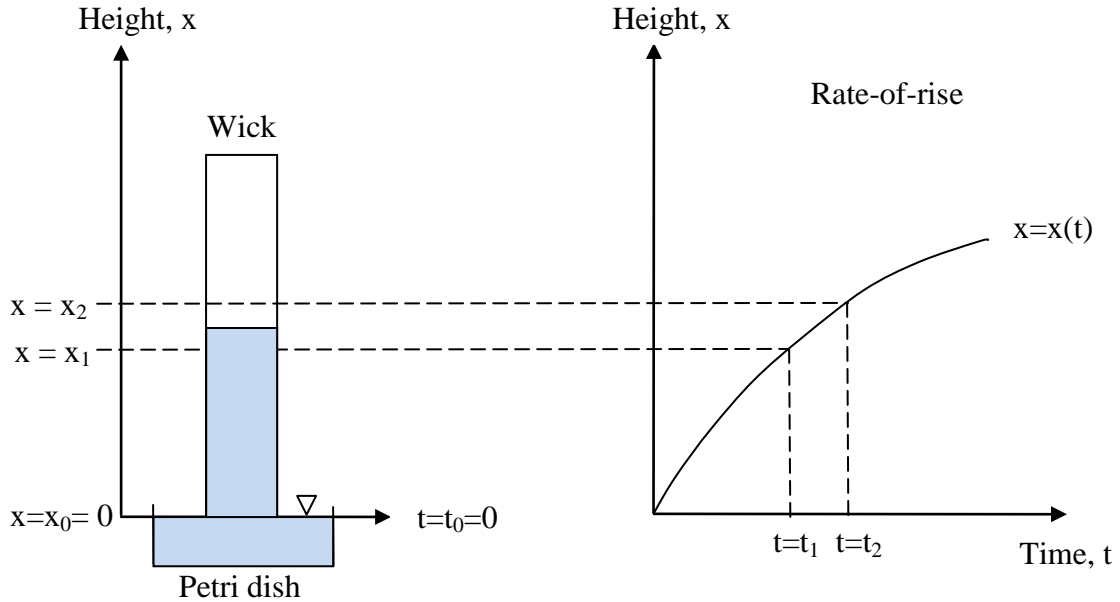


Figure 2-8 Height and time in rate-of-rise experiments

Assuming constant evaporation rate, Γ [kg/(s·m)] and with reference to Figure 2-21, the evaporated mass between (t_1, x_1) and (t_2, x_2) is:

$$m_{evap, (x_1, t_1) \rightarrow (x_2, t_2)} = (t_2 - t_1) \left(\frac{x_2 - x_1}{2} \right) \Gamma \quad (3-22)$$

In Equation (3-22) it is assumed that the average height in the time interval gives a representative height for the calculation of the evaporated mass in the interval. This assumption is strictly correct only when the rate-of-rise in the interval is constant.

The total evaporated mass in the time interval $(t_2 - t_1)$ must also include the evaporation up to height x_1 , i.e:

$$m_{evap, t_1 \rightarrow t_2} = (t_2 - t_1) \left(\frac{x_2 - x_1}{2} + x_1 \right) \Gamma = (t_2 - t_1) \left(\frac{x_2 + x_1}{2} \right) \Gamma \quad (3-23)$$

The evaporated mass in a time interval $(t_n - t_{n-1})$ can now be expressed from Equation (3-23) as:

$$m_{evap, (t_n \rightarrow t_{n-1})} = (t_n - t_{n-1}) \left(\frac{x_n + x_{n-1}}{2} \right) \Gamma \quad (3-24)$$

The total evaporated mass at time t_n is the sum of the evaporated masses of each time interval i:

$$m_{evap,t_n} = \sum_{i=1}^n m_{evap,i} \quad (3-25)$$

At time t_n the liquid has reached height x_n , and the mass of liquid in the wick is given by Equation (3-26).

$$m = \rho \varepsilon A x_n \quad (3-26)$$

The total mass taken up from the petri dish by the wick at time t_n is the sum of the mass evaporated at time t_n and the mass in the wick at time t_n :

$$m_{taken\ up\ at\ time\ t_n} = m_{in\ wick\ at\ t_n} + m_{evaporated\ from\ the\ wick\ at\ time\ t_n} \quad (3-27)$$

Equation (3-26) and (3-25) can now be put into Equation (3-27) and reorganized to yield:

$$x_n = \frac{m_{taken\ up\ at\ time\ t_n} - (t_n - t_{n-1}) \frac{x_{n-1}}{2} \Gamma - \sum_{i=1}^{n-1} \left[(t_i - t_{i-1}) \left(\frac{x_i + x_{i-1}}{2} \right) \Gamma \right]}{\rho \varepsilon A + \frac{(t_n - t_{n-1})}{2} \Gamma} \quad (3-28)$$

Equation (3-28) was used in all mass to height conversions in this study.

Additional comments regarding the rate-of-rise experiment

In Figure 3-6 it can be seen that there is a small weight increase when the wick is taken out of the liquid. This weight increase is the sum of two effects:

1. The weight of the liquid meniscus held up by the wick around its perimeter.
2. The buoyancy of the submerged wick tip in the liquid.

Since the sum of these effects contributes to lift liquid from the balance, the actual mass of liquid pumped up by the wick is smaller than the weight measured by the balance. The error is small and is believed to have little effect on the shape of the (x,t) curve. No correction has therefore been made for this in the calculations.

The Mettler AT261 balance has a readability of 0,01 mg up to 60 g and 0,1 mg up to 200 g. The repeatability is 0,05 mg or better. The uncertainty of the mass measurements is therefore related to the timing and rate of the measurements rather than the measurement itself.

The concentration of model fluid vapour inside the draft shield of the balance was not measured or specifically controllable in this study. However, the linearity of the evaporation curves from the petri dish and the petri dish plus wick indicated that the evaporation rate was constant.

3.1.5 Sintered nickel powder wicks for flat vertical heat pipes

Sintering of nickel powder was one of the wick production methods investigated. Most of the important findings and conclusions are reported in the paper “Sintered nickel powder wicks for flat heat pipes” [38], enclosed at the end of this chapter. Some complementary material is reported in the following paragraphs.

Figure 3-9 shows how the structure of sintered filamentary nickel powder can appear; the sample on the photo was sintered in air at an early stage in the wick development process and not used in any heat pipe.

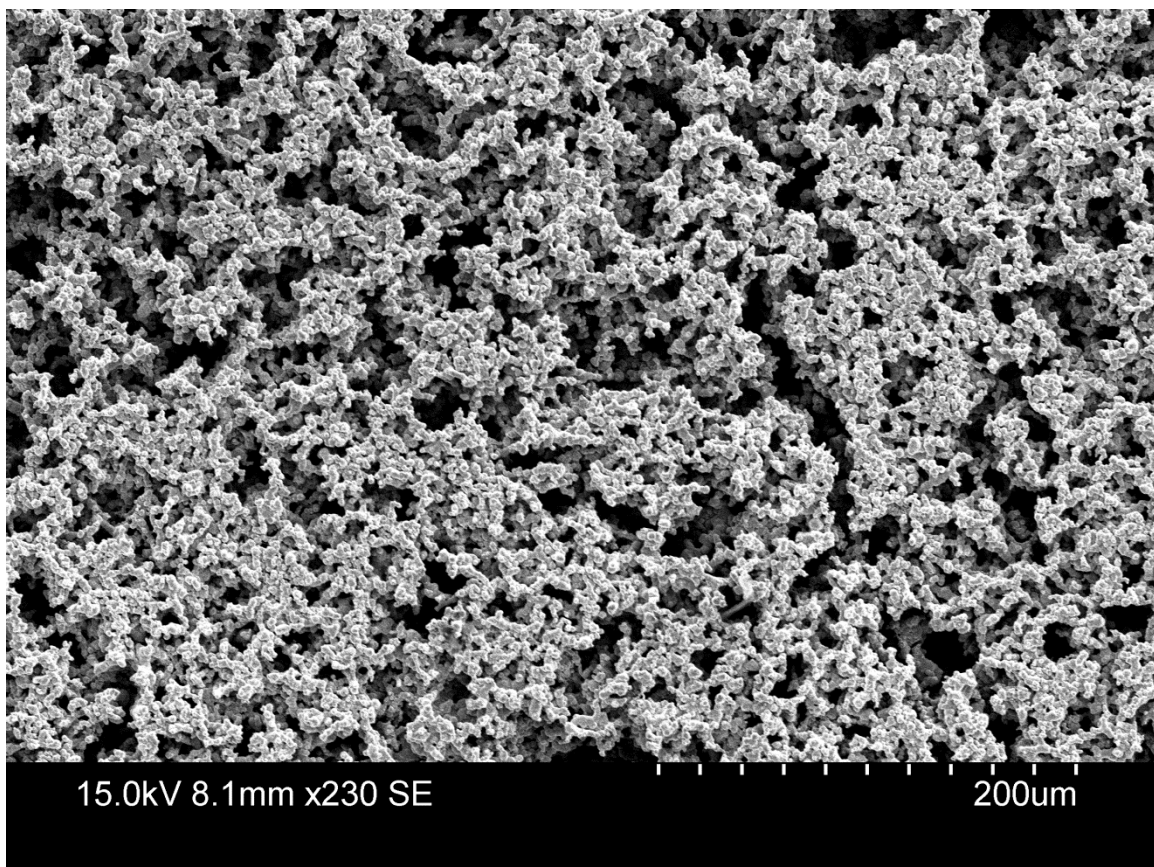


Figure 3-9 A scanning electron microscope photo of sintered filamentary nickel powder

Materials

The nickel powder

The raw material was a filamentary nickel powder; Vale Inco powder T255. The datasheet is enclosed in Appendix D.

Substrate

- With substrate: A 1 mm plate of Ni 201 was used as substrate in some experiments. When the powder was sintered directly onto a metal substrate, there was no thermal contact resistance between the wick structure and the substrate.
- Without substrate: The nickel powder was sintered on alumina (Al_2O_3) plates. There was no adhesion between the alumina and nickel.

Pore former

Wicks of sintered powder can be made from pure metal powder or from metal powder mixed with some kind of pore former (spacing agent). A pore former (spacing agent) can be added to the metal powder to increase the effective pore radius and permeability of the wick. In this case the pore former is burnt away before the final sintering, and it is therefore of a combustible material that will leave little contamination after combustion. In this study synthetic graphite powder with particles smaller than 20 μm , Sigma-Aldrich product no. 282863 was used. A filamentary pore former, carbon fibers, was also tested.

Key variables

Key variables in the production of wicks by powder sintering are:

- Preparation of the powder: Tape casting or mould.
- The sintering temperature.
The mechanical strength of the sintered structure increases with increasing sintering temperature. For Inco powder T255 sintering temperatures in the range 600-1000°C have been used [31, 39-40]. Below 650°C the sinter is very weak, and below 550°C it does not hold together [39].
The porosity of the sintered structure decreases with increasing sintering temperature [39].
- The sintering time.
Sintering times of 5 minutes [39] and 15 minutes [40] have been used for Inco 255. In the latter study press was also applied in order to produce less porous structures.
- Spacing agent type (also called filler/pore former), and the ratio of “nickel powder/spacing agent”.
- Sintering atmosphere (vacuum, inert gas, reacting (reducing) gas).
- Powder type (spherical, filamentary).
- Pressure (weight) applied upon the powder during sintering.

Nickel oxide formation

Nickel oxide formation was one of the key problems to handle in the sintering process. Nickel is, like most other metals, prone to oxidation, and the common reaction is:



A layer of oxide can sometimes be useful for protecting metals from corrosive fluids, but in the sintering process for the wick the oxide causes problems. The nickel oxide has a much higher melting temperature than pure nickel (1998°C vs. 1435°C) [41-42]. The oxidation rate of nickel was expected to be a function of temperature. A thermogravimetric (TG) experiment was carried out to determine the temperature where the Inco 255 powder starts reacting at a high rate with oxygen to form nickel oxide. A small sample of Inco 255 nickel powder was heated in air, from room temperature up to more than 1000°C. The weight of the sample was measured continuously. A high formation rate of nickel oxide was expected to be seen as a weight increase of the sample. The graphs below show the weight of the sample as a function of heating temperature (Figure 3-10 and heating time (Figure 3-11). The increase in the sample weight in Figure 3-10 from about 350°C is attributed to the formation of nickel oxide. From Figure 3-11 it is seen that the oxidation formation process lasted about 75 minutes.

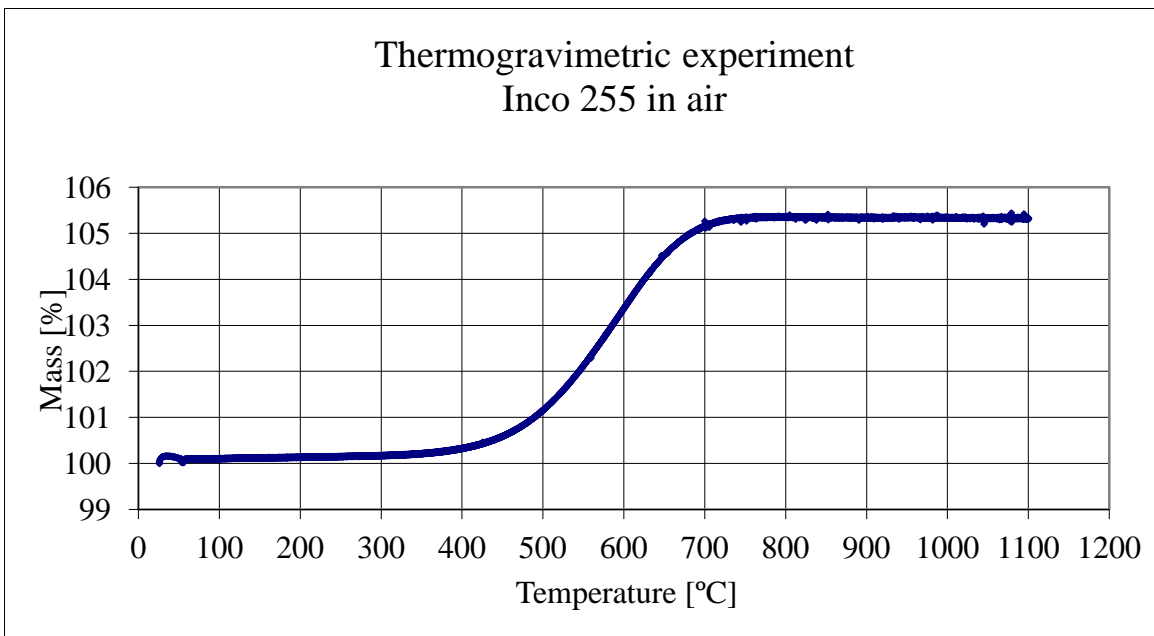


Figure 3-10 TG results vs. temperature

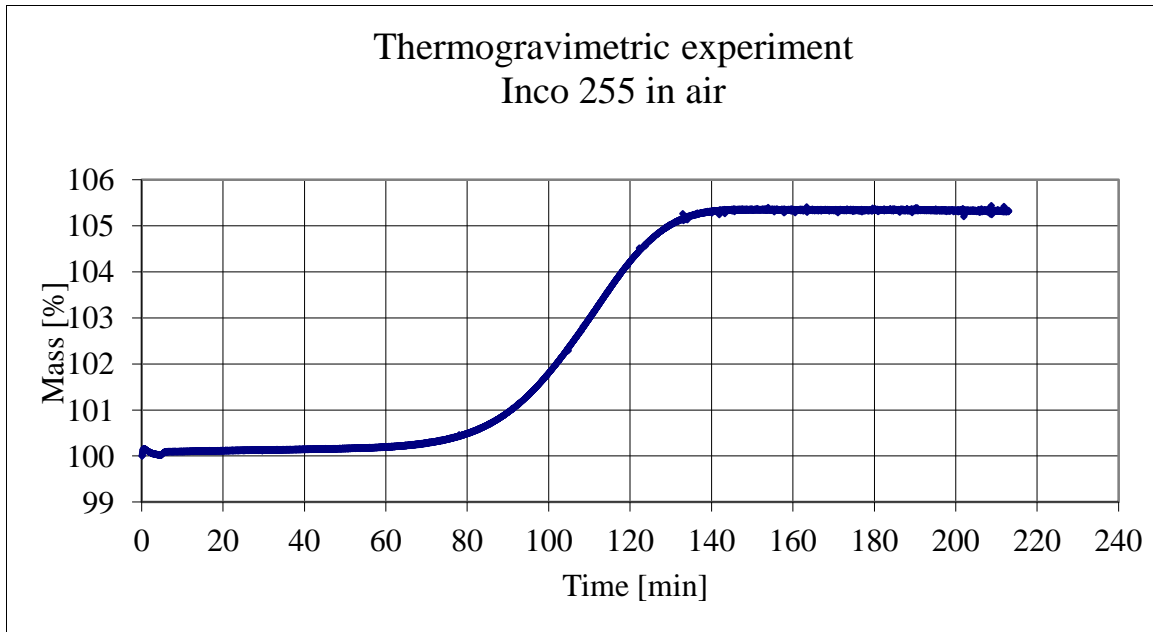


Figure 3-11 TG results vs. time

Pure nickel powder Inco 255 is dark grey. After the TG-experiment the nickel powder sample was green, which is known to be the colour of nickel oxide (NiO). The mechanical strength of the green TG-sample was low, which indicated that little sintering had taken place despite that the temperature had been above 1000°C. The reason for this was probably that nickel oxide was preventing effective sintering. It was concluded that it is important to avoid nickel oxide formation before the sintering. From the TG-experiment it was clear that pre-sintering heat treatment should not be carried out at higher temperatures than 400°C in order to avoid high nickel oxide formation.

The percentage of the nickel sample mass converted to nickel oxide in the TG experiments was estimated like this: The nickel powder sample, 0,161070 g, was assumed to consist of pure nickel from the start. The molar mass of nickel is 58,71 g/mole, so the sample amount was about 0,002743 mole. The mass increase of the sample in the experiment was approximately 5,3% or 0,00854 g. The molar mass of atomic oxygen is 16 g/mole. The green colour indicates that stoichiometric (1:1) NiO was formed [43]. Assuming this the amount of NiO formed was equal to $(0,00854/16) \approx 0,000534$ mole. So about $(0,00053/0,161070) \cdot 100 \approx 19,5\%$ of the nickel powder was converted to nickel oxide during the experiment.

The number of layers of nickel oxide was also estimated. The specific surface area of the Inco 255 powder is, according to the manufacturer's datasheet, typically 0,7 m²/g (BET). The total surface area of the initial TG-sample was therefore about $(0,161070 \cdot 0,7) \approx 0,11$ m². The effective packing radii of O₂ molecules is 0,18 nm [44]. A monolayer of O₂ molecules on the surface of the nickel sample would therefore consist of approximately $(0,11/(\pi(0,18 \cdot 10^{-9})^2)) \approx 1 \cdot 10^{18}$ molecules or $(1 \cdot 10^{18}/6,022 \cdot 10^{23}) \approx 1,7 \cdot 10^{-6}$ mole. Each mole of O₂ gives 2 moles of NiO. If just the first surface layer of the nickel powder reacted with oxygen one would expect that $2 \cdot 1,7 \cdot 10^{-6} \approx 3,3 \cdot 10^{-6}$ mole of NiO was formed. The

quantity actually formed was estimated from the TG result to 0,000534 mole, or about 160 times the estimated nickel oxide amount of the first layer. So, the oxygen molecules were obviously able to diffuse and react quite deep into the solid nickel.

In order to avoid the formation of oxide an atmosphere of hydrogen gas is often used when pure metal powders are sintered. The hydrogen prevents oxidation of the sintered metal surface. An alternative to the hydrogen atmosphere is using a vacuum oven for the sintering.

An atmosphere of oxygen is necessary when the metal powder is mixed with some kind of additive, which is supposed to burn off before the sintering. When oxygen is present during burn-off metal oxides will be formed. The oxides can subsequently be removed by heating the porous structure in a reducing atmosphere containing for instance hydrogen gas.

The preferred working fluid in this study, potassium, is, like hydrogen, in group 1A of the periodic table. Potassium has, like hydrogen, the ability to reduce nickel oxide, as described by Equation (3-30).



A necessary criterion for the reduction to take place is that ΔG is negative, which is the case here.

The concentration of oxygen in potassium therefore depends on the success of the reduction of nickel oxide by use of hydrogen in the filling process.

Sintering time and shrinkage

In order to study the shrinkage of Inco 255 nickel powder under heating/sintering a dilatometer experiment was carried out on a sample of pure Inco 255 nickel powder. In the experiment the sample was heated to a maximum temperature of 622°C. The results are shown in Figure 3-12 and Figure 3-13. In dilatometer experiments one may find that the shrinkage reaches a final value determined by the maximum temperature. Within the the time range and temperatures of the current experiment no final value for the shrinkage was determined; the sample was shrinking during the whole experiment. This showed that not only sintering temperature but also sintering time was important in the sintering of the nickel powder wicks.

For a real wick produced by use of tape casting the shrinkage was about 8% (length) and 10-15% (width). The variation in width was likely caused by local temperature variations over the length of the wick during the heat treatment. The practical implication of the shrinkage was that the wicks had to be made somewhat larger than specified, and then in a final stage cut to the correct dimensions by use of a high speed cutting tool.

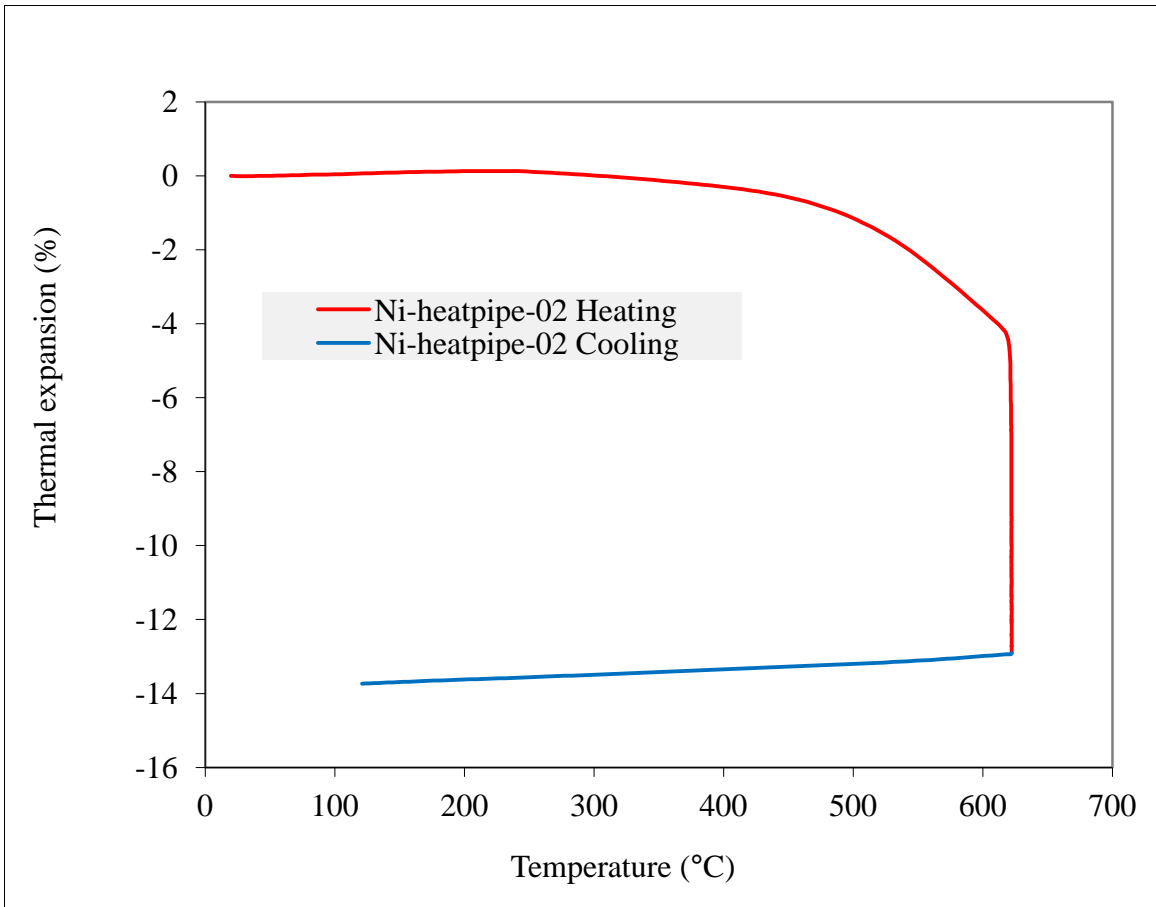


Figure 3-12 Thermal expansion as a function of temperature

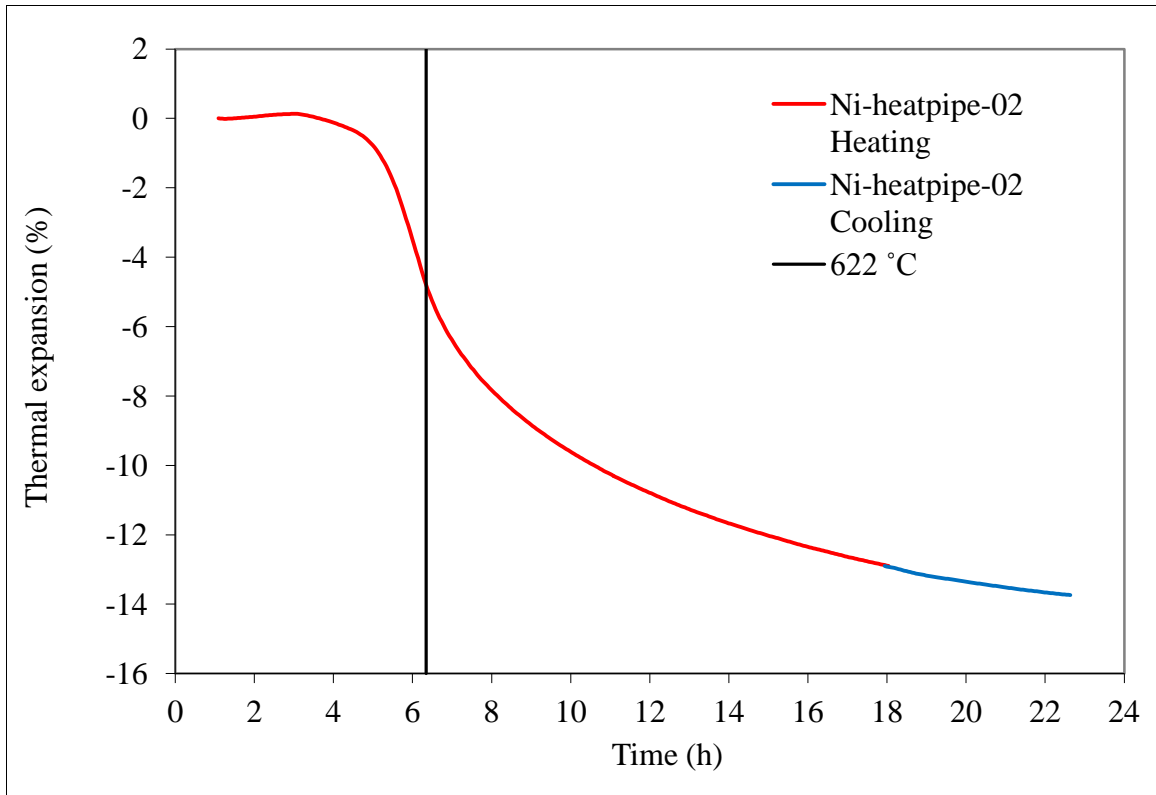


Figure 3-13 Thermal expansion as a function of time

Wick production

Moulding

Moulding was tested both with and without a pore former. When pore former was used the produced wicks did not possess the necessary mechanical strength for heat pipe application. In general the final structure/quality of the wicks was better when the wicks were produced by use of tape casting.

Tape casting

Tape casting, as shown in Figure 3-14, was in this study found to be the best method to prepare the powder before sintering.

The thin film produced by tape casting was cut to samples a bit larger than wick size in order to compensate for shrinking during subsequent heat treatment. The wick thickness was determined by the number of samples (film layers) used to build up the wick. Because of the tape casting additives, see Table 3-2, the pile of film layers had to go through a burn-off process in clean air before sintering in a reducing hydrogen atmosphere.

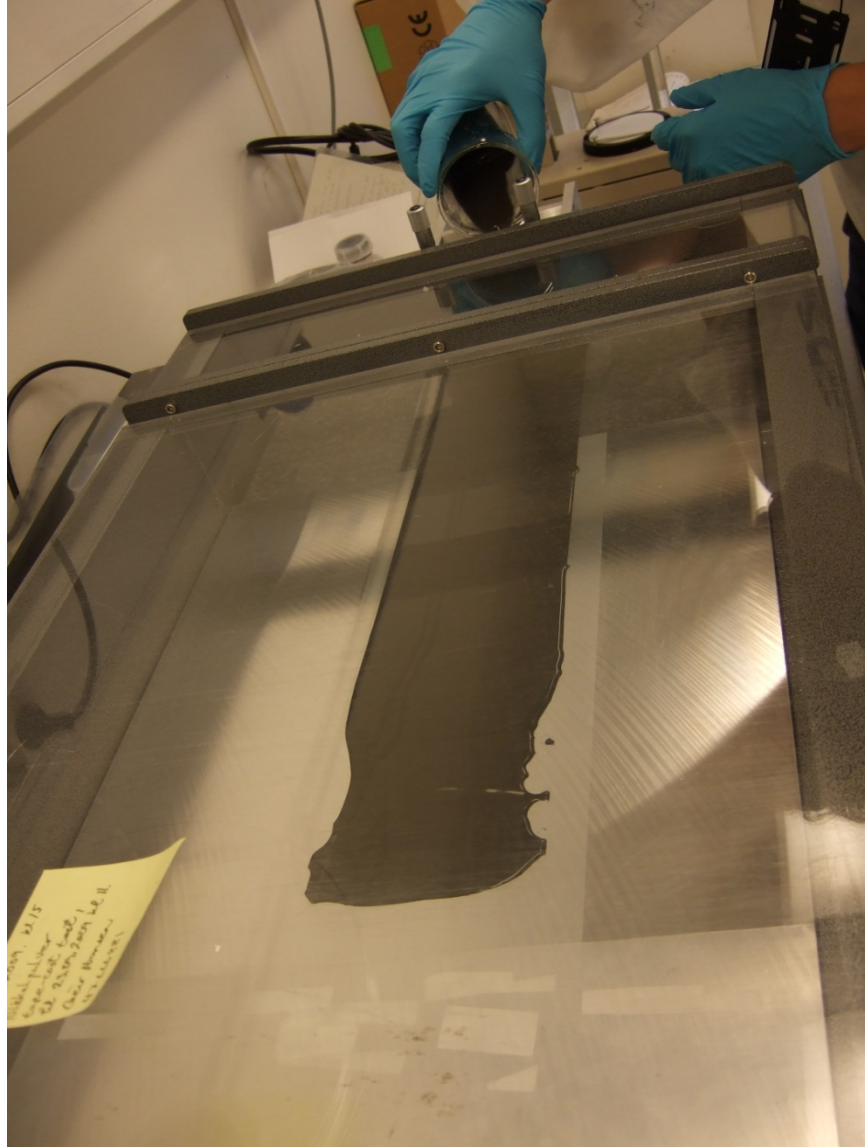


Figure 3-14 Tape casting

The wetting of the carrier tape by the slip is important in tape casting. For the tape casting here the uncoated side of the carrier tape was better wetted than the silicon coated side.

The formulation of the first slip batch produced is shown in Table 3-2. This is a slightly modified version of a recipe for high-surface-area oxide powder in oxidizing sintering atmosphere [45-46]:

Table 3-2 The formulation of the tape casting slip.

Component	Composition (wt%)	Amount (g) in slip	Function
Part 1:			
Nickel powder	53,93	44,54	
Distilled water	22,35 x3	55,38	Solvent
Daravan C	0,1	0,0826	Dispersant
Part 2:			
Polyvinyl alcohol, grade 75-15	3,24 x2		Binder
Distilled water	18,33 x2	35,63	Solvent
Polyethylene glycol, grade 400	1,62	1,34	Plasticizer
Polypropylene glycol, grade P-1200	0,54	0,446	Defoamer

Batching procedure:

Part 1 and part 2 were prepared separately and then added.

Part1:

Nickel powder, distilled water and Daravan C were added to a bottle. The bottle was rotated at 60 rpm for 4 hours.

Part 2:

A large batch of 15% polyvinyl alcohol water solution was made. It took about 3 hours to dissolve the polyvinyl alcohol in distilled water. (The polyvinyl alcohol was crushed in the water by use of a spoon, while the temperature was held at about 60°C). After 3 hours mechanical work there was a lot of air bubbles in the solution. The solution was allowed to rest over the weekend (about 60 hours) in a beaker. The bubbles escaped during the weekend, leaving the polyvinyl alcohol solution glass clear.

The ingredients in part 2 were then added to the bottle with the ingredients of part 1, and the bottle rotated for 16,5 hours at 60 rpm.

After the rotation the slip looked a bit thin and unable to disperse all the metal particles. The slip was aged for about 6 hours, but looked somewhat separated afterwards. Careful stirring, without adding air bubbles to the slip, was used to make the slip homogenous before the tape casting.

Wick made of sintered nickel powder with carbon fiber pore former

The idea behind the carbon fiber pore former was that the fibers will create channels in the porous structure. The channels will increase the permeability of the wick, but not necessarily cause a proportional increase in the effective pore radius. This is advantageous since the ultimate wick has infinite permeability and minimum effective pore radius.

The carbon fiber used in this study was:

HEXEL HexTow
Type: AS7 –GS 12k
LOT: 4013-7E
USA PAN 4 DOFF: 05

The Hextow AS7 carbon fiber has 12000 filaments of diameter 6,9 microns [47]. The carbon content is 94% [47]. Each filament of the carbon fiber has a thin epoxy coating, to make it more compatible with the epoxy used in the production of traditional composite material parts. The epoxy coating is organic and is therefore expected to disappear during the burn-off process.

Inside the carbon fiber there may be small residuals of Si- and Na-components from the production process. These components are the only components that can form some inorganic ash material after the burn-off process [48].

A thermogravimetric experiment was carried out in order to determine the minimum temperature requirement for burn-off. The experiment was run with an atmosphere of clean, dry air at a flowrate of 20 ml/min. The sample weight was 5,2176 mg. The temperature program went from 25°C up to 1100°C at a heating rate of 5 K/min. The result is presented in Figure 3-15. From Figure 3-15 the burn-off started at about 540°C and at about 720°C the crucible was empty.

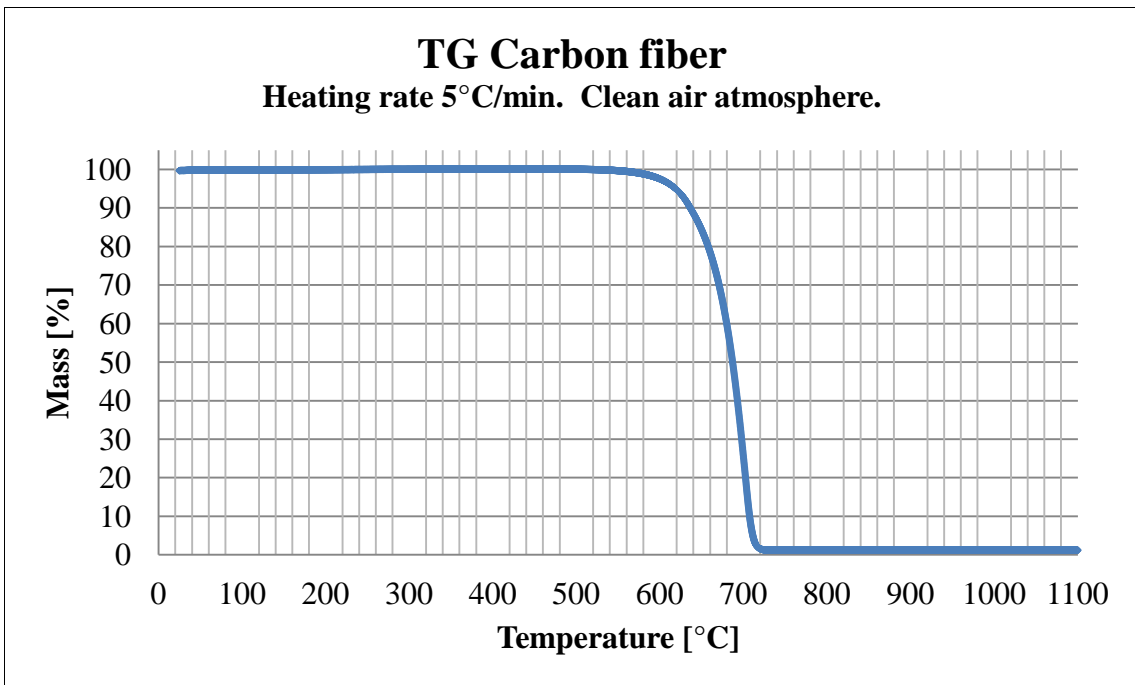


Figure 3-15 The result of a thermogravimetric experiment with carbon fiber

The instrument reported at the end of the experiment a residual mass fraction of 1,25%. The crucible appeared empty, so if there was something left there it had to be as a thin

transparent layer on the bottom of the crucible. For such an amount of residual mass to be any problem in the wick production it must affect the surface tension of the wick material or the working fluid, or create a non-condensable gas.

It turned out to be very difficult to distribute carbon fibers in the nickel powder. Clusters of fibers created large channels in the wick structure. The resulting wicks did suffer from cracks and insufficient mechanical strength. Without any solution to the fiber distribution problem the carbon fiber as pore former was abandoned.

Important findings and conclusions for the wicks made of sintered nickel powder are reported in the paper “Sintered Nickel Powder Wicks for Flat Vertical Heat Pipes” published in *Energies*, vol 8, pp. 2337-2357, 2015, presented in the following.

Article

Sintered Nickel Powder Wicks for Flat Vertical Heat Pipes

Geir Hansen *, Erling Næss † and Kolbeinn Kristjansson †

Department of Energy and Process Engineering, Norwegian University of Science and Technology, Kolbjørn Hejes vei 1a, 7491 Trondheim, Norway; E-Mails: erling.nass@ntnu.no (E.N.); kolbeinn.j.kristjansson@ntnu.no (K.K.)

† These authors contributed equally to this work.

* Author to whom correspondence should be addressed; E-Mail: g.hansen@ntnu.no; Tel.: +47-7359-3938; Fax: +47-7359-3580.

Academic Editor: Enrico Sciubba

Received: 12 January 2015 / Accepted: 16 March 2015 / Published: 25 March 2015

Abstract: The fabrication and performance of wicks for flat heat pipe applications produced by sintering a filamentary nickel powder has been investigated. Tape casting was used as an intermediate step in the wick production process. Thermogravimetric analysis was used to study the burn-off of the organic binder used and to study the oxidation and reduction processes of the nickel. The wicks produced were flat, rectangular and intended for liquid transport in the upwards vertical direction. Rate-of-rise experiments using heptane were used to test the flow characteristics of the wicks. The wick porosities were measured using isopropanol. The heat transfer limitation constituted by the vapour static pressure and the capillary pressure was discussed. The influence on wick performance by using pore former in the manufacturing was studied. When $P_{cap}/P_{sat} > 1$, the use of a pore former to increase the wick permeability will always improve the wick performance. When $P_{cap}/P_{sat} < 1$, it was shown that if the effective pore radius and the permeability increase with an equal percentage the overall influence on the wick capacity is negative. A criterion for a successful pore former introduction is proposed and the concept of a pore former evaluation plot is presented.

Keywords: wick; sintering; pore former; rate-of-rise; heat pipe

1. Introduction

The concept of heat pipes was first described in 1942, but the real development of heat pipes started in the 1960s [1]. Properly designed heat pipes can transport heat at very high rates with a small temperature difference between the cold and the warm end. This is possible because the heat transport inside the heat pipe is based on evaporation, transport and condensation of a suitable working fluid, and thereby also obtaining an apparent thermal conductivity several hundred times that of solid materials such as copper [2]. The heat pipe interior contains a wick, in which the condensate returns from the condenser section to the evaporator section. The driving force in the condensate transport process is the capillary pressure created by the wick and working fluid interaction, in some cases the capillary pressure is supported by the gravity force. The gravity force contributes to the transport process when the condenser section is located above the evaporator section, *i.e.*, the heat pipe is gravity-assisted [3]. The heat pipe is gravity-opposed when the condenser section is located below the evaporator.

Wicks can be produced by several different techniques and from different materials, such as woven metal wires, metal foams, sintered metal powders, or they can be made as grooves in the wall of the heat pipe [4]. Bimodal wicks are made by adding metal powders to metal foams or felts [5–7]. In some cases the wick capacity can be improved by creating internal arteries inside it, forming low-friction flow paths for the liquid [4]. De Schampeleire *et al.* [3] stated that “the number of possible wick types is virtually endless”. They investigated wicks for water/copper heat pipes having 6 mm outer diameter and 200 mm length, for cooling of electronic devices. Specifically, a novel wick made of metal fibers was compared to more traditional wicks made of a screen mesh and a sintered powder, respectively. Under gravity-assisted conditions the screen mesh wick performed best, because of its superior permeability. High permeability means low frictional pressure loss for the fluid flowing through the wick. In the gravity-opposed orientation the screen mesh wick and the metal fibre wick both outperformed the sintered powder wick [3]. However, the properties of sintered powder wicks can be modified and improved by use of pore formers. The pore former, usually an organic material, is mixed with the metal powder and thereafter “burnt off”, leaving a void behind. The burn-off process using an air or oxygen atmosphere is usually a separate process prior to the sintering. The pore former will normally increase the pore size and thereby also increase the effective pore radius of the wick. Different heat pipe applications and different working conditions require different wick properties, it is therefore important to know how the different production parameters such as pore formers affect the wick properties. Li *et al.* [8] investigated experimentally how much the forming pressure and the use of a microcrystalline cellulose (MCC) pore former affected the wick porosity and capillary pumping performance of a sintered powder wick for loop heat pipes, and developed a correlation between porosity, forming pressure and MCC addition. The use of a pore former for wick capacity improvement is analysed further in the current study. A criterion for successful pore former introduction is derived, and the novel concept of a pore former evaluation plot is presented. The ideal pore former can be totally removed from the wick structure, for instance by heat treatment (burn-off) and/or by chemical treatment. The suitability of pure graphite powder and carbon fibers as pore formers are considered in the current study and the required burn-off temperature for graphite powder is determined experimentally. Information about the required burn-off temperature is essential when pore former material is to be selected, if the burn-off temperature is too high the wick material may be damaged.

Compatibility with the working fluid is often the main wick material selection criterion, and the wick material is often a metal. Incompatibility can lead to generation of non-condensable gases, which can displace the working fluid and thereby hamper the heat transfer [9]. However, material compatibility is not sufficient. Proper thermal and/or chemical cleaning of the wick is equally important in order to avoid corrosion, non-condensable gases and to ensure proper wetting of the wick by the working fluid [10,11]. The importance of the wick in the cleaning process is emphasized by the fact that the total surface area of the wick is much larger than the surface area of the container; the surface of the wick can therefore contain much more adsorbed unwanted components than the container wall.

Wicks of sintered nickel powder have been used for many years in heat pipes [1,4]. Nickel has relatively high thermal conductivity, which is an advantage when heat is to be conducted across the wick as in traditional heat pipes. For loop heat pipes high thermal conductivity of the wick is a disadvantage [8,12]. Nickel is compatible with alkali metals, frequently used as working fluids for high temperature heat pipe applications [1]. In the current study a wick of sintered nickel powder was developed, and its suitability for gravity-opposed operation with potassium as working fluid is evaluated. Specifically, the intended application was a special type of heat pipe, having a flat wick in the evaporator section only. Figure 1 shows the working principle.

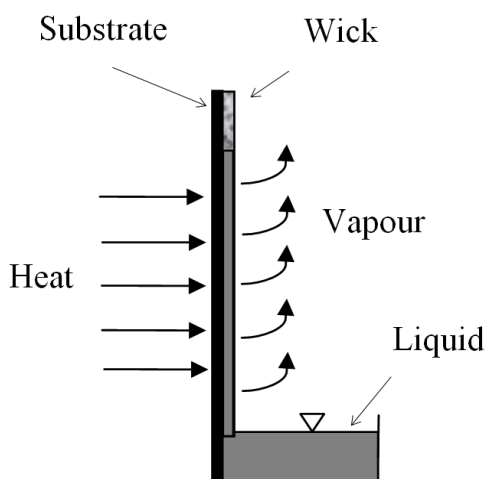


Figure 1. A flat wick attached to a solid substrate subject to a uniform heat flux causing liquid evaporation from the free wick surface. Liquid (condensate) is pumped by the wick from a reservoir at the bottom of the wick. The experiments utilized to characterize the wick in this study were performed without the heat addition and without the solid substrate.

The filamentary nickel powder Inco Type 255 is a popular raw material for wick production [5,8,13]. The filamentary particles make it possible to produce wicks with porosities far above the porosity of any wick produced of monodisperse spherical particles. The porosity of a wick produced from monodisperse spherical particles is theoretically between 26% and 47%, while the porosity of a wick of filamentary particles can be up to ca. 90% [13]. The wick developed in the current study was made of sintered Inco Type 255 nickel powder. The following parameters are known to affect the properties of sintered Inco Type 255 nickel powder [14]:

- Sintering time.
- Sintering temperature.
- Sintering atmosphere.
- Type and amount of pore former (spacing agent).
- Pressure from weights applied during sintering (forming pressure).

Long sintering time, high sintering temperature, and high forming pressure will in general lead to compact wick structures, having low porosity, low permeability and a small effective pore radius. The minimum sintering time, temperature and forming pressure providing sufficient mechanical strength should therefore be the best choices in order to maintain an open, high porosity wick structure. The sintering atmosphere is very important when nickel powder is used, because of the susceptibility of nickel to oxidise at high temperatures. The surface properties of nickel oxide will be different from that of pure nickel, and this will in general affect the interfacial tensions and the contact angle between the solid and the working fluid. In order to avoid oxidation of the nickel, the sintering of nickel powder can be carried out in protective/reducing gas atmosphere [12] or in vacuum [7]. Similarly, nickel oxides, e.g., formed during burn-off, can be reduced to pure nickel by heat treatment under a reducing atmosphere such as H₂ (5 vol%) and N₂ (95 vol%) [14]. The mass increase and colour change from grey to green indicate nickel oxide formation, and vice versa for the reduction. Thermogravimetric analysis (TGA) was utilized in the current work to study the oxidation of the nickel powder, burn-off, and to study reduction of nickel oxide in a 5% H₂ + 95% N₂ atmosphere. Such data were needed in the preparation of the burn-off, sintering and oxide reduction programs.

The wick structure has to be robust to be able to withstand handling and thermal strains and stresses, especially important for high temperature heat pipes and when the heat load is unilateral. In the current study a robust wick was obtained utilizing tape casting [15] as an intermediate step in the wick production. The required burn-off time and temperature level for the removal of the additives used in the tape casting were determined by thermogravimetric analysis, and are reported.

Good thermal contact between the wick and the heat pipe wall reduces the overall heat transfer resistance from the outside of the evaporator to the working fluid. The thermal contact resistance between the wick material and the evaporator surface is eliminated when the wick is sintered to the evaporator surface. Burn-off and sintering directly on the evaporator surface was investigated experimentally in this study.

Wicks for heat pipe use are usually characterized by their porosity, permeability, and effective pore radius related to a specific fluid. A standardized method for porous samples can be applied for the porosity measurements [16]. Permeability can be measured in forced flow experiments [17], but has also been determined together with the effective pore radius in spontaneous free flow experiments, *i.e.*, rate-of-rise experiments [13,18]. The rate-of-rise experiment was chosen in the current study. Model fluids (e.g., acetone, heptane, methanol) are often utilized in rate-of-rise experiments [13], especially when the real working fluid is hazardous (e.g., alkali metals). Heptane was chosen in the current study. Permeability is independent of the type of fluid, but the effective pore radius is not. In order to convert the effective pore radius from one fluid to another, the contact angles of the respective fluids on the wick powder surface are required. The contact angle of the model fluid (heptane) on porous nickel was derived from capillary rise experiments, as described by Hiemenz [19]. According to

Hiemenz [19], the capillary method for contact angle determination “is not highly reliable, but preferable compared to any technique based on the exterior surface of the plug as a liquid support”. The “plug” is in this case the wick. Alkali metals are known to have “strong wetting characteristics” against metals [20]. Hence, the contact angle of potassium on nickel was assumed to be zero [21].

The heat transfer capacity of heat pipes can be restricted by many different heat transfer limitations, which have been given considerable attention in the literature [4,22]. The current paper presents and analyzes a heat transfer limitation which has not been given attention previously; the static pressure limitation. It is shown theoretically how the static pressure limitation will limit the performance of the designed nickel powder wick with potassium as working fluid. To summarize, the following topics are investigated in this study:

- Method of fabrication of the wick.
- Selection of burn-off and sintering temperature programs from thermogravimetric analysis.
- Determination of the wick characteristics.
- Prediction of the wick maximum heat transfer capacity with potassium.
- Criterion for pore former selection.

2. Method of Fabrication of the Wick

Wicks were made by sintering pure Inco Type 255 nickel filament. During this study many wicks were produced by different methods (tape casting or mould, with or without pore former). A production method based on tape casting of a slip without pore former was found to be the most successful with regards to the mechanical properties of the wick. In the following this approach is described in detail, as well as the testing and results for a wick produced by this method. Some results from the work with pore former have also been included. Moulding was attempted, but sufficient mechanical strength was not achieved, hence this method was considered inferior.

In the tape casting, a modified batching procedure for “High-surface-area oxide powder, oxidizing sintering procedure” [15] was used, summarized as: Sinter powder (Inco 255), distilled water and dispersant (Darvan C) were mixed by rolling for about 12 h. A binder (polyvinyl alcohol), a plasticizer (polyethylene glycol) and a defoamer (polypropylene glycol) were then added to the mixture, and the mixture was mixed by rolling for an additional 12 h, after which it was ready for tape casting using a tape casting machine. The tape casting produced a thin (0.2–0.3 mm thick) tape of the mixture. The tape was let to dry for about 12 h in ambient air atmosphere, and was next cut into pieces of desired size. Due to shrinkage during subsequent burn-off and sintering the pieces had to be cut 20%–30% larger than the desired final wick size. The desired wick thickness was achieved by stacking a number of tape pieces on top of each other. For the wick presented in this paper 16 layers of tape were required in order to have a total thickness of 4 mm before burn-off and sintering.

In order to achieve good contact between the tapes and sufficient mechanical strength of the wick, it was necessary to apply pressure upon the pile of tapes during burn-off and sintering. Alumina weights which provided a pressure of 1,300 Pa were used. Ideally, the wick should be sintered directly onto the evaporator surface of the heat pipe as this would eliminate thermal contact resistance between the wick and the evaporator surface. Burn-off and sintering directly on the evaporator surface was tested, but failed because of incomplete burn-off, probably caused by insufficient gas diffusion in the pile of

tapes which were covered by the heat pipe walls and the alumina weights. It was therefore decided to produce the wick outside of the heat pipe, and thereafter attach it to the evaporator surface by a suitable method. Following this new approach, the pile of tapes was put on an alumina plate, and the weights put on top of the pile. This was then all put in the oven which had continuous synthetic air flushing for effective burn-off of the organic material. The burn-off and sintering temperature program was developed from information from thermogravimetric analysis (TGA), together with known sintering temperature requirements for a mechanical strong wick.

3. Selection of Burn-off and Sintering Temperature Programs from Thermogravimetric Analysis

- Thermogravimetric analysis of pure Inco 255 nickel powder in air was carried out to study the oxidation.
- Thermogravimetric analysis was carried out for the tape cast tape in order to determine the programs for burn-off and reduction. In this test a 900 μL crucible was filled with approximately 40 layers of tape. The burn-off TGA was carried out using synthetic air atmosphere, and the reduction in a H_2 (5%) and N_2 (95%) atmosphere.
- A thermogravimetric analysis with pure graphite powder in air was performed. Pore former was not used in the fabrication of the final wick presented in this study, but some work was performed to analyse the suitability of the graphite powder as pore former. Graphite was selected because it leaves very little residues after burn-off. The graphite powder (from Sigma-Aldrich) had particle sizes smaller than 20 μm .
- A thermogravimetric analysis was also performed for the burn-off of a tape casted tape consisting of approximately equal amounts of Inco 255 nickel powder and graphite powder, plus the tape casting additives.

The results from these four TGA experiments are presented graphically in Section 5—Results and Discussion.

4. Determination of the Wick Characteristics

4.1. Capillarity and Flow Characteristics

When a wick is used for liquid transport in the vertical upward direction as shown in Figure 1, its capacity is highly dependent on the effective pore radius and the permeability of the wick structure. The driving force is the capillary pressure, which is a function of the liquid wetting, the liquid surface tension and the pore radius of the wick. The wetting of a solid by a liquid is often expressed by the contact angle. The effective pore radius includes the contact angle information and is defined from a capillary tube model [13]:

$$\Delta P_{cap} = \frac{2\sigma \cos(\theta)}{r} = \frac{2\sigma}{r_{eff}} \quad (1)$$

The relation between the effective radii of two fluids having different contact angles is:

$$\frac{r_{eff,fluid1}}{r_{eff,fluid2}} = \frac{\cos \theta_{fluid2}}{\cos \theta_{fluid1}} \quad (2)$$

In the wick the primary forces opposing the capillary pressure are the hydrostatic pressure and the frictional pressure drop of the flow. Of less importance are fluid momentum changes and friction between the liquid and the substrate, both disregarded in the present analysis. The hydrostatic pressure of the liquid column can be expressed as:

$$\Delta P_g = -(\rho_l - \rho_v)gH \approx -\rho_l gH \quad (3)$$

where H is the height of the liquid level in the wick relative to the fluid bath. The pressure drop due to friction is calculated from Darcy's law [13]:

$$\frac{dP_f}{dy} = -\frac{\dot{V}\mu}{\kappa} = -\frac{\dot{m}\mu}{\kappa A_c \rho} \quad (4)$$

The highest mass flow rate is at the liquid inlet end (*i.e.*, bottom) of the wick. For a constant evaporation rate per unit height of wick, the mass flow rate in the wick becomes a linear function of position (y):

$$\dot{m}(y) = \dot{m}_{y=0} - \frac{\dot{m}_{y=0}y}{H} = \dot{m}_{y=0} \left(1 - \frac{y}{H}\right) \quad (5)$$

The total frictional pressure drop up to height H is determined by integration of Equation (4) between the limits $y = 0$ and $y = H$; with Equation (5):

$$\Delta P_f = -\int_0^H \frac{\dot{m}\mu}{\kappa A_c \rho} dy = -\frac{\mu \dot{m}_{y=0} H}{2\kappa A_c \rho} \quad (6)$$

The overall fluid force balance is comprised of the capillary pressure (Equation (1)), the static head (Equation (3)) and the fluid friction (Equation (6)) and can be expressed as:

$$\frac{2\sigma}{r_{eff}} - \rho gH - \frac{\mu \dot{m}_{y=0} H}{2\kappa A_c \rho} = 0 \quad (7)$$

The wick liquid pumping capacity ($\dot{m}_{y=0}$) is found by solving Equation (7) provided that the wick properties (r_{eff} and κ) are known. The resulting total evaporative heat transfer capacity of the wick is then:

$$\dot{Q} = \dot{m}_{y=0} h_{fg} = \frac{2\kappa A_c \rho}{H\mu} \left(\frac{2\sigma}{r_{eff}} - \rho gH \right) h_{fg} \quad (8)$$

Here, the wick properties r_{eff} (effective pore radius) and κ (permeability) are of particular interest. In general, these parameters yield opposite influences; a smaller effective pore radius will give a higher capillary pressure but will also tend to reduce the permeability. Wick optimization is therefore a task of finding a wick that provides the required liquid lifting height (H) and simultaneously provides sufficient mass transport capacity ($\dot{m}_{y=0}$).

4.2. Wick Porosity

The dimensions of the wick were after the sintering carefully adjusted by use of a high speed cutting tool. The cutoff pieces were used in the porosity experiment, based on the international standard ISO 5017 [16], using isopropanol.

4.3. Rate-of-Rise

The wick flow characteristics were tested in a rate-of-rise experiment, as described by Holley and Faghri [13]. Heptane was used as working fluid, and was introduced into the wick from a Petri dish placed on a balance while the wick was hanging from a stand. Figure 2 shows the setup.

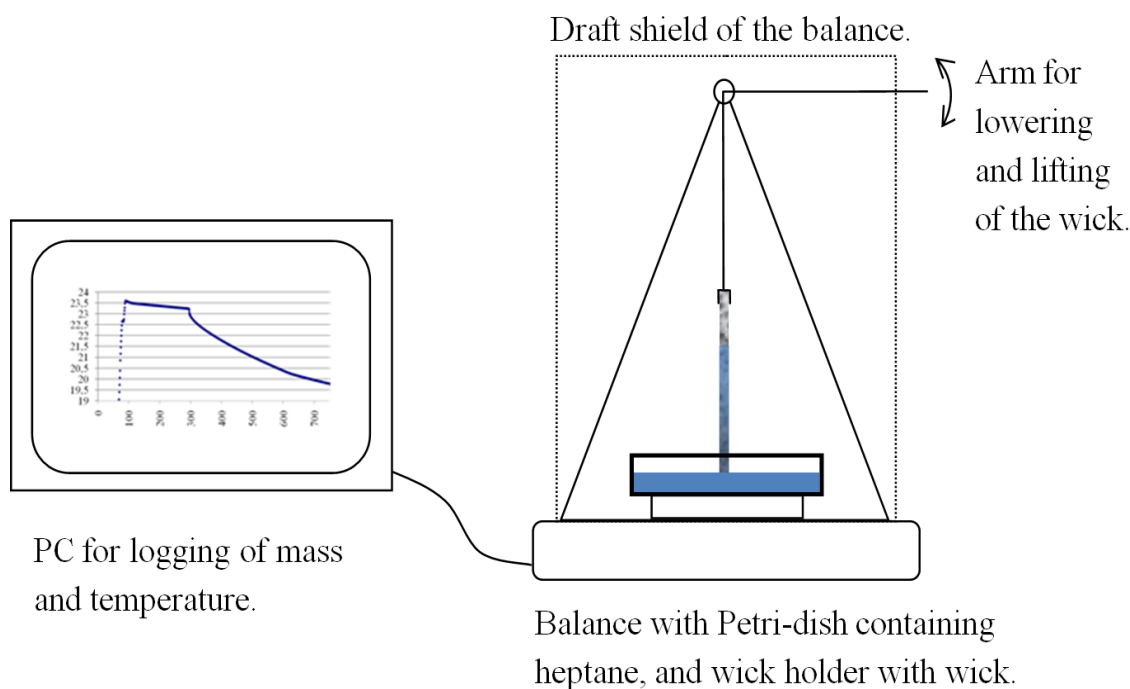


Figure 2. The rate-of-rise setup.

The mass uptake was measured by a balance (AT261 Deltarange with 10 μg resolution, manufactured by Mettler Toledo, Greifensee, Switzerland) connected to a PC running the LabView™ logging program. The evaporation rate from the surface of the heptane pool of the Petri dish was measured by recording the weight loss vs. time. Next, the wick tip was brought in contact with the heptane, and the weight loss was measured by the balance during the capillary rise of heptane in the wick. When the wick tip was submerged, the liquid meniscus around the wick imposed an upward force on the Petri dish causing a small drop in the force measured on the balance. Contrary to this, a small force increase on the balance caused by the submerged part of the wick is expected. These forces partly cancel each other and they do not change much during the experiment, *i.e.*, they are not significant for the shape of the mass-time curve used for the data reduction. No corrections of the recorded curves were therefore made. Finally, the combined evaporation rate from the wick and the Petri dish was measured when the liquid had reached the maximum height in the wick. The evaporation rate from the wick was determined by subtracting the evaporation rate of the pool in the Petri dish from the combined evaporation rate. Similarly, the weight measurements during capillary rise were corrected for the evaporation from the heptane pool surface of the Petri dish. A mathematical model for the rate-of-rise experiment taking evaporation from the wick into account was developed by Holley and Faghri [13], whose solution is presented as Equation (9). The derivation of Equation (9) is involved, however, it describes the rate-of-rise of a liquid which is spontaneously wetting an initially dry vertically mounted wick and takes evaporation into account. A high evaporation rate decreases the rate-of-rise. Equation (9) is discussed in

more detail in the paper by Holley and Faghri [13]. A MatLab™ script was used in the present work to fit the measured mass-time history to Equation (9):

$$C_1 \ln\left(1 - \frac{y}{C_1}\right) - C_2 \ln\left(1 - \frac{y}{C_2}\right) = -\frac{\Gamma(C_1 - C_2)}{2\varepsilon\rho A_c} t \quad (9)$$

The constants C_1 and C_2 were the roots to the quadratic equation, Equation (10), where C is the variable [13]:

$$C^2 + \frac{2\rho^2 g A_c \kappa}{\mu\Gamma} C - \frac{4\sigma\rho A_c \kappa}{r_{\text{eff}} \mu\Gamma} = 0 \quad (10)$$

The MatLab™ script determined the best pair of (r_{eff}, κ) by comparing the closed form solutions with experimental data and selecting the pair of (r_{eff}, κ) which caused the minimum mean absolute deviation (MAD).

5. Results and Discussion

5.1. Thermogravimetric Analysis and Temperature Programs

5.1.1. Nickel Oxide Formation

Nickel oxide formation occurred from around 300 °C, as can be seen in Figure 3, showing the mass/temperature plot of a thermogravimetric analysis performed using pure Inco 255 nickel powder in air. Increasing recorded mass indicates oxide formation on the powder surface.

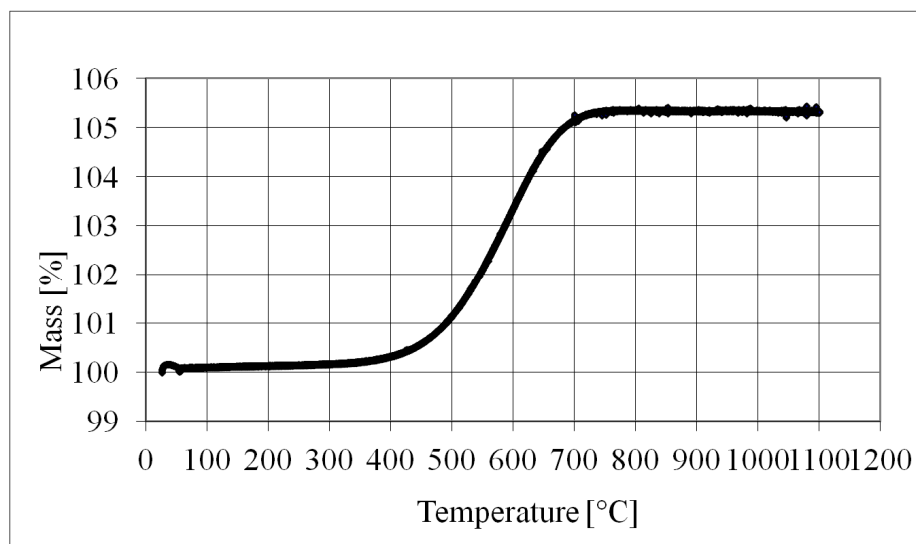


Figure 3. Thermogravimetric analysis of pure Inco 255 nickel powder in air.

5.1.2. Burn-off and Reduction

The result of a thermogravimetric analysis with the actual tape casted tape is shown in Figure 4.

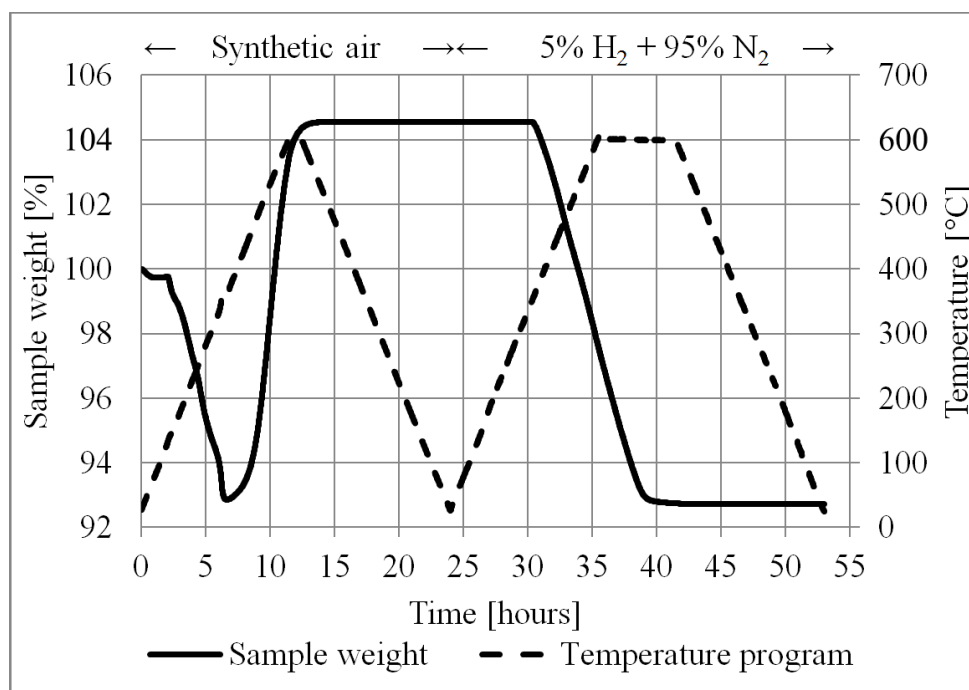


Figure 4. Thermogravimetric analysis of tape cast tape burn-off and reduction.

The first 24 h of this TGA temperature program was the burn-off sequence, using synthetic air atmosphere. The sample weight started to decrease rapidly at about 140 °C, indicating burn-off of the organic material in the tape. At about 350 °C the sample weight started increasing, likely due to a very high nickel oxide formation rate. The temperature was maintained at 600 °C for one hour. The sample weight then stabilized, indicating that the high rate of oxide formation had ended. After 24 h the temperature was at room temperature again and the gas flow was changed from synthetic air to a mixture of 5% (vol) H₂ + 95% (vol) N₂. Heating was started again, and at a temperature of about 350 °C the sample weight started decreasing, indicating that the nickel oxide was being reduced to pure nickel. Above 350 °C the rate of weight loss during reduction was almost constant, even when the temperature was increased up to 600 °C. This indicated that another parameter than temperature was limiting the rate of reduction, most likely the gas diffusion in the sample (pile of tapes) in the crucible, and/or limited molecular transport on/in the surface of the nickel oxide. The efficiency of the burn-off and reduction process could not be measured/quantified, hence the surface was investigated using microscope. No signs of unburned organics or green nickel oxide were found.

5.1.3. The Temperature Program

The final oven temperature program chosen for the burn-off and sintering process of the real wick is shown in Figure 5. The TGA-data of Figure 4 were utilized in the planning of the process. The requirements were:

- Sufficient time and temperature for the burn-off.
- Sufficient time and temperature for proper sintering and acceptable mechanical properties.
- Sufficient time and temperature for the reduction of the nickel oxide.

In general, too much time and/or too high temperature should be avoided in all parts of the program as this would make the wick unnecessary compact.

The first stage, *i.e.*, the burn-off in synthetic air, was carried out at a maximum level of about 360 °C. The gas composition was changed from synthetic air to a mixture of 5% H₂ + 95% N₂ after about 29 h. The second stage, *i.e.*, the sintering and reduction, started with a short temperature peak of about 580 °C to ensure proper sintering and mechanical properties of the wick. In order avoid too much compaction of the wick the temperature was then reduced to 400 °C. To ensure sufficient time for the reduction, it was decided to keep the wick for 8 h at about 400 °C.

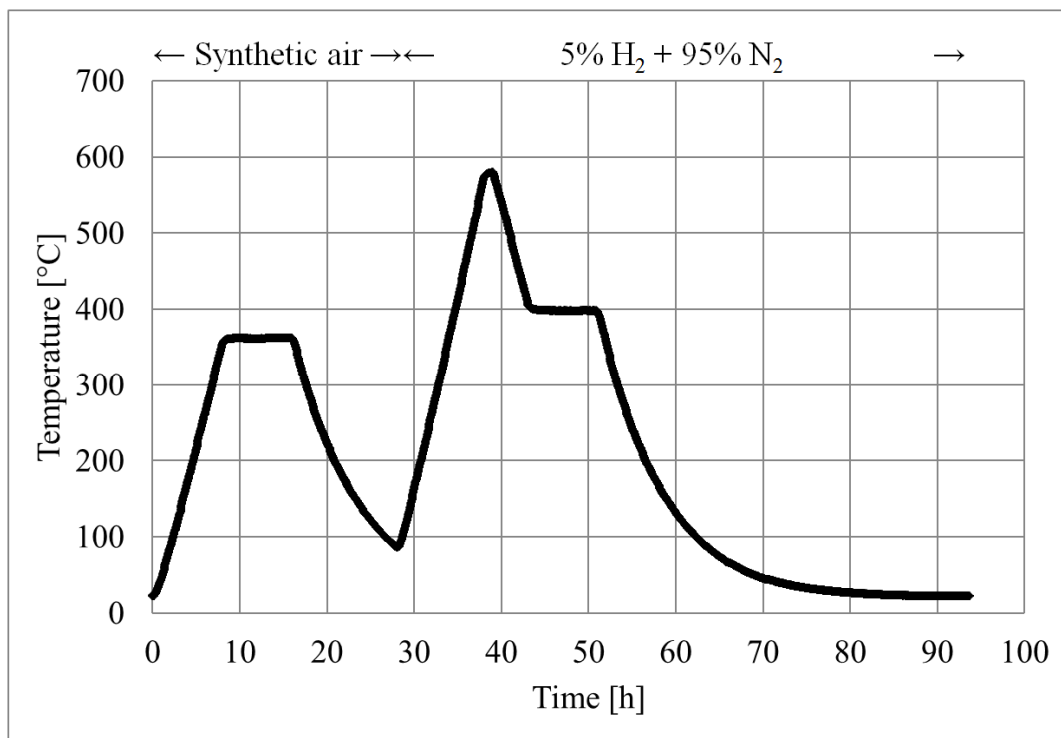


Figure 5. The temperature in the oven during the burn-off, the sintering and the reduction.

The tape layer structure could be observed after the sintering, but the resulting wick was mechanically strong.

5.1.4. Pure Graphite Powder

The thermogravimetric analysis with the pure graphite powder in air is shown in Figure 6.

The result shows that a burn-off temperature of 800 °C will oxidize all the graphite to CO or CO₂ gas.

5.1.5. Tape Containing Pore Former

The thermogravimetric analysis performed for the burn-off in air of a tape casted tape consisting of approximately equal amounts of Inco 255 nickel powder and graphite powder, plus the tape casting additives is shown in Figure 7.

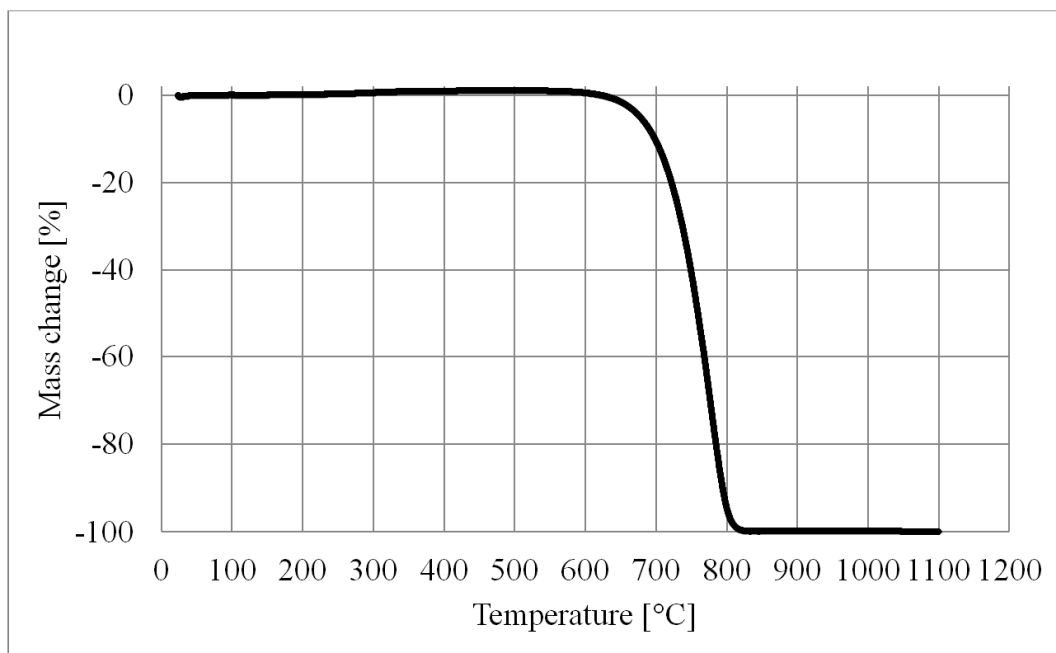


Figure 6. Thermogravimetric analysis with pure graphite powder in air, heating rate 5 K/min.

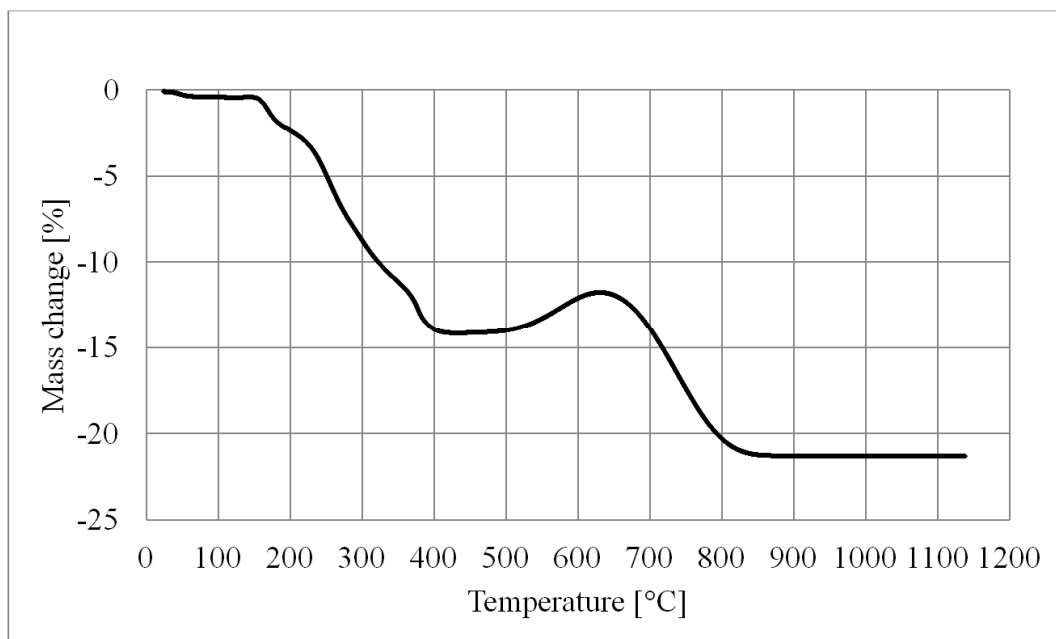


Figure 7. Thermogravimetric analysis of tape casted tape in air, heating rate 5 K/min.

The weight changes of the sample can be explained as follows: From 150 °C to 400 °C the weight decreased because the tape casting additives were being burnt off. From around 300 °C nickel oxide was formed, causing a weight increase. From around 600 °C the graphite started oxidizing and leaving the sample. Just above 800 °C the weight stabilized, indicating that all the graphite was gone and no more nickel oxide was being formed.

5.2. The Contact Angle

From a series of capillary rise experiments with nickel foam wicks and heptane the contact angle of heptane on nickel was determined to 58.4° [23]. For potassium on nickel a contact angle of 0° was assumed [21].

5.3. Wick Porosity

The porosity measured from three samples of the wick produced by tape casting were $\varepsilon_1 = 0.801$, $\varepsilon_2 = 0.79$ and $\varepsilon_3 = 0.806$, which yielded an average result of $\varepsilon \approx 0.80$. The applied measurement method ISO 5017 declares that “the values of porosity shall be given to the nearest 0.1% (V/V)” [16]. In the current study the sizes of the samples were smaller than specified by the standard, this could have led to somewhat larger variations in the results than expected from the standard. The uncertainty is set equal to the measurement variability, *i.e.*, $\pm 0.7\%$.

5.4. Rate-of-Rise

The height vs time data from the rate-of-rise experiment for the wick produced by tape casting is shown in Figure 8. The height values were calculated numerically from the mass data from the balance, taking the evaporation into account. The evaporation rate from the wick was determined from the experiment. The measured points in Figure 8 are completely covering the “Fit” line generated from the rate-of-rise theory.

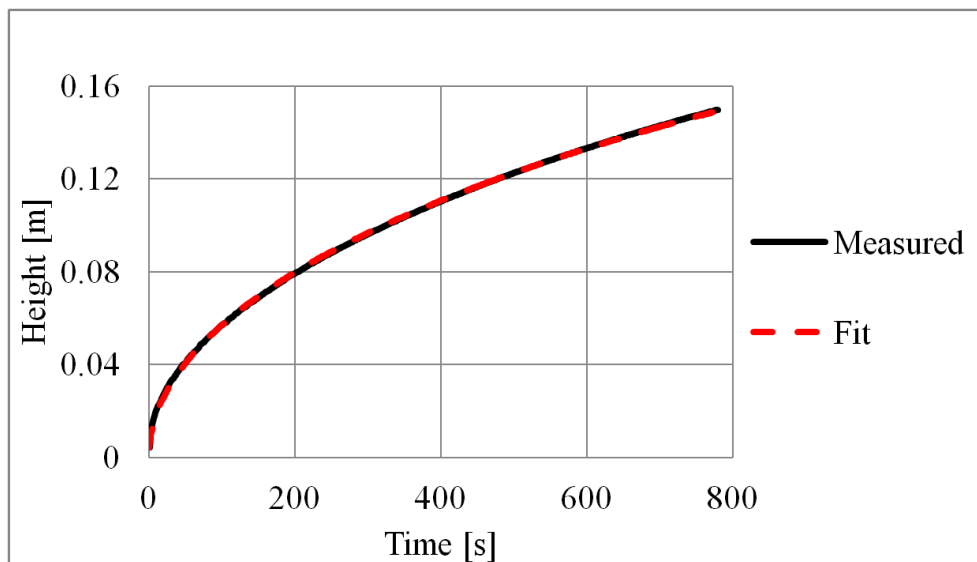


Figure 8. Rate-of-rise data for the wick produced by tape casting.

The permeability was determined to $0.108 \cdot 10^{-12} \text{ m}^2$ and the effective pore radius with heptane to $0.826 \cdot 10^{-6} \text{ m}$. From Equation (2) the effective pore radius with potassium then became $0.43 \text{ }\mu\text{m}$. The sensitivity of these values to changes in key variables is discussed in Section 5.6—Sensitivity Analysis. The thermophysical data for heptane and potassium were taken from Faghri [4].

5.5. Prediction of the Wick Maximum Heat Transfer Capacity with Potassium

Static Pressure Limitation

The capacity of the wick made by tape casting, 2.825 mm thick, operated with potassium at 500 °C would according to Equation (8) have been approximately 94 kW/m² uniform heat flux over the entire surface of 25 × 150 mm. Unfortunately the actual capacity for potassium at 500 °C is much less (only 844 W/m²), due to a heat transfer limitation which has not been given attention in literature: In a heat pipe the capillary pressure can never be higher than the vapour static pressure of the working fluid. For alkali metals, which have very low vapour static pressures, this limitation is of particular interest, especially where large driving pressures are needed, like in long vertical heat pipes with the capillary force working against the gravity. This limitation is termed the “static pressure limit” as it is the vapour static pressure of the working fluid that limits the available driving pressure.

A reduction of the wick height reduces the pressure losses and increases the heat transfer capacity. The tape casted wick could have handled a uniform heat flux of 9069 W/m² if its height was reduced to 50 mm. An example of how the static pressure limit of the wick appears in a temperature vs. heat flux plot is shown in Figure 9. The plot is for the tape casted wick, 150 mm and 50 mm high, with potassium as working fluid. The capillary pressure is equal to the vapour static pressure at the peaks where the lines representing SPL and CPL intercept. The vapour static pressure of potassium is the limiting pressure for the operation temperatures below the interception point. For temperatures above the interception point the capillary pressure becomes the limiting pressure. For the tape casted wick and using potassium, the interception is obtained at a temperature of about 883 °C. However, this temperature is so high that it would cause sintering of this wick during use.

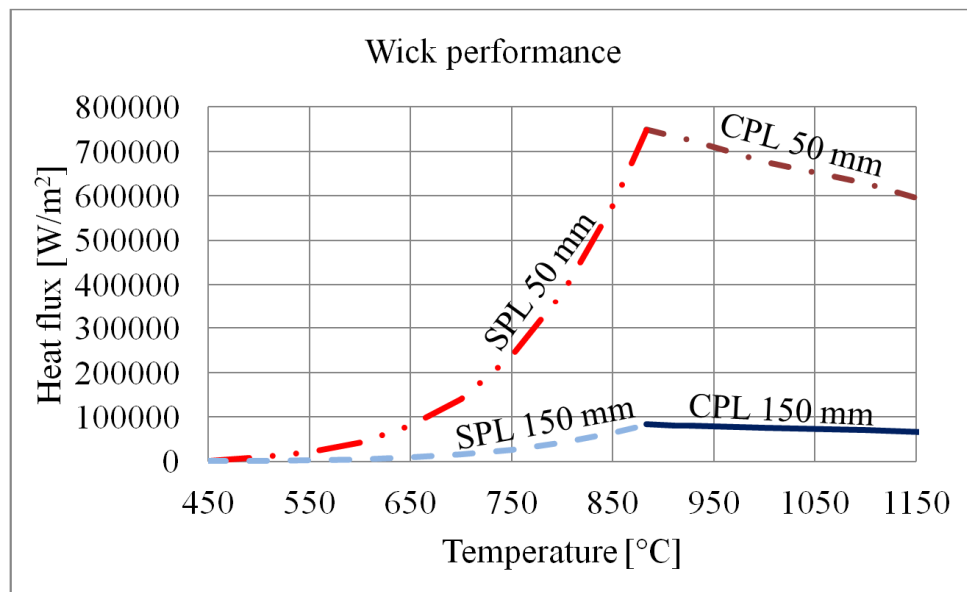


Figure 9. The theoretical performance of the tape cast wick with potassium working fluid. SPL = Static pressure limited. CPL = Capillary pressure limited.

The exponential form of the SPL curves is caused by the increase in vapour static pressure of the potassium with increasing temperature. The drop in capacity in the CPL region with increasing T is due to

the combined effect of the fluid physical properties (viscosity, surface tension, density and latent heat of vapourization).

5.6. Sensitivity Analysis

A sensitivity analysis was carried out to see the influence of changes in temperature, porosity, evaporation rate and length measurements on the heat transfer capacity of the wick produced by tape casting. The parameters were varied one by one and the corresponding combinations of effective pore radius and permeability determined. The corresponding heat transfer capacities were calculated by use of Equation (8).

The Influence of Parameter Variations Above and Below $P_{cap}/P_{sat} = 1$

It was noticed that small changes in the parameters could cause quite large changes in the effective pore radius and permeability. This finding was also reported by Nam *et al.* [24] who, in order to overcome the large uncertainties, predicted the permeability by numerical simulations, and used this permeability value together with the rate-of-rise data to determine the effective pore radius. Separate determination of the permeability was also used by Deng *et al.* [12,25].

Despite of the high sensitivity of (r_{eff}, κ) to changes in the parameters, the corresponding heat transfer capacities were almost unaffected as long as the capillary pressure was the limiting pressure, indicating that the new sets of effective pore radius and permeability were all on an iso-capacity line. However, the large changes in the permeability propagated to large uncertainties in the calculated capacities for temperatures where the vapour static pressure of the potassium was the limiting pressure, since in this range the large permeability changes were not balanced by corresponding changes in the capillary pressure.

Changes in the heat transfer capacity were calculated for the temperatures 850 °C and 1050 °C to illustrate how changes in the parameters had different impacts above and below $P_{cap}/P_{sat} = 1$. The results are presented in Table 1.

Table 1. The heat transfer capacity sensitivity due to parameter changes above and below $P_{cap}/P_{sat} = 1$.

Parameter	Change	Change in heat transfer	Change in heat transfer
		capacity at 850 °C (vapour static pressure limited)	capacity at 1050 °C (capillary pressure limited)
Temperature	+1.2 K	−28%	−0.2%
Porosity	+1%	−40%	−0.9%
Evaporation rate	+1%	−28%	−0.05%
Cross sectional area	+1%	−47%	−6%

The large differences between the sensitivities for the calculated capacities above and below $P_{cap}/P_{sat} = 1$ are clearly seen. Plots of the mean absolute deviation (MAD) between the calculated and measured time-height-data did show that there were many pairs of (r_{eff}, κ) that had near identical MAD. All these different pairs of (r_{eff}, κ) would give an apparently close to perfect curve fit of the height-time measurements (Figure 8). The calculated sets of (r_{eff}, κ) for each parameter perturbation in Table 1 varied significantly (as implicitly indicated by the vapour-static-pressure-limited performance sensitivity), but had no significant impact on the capillary-pressure-limited performance. Hence, the rate-of-rise results are useful in the CPL range, even though the individual real values of r_{eff} and κ are “unknown”.

The permeability has to be known with higher certainty for more reliable wick capacity predictions in the temperature range where the vapour static pressure is limiting.

5.7. Criterion for Pore Former Selection

Improved wick performance for potassium/alkali metals would be obtained in both the vapour static pressure limited region and the capillary pressure limited region if the permeability of the wick could be increased without affecting the effective pore radius. However, an increase in the permeability is normally accompanied by an increase in the effective pore radius, and it is therefore necessary to consider the consequences of changes in these parameters together. For wicks made of sintered powder the permeability (and thereby also inevitably the effective pore radius) can be increased by use of a pore former. The permeability and the effective pore radius will generally not experience the same relative change. The consequence for the wick capacity in the vapor static pressure limited region depends on the permeability change, and the consequence in the capillary pressure limited region depends on the relative changes of the permeability and the effective pore radius. The consequence for the wick performance will generally be different in the vapour static pressure limited region and the capillary pressure limited region, because the vapour static pressure is unaffected by changes in the effective pore radius while the capillary pressure is directly a function of the effective pore radius.

In the vapour static pressure limited region the wick performance will always be improved by increased permeability. In order for the pore former to cause general capacity improvement in the capillary pressure limited region, the relative changes in effective pore radius and permeability have to satisfy the criterion for wick capacity improvement by use of pore former, which is derived below.

From Equation (8) it is seen that a proportional increase of the effective pore radius and the permeability actually reduces the wick capacity. Wick improvement requires that the permeability increases more than the effective pore radius, and the exact requirement can be derived from Equation (8). If the increase in effective pore radius is expressed by the factor k_r and the increase in permeability is expressed by the factor k_κ then Equation (8) becomes:

$$\dot{Q} = \dot{m}_{y=0} h_{fg} = \frac{2\kappa k_\kappa A_c \rho}{H \mu} \left(\frac{2\sigma}{r_{eff} k_r} - \rho g H \right) h_{fg} \quad (11)$$

By combining Equation (11) and Equation (8) the relation between k_κ and k_r appears as:

$$k_\kappa = \frac{\frac{2\sigma}{r_{eff}} - \rho g H}{\frac{2\sigma}{r_{eff} k_r} - \rho g H} \quad (12)$$

In Figure 10 the factor k_κ is plotted against the factor k_r for different effective pore radii using Equation (12), with $H = 0.1$ m and properties for heptane at temperature 20 °C.

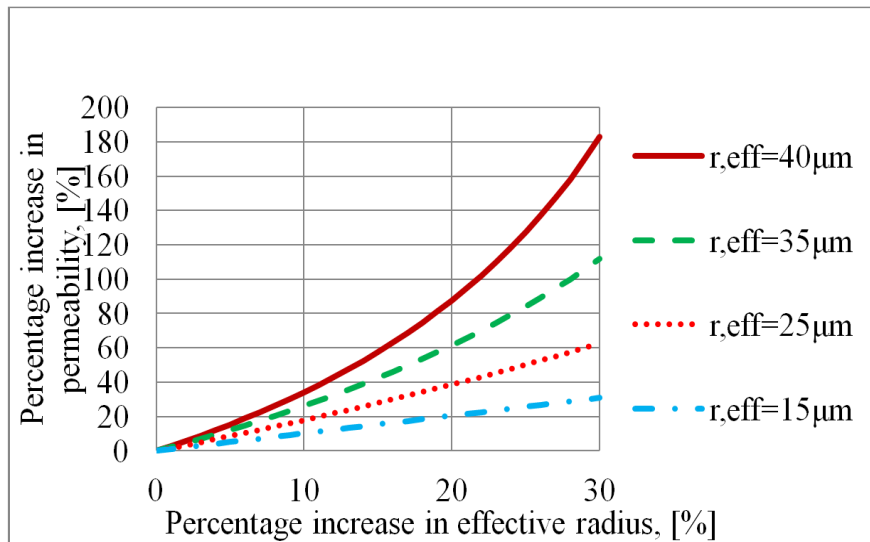


Figure 10. Pore former evaluation plot for $H = 0.1$ m and heptane at $20\text{ }^\circ\text{C}$.

The lines in Figure 10 are iso-capacity lines, *i.e.*, the wick capacities are unchanged along the lines. For effective pore radii up to about $15\text{ }\mu\text{m}$ the lines are almost linear, *i.e.*, the capillary term is completely dominating. With increasing effective pore radii the lines become more curved, *i.e.*, in order to maintain the wick capacity the permeability has to increase more than the effective radius. When an iso-capacity line curves upwards the overall effect of a change $k_r = k_k$ on the wick capacity is negative. The use of a pore former is only successful if it leads to a point above the line, see Figure 11. For instance, in Figure 10, for $r_{\text{eff}} = 35\text{ }\mu\text{m}$ a 20% increase of the effective pore radius has to be accompanied by more than 60% increase of the permeability in order to have an overall heat transfer capacity improvement for the wick.

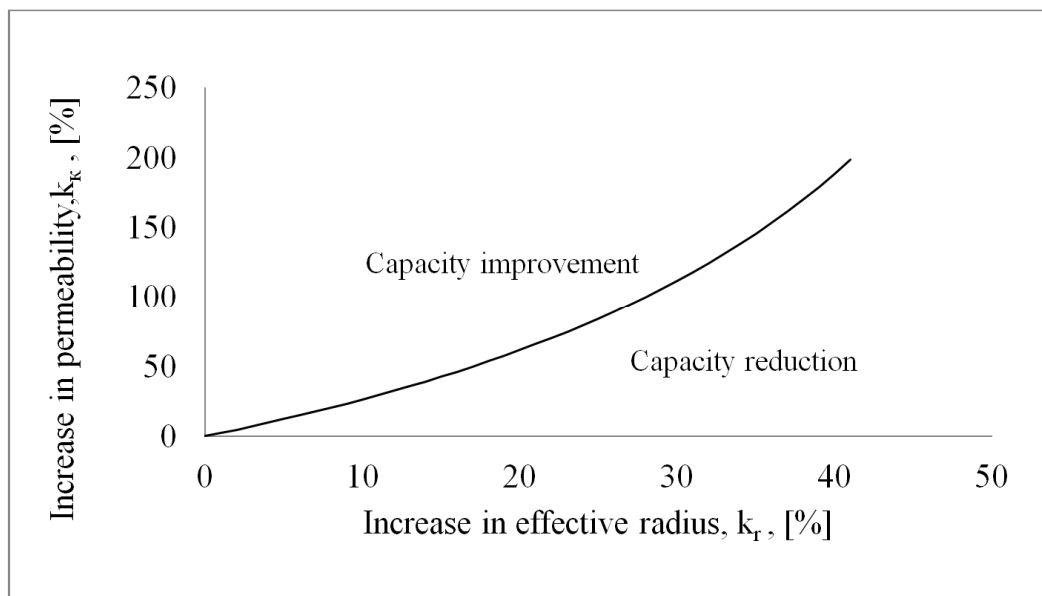


Figure 11. Pore former evaluation plot.

One way to achieve larger increase in the permeability than in the effective pore radius may be to use a pore former consisting of long filaments, creating longitudinal channels in the sintered metal powder. A potential candidate is using carbon fibers arranged in the wick flow direction.

6. Conclusions

- The capillary pressure inside a heat pipe can never exceed the vapour static pressure of the working fluid. This will limit the heat transfer capacity and the useful operating temperature range for heat pipes with wicks with small effective pore radii operated with working fluids with low vapour static pressures, for instance alkali metals.
- Determination of the effective pore radius and the permeability from a rate-of-rise experiment alone can lead to great uncertainties about the actual values. Many different pairs of (r_{eff} , κ) give good curve fits, and in such case they can all be used for approximate wick capacity predictions for ($P_{\text{cap}}/P_{\text{sat}} < 1$). For wick capacity predictions for ($P_{\text{cap}}/P_{\text{sat}} > 1$) the permeability has to be known with higher accuracy.
- In the vapour static pressure limited region the use of a pore former which increases the wick permeability will always improve the wick performance.
- In the capillary pressure limited region, a pore former evaluation plot may be made in order to analyse the effects of using a pore former. If the effective radius and permeability increase with an equal percentage the overall effect on the wick heat transfer capacity is negative. A pore former which increases the permeability more than the effective pore radius would be a better choice than a powderous pore former. One such candidate can be carbon fibers.
- The oxidation of Inco 255 nickel powder accelerates at about 350 °C.
- The reduction of nickel oxide in 5% H_2 + 95% N_2 accelerates at about 350 °C.
- In order to burn off a graphite powder pore former a temperature of about 800 °C is required.

Acknowledgments

The authors would like to thank Elkem and the Research Council of Norway for funding this work. Thanks to Mr. Rhodri Bowen of Vale Inco Europe Ltd for supplying Inco 255 nickel powder. Thanks to Dr. Vegar Øygarden for assistance on pure nickel powder TGA and to Dr. Ove Paulsen for valuable and inspiring talks on sintering.

Author Contributions

Geir Hansen carried out the experimental work, data reduction, and prepared the first draft of the paper. The MatLab™-code for the rate-of-rise analysis and the pore former success criterion were made by Kolbeinn Kristjansson. Geir Hansen and Erling Næss have equally contributed on the analysis and paper preparation.

Symbols

A_c	wick cross sectional area, m^2
C	constant
E	Deviation
g	gravity constant, $g = 9.81 \text{ m/s}^2$
H	height, m
h_{fg}	latent heat of evaporation, kJ/kg

k_{κ}	factor expressing change in permeability
k_r	factor expressing change in radius
\dot{m}	mass flow rate, kg/s
P	pressure, Pa
\dot{Q}	heat flow rate, W
r	radius, m
r_{eff}	effective radius, m
t	time, s
V	volume
\dot{V}	velocity, m/s
y	height, m

Greek symbols

Γ	evaporation rate per unit height of wetted wick, kg/(m·s)
ε	porosity
θ	solid-liquid-vapour contact angle, degrees
κ	permeability, m ²
μ	dynamic viscosity, kg/(m·s)
ρ	density, kg/m ³
σ	surface tension, N/m

Subscripts

cap	capillary
eff	effective (pore radius)
f	friction
g	gravity
l	liquid
sat	saturated
v	vapour

Conflicts of Interest

The authors declare no conflict of interest.

References

1. Reay, D.A.; Kew, P.A.; Dunn, P.D. *Heat Pipes*; Elsevier: Amsterdam, The Netherlands, 2006.
2. Çengel, Y.A. *Heat and Mass Transfer: A Practical Approach*; McGraw-Hill: Boston, MA, USA, 2007.
3. De Schampheleire, S.; De Kerpel, K.; Deruyter, T.; De Jaeger, P.; De Paepe, M. Experimental study of small diameter fibres as wick material for capillary-driven heat pipes. *Appl. Therm. Eng.* **2015**, *78*, 258–267.
4. Faghri, A. *Heat Pipe Science and Technology*; Taylor & Francis: Washington, DC, USA, 1995.

5. Franchi, G.; Huang, X. Development of composite wicks for heat pipe performance enhancement. *Heat Transf. Eng.* **2008**, *29*, 873–884.
6. Huang, X.; Franchi, G. Design and fabrication of hybrid bi-modal wick structure for heat pipe application. *J. Porous Mat.* **2008**, *15*, 635–642.
7. Huang, X.; Franchi, G.; Cai, F. Characterization of porous bi-modal ni structures. *J. Porous Mat.* **2009**, *16*, 165–173.
8. Li, J.; Zou, Y.; Cheng, L.; Singh, R.; Akbarzadeh, A. Effect of fabricating parameters on properties of sintered porous wicks for loop heat pipe. *Powder Technol.* **2010**, *204*, 241–248.
9. Kim, H.J.; Lee, S.-H.; Kong, Y.C.; Jang, S.P.; Choi, J.H.; Koo, J. Long-term reliability of the thermal performance of a flat-plate heat pipe using a prognostics method. *Int. J. Heat Mass Transf.* **2015**, *82*, 369–372.
10. Sheehan, J.; Queheillalt, D.T.; Norris, P.M. An evaluation of the wicking characteristics of stochastic open-cell nickel foams. In Proceedings of the 2006 ASME International Mechanical Engineering Congress and Exposition, IMECE2006, Chicago, IL, USA, 5–10 November 2006.
11. Shirazy, M.R.S.; Blais, S.; Frechette, L.G. Mechanism of wettability transition in copper metal foams: From superhydrophilic to hydrophobic. *Appl. Surf. Sci.* **2012**, *258*, 6416–6424.
12. Deng, D.; Liang, D.; Tang, Y.; Peng, J.; Han, X.; Pan, M. Evaluation of capillary performance of sintered porous wicks for loop heat pipe. *Exp. Therm. Fluid Sci.* **2013**, *50*, 1–9.
13. Holley, B.; Faghri, A. Permeability and effective pore radius measurements for heat pipe and fuel cell applications. *Appl. Therm. Eng.* **2006**, *26*, 448–462.
14. Tracey, V.A. Sintering data for inco nickel powder type 255. In *Technical Note*; INCO: New York, NY, USA, 1979.
15. Mistler, R.E.; Twiname, E.R. *Tape Casting Theory and Practice*; The American Ceramic Society: Westerville, OH, USA, 2000.
16. *Dense Shaped Refractory Products—Determination of Bulk Density, Apparent Porosity and True Porosity*; International Organization for Standardization: Geneva, Switzerland, 1998.
17. Adkins, D.R.; Dykhuizen, R.C. Procedures for measuring the properties of heat-pipe wick materials. In Proceedings of the 28th Intersociety Energy Conversion Engineering Conference, Atlanta, GA, USA, 8–13 November 1993; American Chemical Society: Washington, DC, USA, 1993; Volume 2, pp. 911–917.
18. Shirazy, M.R.S.; Frechette, L.G. Investigation of capillary properties of copper metal foams by the rate of rise method in the presence of evaporation. In Proceedings of the 13th InterSociety Conference on Thermal and Thermomechanical Phenomena in Electronic Systems, ITherm 2012, San Diego, CA, USA, 30 May–1 June 2012; IEEE Computer Society: San Diego, CA, USA, 2012; pp. 710–716.
19. Hiemenz, P.C. *Principles of Colloid and Surface Chemistry*; Dekker: New York, NY, USA, 1986.
20. Dwyer, O.E. *Boiling Liquid-Metal Heat Transfer*, 1st ed.; American Nuclear Society: Hinsdale, IL, USA, 1976.
21. Barlow, M.; Planting, P.J. Wetting of metal surfaces by liquid alkali metals. *Z. Metallk.* **1969**, *60*, 719–722.
22. Reay, D.A.; Kew, P.A.; McGlen, R.; Dunn, P.D. *Heat Pipes: Theory, Design, and Applications*; Butterworth-Heinemann, an imprint of Elsevier: Kidlington, Oxford, UK, 2014.

23. Hansen, G.; Næss, E. Performance of compressed nickel foam wicks for flat vertical heat pipes. *Appl. Therm. Eng.* **2015**, *81*, 359–367.
24. Nam, Y.; Sharratt, S.; Byon, C.; Sung Jin, K.; Ju, Y.S. Fabrication and characterization of the capillary performance of superhydrophilic cu micropost arrays. *J. Microelectromech. Syst.* **2010**, *19*, 581–588.
25. Deng, D.; Tang, Y.; Huang, G.; Lu, L.; Yuan, D. Characterization of capillary performance of composite wicks for two-phase heat transfer devices. *Int. J. Heat Mass Transf.* **2013**, *56*, 283–293.

© 2015 by the authors; licensee MDPI, Basel, Switzerland. This article is an open access article distributed under the terms and conditions of the Creative Commons Attribution license (<http://creativecommons.org/licenses/by/4.0/>).

3.1.6 Performance of compressed nickel foam wicks for flat vertical heat pipes

Compression of nickel foam was one of the wick production methods investigated. This chapter was published as a separate paper “Performance of compressed nickel foam wicks for flat vertical heat pipes” in Applied Thermal Engineering, vol 81, pp. 359-367, 2015, presented in the following pages.



Research paper

Performance of compressed nickel foam wicks for flat vertical heat pipes



Geir Hansen*, Erling Næss

Department of Energy and Process Engineering, Norwegian University of Science and Technology, Kolbjørn Hejes vei 1a, 7491 Trondheim, Norway

HIGHLIGHTS

- Wicks for flat vertical heat pipes were produced from compressed nickel foam.
- Wicks of different degrees of compression were produced.
- Effective pore radius and permeability were determined by rate-of-rise using heptane.
- Porosity was determined using isopropanol.
- Wick performance was estimated for potassium as working fluid.

ARTICLE INFO

Article history:

Received 7 August 2014

Accepted 18 February 2015

Available online 26 February 2015

Keywords:

Heat pipe

Wick

Nickel foam

Sintering

Rate-of-rise

ABSTRACT

The fabrication and performance of wicks for vertical flat heat pipe applications produced by compression of nickel foams has been investigated. The permeabilities and the effective pore radii for the wicks were estimated from rate-of-rise experiments, using the model fluid heptane. The porosities of the wicks were measured using isopropanol. The results, which are new and of vital importance for optimum use of such wicks, show that the permeabilities and the effective pore radii are in the upper range for heat pipe use. The joining pressure required during the sintering of the wicks was determined, and it was discovered that the nickel foams turned hydrophilic during the sintering.

© 2015 Elsevier Ltd. All rights reserved.

1. Introduction

Well designed heat pipes have the ability to transport heat at high rates and at minimal temperature drop. The main reason for their high effectiveness is that the heat internally in the heat pipe is transported by vapour, utilizing evaporation and condensation of a working fluid. Heat pipes are in use in many fields and at many temperature levels, from cryogenic applications to the high temperatures in the metallurgical industries [1,2]. The number of available working fluids, especially for operation in the extreme temperatures, is limited. The same is true for the number of compatible construction materials and wicks. Inside the heat pipe the condensate is transported to, and distributed over the evaporator section by capillary forces created by a porous wick structure. The most attractive wick provides a high capillary pressure and at

the same time an acceptable flow resistance. The heat pipe for a specific application is unfortunately often selected from a quite limited selection of heat pipe container materials, wick materials and structures, and working fluids. This is especially true for heat pipes needed for the extreme working temperatures. The current study was undertaken to provide wick design data for the wick of a vertical flat hybrid heat pipe/thermosyphon with potassium as working fluid, for operation up to 650 °C in the metallurgical industry. Model fluids (heptane and isopropanol) were used to characterize the wicks, as the characterization experiments would be very difficult to carry out with potassium due to its reactivity with air and moisture. Overviews over established materials, structures and working fluids suitable for different working temperatures are available in textbooks [1–4]. Recently Dillig et al. [5] carried out experiments with planar heat pipes using sodium as working fluid and different types of wick structures (screen mesh, sintered plates and grooves). The capillary limitation was identified as one of the main challenges in their study, underlining the importance of the wick structure optimization.

* Corresponding author. Tel.: +47 73593938; fax: +47 73593580.
E-mail address: g.hansen@ntnu.no (G. Hansen).

Nomenclature

Symbols

A_c	wick cross sectional area, m^2
g	gravity constant = 9.81 m/s^2
H	height, m
h_{fg}	latent heat of evaporation, J/kg
m	mass, kg
\dot{m}	mass flow rate, kg/s
P	pressure, Pa
\dot{Q}	heat flow rate, W
r	radius, m
r_{eff}	effective pore radius, m
t	time, s
T	temperature
V	volume, m^3
W	width, m
y	height, m

Greek symbols

ε	porosity, –
θ	solid–liquid–vapour contact angle, degrees ($^\circ$)
κ	permeability, m^2
μ	dynamic viscosity, $kg/(m \text{ s})$
ρ	density, kg/m^3
σ	surface tension, N/m
δ	thickness, m
Δ	difference

Subscripts

cap	capillary
eff	effective (pore radius)
evap	evaporation
fric	friction
g	gravity
hs	hydrostatic
l	liquid
v	vapour
0	uncompressed

Wick optimization and development are also given much attention by researchers working on lower temperature systems, particularly wicks of grooves and/or sintered powders for loop heat pipe applications in the computer industry [6]. Usually the goal is to achieve high capillary pressure and high permeability, but the weight of the wick structure can also be a parameter for optimization [7]. For conventional single phase cooling systems various methods of surface optimization exist [8,9], however, the present paper deals with experimentally obtained characteristics of compressed nickel foam which may in the future lend itself to similar optimization.

Wick technologies can be combined. Recently Li et al. [10] analysed the performance of a cylindrical heat pipe with a composite wick having high permeability axial grooves which were covered (but not filled) by a layer of sintered copper powder. The performance was compared to the performance of a heat pipe with larger grooves filled with copper powder. The heat pipe with the active grooves had lower total thermal resistance, but the same maximum heat transfer rate as the heat pipe without active grooves. Jiang et al. [11] successfully developed and tested a novel porous crack composite wick for microchip cooling for working temperatures below $60 \text{ }^\circ\text{C}$. Solomon et al. [12] used nanoparticles of copper to coat screen type wicks, and found that this reduced the thermal resistance in the evaporator of the heat pipe but increased the resistance of the condenser. The overall result was positive, since the total resistance was reduced.

Compression of nickel foam, as described by Sheehan et al. [13] and Queheillalt et al. [14], is one method of producing wicks which has so far not been given much attention. The method is particularly interesting because the degree of compression, and thereby the pore size and the wick properties can be tailored to best fit the requirement of the application at hand. Recently Silk and Myre [15] used compression to obtain the desired pore size for a carbon wick structure, for loop heat pipes using water as working fluid. Several layers of compressed foam can be sintered together to increase the total capacity of the wick. Huang, Franchi and Cai [16] created bimodal nickel wicks for heat pipes by sintering filamentary nickel powder onto uncompressed nickel foam. In the future even more tailor made wicks are anticipated, e.g. by sintering nickel powder onto compressed nickel foam.

Nickel foam was chosen as wick material by Queheillalt et al. [14] because it was considered compatible for a heat pipe using

water as working fluid. Material compatibility makes nickel equally relevant for high temperature heat pipes using alkali metals such as potassium or sodium as working fluids. Stainless steel 304 is also compatible with potassium and sodium [1], but has a much lower thermal conductivity than nickel. Nickel foams are currently produced for the battery industry in large batches according to customer specifications. Unmodified foams usually have pore sizes of a few hundred microns, which are too large for heat pipe wick applications. The foams are usually characterized by the density, pore size and thickness. For heat pipe wick applications additional data are needed, especially related to the wettability and the flow characteristics of different wick and working fluid combinations. The key parameters for the flow characteristics are the permeability and the effective pore radius of the wick. The effective pore radius depends on the wettability, commonly described by the contact angle [17]. The porosity of the wick is another important parameter which is required in design processes, for instance in order to precisely calculate the amount of working fluid required in the heat pipe. In the present work the following elements have been investigated for the compressed nickel foam wicks:

- The wettability with water before and after the oxide reduction process.
- The joining pressure required on the layers during the sintering to achieve a mechanically strong multilayer wick.
- Porosities at different wick compression.
- Contact angles with heptane, estimated from measurements of maximum capillary rise and evaporation rates from the wicks.
- Effective pore radius and permeability estimates from rate-of-rise experiments with heptane.
- The effect of heptane evaporation and experiment duration on the rate-of-rise experiment results.
- The heat transfer capacity with potassium as working fluid.

2. Theory

In most heat pipe design calculations the wick is characterized by its porosity, permeability and effective pore radius. The theories behind the experimental determination of these parameters are based on assumptions which are mentioned in conjunction with the specific equations, however two recurring assumptions are:

- A capillary tube model is used to represent the wick.
- The density of the liquid phase is large compared to the density of the vapour phase, hence the vapour density can be neglected.

The permeability, κ , characterizes the frictional pressure drop characteristics of the liquid flowing in the wick as shown by Eq. (1) [18].

$$\frac{dP_{fric}}{dy} = -\frac{\dot{m}\mu}{\kappa A_c \rho} \quad (1)$$

where y is defined as positive in the upwards direction from the liquid bath level. This flow direction may also be called the vertical in-plane direction, and it is perpendicular to the “through thickness” flow direction as studied by Sheehan et al. [13].

If uniform evaporation is assumed over the wetted wick height, H , (as is the case for most heat pipes), Eq. (1) can be integrated to yield the total frictional pressure drop:

$$\Delta P_{fric} = -\frac{\mu_l}{\kappa \rho_l A_c} \dot{m}_{max} \left(\frac{H}{2} \right) \quad (2)$$

where \dot{m}_{max} is the mass flow rate at the fluid entrance end of the wick.

For vertical wicks there is also a hydrostatic pressure drop created by the liquid column in the wick [18]:

$$\Delta P_{hs} = -\frac{g m_l}{\varepsilon A_c} = -\rho_l \cdot g \cdot H \quad (3)$$

The “pumping” pressure balancing the pressure drops is the capillary pressure. According to Eq. (4), which was derived from an ideal circular capillary tube, the influence of the contact angle (θ) is merged into the effective pore radius [18]. The capillary pressure becomes:

$$\Delta P_{cap} = \frac{2\sigma \cos(\theta)}{r} = \frac{2\sigma}{r_{eff}} \quad (4)$$

If the effective pore radius is determined from an experiment using a model fluid, the effective pore radius with the actual working fluid can be calculated from Eq. (5), provided that the contact angles of the respective fluids on the wick surface are known:

$$\frac{r_{eff,fluid\ 1}}{r_{eff,fluid\ 2}} = \frac{\cos \theta_{fluid\ 2}}{\cos \theta_{fluid\ 1}} \quad (5)$$

If it is assumed that there is no evaporation of liquid from the wick, the maximum rise of liquid in the wick can be determined by balancing the capillary pressure to the hydrostatic pressure of the liquid in the wick [14]:

$$H = \frac{2\sigma \cos \theta}{g r (\rho_l - \rho_v)} \approx \frac{2\sigma \cos \theta}{g r (\rho_l)} = \frac{2\sigma}{g r_{eff} \rho_l} \quad (6)$$

where the last 2 terms presuppose $\rho_l \gg \rho_v$, which is often justifiable. Eq. (6) can alternatively be used to determine the contact angle if the actual radius, r , and the maximum wetted height, H , are known. The maximum wetted height (i.e. the observed height) may be read visually from a capillary rise experiment by use of a ruler, alternatively the maximum wetted height can be calculated from weight measurements of the amount of liquid wetting the wick, further discussed in the next section. Normally, there will be liquid evaporating from the wick surface, hence there will be flow in the wick even when the maximum height is reached; i.e. there is a pressure drop term due to friction in addition to the gravitational pressure term. Assuming uniform evaporation on the wick surface,

the pressure balance at the maximum wetted height (steady state condition) requires

$$\Delta p_{cap} + \Delta p_{hs} + \Delta p_{fric} = 0 \quad (7)$$

i.e.

$$\frac{2\sigma}{r_{eff}} = \rho_l g H + \frac{\mu_l}{\kappa \rho_l A_c} \dot{m}_{max} \left(\frac{H}{2} \right) \quad (8)$$

where \dot{m}_{max} is the evaporating liquid mass flow rate. Eq. (8) can be combined with Eq. (4) to yield:

$$\theta = \cos^{-1} \left(\left(\frac{r}{2\sigma} \right) \left(\rho_l g H + \frac{\mu}{\kappa \rho_l A_c} \dot{m}_{max} \left(\frac{H}{2} \right) \right) \right) \quad (9)$$

Eq. (9) is an implicit equation as the maximum evaporating mass flow rate, \dot{m}_{max} , is a function of the permeability, κ , and the effective pore radius, r_{eff} , as seen from Eq. (8), and the effective pore radius is again a function of the contact angle, θ . In order to estimate θ from Eq. (9) it is thus necessary to have information about the (physical) pore radius, r , the maximum wetted height, H , the permeability, κ , and the evaporating mass flow rate, \dot{m}_{max} . In the following some methods to determine these parameters are presented and discussed, and calculations are carried out for the nickel foam wicks and using heptane, as a model working fluid.

According to Queheillalt et al. [14] the pore radius, r , of the nickel foam after compression may be estimated from:

$$r = r_0 \frac{\delta}{\delta_0} \quad (10)$$

where r_0 is pore radius of the uncompressed foam and (δ/δ_0) is the thickness ratio.

Eq. (10) was tested experimentally by Queheillalt et al. [14] for wicks of compressed nickel foam together with water. Perfect wetting, i.e. $\cos(\theta) = 1$, was assumed. Their predicted equilibrium pumping heights by use of Eq. (6) and Eq. (10) were, interpreted from their data, approximately 25% too high compared to their experimental results with water. They attributed this difference to tortuous pore morphology not being accounted for in the capillary tube model. However, the predicted heights would also have been lower if a contact angle $\theta > 0^\circ$ had been assumed instead of perfect wetting ($\theta = 0^\circ$).

If the physical pore radius, r , is determined from Eq. (10) and the effective pore radius, r_{eff} , is determined by an independent method, such as a rate-of-rise experiment, the contact angle can be estimated from Eq. (11):

$$\theta = \cos^{-1} \left(\frac{r}{r_{eff}} \right) \quad (11)$$

When the permeability and effective pore radius are known, the maximum obtainable mass flow rate for a given application can be determined from the pressure balance between the capillary pressure, the hydrostatic pressure, and the frictional pressure. The momentum change of the fluid is small and is therefore disregarded. The resulting maximum heat duty of a particular wick/fluid combination is calculated from

$$\dot{Q} = \dot{m}_{y=0} h_{fg} = \frac{2\kappa A_c \rho}{H \mu} \left(\frac{2\sigma}{r_{eff}} - \rho g H \right) h_{fg} \quad (12)$$

2.1. Rate-of-rise experiments

The permeability and the effective pore radius may be determined from a rate-of-rise experiment, in which the rate of wetting of an initially dry vertical wick is measured. Historically the rate of rise has been determined by different experimental techniques, usually based on visual detection or mass measurements, and the data analysis in each case depends on the technique applied. In this study the rate-of-rise was derived from measurements of the total liquid mass uptake, measured as mass loss from a liquid pool. In this way the total mass uptake included both the mass of liquid in the wick and the cumulative mass of liquid evaporating from the wick. Heptane was used as model fluid in the rate-of-rise experiments, since the reactivity of potassium with air and moisture makes rate-of-rise experiments with potassium very complicated. Holley and Faghri [18] derived time-height relationships for rate-of-rise experiments both with and without evaporation of the model fluid from the wick. They, like in this study, measured the mass uptake from a liquid reservoir. In the analysis of their experimental data they assumed no evaporation, as it was most convenient for reducing the data, and thereafter estimated the consequences of evaporation. They derived Eq. (13) for the change of mass with time [18].

$$-\left[\frac{2\sigma}{r_{\text{eff}}} \ln\left(1 - \frac{gr_{\text{eff}}}{2\sigma A_c \epsilon} m\right) + \frac{g}{A_c \epsilon} m \right] = \frac{\kappa \rho^2 g^2}{\epsilon \mu} t \quad (13)$$

All the liquid entering the wick was converted to height, y , by use of Eq. (14). This implied that the calculated wetted height was artificial as it differed from the real observable height (provided that the mass measured is the cumulative total mass uptake from the reservoir, as in this study).

$$y = \frac{m}{\rho A_c \epsilon} \quad (14)$$

The error of this approach increases with increasing time and with increasing evaporation rates, i.e. volatile fluids cause larger “evaporation errors” than less volatile fluids. The error due to evaporation is also larger for low permeability wicks [18], as evaporation then takes place over a longer period of time. This is further analysed in the Results and discussion section.

It may take a significant time to reach an absolute maximum height; Fries et al. [19] reported typically 5 days for their systems consisting of stainless steel Dutch twilled weave and different model fluids resembling satellite propellants, all having near zero static contact angle on the weave. For uncompressed nickel foam and water, Huang, Franchi and Cai [16] reported ca. one hour to reach final height, while for their bimodal wicks the front was still

moving after about 24 h. In order to limit the experimental time they decided to measure all capillary heights 400 min after immersion. In contrast to this Holley and Faghri [18] used data for typically the first 50–200 s in their rate-of-rise analysis. Fries et al. [19] analysed the time needed to reach 99% of maximum height, and found that this time increased with decreasing evaporation rate. Contrary to this, the error related to ignoring the evaporation in the rate-of-rise analysis increases with increasing evaporation rate and with increasing duration of the experiment.

The working fluid in the rate-of-rise experiments in this study was heptane. A petri dish with heptane was resting on a balance and the wick was hanging from a stand, see Fig. 1.

The rates of rise of heptane in the wicks were calculated from the mass uptake when the lower tips of the wicks were immersed in the heptane. The mass-time data from the balance was recorded with a PC running LabView. Before the wick tip was immersed, the evaporation rate of heptane from the petri dish was determined. Next, the wick tip was immersed and the heptane rose up to the maximum height. At the maximum height there was evaporation of heptane both from the entire wetted surface of the wick as well as from the petri dish. The evaporation rate from the wick was calculated by subtracting the evaporation rate from the petri dish from the total measured evaporation rate from the dish and wick. Constant, uniform evaporation flux was assumed from the wick surface. The temperature of the heptane in the petri dish was measured before the immersion and after the wick was pulled out of the heptane and the thermophysical data for the heptane were determined at the average of these two temperatures.

The analysis of the rate-of-rise data was carried out according to:

1. The height-time data were determined from the measured mass-time data by use of a MatLab-script [20]. The mass-to-height calculations involved subtraction of the evaporated mass from the measured mass-time data and conversion to height by taking the wick cross-sectional area and porosity into account.
2. The rate-of-rise relationship assuming no evaporation, Eq. (13), was fitted to the calculated height-time data series. The independent variables were the effective pore radius and the permeability.

The approach did not take into account the evaporating mass flow rate in the determination of the effective pore radius and the permeability, and the calculated effective pore radii and permeabilities were therefore slightly conservative. Alternatively, a simple conversion of the measured mass data directly to height by use of Eq. (14) would have overestimated the heights compared to the real heights.

3. Wick fabrication

In this study two different nickel foams were used, with the manufacturer's specifications for the uncompressed foams given in Table 1.

From these foams, 12 two-layer compressed wicks were produced; wicks 1–4 based on Foam 1 and wicks 5–12 based on Foam 2. All wicks had dimensions $W \times H 25 \times 100$ mm. Wick no. 12 was considered the final wick in this study, and was therefore analysed most thoroughly.

3.1. Nickel oxide

Nickel foam as delivered from the factory has a “skin” of nickel oxide. The nickel oxide is mechanically harder than pure nickel, and has higher melting point. It was therefore necessary to let the nickel

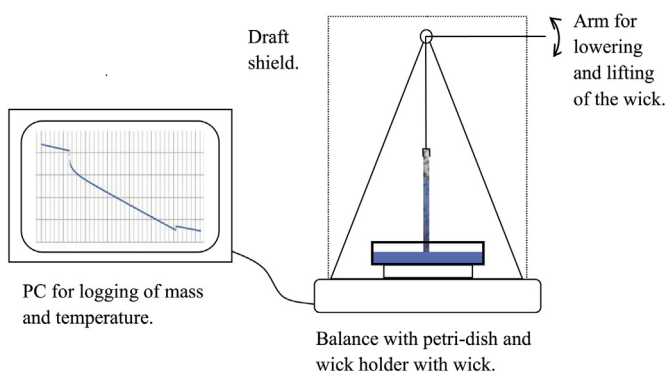


Fig. 1. The rate-of-rise setup.

Table 1
Manufacturer's data for the uncompressed nickel foams used in this study.

Parameter	Thickness	Pore size	Density
Foam 1	1.45 mm	450 microns	380 g/m ²
Foam 2	1.7 mm	580 microns	429 g/m ²

foam go through a reduction process in which the nickel oxide was reduced to pure nickel before the compression process. The oxidized nickel foam was first cut with scissors to pieces of size 25 × 100 mm. The pieces were then reduced in an oven for 60 min at 800 °C in an atmosphere consisting of 95% Ar + 5% H₂ gas. The sample pieces were kept in the same atmosphere also during the heat-up period to 800 °C and during the subsequent cool-down to room temperature. After this treatment the nickel foam appeared shiny just as pure unoxidized nickel metal. A maximum reduction temperature of 800 °C was selected to be in line with the successful thermal cleaning of Queheillalt et al. [14]. Strictly, we have experienced from previous thermogravimetric analyses that the rate of nickel oxide reduction accelerates at about 350 °C. We have also experienced from prior heating tests that oxidized nickel foam is mechanically rigid and visually unaffected by heat treatments even above 1000 °C.

3.2. Compression

The de-oxidized pieces of nickel foam were compressed by use of a rolling press, model MR100, which was calibrated by use of feeler gauges. During the compression the pieces of nickel foam increased both in length and width, depending on the thickness ratio. As an example, for the thickness ratio of $\delta/\delta_0 = 0.16$ the length of an initially 100 mm long sample increased by 7%. The pieces were cut to correct size by use of scissors after the compression.

3.3. The joining pressure requirement

The wicks were made from two compressed nickel foam layers. The two layers were sintered together at 1100 °C maximum temperature in a gas atmosphere containing 95% Ar + 5% H₂. The temperature program is shown in Fig. 2, here represented by the temperature measured inside the oven during the actual reduction (first peak) and sintering (second peak) in this case for wicks 5–8.

During sintering the layers were resting on flat plates of alumina, and alumina plates were also put upon the layers as weights in order to provide contact pressure between the foam layers and avoid buckling. The results from the load pressure requirement study are found in the Results and discussion section.

3.4. Porosity measurements

The porosities were measured for samples cut off wicks 1–8, in addition to samples of uncompressed foam. The porosities were measured using isopropanol, following the procedure described in Ref. [21]. Following this procedure, the porosity was determined from weight measurements of the dry sample, the sample weight submerged in isopropanol and the weight of the sample fully saturated with isopropanol. For wicks 9–12 the porosities were estimated by linear interpolation between the porosities measured for wicks 5 and 6.

3.5. Contact angles with heptane

The contact angles were calculated by use of Eq. (9). Since $\rho_v \ll \rho_l$, the vapour density was disregarded in the calculation. The

maximum capillary height was determined from the rate-of-rise mass data recalculated to heights. As the time required to reach absolute maximum height was in general believed to be very long, the final heights used in these calculations were “quasi-equilibrium” final heights at which the liquid fronts had visually stopped advancing. The pore radius, r , for the different thickness ratios was estimated by use of Eq. (10).

3.6. Wettability

A wettability test using water was carried out using a small piece of nickel foam immediately after the reduction (de-oxidation) process. Spontaneous imbibition occurred. In a similar wettability test performed before the reduction process there was no imbibition, i.e. the untreated nickel foam was hydrophobic. Similarly, in wettability tests carried out about 7, 23 and 48 h after the reduction it was observed that the foam was becoming more and more hydrophobic. After 48 h there was no spontaneous imbibition at all. The observed wettability change from hydrophilic to hydrophobic was likely due to adsorption of volatile organic compounds from the air, as described and analysed for copper metal foams by Shirazy et al. [22]. Similar arguments were used by Sheehan et al. [13] in their study using nickel foam. The observations made in the present work using nickel foam and water were very similar to the results presented by Shirazy et al. [22] using copper foam and water. Even the observed times for the complete wettability transitions in air were similar (48 h). If their theory for copper is transferred to nickel, both the pure nickel surface as well as the oxidized nickel surface are hydrophilic. Following their theory further, the wettability transition from hydrophobic to hydrophilic in the de-oxidation process was caused by desorption of adsorbed organic compounds from the nickel surface, rather than by the removal of oxygen. In a subsequent wettability test a hydrophobic nickel foam sample was rinsed in acetone and then dried for 5 min in air before a new wettability test with distilled water was carried out. It was observed that cleaning with acetone did not make the sample hydrophilic, i.e. cleaning with acetone could not replace the thermal cleaning process.

It should also be noted that heptane, which was used here as test fluid in the rate-of-rise experiments, was always found to wet nickel spontaneously. No analogous experiments were carried out to try to quantify potential changes in the wettability of the nickel-heptane system during the critical 48 h after the reduction process.

The fabrication procedure of the nickel foam wicks is summarized in Fig. 3.

4. Results and discussion

4.1. The contact pressure requirement

The compressed nickel foams were sintered together in order to ensure sufficient bonding. By trial and error a contact pressure of 1.2 kPa during sintering was found to give sufficient bonding without affecting the porosity.

4.2. Porosity

The results of the porosity measurements using isopropanol as model fluid are shown in Fig. 4.

Different contact pressures were applied during the sintering of the wicks made from Foam 1 in the porosity plot, Fig. 4, but as long as the different pressures did not cause measurable differences in the thicknesses, the differences in pressures had no impact on the porosities. For the uncompressed foams (thickness ratio = 1) the porosity samples consisted of only 1 layer. From Fig. 4 it is observed

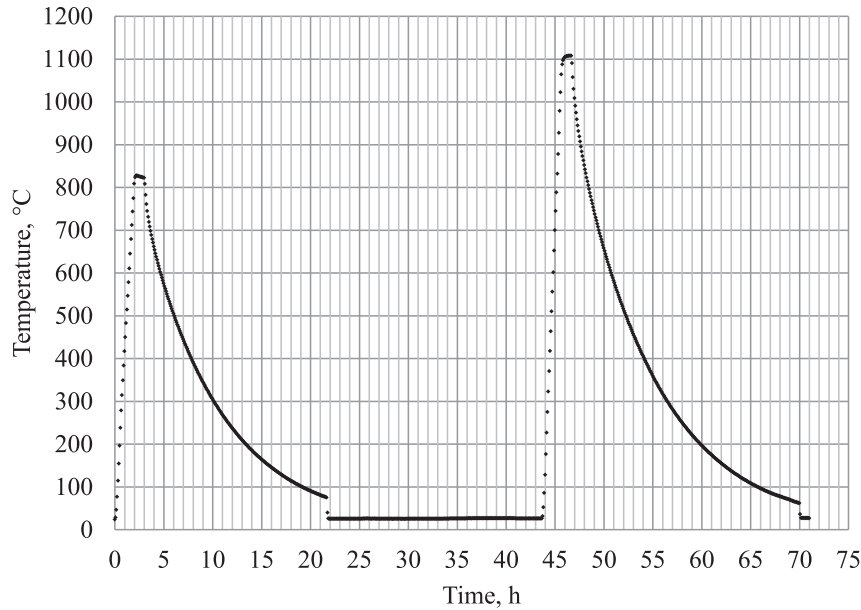


Fig. 2. Measured temperature in oven during reduction and sintering.

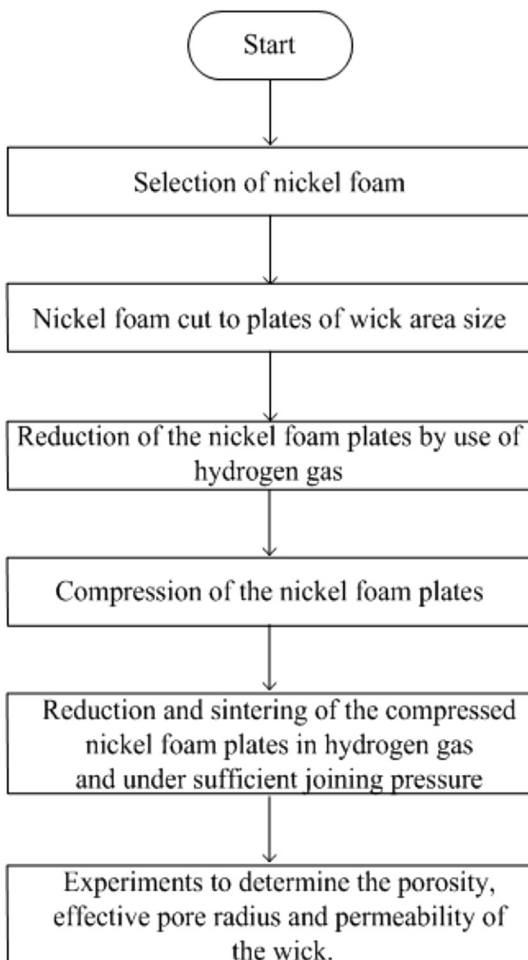


Fig. 3. The fabrication process of the nickel foam wicks.

that the porosity decreases at an increasing rate for decreasing thickness ratio, this is because the volume of the solid material is unchanged while the volume of the void is reduced by the compression. Starting from the porosity of uncompressed foam and assuming 1-D compression, the porosities for different thickness ratios can be predicted approximately. However, such a 1-D model will not be strictly correct because the real compressions also increase the foot-print. Hence, the 1-D theoretical model under-predicts the porosities, and in this study the maximum error was about 11% for the smallest thickness ratio.

4.3. Contact angle

The contact angles for heptane on nickel foam, calculated by Eqs. (9) and (10) using data from 4 experiments with Foam 1 wicks and 8 experiments with Foam 2 wicks had an average value of $58.4^\circ \pm 1.3^\circ$ at 95% confidence level [23]. The average temperature of the experiments was 20.7°C . The maximum lifting heights used were the maximum “quasi-equilibrium” heights in the rate-of-rise experiments with heptane, which were carried out 2–4 days after the wicks were sintered. The time period between the sintering and the rate-of-rise experiment is believed to be of less importance when heptane is used than for water, because with heptane there

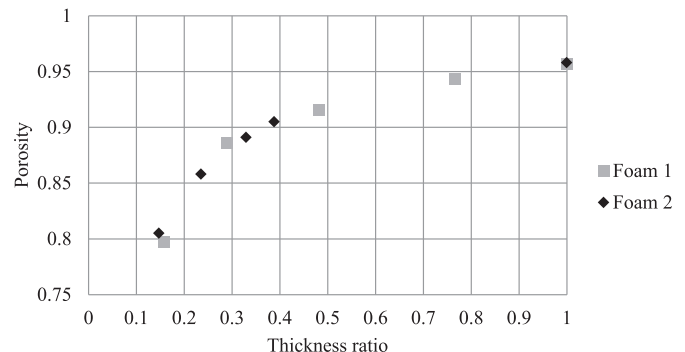


Fig. 4. Measured porosities for wicks of different thickness ratios.

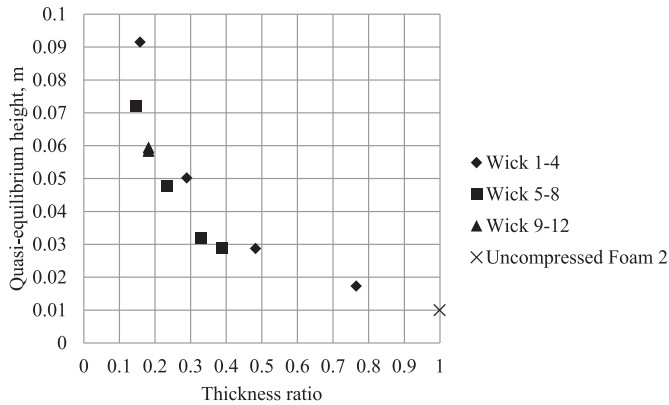


Fig. 5. Quasi-equilibrium maximum heights.

was no observable wettability transition taking place. The maximum “quasi-equilibrium” heights for the different thickness ratios are shown in Fig. 5, and were generally higher for wicks 1–4 than for wicks 5–12 because of the smaller pore size of foam no. 1 than of foam no. 2 (see Table 1).

4.4. Rate-of-rise experiments

Fig. 6 shows the total mass of heptane imbibing into wick no. 12. The evaporation rate of heptane from the wick is subtracted from the measured weight loss by the balance, yielding the mass remaining in the wick [20]. Fig. 7 shows the corresponding wetted heights, where the “calculated observed height” would correspond to an observed height. Fig. 8 shows the rate-of-rise calculated from the “calculated observed height”.

As described previously, the “calculated observed heights” data series was used together with the rate-of-rise theory without evaporation to determine the effective pore radius and permeability. This approach was considered to give slightly conservative estimates (i.e. underestimate the wick capacity) since the frictional pressure drop due to evaporating mass was not taken into account.

If the total mass data series were converted to heights by use of Eq. (14), and the effective pore radius and permeability were determined by use of the theory assuming no evaporation, then it is clear from Figs. 6 and 7 that the errors in the effective pore radius and permeability would have increased considerably with time. This was also emphasized by Holley and Faghri [18], who stated that the error due to evaporation would be largest for low permeability wicks. They calculated effective pore radius and permeability assuming no evaporation for experiments which had duration of 50–200 s. They estimated the errors due to evaporation

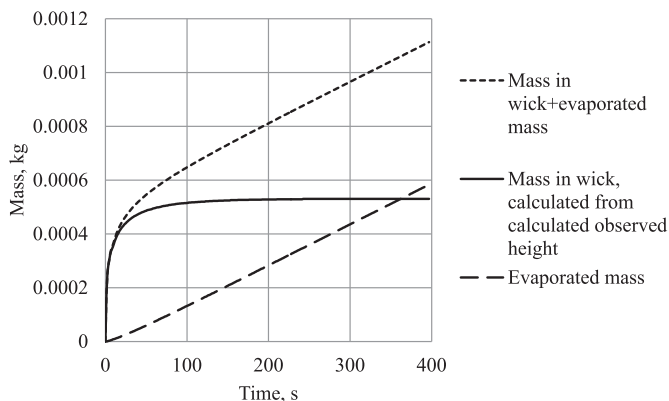


Fig. 6. Masses of heptane during the rate-of-rise experiment for wick 12.

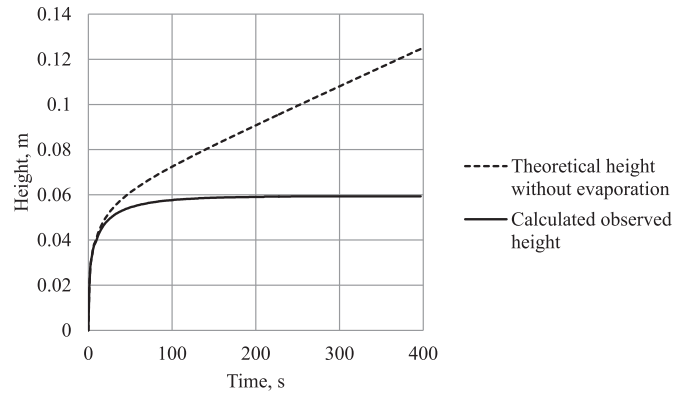


Fig. 7. Heights of heptane in wick 12 during the rate-of-rise experiment.

by use of measurements of the evaporation rates from saturated wick samples. In the present work, this error is eliminated by use of the “calculated observed height” data series. This approach is, however, not strictly correct, as the mass flow due to evaporation is not taken into account in the calculation of the effective pore radius and the permeability. The magnitude of the error can be deduced from Fig. 6 where it is seen that the mass evaporated from the wick constituted a very small part of the total mass uptake during the first seconds of the experiment, after 50 s it constituted about 12%, after 100 s about 25%.

The effective pore radius and permeability for the different thickness ratios are shown in Figs. 9 and 10 respectively. Due to the very low equilibrium height (≈ 10 mm) and the short duration of the rate-of-rise experiment the uncertainty of the permeability calculation for the uncompressed foam is so high that the value has been omitted from the trendline in Fig. 10.

It is unlikely that any heat pipe would require a wick with larger pore size than the pore size of the uncompressed nickel foams, because the capillary pressure would be very low. After considerable compression the nickel foam wicks still had effective pore radii and permeabilities in the upper range, for instance compared to the effective pore radius and permeability of a “traditional” wick of sintered Inco 255 nickel powder, e.g. $11.9 \mu\text{m}$ and $3.4 \mu\text{m}^2$ respectively [18].

4.5. Calculated heat transfer capacity with potassium

In the calculation of the heat transfer capacity using potassium as working fluid the effective pore radius determined from the rate-

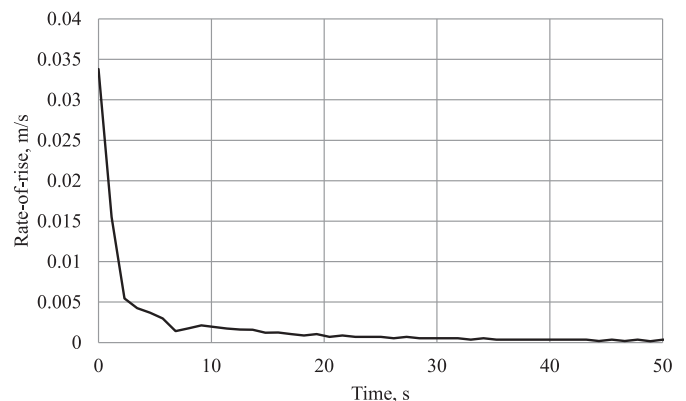


Fig. 8. Rate-of-rise of heptane in wick 12 during the rate-of-rise experiment.

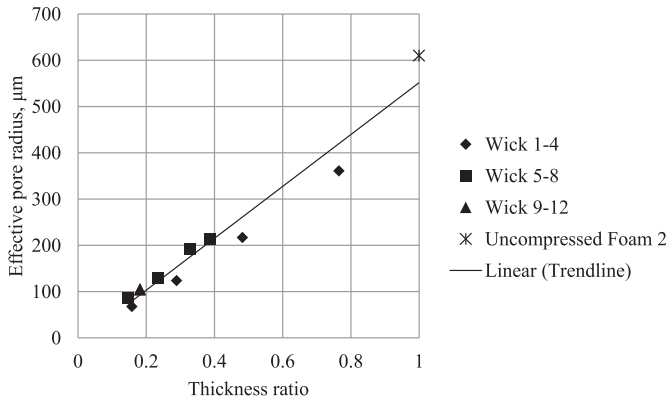


Fig. 9. Effective pore radius.

of-rise experiment with heptane is converted to an effective pore radius for potassium, by use of Eq. (5). From the contact angle calculations performed, a contact angle of 58.4° was used for the heptane on the wick surface. A contact angle of 0° of potassium on the nickel wick surface was assumed [24]. For wick no. 12 at 500°C the heat transfer capacity with potassium was calculated to $950 \cdot 10^3 \text{ W/m}^2$ with the same wetted height (0.0593 m) as for the heptane by use of Eq. (12). Wick 12 was 0.63 mm thick and the evaporation was assumed to take place on one side only.

5. Uncertainty analysis

The uncertainty analysis was carried out according to the procedure presented by Moffat [25].

Each variable has an uncertainty which is known or assumed, and the propagation of these uncertainties to the final results (the contact angle, the permeability, the effective pore radius and the heat transfer capacity) were calculated by varying each variable, one by one, in positive and negative direction. The analysis was carried out for wick 12, but the tabulated uncertainties are considered representative for all wicks as the equations, equipment and experimental approach were similar.

The analysis showed that the uncertainty mainly comes from the wick thickness measurements, made by use of vernier calipers (uncertainty of $\pm 0.03 \text{ mm}$), and the pore radius of the uncompressed foam (assumed uncertainty of $\pm 10\%$). The uncertainty of the measured weight loss contributed negligibly to the overall uncertainty. The permeability is very sensitive to uncertainties in the wick cross-sectional area, and this propagates to the

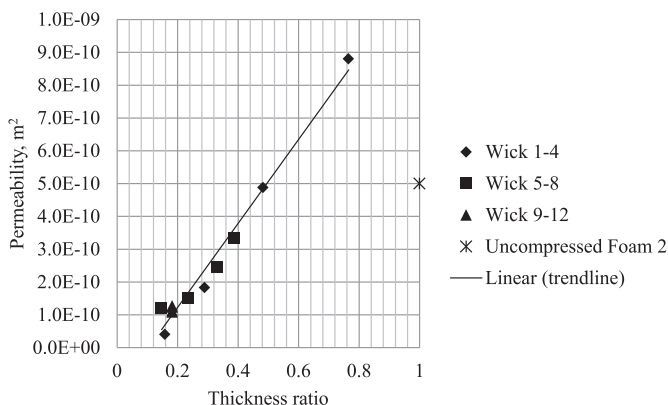


Fig. 10. Permeabilities.

Table 2
Results of the uncertainty analysis.

	Uncertainty estimate	
Porosity	$\pm 0.1\%$	(Known)
Effective pore radius, r_{eff}	$\pm 2\%$	(Estimated)
Contact angle, heptane on wick	$\pm 8.9\%$	(Calculated)
Permeability, κ	$\pm 26\%$	(Calculated)
Heat transfer capacity, \dot{Q}	$\pm 26.7\%$	(Calculated)

uncertainty of the heat transfer capacity. The consequences of the uncertainties of the thermophysical properties of heptane and the temperature measurements are negligible. For the porosity measurements the uncertainty claimed by the standard [21] is reported.

The significant uncertainties were added by the root of the sum of squares (RSS), and the results are shown in Table 2.

The uncertainty related to the use of the capillary tube model as a model for the wick structure was not taken into consideration.

6. Conclusions

Wicks for heat pipes have been made from compressed nickel foam. Wick properties are important in the design of heat pipes and are highly dependent on the degree of compression of the wick. Experiments have been carried out in order to determine porosity, effective pore radius, permeability and maximum lifting height for wicks of different degrees of compression. The results are presented graphically.

The nickel foam wicks fabricated in this study have high effective pore radius and high permeability compared to wicks made of sintered nickel powder of type Inco 255. The compressed foam wicks are in the upper range of pore sizes applicable for heat pipes due to the large pore sizes of the nickel foams in uncompressed form.

Experiments have shown that wicks of compressed nickel foam are hydrophilic immediately after the sintering at 1100°C , but turn hydrophobic during 48 h storage in lab air. The wettability transition may be caused by adsorption of organic components from the air as indicated by Sheehan et al. [13] and reported for copper metal foams by Shirazy [22].

The contact angle of model fluid heptane on sintered (reduced) nickel foam wicks was determined to $58.4 \pm 1.3^\circ$, measured 2–4 days after sintering, whereas perfect wetting of 0° was assumed for potassium/nickel.

A pressure of 1.2 kPa can safely be applied to compressed nickel foam layers during sintering at 1100°C , and this will provide a mechanically strong multilayer wick.

Material compatibility makes wicks of compressed nickel foam relevant for heat pipes using potassium as working fluid.

Acknowledgements

The authors would like to thank Elkem and the Research Council of Norway for funding this work. Thanks to Rhodri Bowen and Vale Inco Europe Ltd. for providing nickel foam for wicks 1–4. Dr. Ove Paulsen and engineer Ove Darell at SINTEF have provided valuable technical assistance with the sintering oven.

References

- [1] D.A. Reay, P.A. Kew, P.D. Dunn, *Heat Pipes*, Elsevier, Amsterdam, 2006.
- [2] A. Faghri, *Heat Pipe Science and Technology*, Taylor & Francis, Washington, D.C., 1995.
- [3] G.P. Peterson, *An Introduction to Heat Pipes: Modeling, Testing, and Applications*, Wiley, New York, 1994.

- [4] C.C. Silverstein, Design and Technology of Heat Pipes for Cooling and Heat Exchange, Hemisphere Pub. Corp., 1992.
- [5] M. Dillig, J. Leimert, J. Karl, Planar high temperature heat pipes for SOFC/SOEC stack applications, *Fuel Cells* 14 (2014) 479–488.
- [6] J. Choi, W. Sano, W. Zhang, Y. Yuan, Y. Lee, D.-A. Borca-Tasciuc, Experimental investigation on sintered porous wicks for miniature loop heat pipe applications, *Exp. Therm. Fluid Sci.* 51 (2013) 271–278.
- [7] X. Yang, Y.Y. Yan, D. Mullen, Recent developments of lightweight, high performance heat pipes, *Appl. Therm. Eng.* 33–34 (2012) 1–14.
- [8] M.R. Hajmohammadi, M. Rahmani, A. Campo, O. Joneydi Sharizatadeh, Optimal design of unequal heat flux elements for optimized heat transfer inside a rectangular duct, *Energy* 68 (2014) 609–616.
- [9] M.R. Hajmohammadi, A. Campo, S.S. Nourazar, A.M. Ostad, Improvement of forced convection cooling due to the attachment of heat sources to a conducting thick plate, *J. Heat Transfer* 135 (2013) 124504.
- [10] Y. Li, H.-f. He, Z.-X. Zeng, Evaporation and condensation heat transfer in a heat pipe with a sintered-grooved composite wick, *Appl. Therm. Eng.* 50 (2013) 342–351.
- [11] L. Jiang, H. Yong, Y. Tang, Y. Li, W. Zhou, L. Jiang, J. Gao, Fabrication and thermal performance of porous crack composite wick flattened heat pipe, *Appl. Therm. Eng.* 66 (2014) 140–147.
- [12] A.B. Solomon, K. Ramachandran, B.C. Pillai, Thermal performance of a heat pipe with nanoparticles coated wick, *Appl. Therm. Eng.* 36 (2012) 106–112.
- [13] J. Sheehan, D.T. Queheillalt, P.M. Norris, An evaluation of the wicking characteristics of stochastic open-cell nickel foams, in: 2006 ASME International Mechanical Engineering Congress and Exposition, IMECE2006, November 5, 2006–November 10, 2006, American Society of Mechanical Engineers, Chicago, IL, United States, 2006.
- [14] D.T. Queheillalt, G. Carbajal, G.P. Peterson, H.N.G. Wadley, A multifunctional heat pipe sandwich panel structure, *Int. J. Heat Mass Transfer* 51 (2008) 312–326.
- [15] E.A. Silk, D. Myre, Fractal loop heat pipe performance testing with a compressed carbon foam wick structure, *Appl. Therm. Eng.* 59 (2013) 290–297.
- [16] X. Huang, G. Franchi, F. Cai, Characterization of porous bi-modal Ni structures, *J. Porous Mater.* 16 (2009) 165–173.
- [17] P.C. Hiemenz, Principles of Colloid and Surface Chemistry, Dekker, New York, 1986.
- [18] B. Holley, A. Faghri, Permeability and effective pore radius measurements for heat pipe and fuel cell applications, *Appl. Therm. Eng.* 26 (2006) 448.
- [19] N. Fries, K. Odic, M. Conrath, M. Dreyer, The effect of evaporation on the wicking of liquids into a metallic weave, *J. Colloid Interface Sci.* 321 (2008) 118–129.
- [20] K. Kristjansson, Unpublished Work, NTNU, 2009.
- [21] Dense Shaped Refractory Products – Determination of Bulk Density, Apparent Porosity and True Porosity, International Organization for Standardization, 1998.
- [22] M.R.S. Shirazy, S. Blais, L.G. Frechette, Mechanism of wettability transition in copper metal foams: from superhydrophilic to hydrophobic, *Appl. Surf. Sci.* 258 (2012) 6416–6424.
- [23] A.J. Wheeler, A.R. Ganji, Introduction to Engineering Experimentation, Pearson/Prentice Hall, Upper Saddle River, N.J., 2004.
- [24] M. Barlow, P.J. Planting, Wetting of metal surfaces by liquid alkali metals, *Z. Metallk.* 60 (Sept. 1969) 719–722. Other Information: Orig. Receipt Date: 31-DEC-69, (1969) Medium: X.
- [25] R.J. Moffat, Describing the uncertainties in experimental results, *Exp. Therm. Fluid Sci.* 1 (1988) 3–17.

3.1.7 Conclusions of the wick study

For the hybrid heat pipe using potassium as working fluid the wicks developed by sintering of pure Inco 255 nickel powder did not meet the requirements. The effective pore radius was smaller than necessary and the permeability was far too small, e.g. $0,108 \cdot 10^{-12} \text{ m}^2$ for the mechanically best wick. With this wick the performance of the hybrid heat pipe would have been very limited by the vapour static pressure limit [38], e.g. the capacity of the 150 mm high wick was calculated to only 844 W/m^2 at 500°C .

A spacing agent (filler) was introduced to increase the pore effective radius and permeability of the produced wick. The graphite powder pore former did increase both the effective pore radius and the permeability, however, without giving a wick with sufficient mechanical strength and capacity. Attempts were made to use carbon fibers as pore former, but no suitable method was found to distribute the carbon fibers in the powder.

The criterion for a successful pore former was analysed, and the analysis showed that [38]: “When $P_{cap}/P_{sat} > 1$, the use of a pore former to increase the wick permeability will always improve the wick performance. When $P_{cap}/P_{sat} < 1$, it was shown that if the effective pore radius and the permeability increase with an equal percentage the overall influence on the wick capacity is negative.”

The wicks of compressed nickel foam had properties in the range suitable for the hybrid heat pipe. The permeability could be selected within a range depending on the initial properties of the foam and the degree of compression. For nickel foams studied, the permeability could be varied from about $40 \cdot 10^{-12} \text{ m}^2$ to about $880 \cdot 10^{-12} \text{ m}^2$. The corresponding values for the effective pore radius with heptane were $68\text{-}361 \cdot 10^{-6} \text{ m}$ [30]. These findings were utilized in the production of the wick for the hybrid heat pipe, reported in Chapter 3.3.

3.2 Experimental hybrid heat pipe

3.2.1 Heat pipe operation

Traditional heat pipes, and many special heat pipes, have been analysed in several textbooks, see for instance the references [21, 23, 49-51]. Reay and Harvey [52] recently reviewed the role of heat pipes in intensified unit operations. In addition to being used for traditional heat transfer and temperature control purposes, heat pipes have also been plasma-sprayed with catalyst materials and used in chemical reactors [52]. Heat pipes utilizing alkali metals as working fluids are considered for the cooling of molten salt nuclear reactors [53] as well as for Stirling heat engines for space applications [54]. Ceramic heat pipes utilizing sodium or zinc are being developed, tested and investigated for the temperature range 800-1200°C [55].

The traditional heat pipe has a wick structure in the evaporator section, the adiabatic section and the condenser section. The traditional heat pipe can operate against gravity if the wick structure provides sufficient capillary pressure, so the evaporator section can be at a higher level than the condenser section.

The traditional thermosyphon, on the other hand, does not have any wick structure. The condensate is returned to the evaporator part by gravity, i.e. the condenser has to be located at a higher level than the evaporator.

The hybrid heat pipe investigated in this study has a wick structure in the evaporator part, but relies on gravity for the return of the condensate. The purpose of the wick structure in the evaporator is to distribute the condensate over the evaporator surface.

3.2.2 Heat transfer limitations

Figure 3-16 shows various limits as a function of operating temperature for traditional heat pipes [21]. The different limits are discussed in the following, with reference to the hybrid heat pipe application. The main objective of this study was to determine the capacity limits of the wick.

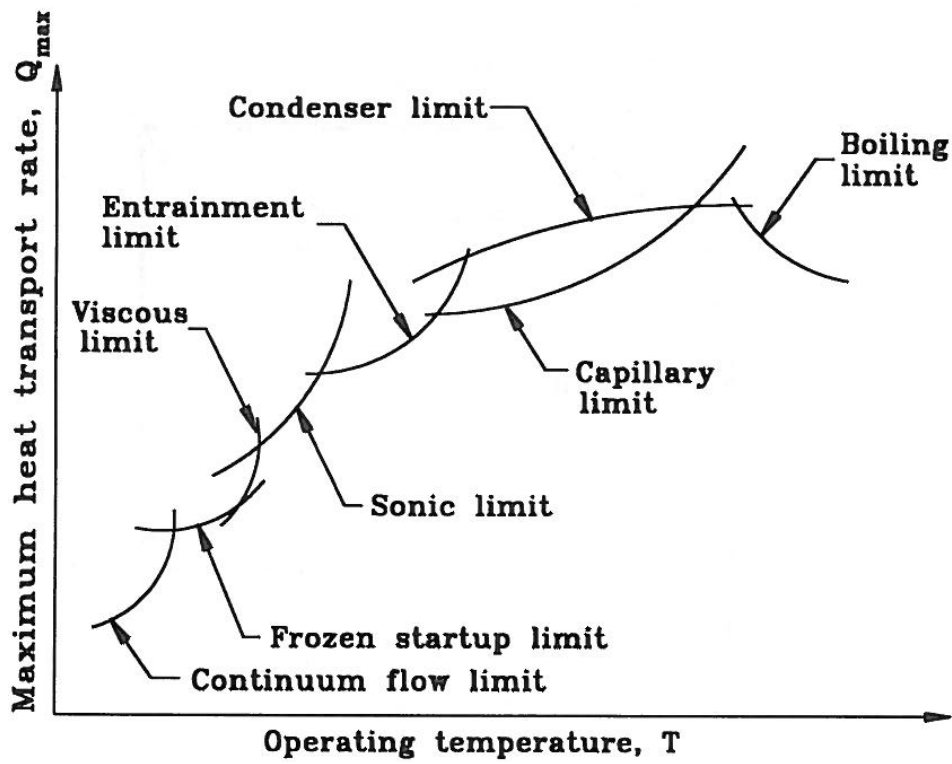


Figure 3-16 Heat transfer limitations, from Faghri [21]

The continuum flow limit

Discontinuous vapour flow can occur in very small heat pipes (micro heat pipes) and when a heat pipe is operating at very low pressures [21]. The vapour pressure of potassium is less than 0.1 bar below 500°C, see Figure 2-11. According to Reay, Kew and Dunn [23] the useful working range for potassium is 500-1000°C (indicative only). The low heat transport capability of a heat pipe operated at the continuum flow limit will cause a large temperature gradient along the heat pipe length [21]. The continuum flow limit is therefore distinguishable from the sonic limit which also will give large temperature variations along the heat pipe length; typically decreasing temperature in the evaporator and increasing temperature in the condenser [11].

The frozen startup limit

The frozen startup limit is an evaporator dryout situation caused by refreezing of the working fluid in the condenser or the adiabatic zone during startup [21]. The limit will not be analysed further here as it was avoided by keeping the temperature of the entire hybrid heat pipe above the solidification temperature (63,7°C) of potassium during startup; heated N_2 gas was used for this purpose.

The viscous limit/vapour pressure limit [21]

The pressure difference between the evaporator and the condenser is causing transport of vapour from the evaporator to the condenser. The lower limit for the vapour pressure in the condenser is zero. When the temperature in the evaporator is low (for instance during heat pipe startup) and the vapour pressure of the working fluid is low (as for liquid metals operating below their operating range, or during startup) the pressure difference between the evaporator and the condenser may not be sufficient to overcome the viscous forces [23]. In general the viscous limit is only considered to be a problem in some cases during start-up [23]. For laminar flow of an ideal gas in an isothermal cylindrical heat pipe with large length/diameter ratio and uniform heat input and output so that $q=q(z)$ only, the following expression was derived for the viscous limit [21, 56]:

$$\bar{q}_{viscous} = \frac{D_v^2 h_{fg} \rho_v p_v}{64 \mu_v L_{eff}} \quad (3-31)$$

where $\bar{q}_{viscous}$ is the average axial heat flux over the cross section of the vapour channel.

The effective length of the heat pipe was defined as [21, 56]:

$$L_{eff} \equiv \frac{1}{\bar{q}_{max}} \int_0^{L_v} \bar{q}(z) dz \quad (3-32)$$

During startup the flow of vapour in the hybrid heat pipe is likely going through the viscous limit, however it may not be observed as it is eliminated by increasing heat flux and temperature.

The sonic limit [21]

When the gas flow in a heat pipe reaches a Mach number of 1 the sonic limit is reached. The sonic limit may be encountered:

- During startup of high-temperature heat pipes.
- When the heat transfer resistance in the condenser is low.
- When the supplied heat flux is low.

A heat pipe operating at or in the vicinity [50] of the sonic limit will have a significant temperature drop along its length, due to large vapour pressure drop inside. When the sonic limit is encountered it is possible to move away from it by increasing the evaporator temperature.

A closed-form relation for the sonic limit, Equation (3-33), was derived from conservation of mass, momentum and energy while friction was neglected [21]:

$$Q_{Sonic} = \frac{\rho_v c_v h_{fg} A_v}{\sqrt{2(\kappa + 1)}} \quad (3-33)$$

where the properties are evaluated at the evaporator end cap conditions, and c_v is the velocity of sound. A_v is the cross-sectional area of the vapour channel.

Equation (3-33) is acceptable for approximate calculations, but for more detailed analysis the friction has to be taken into account. According to Faghri [21] the friction is important for “the location of the sonic point”, the flow in the condenser (subsonic or supersonic), and it generally decreases the sonic limit.

The sonic limit is likely passed through during the startup of the hybrid heat pipe, as it is for all heat pipes starting from frozen state.

The flooding and entrainment limits

When the vapour and the condensate are flowing in opposite directions in the same pipe there is a risk that the shear force between vapour and the condensate can cause flooding and entrainment. Flooding is reached when the condensate can no longer return to the condenser. Entrainment of droplets from the condensate film by the vapour can occur after the flooding, if there is sufficient heat input to cause instability of the liquid-vapour interface [21]. The probability for flooding increases with increasing vapour velocity. High vapour velocity can be caused by for instance high heat flux or a narrow flow channel. Growing surface waves, which is the precursor to droplet entrainment, are likely to be retarded by a capillary structure [21]. The flooding and entrainment is therefore more likely to occur in systems where the condensate is not flowing in a wick. In the hybrid heat pipe the condensate is flowing downward on a smooth wall and in direct contact with the upward flowing vapour.

Several semi-empirical expressions for flooding and entrainment limits have been developed, and their predictions vary a lot [49, 57-58]. Peterson [49] compared seven models for entrainment in a copper-water thermosyphon and found a factor of 5 between them. Peterson [49] also pointed out that the models depend on constants which require much experimental data.

Historically, many studies of flooding have utilized two correlations, which both have been found to have shortcomings [21]:

- The Wallis correlation, which balances inertia and hydrostatic forces, but does not take surface tension into account [21].
- The Kutateladze correlation, which balances inertia, buoyant and surface tension forces, but does not take the diameter (or another characteristic dimension) of the flow channel into account [21].

Together the Wallis and Kutateledze correlations are (probably) containing the major parameters influencing flooding; the phase densities and velocities, a charactersitic dimension, the phase viscosities and the gas-liquid interfacial tension.

According to Zapke and Kröger [59-61], the proposed correlations for flooding often succeed in predicting the researcher’s own data but fail to correlate other researcher’s data. Zapke and Kröger [61] found that the phase Froude numbers (i.e. inertia forces over external field and characteristic length) and the Ohnesorge number (i.e. viscous

forces over inertial and surface tension forces) best correlated their experimental data as well as the data from 2 other investigations. Zapke and Kröger [60] also listed 11 other different dimensionless groups that had been used by previous investigators for correlating flooding data. The choice of characteristic dimension in the gas Froude number was critical for the success of the correlation method of Zapke and Kröger. Their flooding data for a rectangular channel (like the hybrid heat pipe in the present study) failed to correlate when the hydraulic diameter was used as characteristic dimension. Instead, the long side of the rectangular cross section of the flow channel was successfully applied as characteristic dimension.

Another factor of particular interest for the present study is the effect of the liquid viscosity on flooding. Zapke and Kröger, referring to a theoretical study by Cetinbudaklar and Jameson [62], concluded that the liquid films become more unstable, and more prone to flooding, with increasing liquid viscosity. The surface tension of the liquid film, and its variation with temperature, is also important; waves are more easily formed when the surface tension is reduced [21].

Faghri et al. [21, 63] claimed to have the most general flooding correlation for thermosyphons, obtained by improving on existing correlations. Results within 15% were obtained for water, but for other fluids the deviations were “significant”. A density correction was therefore introduced to account for the different liquid-vapour density ratios of different working fluids. Zapke and Kröger [60] did, however, suggest that the initial shortcoming of the Faghri correlation was due to the fact that it was based on a “Kutateladze-type” correlation. The correlation of Faghri for the maximum heat transfer rate [21] before flooding is:

$$Q_{\max} = Kh_{fg} A \left[g \sigma (\rho_l - \rho_v) \right]^{1/4} \left[\rho_v^{-1/4} + \rho_l^{-1/4} \right]^{-2} \quad (3-34)$$

where

$$K = \left(\frac{\rho_l}{\rho_v} \right)^{0.14} \tanh^2 \left(Bo^{1/4} \right) \quad (3-35)$$

and Bo (the Bond number) is the dimensionless diameter [63]:

$$Bo = D \left[g (\rho_l - \rho_v) / \sigma \right]^{1/2} \quad (3-36)$$

The capillary limit

The capillary limit is the maximum capacity of the wick when operating the heat pipe. The rate-of-rise experiment gave the effective pore radius and permeability of the wick. From the effective pore radius and permeability it was possible to calculate the capacity of the wick as maximum mass flow or heat transport rate for a certain working fluid at a certain temperature. This capacity calculation for the wick alone was based on the pressure balance, Equation (2-16). For simplicity the wick capacity as calculated from Equation (2-16) is sometimes used as the capillary limit of the heat pipe [23]. In a more thorough analysis more terms are taken into account; in a standard heat pipe the capillary

pressure of the wick also has to overcome the pressure drop in the vapour and the pressure drops at the liquid vapour interfaces [21]. The pressure balance then becomes:

$$\Delta P_{cap,max} \geq \Delta P_{hs} + \Delta P_f + \Delta P_v + \Delta P_{e,\delta} + \Delta P_{c,\delta} \quad (3-37)$$

where $\Delta P_{e,\delta}$ and $\Delta P_{c,\delta}$ denote the pressure drop associated with the liquid-vapour and vapour-liquid interface heat transfer resistance in the evaporator and condenser respectively.

Different models for the pressure drop of the vapour phase under different conditions have been analysed and compared by Faghri [21]. A closed form expression for the capillary limit was derived for laminar incompressible vapour flow when the wet point was near the condenser end cap [21]. The wet point was defined as the location where the pressures in the vapour and liquid are equal [21, 49].

The condenser limit

The condenser limit is characterized by insufficient heat transfer in the condenser section of the heat pipe. For the hybrid heat pipe this can occur if part of the condenser is occupied by non-condensable gas.

The boiling limit

If nucleate boiling in the wick occurs, it will impede the flow of liquid in the wick. The superheat required for the onset of boiling is so high for liquid metals that boiling in such heat pipes rarely occurs.

The pressure difference between the inside and outside of a spherical vapour bubble in liquid is given by Equation (2-2). Because of the very low vapour pressure of potassium in the temperature range (400-650°C), the pressure difference corresponds to a very high superheat. For example, for potassium at 400°C the pressure difference for a cavity of radius 5 μm corresponds to a superheat of about 160 K. Potassium is known to wet metal surfaces very well. Large cavities in the evaporator surface are therefore effectively wetted and filled with potassium. Only in the smallest, non-wetted cavities may there be some non-condensed vapour for boiling nucleation.

The critical superheat for boiling incipience in the wick structure (i.e. under the meniscus) is given by Equation (3-38) according to Faghri [21].

$$\Delta T_{crit} = \frac{2\sigma T_v}{h_{fg} \rho_v} \left(\frac{1}{r_b} - \frac{1}{r_{men}} \right) \quad (3-38)$$

Faghri points out that the term $1/r_{men}$ reduces the critical superheat substantially, especially when the radius of the meniscus is very small. As an approximation the effective radius can be used as the radius of the meniscus, r_{men} [21]. Boiling will more easily occur in a wick with fine structure than coarse structure.

The vapour static pressure limit

During work on a numerical model for vertical wicks exposed to non-uniform heat fluxes an operating limit which is not included in Figure 3-16 was evident [1, 33]. The limit is most easily understood from a simple model of a vertical wick operating in a closed chamber, see Figure 2-30 [1]. Just one meniscus is drawn and magnified for simplicity.

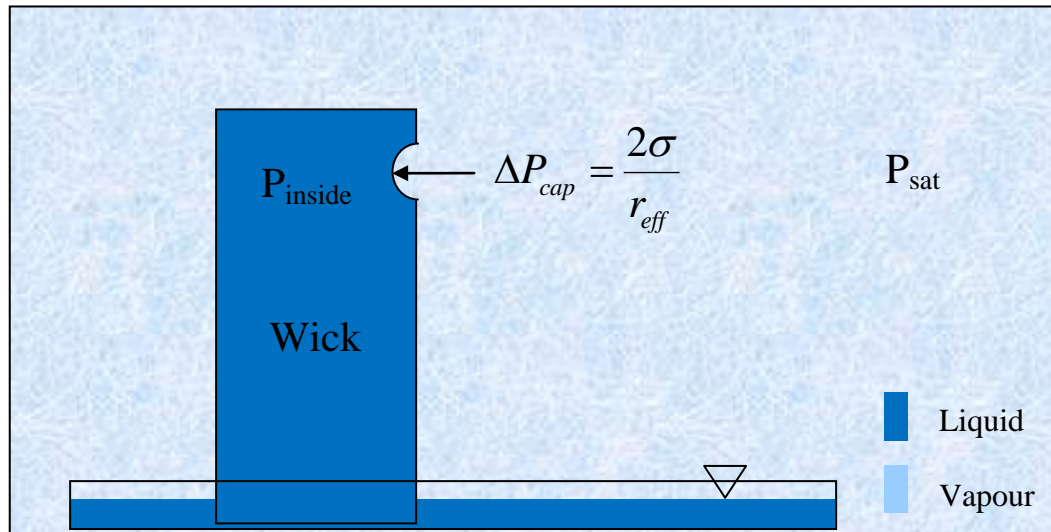


Figure 2-17 A simple and useful model [1]

The static pressure limit follows from the following fundamental aspects related to Figure 2-30:

1. The pressure inside the wick (P_{inside}) can never be less than zero.
2. The pressure on the outside of the wick is the vapour pressure (P_{sat}) of the working fluid.
3. From point 1 and 2, the pressure difference between the outside and the inside of the wick can never be larger than $P_{\text{sat}} - P_{\text{inside, minimum}} = P_{\text{sat}} - 0 = P_{\text{sat}}$. As a consequence: The capillary pressure can never be larger than the vapour pressure of the working fluid.

It is therefore necessary to consider two different cases [33]:

$$\underline{\Delta P_{\text{cap}} < P_{\text{sat}}}$$

If the capillary pressure is smaller than the vapour pressure, there is no problem with regards to the vapour static pressure limit. The minimum pressure inside the wick will be $P_{\text{sat}} - \Delta P_{\text{cap}}$ [33]. The full capillary pressure will drive the liquid through the wick.

$$\underline{\Delta P_{\text{cap}} > P_{\text{sat}}}$$

A capillary pressure which is larger than the vapour pressure is a violation of point 3 above, and can not occur. In such case the minimum pressure inside the wick is ideally zero [33], in practice somewhat above zero [1]. The capillary pressure calculated from Equation (2-8) is no longer forcing the liquid into the wick. The effective capillary

pressure is reduced; it can not exceed the vapour pressure. The effective capillary pressure is reduced through changes in the contact angle [33], i.e. for a circular tube model in accordance with Equation (2-7).

The vapour static pressure limit is relevant for the study of the hybrid heat pipe because of the very low vapor pressure of potassium, as shown in Figure 2-11.

3.3 The hybrid heat pipe

In the present study potassium was determined as the best suited working fluid for the temperature range 400-650°C. A novel hybrid heat pipe concept was presented as a promising concept for the cooling panels. Compression and sintering of nickel foam was considered to be a suitable method for making the wick for the hybrid heat pipe.

The intent of the next parts of the study was to:

- Design and build an experimental model of the hybrid heat pipe, utilizing potassium working fluid.
- Design and build a high vacuum rig for filling potassium into the hybrid heat pipe and sealing it.
- Construct a test rig for the hybrid heat pipe.
- Carry out experiments on the hybrid heat pipe in the test rig. The maximum heat flux that the hybrid heat pipe could handle at different working temperatures were of particular interest. The heat transfer capacity was planned to be determined by the capacity of the wick.
- Develop and verify models related to the thermo-hydraulic performance of the hybrid heat pipe with potassium working fluid.

The study was limited to the thermal hydraulic performance, and did not consider issues related to corrosion, long term degradation, mechanical considerations (except thermal expansion), etc. since the construction material (Ni 201) is unlikely to be used in an industrial installation.

3.4 Design and manufacture

Material selection

SS304/SS316 and nickel are materials reported to be compatible with potassium [11]. For the test unit it was also desirable to have a high thermal conductivity in order to avoid overheating of the heater cartridges, hence Nickel 201 (with a thermal conductivity of 58.2 W/(m·K) at 500°C [64]) was chosen. All the physical properties for Ni 201 used in this study are listed in Appendix E.

Dimensions

When deciding the dimensions of the hybrid heat pipe unit the following points were of importance:

1. To make the unit large enough so that the measurements and observations were directly relevant for industrial applications.
2. Not to make the unit larger than necessary, in order to keep the required amount of the working fluid (potassium) at a low level.

3. To make the cross sectional area of the unit so large that there would not be problems related to the sonic limit or entrainment limit. The main purpose of this study was to study the performance of the wick.

In addition the available production facilities imposed limitations on the dimensions of the hybrid heat pipe.

The heat and mass transfer mechanisms of main interest in this study were taking place in the evaporator part, in the wick and in the condenser part. The adiabatic section was of less interest in this study, and was therefore skipped.

The experimental hybrid heat pipe is shown in Figure 3-18. To the left the hybrid heat pipe is fully assembled. To the right the hybrid heat pipe is shown in two parts, as it was before the final assembling (welding). The inner volume is a channel with rectangular cross section. The dimensions of the hybrid heat pipe are shown in Table 3-3.

Table 3-3

	Height	Inner width	Inner depth
	[m]	[m]	[m]
Evaporator section	0,150	0,025*	0,0104 **
Adiabatic section	0,0	-	-
Condenser section	0,142	0,025	0,01155

* The width of the wick was slightly less: 0,0248 m.

** When taking the wick thickness into account.

In addition to the main volume of the hybrid heat pipe there was a smaller cylindrical volume on the top, caused by the filling tube. The filling tube had outer diameter Ø6 and 1 mm wall thickness.

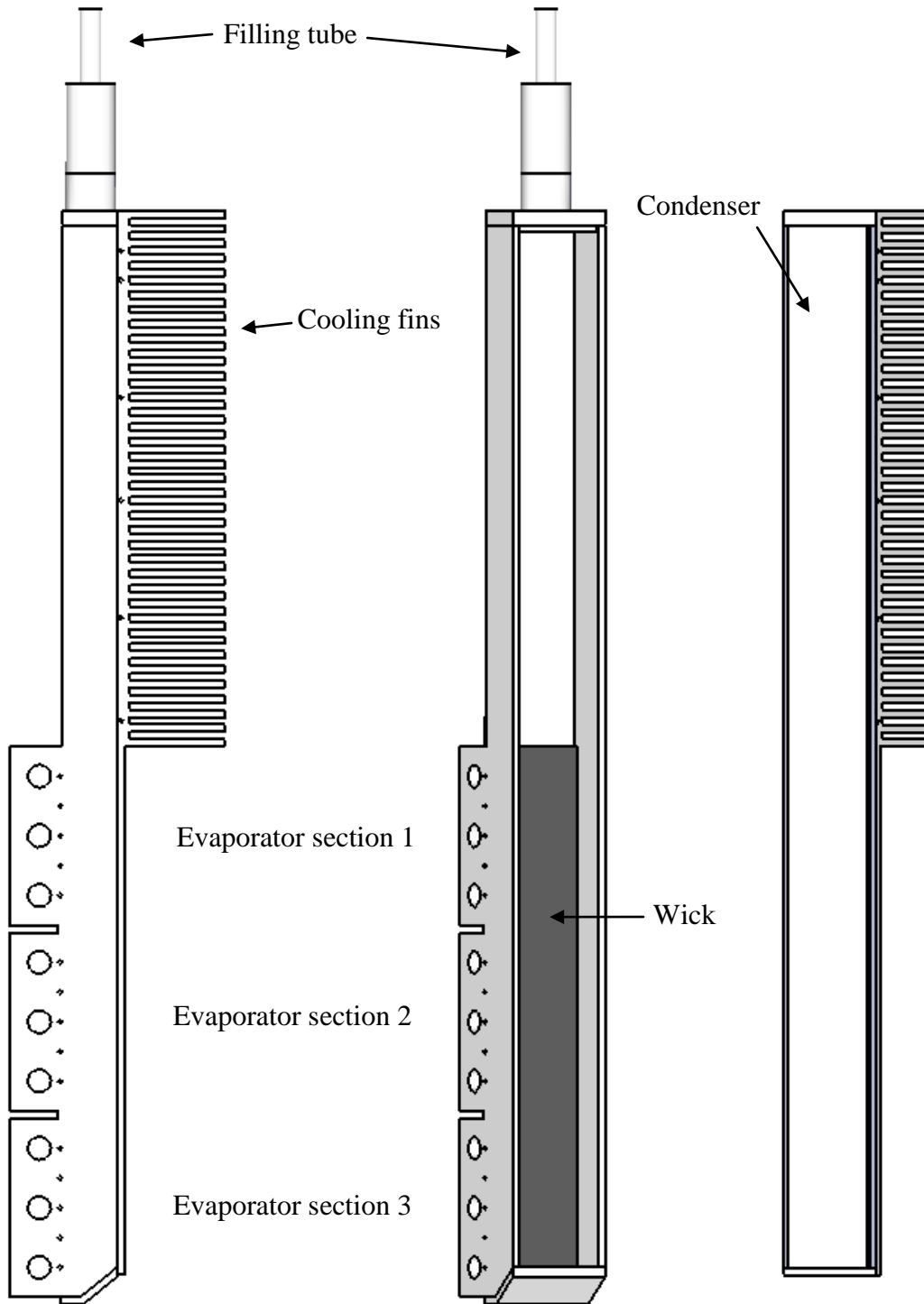


Figure 3-18 The hybrid heat pipe assembled (to the left) and in two parts (to the right)

The large holes in the evaporator section were made for the 225 W, $\text{Ø}6,35$ mm cartridge heaters. The small holes were wells made for $\text{Ø}1$ thermocouples. The depth of the thermocouple wells was 50% of the width of the hybrid heat pipe. The evaporator was divided into 3 sections, and each section contained 3 cartridge heaters. The wick is

shown in dark grey colour in Figure 3-18. The dimensions of the wick are shown in Table 3-4.

Table 3-4 The wick

Thickness	0,00115	[m]
Length	0,15	[m]
Width	0,0248	[m]
Weight	0,0060956	[kg]

The wall between the cartridge heaters and the vapour channel was 5 mm thick, and the Ø1 mm thermocouples wells were located in the middle of the wall (i.e. with 2 mm wall on each side).

The condenser was on the inside a flat wall. On the outside there were 37 rectangular fins with uniform cross sectional area. Data for the fins are shown in Table 3-5.

Table 3-5 The fins

Number of fins	37	
Fin length*	0,026	[m]
Fin thickness	0,002	[m]
Fin width	0,029	[m]
Fin spacing	0,002	[m]

*Active length=0,025 m because 1 mm is countersunk into the back wall.

Manufacturing

The evaporator part and condenser parts were manufactured from a 0,0318x0,0318 m rod of Ni 201. The fins were made by use of Electrical discharge machining (EDM Wire). The parts were weld together by electron beam (EB) welding, under vacuum. The welds were tested by use of helium and mass spectrometry.

Electron Beam welding

The evaporator, the condenser, the bottom, the top lid and the filling tube were welded together by use of electron beam welding performed at the Institute for Energy Technology (IFE), Norway. Electron beam welding was also applied to spot weld the wick to the evaporator surface.

Electron beam welding was chosen because:

1. Oxidation of the nickel was avoided by welding under vacuum ($P \approx 1 \cdot 10^{-3}$ Pa).
2. No additional material was necessary.
3. Very concentrated welding zones.
4. Very little heating of the sample outside of the welding zone.

The heat pipe was leak tested by use of a helium leak detector. A leak rate of $1 \cdot 10^{-9}$ mbar·l/s was achieved after just a couple of minutes of evacuation, which indicated that the welds were sealing adequately.

Cartridge heaters

Heat was provided to the test hybrid heat pipe by 9 cartridge heaters placed in precisely drilled holes in the evaporator section. The evaporator part was made from a block of solid nickel and divided into 3 sections which each had 3 cartridge heaters. The 3 groups of cartridge heaters were controlled individually so that the different sections of the evaporator could be exposed to different heat fluxes.

The actual cartridge heaters were from Omega Engineering, Inc., the specifications are listed in Table 3-6.

Table 3-6

Type	CIR-10121/240V
Length	31,75mm
Diameter	6,35mm
Unheated length (at both ends)	6,35mm
Sheath material	Incoloy
Heat rate	225 W
Heat rate per cartridge surface area (area of ends not included)	601401W/m ²
Maximum work temperature	760°C
Fiberglass insulated leads of manganese nickel, stranded and flexible, maximum temperature 200°C	
Standard lead length	254mm

The cartridge heaters were tested for inductive load and were found to represent ohmic load only.

For effective heat transfer it was important to minimize the thermal contact resistance between the cartridge heaters and the nickel block.

High temperature of the cartridge heaters can also cause oxidation of the heat pipe surface, unless it is protected by an inert gas. Considerable heat transfer problems caused by oxidation have been reported [8]. A thermogravimetry experiment carried out in the wick study section showed that nickel oxide starts forming rapidly from about 400°C, see Chapter 3.1.5. As the operating temperature of the cartridge heaters was up to 760°C, heavy oxidation of the heated surface could occur if oxygen was present. Due to the high reactivity of the potassium with oxygen the heat pipe was installed in a closed safety chamber, filled with nitrogen gas. By this the nickel oxidation problem was reduced.

Before the mounting of the cartridge heaters the hybrid heat pipe was heated to about 200°C in a laboratory oven, this was done to increase the diameter of the holes for the cartridge heaters. The cartridge heaters were mechanically weak, and prone to bend and bulge if non-axial force was applied. The cartridge heaters were therefore mounted one by one in a milling machine, centered exactly above the hole, and then forced into the hole by use of the arm of the milling machine. The hybrid heat pipe was reheated in the

oven between the mounting of each cartridge heater. This method resulted in tight fits between the cartridge heaters and the evaporator block. Figure 3-19 shows the cartridge heaters mounted. By accident, the lower hole was made a bit large so the cartridge heater could be mounted in it without use of the milling machine. It turned out that this cartridge heater broke down already in the first experiment, while all the other cartridge heaters survived all the experiments.



Figure 3-19 The hybrid heat pipe with the heater cartridges

Wick development

From the wick study it was concluded that a wick produced by compression of nickel foam would be suitable for the hybrid heat pipe.

The final wick was made from nickel foam acquired from Hart Materials Limited, England. The wick was produced from 4 layers of compressed nickel foam. From capacity calculations it was decided to compress the foam to $(\delta/\delta_0) \approx 0,17$. The data for the hybrid heat pipe wick are presented in Table 3-7.

The physical radius after compression

Queheillalt et al. [65] proposed Equation (3-39) for the physical radius of the foam after compression. This equation was, however, considered only to be approximate.

$$r = r_0 \frac{\delta}{\delta_0} \quad (3-39)$$

The porosity

The porosity of the final wick was determined from 3 cut-off pieces from the wick, in a standard porosity experiment as described in Chapter 3.1.4.

Effective pore radius and permeability

The wick permeability and effective pore radius were determined from a rate-of-rise experiment as described in Chapter 3.1.4. The results, as obtained for the model fluid heptane, are shown in Table 3-7. The contact angle for heptane on the wick was estimated from the maximum capillary rise, as described by Hiemenz [29].

The effective pore radius obtained for heptane was converted to an effective pore radius for potassium, by use of Equation (2-10) using the contact angles $60,15^\circ$ for heptane and

0° for potassium. The contact angle for heptane (60,15°) was the value obtained for the hybrid heat pipe wick alone.

Table 3-7 Data for the hybrid heat pipe wick

	Untreated	Compressed
Thickness 1 layer	1,7 mm	
Pore size	580 μm	
Density	429 g/m ²	
Thickness of 4 layers	6,8 mm	1,15 mm
Physical radius	0,29 mm	0,049 mm
Porosity		
Sample 1		0,829
Sample 2		0,825
Sample 3		0,798
Average		0,82
Permeability		73·10 ⁻¹² m ²
Effective pore radius with heptane		102·10 ⁻⁶ m
Contact angle for heptane on the wick		60,15°
Effective pore radius with potassium		50,8·10 ⁻⁶ m

Wick attachment to the evaporator surface

Four methods for attaching/pressing the wick to the evaporator surface were considered:

1. Sintering the wick directly to the evaporator surface.
2. A frame around the edges of the wick.
The frame was supposed to press the wick to the evaporator surface. The weakness of this concept was believed to be that the press may be reduced/disappear when the heat pipe expands due to temperature increase.
3. Springs.
Springs have to be of a material compatible with potassium and maintain strength even when the temperature increases up to 500-600°C.
4. Electron beam spot welding.
An electron beam weld can be concentrated to a tiny area, which was important in order to limit the damage to the wick. In a test where a sample wick was spot welded to a nickel plate the heat affected area of each spot weld was visually determined to less than Ø1mm.

Based on an evaluation of arguments for and against it was decided to go for electron beam spot welding. The consequences of the spot welding on the capacity of the wick was analysed by use of Comsol Multiphysics. The actual spot welded wick can be seen to the left in Figure 3-20, and the wick model with holes is shown to the right.

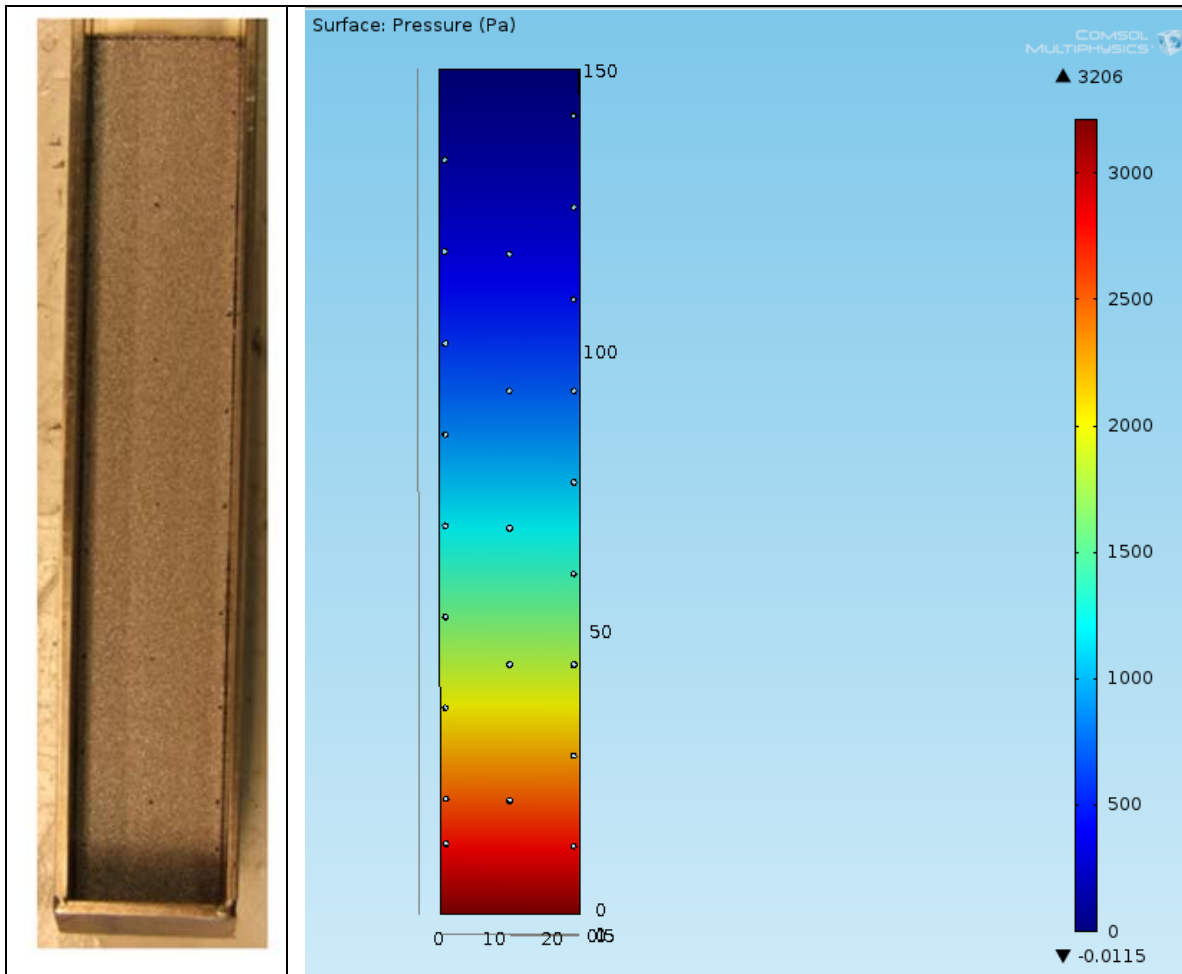


Figure 3-20 The wick and the Comsol model

Data used in the analysis are listed in Table 3-8 and Table 3-9.

Table 3-8

Wick height	150 mm
Wick width	24,8 mm
Wick thickness	1,15 mm
Wick porosity	82%
Wick permeability	$73 \cdot 10^{-12} \text{ m}^2$
Wick effective pore radius measured with heptane	$102 \cdot 10^{-6} \text{ m}$
Capillary pressure with heptane ($\theta=60,15^\circ$) from Eq. (2-8)	406 Pa
Capillary pressure with potassium ($\theta=0^\circ$) from Equation (2-11)	3206 Pa

Fluid: Potassium at 500°C, fluid data from Appendix E in Table 3-9.

Table 3-9

Density	727 kg/m ³
Dynamic viscosity	1,649·10 ⁻⁴ Ns/m ²
Vapour pressure	4161 Pa

The pressure drop from the bottom to the top of the wick was calculated by use of Comsol Multiphysics, and included the gravity term and Darcy's law for frictional pressure drop.

For wick models with and without holes the evaporation rates were adjusted so that the pressure at the top of the wicks was approximately zero. The difference in maximum evaporation rate between the wicks proved to be less than 1%.

Conclusions:

The 17 holes of diameter 1 mm reduced the total surface area of the wick by 0,36%.

The reduction in wick total heat transfer capacity (W) was less than 1%.

Thermal expansion

The hybrid heat pipe was designed to simulate the unilateral heat flux coming from the electrolysis bath. The unilateral heat flux causes asymmetrical thermal expansion of the hybrid heat pipe, contrary to normal heat pipes and thermosyphons which are almost isothermal during steady state operation. The consequences of the unilateral heating at steady state conditions were analysed by use of Comsol Multiphysics. In this model a frame around the fin base was set as the "fixed constraint", resembling the way the hybrid heat pipe was fixed in the test rig. Figure 3-21 shows the temperature distribution and the horizontal deformations calculated for one of the high heat flux cases, with about 200 W supplied to each cartridge heater in the two upper evaporator sections and about 100 W supplied to each of the two active cartridge heaters in the lower evaporator section (the deformation is exaggerated in the illustration). No power was supplied to the lower cartridge heater in the Comsol model, because the real cartridge was fried in one of the first experiments.

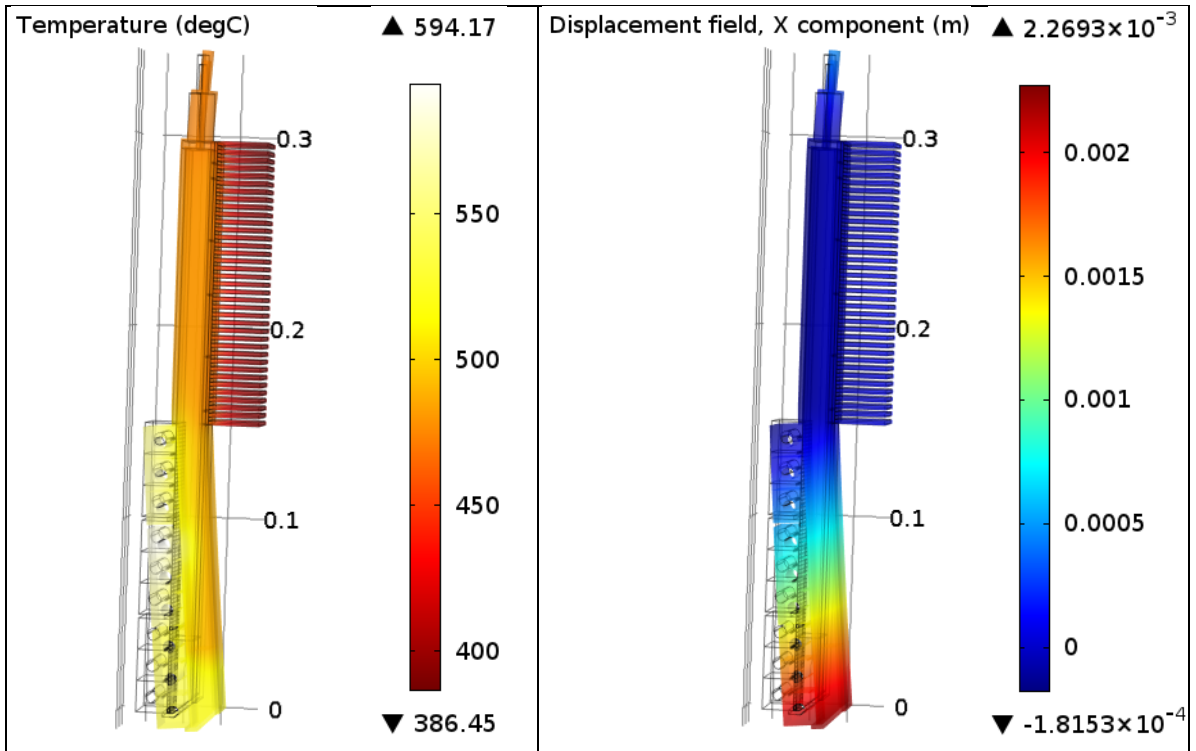


Figure 3-21 Temperature and displacement field, respectively

The horizontal displacement from the top to the bottom of the evaporator was calculated to be ca. 2,3 mm. It is not unlikely that this displacement could have weakened the wick sintering (which is holding the 4 layers of nickel foam together) or damaged welding spots attaching the wick to the evaporator surface.

Thermal displacement must also be taken into account in an industrial application, to ensure that there will not be thermal contact problems between the hybrid heat pipe and the side-lining material, especially if the panel is to be installed in the sidewall with side lining material on both sides.

Potassium inventory

The amount of potassium required in the test hybrid heat pipe was calculated by considering the liquid phase only, the potassium in gas phase was neglected due to its low density. The density of 750 kg/m^3 for liquid potassium at 400°C was used in the calculations.

Table 3-10 shows how the liquid potassium is approximately distributed in the hybrid heat pipe under stable operation. The mass in the condensate film was estimated by use of the laminar Nusselt film condensation theory.

Table 3-10 Potassium inventory

	Mass of potassium
	[g]

Condensate film (0,292m total height)	1,3
Wick (0,150m high, 0,0248m width, 1,15mm thick, 82% porosity)	2,6
15 mm liquid pool at the bottom	1,7
Total amount of potassium required	5,6

In order to ensure that the amount of working fluid would be sufficient under all operating conditions a total amount of 10,2 g potassium was filled into the hybrid heat pipe. Taking into account the amount of potassium contained by the wick and the condensate film, the height of the potassium liquid pool was estimated to 38 mm, i.e., the height of the free wick above the pool was about 112 mm.

Filling and sealing of the hybrid heat pipe

The high reactivity of potassium called for special tools and routines. A special high vacuum rig utilizing induction welding was built for the filling and sealing of the hybrid heat pipe. The rig is described in Appendix F. The high vacuum and induction welding stages of the process were tested successfully. However, the filling process failed because of the stickiness and high reactivity of potassium. Problematic oxidation of potassium occurred even in the available argon-gas-filled glove box, containing less than 10 ppm oxygen. Due to these problems an external laboratory (University of Stuttgart) filled the required amount of potassium into the hybrid heat pipe, and sealed it.

The filling and sealing approach designed in the current study could have been successful if a better glove box had been available. Still, a more rigorous routine for transferring the potassium from the glass ampoule to the hybrid heat pipe in the glove box must have been developed and tested. A heated syringe may be the best tool for this purpose; pouring melted potassium out of the glass ampoule turned out to be impossible.

3.5 Test rig, instrumentation and calibration

General overview of the test facility

The test facility is shown in Figure 3-22.

The heat pipe was placed inside a safety chamber filled with N₂-gas in order to prevent contact between potassium and air in case of heat pipe rupture. A HES analysis is enclosed in Appendix G. The nitrogen gas in the safety chamber would also reduce the oxidation of the nickel heat pipe envelope. The safety chamber was a vertically mounted cylinder of height 1130 mm, inner diameter 508 mm and with 3 mm wall thickness. The material of the cylinder was stainless steel 304L. On the top of the cylinder there was a 17 mm thick stainless steel lid of outer diameter 554 mm. All thermocouples, electrical wires and nitrogen gas pipes were going through gas tight fittings in the lid. The chamber was during operation filled with Rockwool insulation and nitrogen gas. Fiberfrax insulation was used closest to the hybrid heat pipe. The chamber was flushed

and maintained at an overpressure of 0,2 barg during the experiments in order to prevent any significant concentration of O₂.

Inside the safety chamber the condenser section of the hybrid heat pipe was connected to the nitrogen gas circuit, shown in Figure 3-22. The hybrid heat pipe was cooled by use of the nitrogen gas flowing between the fins of the condenser section. A side channel blower, Rietschle SAH 55, 400V/3 phase, was providing the pressure required to circulate the nitrogen gas through the circuit at the desired rate. This standard blower had a nominal leak rate of about 1%, it was therefore dismantled and sealed with Elastosil E43. Thereafter the blower proved leak-tight for days in a static pressure test at 0,5 barg. The maximum pressure that the blower could deliver was about 420 mbar. After the nitrogen had received heat from the heat pipe it was cooled by use of tap water in an AlfaNova fusion-brazed plate 316 stainless steel heat exchanger. This gasket-free heat exchanger was selected because it would represent an all metal barrier between the water and the nitrogen. The technical specifications of the heat exchanger are enclosed in Appendix H. The cooling water flow rate was controlled manually by a valve downstream of the heat exchanger.

Tubes of stainless steel were chosen for the nitrogen circuit because they would withstand the maximum temperature and pressure conditions appearing in the circuit.

An electrical heating cable around the nitrogen tube after the side channel blower heated the nitrogen up to 50°C before it entered the heat pipe condenser. The heating cable was controlled by use of a PID controller in LabView, connected to a phase angle firing thyristor.

The flow of nitrogen gas to the condenser section of the hybrid heat pipe could be adjusted in several ways; by the speed of the side channel blower, by use of a control valve with electrical actuator, or by use of a manual bypass. The control valve in the nitrogen circuit was a Samson 3241 with electric actuator. The valve has $K_{vs}=2,5$ and linear characteristic. K_{vs} is K_v + the safety margin of the manufacturer.

The nitrogen temperatures were measured as indicated by T1-T7 in Figure 3-22. The amount of heat taken up by the nitrogen gas was determined by use of the measured mass flow rate and the temperatures before and after the hybrid heat pipe condenser.

The test rig was also equipped with electronics to heat and control the hybrid heat pipe. Heat input to the hybrid heat pipe evaporator was provided by 9 cartridge heaters, divided in 3 groups (one for each evaporator section). Phase angle firing thyristor power control was chosen for each of the 3 groups of cartridge heaters, providing smooth and flexible power control. The thyristors were of type Eurotherm TE10A Phase Angle Power controllers with adjustable working range.

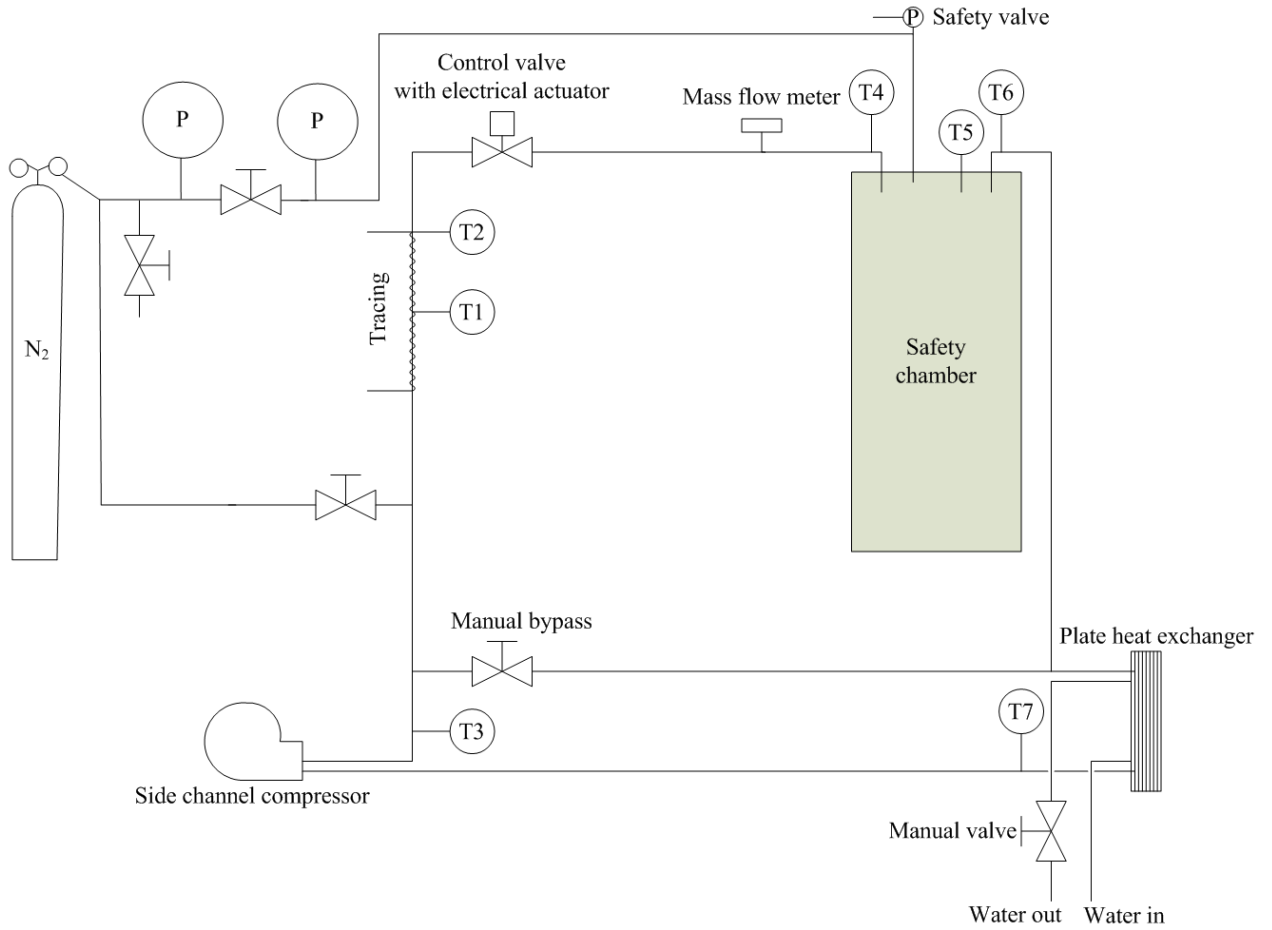


Figure 3-22 The test facility

3.6 Instrumentation and calibration

Temperature measurements

Type N thermocouples were selected in this study, since they have better thermoelectric stability than type K thermocouples [66], and a working range (0-1200°C) suitable for

this study. All thermocouples were from the same production batch. All thermocouples were mineral insulated metal sheathed, one meter long, and had a diameter of 1 mm.

The thermocouples were delivered with a calibration certificate for the first and the last thermocouple of the batch, see Appendix I. However, all the thermocouples used for the hybrid heat pipe were in addition calibrated hooked onto the logging system, by use of a portable calibrator type JOFRA 65-RTC-700 C with an accuracy of $\pm 0,11^{\circ}\text{C}$.

Tight thermowells were installed in the tubes of the nitrogen gas cooling circuit. The wells were several cm long, i.e. the length/diameter ratios were high and eliminated errors due to heat conduction in the well.

Wells were drilled for the thermocouples in the evaporator and condenser sections of the hybrid heat pipe. Thermocouples were also clamped to the outside of the adiabatic sides of the hybrid heat pipe.

In this study the thermocouples were assumed to be in the center of the holes of the wells.

The spatial positions of the thermocouples become especially important when temperatures are to be measured in temperature gradients, e.g. when temperatures measured in the wall in front of the active cartridge heaters are to be extrapolated to surface temperatures. From Fourier's law of heat conduction [67] it is easily seen that the error in temperature following an error in the position (in the direction of heat transfer) increases with increasing temperature gradient, or in other words; for the same heat flux the error increases with decreasing material conductivity.

Errors related to the thermocouples positions are also relevant for the temperature measurements taking place inside the thermowells. Specifically, the $\text{\O}1$ mm metal sheathed thermocouples were forced into 0,0145 m deep wells drilled into the evaporator and condenser walls of the hybrid heat pipe. The diameters of the pockets were assumed to be approximately $\text{\O}1,1$ mm, as they were carefully enlarged from $\text{\O}1$ just to allow the thermocouples in. In these tight pockets the freedom of movement of the thermocouples was minimized. If the thermocouples were unsheathed, or the thermowalls were not so tight, the thermocouples would have had more freedom to contact one side of the well better than the other. In an early analysis of such variations Wilcox and Rohsenow [68] assumed Gaussian distribution of the temperature measurements in the thermocouple well. However, with the tight wells in the present study such variations seem unlikely, and the temperature measurements have therefore been localized to the center of the wells.

Pressure measurements

The pressure inside the heat pipe was not measured directly, it was estimated from the temperature measurements at the adiabatic wall of the condenser part. The accuracy of the pressure estimates was equal to the accuracy of the temperature measurements plus the uncertainty of the saturated temperature/pressure table.

The pressure of nitrogen in the cooling circuit was measured by use of manometers and adjusted manually to the working pressure 200 mbarg.

Nitrogen mass flow measurement

The mass flow rate of nitrogen gas was measured by use of an insertion volume flow meter from Sierra Instruments, Inc. The flow meter, Sierra 620S, had two platinum resistance temperature sensors. One of the sensors (the temperature sensor) measured the temperature of the gas. The other sensor (the velocity sensor) was heated to a constant temperature above the gas temperature. The measuring principle was most precisely described in the Instruction Manual as: “The electrical power required to maintain a constant temperature differential is directly proportional to the gas mass flow rate”. The sensor assembly was positioned in the center of the tube. The flow rate was calculated from the single measurement at the center, utilizing data for the ratio of the average velocity to center-line velocity based on a four-segment velocity profile covering laminar and turbulent flow. This required a relatively undistorted velocity profile, which again required straight tube lengths of at least 25 tube diameters upstream and 10 tube diameters downstream the mass flow meter. The flow meter was located upstream of the heat pipe condenser.

The flow meter was factory calibrated for nitrogen gas at a working pressure of 1,2 bara and a temperature of 50°C. According to its calibration report: For temperatures outside of the calibration point a temperature coefficient of $\pm 0,04\%$ of reading per °C applied within $\pm 25^\circ\text{C}$ from the calibration temperature. For pressure outside of the calibration point a pressure coefficient of 0,02% per psi applied; the sensitivity of the nitrogen flow meter to errors in the cooling circuit pressure (200 mbarg) was therefore negligible. The accuracy of the flow meter was $\pm 1\%$ of full scale and $\pm 0,5\%$ of reading.

Power measurements

Since the cartridge heaters only represent ohmic resistance, the supplied power, P, to the cartridge heaters was determined from measurements of the voltage, U, and the current, I, and calculated by use of Equation :

$$P = U \cdot I \quad (3-40)$$

A current input module type National Instruments® NI 9227 was used to measure the current. An analog input module type National Instruments NI 9225 was used for the voltage measurements. The high sampling rates of these modules ($50 \cdot 10^3$ samples/second/channel) made them suitable as a power metering system for phase angle controlled loads. Several different tests were performed to verify the correctness of the power measurements, see Appendix I. The uncertainty of the power determination was less than 0,2%, calculated from the specifications of the input modules.

Data acquisition

The data were acquired through a LabVIEW program. A screen dump of the front panel is enclosed in Figure 3-23.

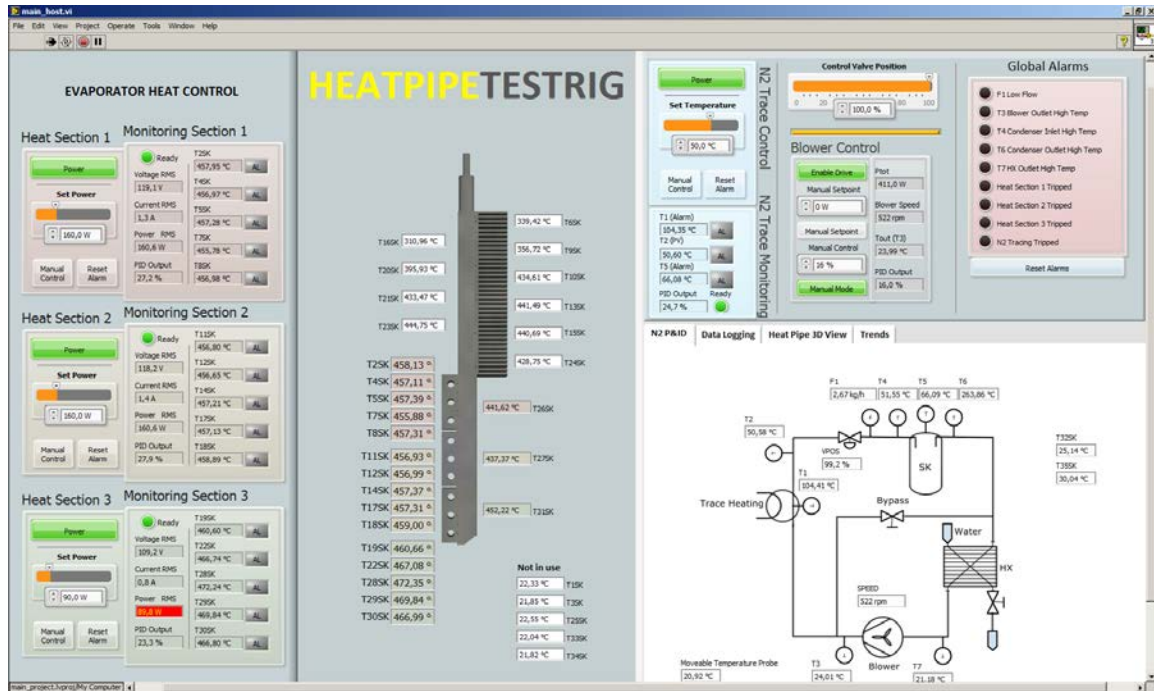


Figure 3-23 The front panel of the heat pipe test rig

The following parameters could be set through the front panel:

- Power input to each evaporator section.
- RPM for the side channel blower.
- The opening of the electrically controlled valve on the nitrogen loop.
- Temperature of the nitrogen before the condenser of the hybrid heat pipe.
- Data sampling rate.

Monitoring and control

The main measurement consisted of temperature measurements in the evaporator and condenser walls by use of thermocouples. Thermocouples were also placed on the outside walls of the hybrid heat pipe, on the “adiabatic” sides of the evaporator and condenser.

A wick dryout situation was expected to be seen as an increase in the local wall temperature. When the capacity of the wick was exceeded dryout was expected to occur first at the top of the wick.

The flow and the temperatures of the N₂ gas in/out were measured outside of the safety chamber. The test rig was designed to offer several control possibilities. The nitrogen flow could be changed by adjusting the:

- Variable speed of the side channel blower.
- Variable opening of the electrically controlled valve.

A third nitrogen flow adjustment option, a manual bypass, was not utilized in the current study.

The temperature of the nitrogen entering into the condenser section of the hybrid heat pipe was kept constant at 50°C by the heating element (tracing), utilizing a phase angle firing thyristor and a PID controller in LabView.

3.7 Calculation model/Heat flow analysis

Introduction/goals/purpose

The main goal of the experimental study was to investigate the performance and limitations of the compressed nickel foam wick under real working conditions, i.e. in a hybrid heat pipe with potassium working fluid at working temperatures up to 650°C.

A simplified sketch of the hybrid heat pipe is shown in Figure 3-7. Heat is supplied to the evaporator. The wick is distributing liquid potassium over the hot evaporator surface. Liquid potassium evaporates from the wick, and the vapour flows upwards to the flat vertical condenser wall, where it condenses. The condensed potassium flows down to the bottom of the heat pipe where the wick pumps it up to cool the evaporator surface again.

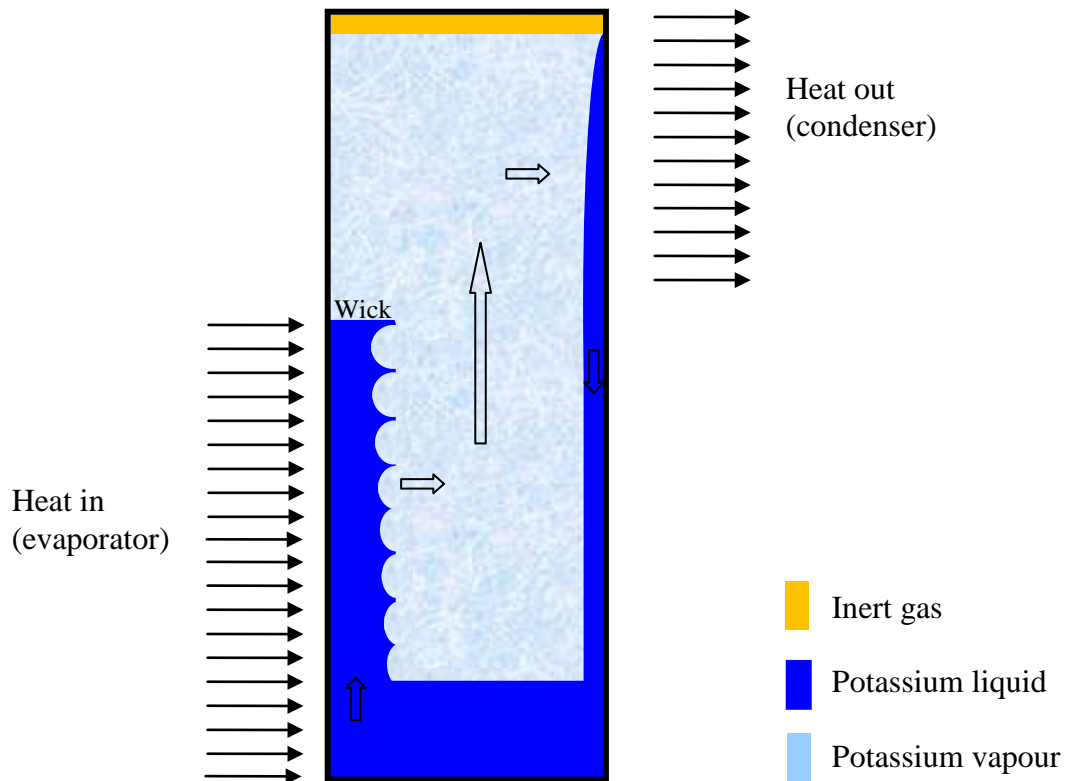


Figure 3-24 A simplified sketch of the hybrid heat pipe

3.8 Thermal resistance network

The heat flow distribution in the hybrid heat pipe was modeled using the thermal resistance approach, as described in e.g. [69].

A specific thermal resistance R'' [$\text{m}^2 \cdot \text{K}/\text{W}$] is defined as:

$$R'' = \frac{\Delta T}{q} \quad (3-41)$$

The resistance network for the hybrid heat pipe is shown in Figure 3-25: The heat from the heater cartridges enters the network from the lower left, and leaves the network at the upper left (heat loss) and right (condenser).

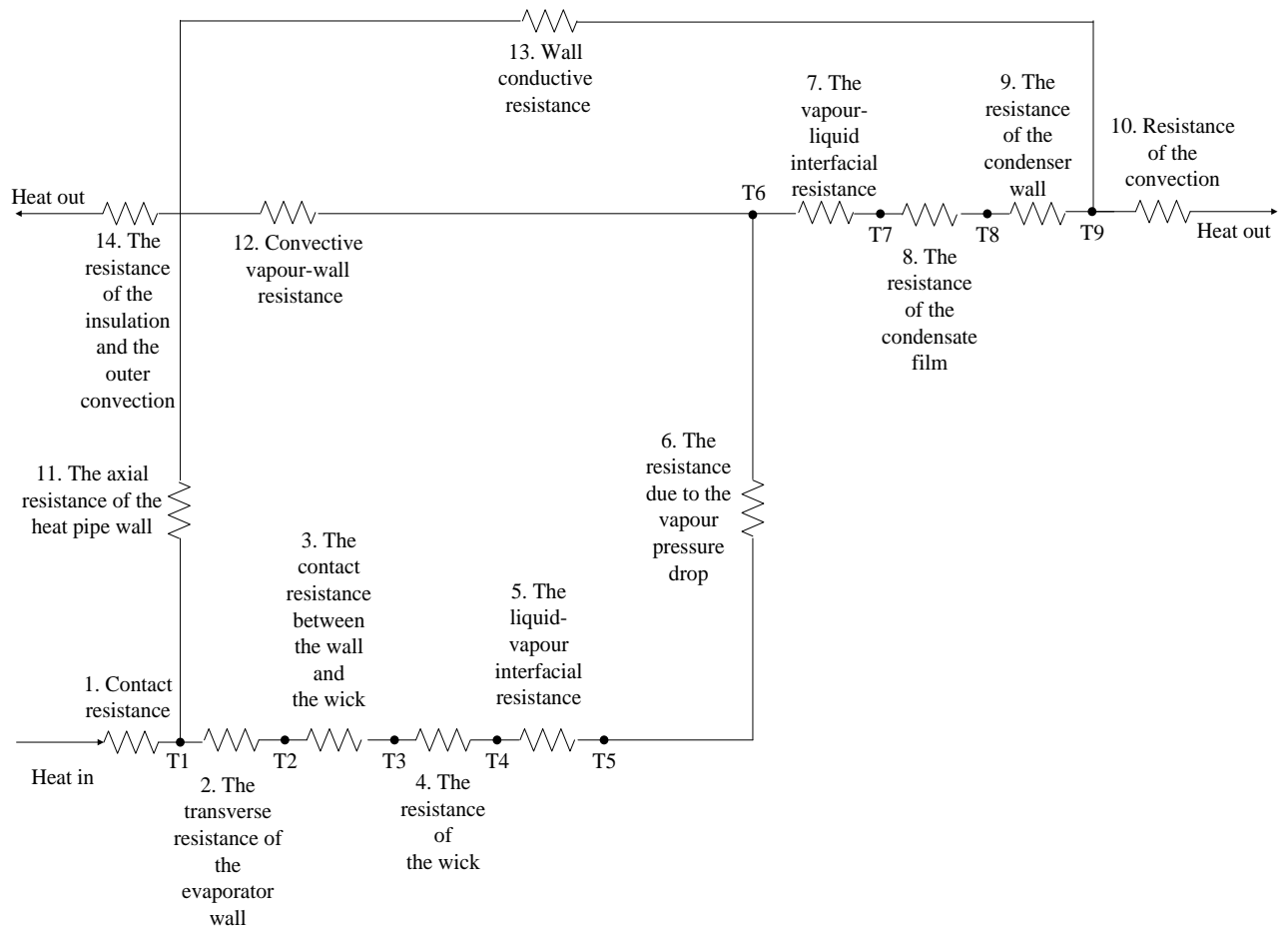


Figure 3-25 The thermal resistance network of the hybrid heat pipe

The different thermal resistances and expressions are listed in Table 3-11.

Table 3-11 The thermal resistances

	Thermal resistance	Expression for R'' [(m ² ·K)/W]	
R ₁	Contact resistance between cartridge heater and evaporator block.	-	Assumed small and disregarded in this study.
R ₂	The transverse resistance of the evaporator wall.	$\frac{L}{k_{Ni201}}$	
R ₃	The contact resistance between the wall and the wick.	-	Assumed small and disregarded in this study.
R ₄	The resistance of the wick.	$\frac{2L}{(1-\varepsilon)k_{solid} + \varepsilon k_{fluid} + \frac{k_{fluid} \cdot k_{solid}}{\varepsilon k_{solid} + k_{liquid} (1-\varepsilon)}}$	
R ₅	The liquid-vapour interfacial resistance.	$\frac{1}{\left(\frac{2\alpha}{2-\alpha}\right)\left(\frac{h_{fg}^2}{T_v \nu_{fg}}\right)\sqrt{\frac{M_v}{2\pi R_u T_v}\left(1-\frac{p_v \nu_{fg}}{2h_{fg}}\right)}}$	
R ₆	The resistance due to the vapour pressure drop.	-	Assumed small and disregarded in this study.
R ₇	The vapour-liquid interfacial resistance.	$\frac{1}{\left(\frac{2\alpha}{2-\alpha}\right)\left(\frac{h_{fg}^2}{T_v \nu_{fg}}\right)\sqrt{\frac{M_v}{2\pi R_u T_v}\left(1-\frac{p_v \nu_{fg}}{2h_{fg}}\right)}}$	
R ₈	The resistance of the condensate film.	$\frac{\left(\frac{3\mu_l \Gamma}{g \rho_l (\rho_l - \rho_v)}\right)^{\left(\frac{1}{3}\right)}}{k_l}$	
R ₉	The resistance of the condenser wall.	$\frac{L_{wall}}{k_{Ni201}}$	
R ₁₀	Resistance of the convection.	$\frac{1}{h_{convection}}$	
R ₁₁	The axial resistance of the heat pipe wall.	$\frac{L_{axial}}{k_{Ni201}}$	Assumed large and disregarded in this study.
R ₁₂	Convective vapour-wall resistance	$\frac{1}{h_{convection}}$	

R ₁₃	Wall conductive resistance	$\frac{L_{wall}}{k_{Ni201}}$	
R ₁₄	The resistance of the insulation (cylindrical) and the outer convection, both defined in terms of the inner area of the insulation.	$\frac{r_{inner}}{k_{insulation}} \ln\left(\frac{r_{outer}}{r_{inner}}\right) + \frac{r_{inner}}{r_{outer}} \frac{1}{h_{convection}}$	

Each of the thermal resistances in Table 3-11 is described in the following. The resistance network has a unique solution when all the thermal resistances, the power input, the power output, and the surrounding temperature are known. This fact was utilized in a spreadsheet calculation model for the hybrid heat pipe.

Cartridge heater contact resistance, R₁

In order to minimize the thermal contact resistance between the cartridge heaters and the evaporator block the cartridge heaters were forced into the holes in the evaporator sections. Any tighter fit than achieved by this mounting process is hard to imagine, and the resulting thermal contact resistance between the cartridge heaters and the evaporator material was therefore very small and assumed negligible.

The transverse resistance of the container walls, R₂

The heat flow by conduction through the walls was described by Fourier's law and was taken into account.

The thermal resistance of the insulation and the outer convection, R₁₄

The hybrid heat pipe was insulated with 3-4 layers of Fiberfrax insulation of total thickness 5-6 mm, the remaining space between the hybrid heat pipe and the safety chamber was filled with Rockwool. In the calculation model it was assumed that all the space between the hybrid heat pipe and the safety chamber was filled with insulation (Rockwool).

In general, maximum insulation was sought in order to minimize the heat losses. Hultin [57] pointed out that high heat loss through the insulated (ideally adiabatic) walls of the hybrid heat pipe, can cause undesired condensation of working fluid vapour on these walls.

The contact resistance between the wall and the wick, R₃

The wick was attached to the evaporator surface by electron beam spot welding. The welding spots were thermal bridges (with no thermal resistance) between the evaporator surface and the wick material, but they represented just 0,36% of the total wick area (as shown in chapter 3.4). Most of the evaporator surface was therefore in contact with either solid wick material or liquid potassium, and in both cases there would be a contact

resistance. Figure 3-9 is a simplified sketch showing the evaporator wall and the 3 types of contacts. The corresponding heat flows are $q_{\text{evaporator surface-wick material}}$, $q_{\text{welding spot}}$ and $q_{\text{evaporator surface-potassium}}$, respectively.

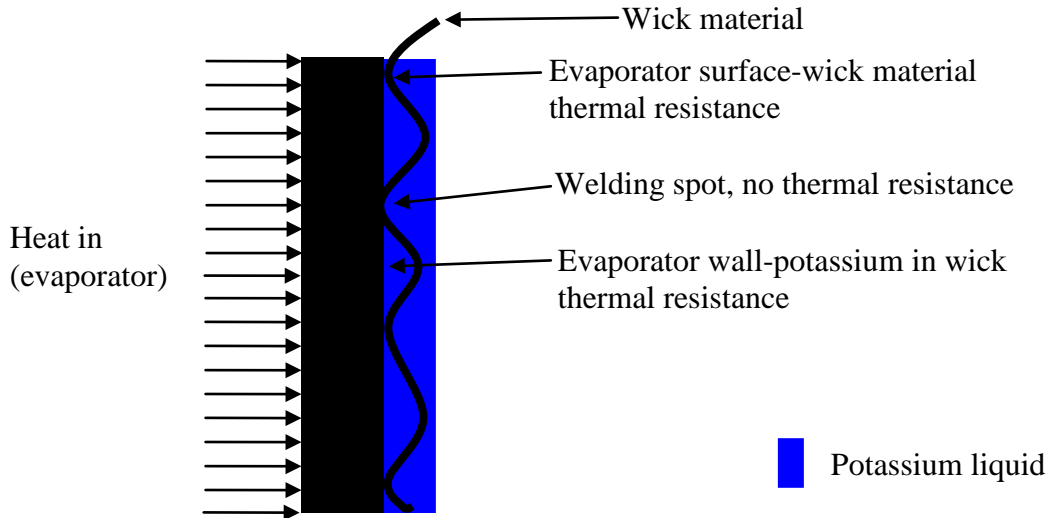


Figure 3-26 The three types of contacts at the evaporator wall

There is no thermal contact resistance at the welding spots, and the two thermal resistances are in parallel. However, for the nickel wick saturated with potassium the contact resistances were small and disregarded.

The thermal resistance of the wick, R_4

Different models exist for the effective thermal conductivity of a porous structure/wick filled with liquid. The models can be wick specific [21] or the more general parallel and serial resistance coupling models. The choice of model becomes most significant when the thermal conductivities of the porous material and the fluid are significantly different. For the porous material and the fluid used in this study, nickel and potassium, the thermal conductivities are not very different so the choice of model becomes less important. In order to illustrate this the effective thermal conductivity has been calculated by use of the parallel and the serial model, which represent the extreme high and low effective conductivities [1, 21]. The results are presented in Table 3-12.

The parallel coupling model is given by Equation (3-42) [21]:

$$k_{\text{eff,parallel}} = (1 - \varepsilon)k_{\text{solid}} + \varepsilon k_{\text{fluid}} \quad (3-42)$$

The serial coupling model is given by Equation (3-43) [21]:

$$k_{\text{eff,serial}} = \frac{k_{\text{fluid}} \cdot k_{\text{solid}}}{\varepsilon k_{\text{solid}} + k_{\text{liquid}} (1 - \varepsilon)} \quad (3-43)$$

where $\varepsilon = 0.82$ is the porosity of the evaporator wick.
 The thermophysical properties for Nickel are taken from Appendix E.

Table 3-12 The effective thermal conductivity of the wick

Temperature	k_{Nickel}	$k_{\text{Potassium}}$	$k_{\text{eff, parallel model}}$	$k_{\text{eff, serial model}}$	Δk_{eff}	$k_{\text{avg.}}$
[°C]	[W/(m·K)]	[W/(m·K)]	[W/(m·K)]	[W/(m·K)]	%	
63,6	87,0	51,8				
100	83,0	50,9				
200	74,9	48,3	53,1	51,6	-2,8	52,3
300	67,9	45,7	50,0	48,6	-2,8	49,1
400	66,7	43,1	47,4	46,0	-3	47,0
500	67,7	40,6	45,5	43,7	-4	44,6
600	69,5	38,0	43,7	41,4	-5,3	42,5
700	70,9	35,4	41,9	38,9	-7,2	40,4
					Average:	46,0

$$\text{where } \Delta k_{\text{eff}} = \frac{k_{\text{eff, par.}} - k_{\text{eff, ser.}}}{k_{\text{eff, par.}}} \cdot 100.$$

From Table 3-12 it can be seen that the difference (Δk_{eff}) between the parallel and serial model is between -2,8 to -7,2 % for temperatures ranging from 200 to 700°C. Since the real hybrid heat pipe wick is not classified as purely parallel or serial it was decided to use the average of these two models in calculations. This is considered adequate for the present model. Hence,

$$R_4'' = \left[\frac{1}{k_{\text{eff, ser.}}} + \frac{1}{k_{\text{eff, par.}}} \right] \frac{L}{2} \quad (3-44)$$

where L is the thickness of the wick.

The liquid-vapour and vapour-liquid interfacial resistances, R_5 and R_7

The interfacial resistance has in most engineering calculations been neglected, because its magnitude has usually been much smaller than the other resistances. When the interfacial resistance has been neglected in film condensation studies, the temperature at the vapor-liquid interface was implicitly assumed to be equal to the saturation temperature of the vapor. This assumption is justified as long as the interfacial resistance is small compared to the resistance of the condensate film. The situation can be different when the fluid is a liquid metal, such as potassium. The high thermal conductivity of potassium makes the thermal resistance in the thin condensate film small. The resistance at the liquid-vapor interface can therefore be of the same order of magnitude as the film resistance, and has to be taken into account [70].

The derivation of the interfacial resistance for vapourization and condensation starts from the gas kinetic theory [71], and is quite involved. Several expressions exist for the interfacial resistance, depending on the simplifying assumptions applied. In order to arrive at an explicit expression Carey [72] assumed $(p_v - p_l) / p_v \ll 1$, $(T_v - T_l) / T_v \ll 1$ and small values of a , where a was defined by Eq. (3-45),

$$a = \frac{q_i}{\rho_v h_{lv}} \left(\frac{M_v}{2R_u T_v} \right)^{1/2} \quad (3-45)$$

The final expression developed by Carey [21, 72]:

$$\frac{1}{R_\delta''} = h_\delta = \left(\frac{2\alpha}{2-\alpha} \right) \left(\frac{h_{fg}^2}{T_v v_{fg}} \right) \sqrt{\frac{M_v}{2\pi R_u T_v}} \left(1 - \frac{p_v v_{fg}}{2h_{fg}} \right) \quad (3-46)$$

In cases where the capillary pressure is of the same magnitude as the vapour pressure, as discussed in Chapter 3.2.2, the assumption $(p_v - p_l) / p_v \ll 1$ does not hold. It was therefore decided to compare the results from Eq. (3-46) to an implicit expression, for which the assumptions of Carey have not been applied.

The implicit expression [21]:

$$\frac{1}{R_\delta''} = \frac{q_\delta}{\Delta T} = \alpha h_{fg} \sqrt{\frac{M_v}{2\pi R_u}} \left[\frac{\Gamma p_{sat}(T_v)}{\sqrt{T_v}} - \frac{p_{sat}(T_l)}{\sqrt{T_l}} \right] \quad (3-47)$$

The accommodation coefficient, α , was assumed to be unity [21, 68]. Γ is a factor which describes the effects of bulk gas motion in the gas kinetic expressions for the flux of molecules normal to a planar surface [72], and was described by Equation (3-48) at moderate and high temperatures [21]:

$$\Gamma \approx 1 + a\sqrt{\pi} = 1 + \frac{q_i}{\rho_v h_{lv}} \left(\frac{M_v}{2R_u T_v} \right)^{1/2} \sqrt{\pi} \quad (3-48)$$

The interfacial resistance, R_δ'' , was calculated and plotted for potassium at different temperatures by use of the explicit expression, Eq. (3-46), and by use of the implicit expression, Eq. (3-47), and the results are shown in Figure 3-27. The differences between the results are for the specific temperatures in the range 3,2-7,9 %. For this study the explicit expression, Equation (3-46), is therefore acceptable.

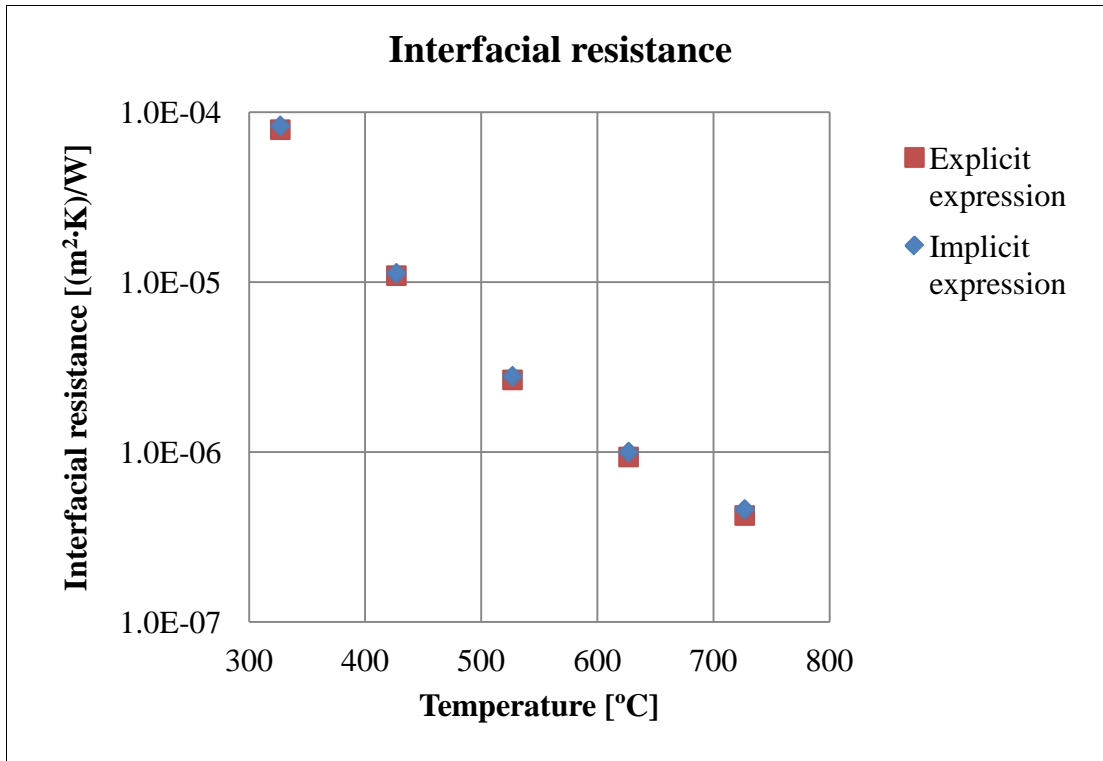


Figure 3-27 Interfacial resistance

When the interfacial resistance is taken into account, the temperature difference across a condensate film will be represented by $(T_{\text{interface}} - T_{\text{wall}})$ rather than $(T_{\text{sat}} - T_{\text{wall}})$ used in the traditional Nusselt condensation theory. The same is true for the evaporator.

Resistance of the condensate film, R_g

The potassium condenser of the hybrid heat pipe is a vertical plate. Condensation on a vertical plate is usually treated by Nusselt film condensation theory. For condensation of metal vapours the original Nusselt theory may predict too high heat transfer coefficients [70], due to some of the simplifying assumptions on which it was based. The assumptions made in the Nusselt film condensation theory are briefly summarized in Table 3-13, together with a list of papers of particular importance for the development of the theory for laminar film condensation of liquid metals on a vertical plate.

The ratio of sensible to latent heat absorbed during condensation is called the Jakob number [69], and it is an important dimensionless number in the theories for condensation of metal vapours. The formal definition of the Jakob number (Ja) is shown in Equation (3-49):

$$Ja = \frac{c_p (T_{\text{surface}} - T_{\text{sat}})}{h_{fg}} \quad (3-49)$$

The significance of the Jakob number in the condensation theory is discussed in the following.

Energy transfer by advection in the condensate film

In the original Nusselt theory the heat transfer through the condensate film was assumed to be caused by conduction only, and the temperature profile through the film was assumed to be linear. Under steady state, with constant fluid properties and with no advection in the condensate film the temperature profile through the condensate film becomes linear. In order to improve the condensation analysis Rohsenow [73] included the advection taking place in the film in the perpendicular direction to the vertical flat plate. The inclusion of this “cross flow” made the temperature profile through the film curved. By comparing equations with and without cross flow Rohsenow [73] found that the cross flow increased the heat transfer coefficient. He also found that the effect of the cross flow became more important with increasing Ja, and stated that for Ja below 0,2 the equation derived without cross flow (i.e. Nusselts original assumption) may be used.

The inertia term of the momentum equation

In the original Nusselt film condensation theory the inertia terms of the momentum equation were assumed to be small compared to the friction (viscous) term, and the inertia terms were therefore neglected. In such cases the liquid film is said to be friction restrained. For low Prandtl-number liquids (or rather low *film Prandtl number* according to Bejan [74]), the inertia terms in the momentum equation can not be neglected. This is the case for liquid potassium, and makes the condensation of potassium inertia-restrained [74]. The range where inertia is important and its effect on the average Nusselt number as a function of $Pr_{\text{film}}=Pr_l/Ja$ is given by Figure 3-28 from Bejan [75]. The Figure of Bejan was developed from the work of Chen [76].

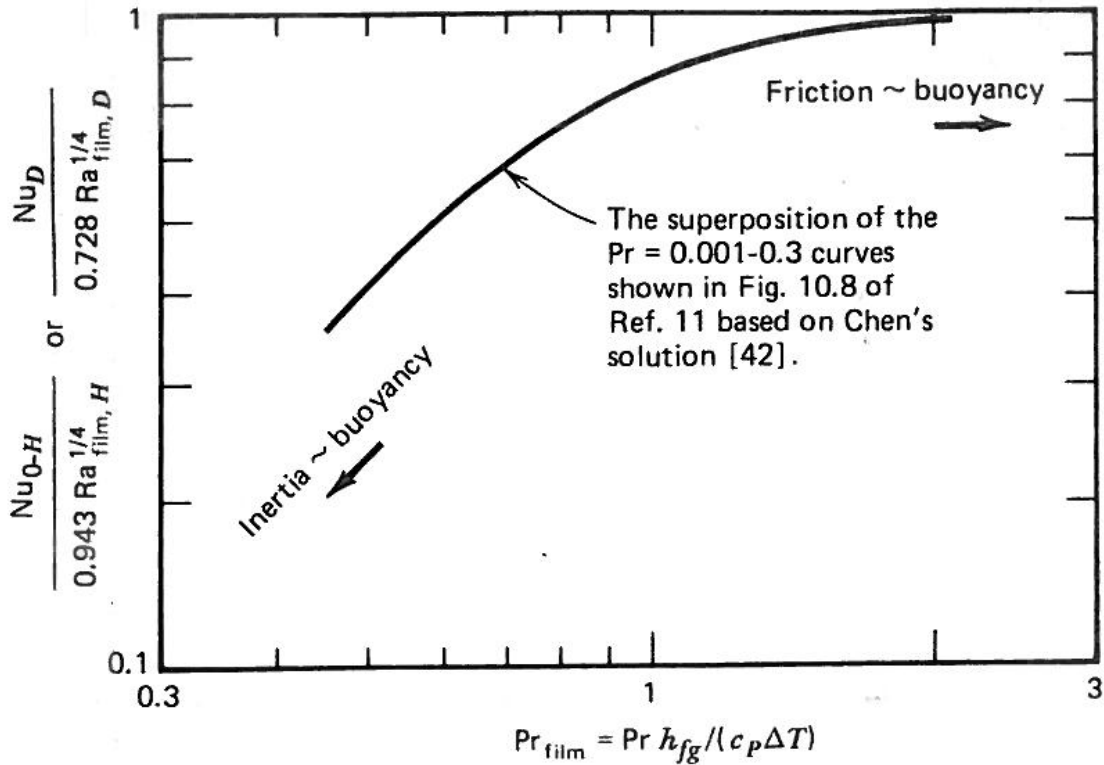


Figure 3-28 Correction factor for inertia/friction restrained condensate film [74-75]

For the present work using potassium, the Jakob numbers are so small that $(Pr/Ja) \gg 1$, and the Nusselt condensation theory is considered valid. The physical interpretation of this is that the small Prandtl numbers for the potassium liquid are “neutralized” by large latent heats of evaporation and small ΔT , caused by thin film and high thermal conductivity of liquid potassium.

A short summary of the historical development of the condensation theory is shown in Table 3-13.

Table 3-13 Historical development of condensation theory

Year	Author(s)	Ref.	Contribution
1916	Nusselt, W.		<p>Laminar film condensation analysis based on the following assumptions (abbreviated) [69]:</p> <ul style="list-style-type: none"> • Laminar flow and constant fluid properties. • Pure vapour at saturation temperature, heat transfer from gas to film only by the latent heat of condensation (i.e. h_{fg}). • No shear stress between the liquid film and the vapour. • No momentum (acceleration) energy transfer in the film and no energy convection in the film. I.e. heat transfer in the film by conduction only. <p>In this standard Nusselt's model the temperature profile in the film becomes linear.</p>
1956	Rohsenow, W.M.	[73]	<p>Included the effects of:</p> <ul style="list-style-type: none"> • Film subcooling. • "Cross flow" created by the continuous addition of liquid to the film. <p>The subcooling increased the heat transfer coefficient. The cross flow made the temperature profile through the film curved and increased the heat transfer coefficient.</p>
1959	Sparrow, E.M. Gregg, J.L.	[77]	<p>Carried out boundary-layer theory analysis of laminar film condensation, which confirmed Rohsenow's results. Included in addition fluid-acceleration in the analysis. For decreasing Pr the acceleration was shown to have increasingly negative effect on Nu. The negative effect decreased with decreasing $(c \cdot \Delta T / h_{fg})$, which may also be seen as it decreased with decreasing film thickness.</p>
1961	Koh, J.C.Y. Sparrow, E.M. Hartnett, J.P.	[78]	<p>In addition to the effects included in the 1959-paper by Sparrow and Gregg this paper included the effect of the interfacial shear between the liquid film and the vapour. The vapour was assumed stationary at a distance away from the interface. The negative effect of the interfacial shear on the heat transfer was found to increase with decreasing Pr, but the effect decreased with decreasing film thickness.</p>
1961	Chen, M.M.	[76]	<p>Included (like Koh, Sparrow and Hartnett) the interfacial shear in the analysis, and obtained similar results. Presented in addition the results as an approximate correction formula to the traditional Nusselt theory for the heat transfer coefficient. The correction formula has been adopted by VDI [79] for the condensation of metal vapours.</p>

Experimental studies of metal vapour condensation

Experimental studies of metal vapour condensation are truly very difficult to carry out, and some major challenges were identified by Wilcox and Rohsenow [68]. The magnitudes of the thermal resistances at the interface, and in the film, are in the case of liquid metals very small, which require very precise temperature measurements. Both Wilcox and Rohsenow [68] and Ishiguro et al. [80] determined the condenser block surface temperature by extrapolation of several temperature measurements in the condenser block. In order to reduce the uncertainty of the extrapolation they used 6 and 12 thermocouples respectively in the condenser block (i.e. the thermocouple positions were on a straight line perpendicular to the surface).

The condensation model of this study

From the arguments presented in the previous chapters the Nusselt laminar film condensation theory was applicable for the current study. The resistance of the condensate film was calculated from Equation (3-50) and (3-51).

$$R_g'' = R_\delta'' = \frac{\delta}{k_l} \quad (3-50)$$

where the film thickness, δ , is [69]:

$$\delta = \left(\frac{3\mu_l\Gamma}{g\rho_l(\rho_l - \rho_v)} \right)^{\left(\frac{1}{3}\right)} \quad (3-51)$$

Γ is here the mass flow rate per unit width of the condenser.

The resistance of the condenser wall including the fins, R_9 and R_{10}

The heat transfer in the condenser wall is by heat conduction as described by Fourier's law. The heat transfer from the fins and the fin base to the cooling gas, nitrogen, is by forced convection. The fins and the back plate created rectangular channels for the nitrogen gas when the hybrid heat pipe was installed in the test rig. The photo in Figure 3-29 was taken during installation of the hybrid heat pipe in the test rig, and shows the channels.

For rectangular channels with constant wall temperature or heat flux and fully developed laminar velocity and temperature profiles the Nusselt numbers are tabulated in e.g. [81]. The heat transfer in the entry length is generally higher than for fully developed flow, so an assumption of fully developed flow for the whole tube length will give a conservative estimate of the heat transfer. For N_2 at the actual temperatures (around 50-200°C) the Prandtl number is approximately 0,7, which implies that in the actual case the temperature profile develops slightly faster than the velocity profile [82].

Because of the unilateral heat flux there will be a temperature drop in the channel walls (i.e. the fins) from the heated side to the unheated side of the channels. The problem is quite analogous to the temperature drops in fins, so the temperature drop was in the calculation models taken into account by a fin efficiency factor. As an approximation,

the fin efficiency for a straight fin of uniform cross section and with adiabatic tip was applied [69]:

$$\eta_f = \frac{\tanh(mL)}{mL} \quad (3-52)$$

where

$$m \equiv \sqrt{\frac{hP}{kA_c}} \quad (3-53)$$

The specific thermal resistance for the convective heat transfer from the fin and the unfinned surfaces, to the nitrogen gas:

$$R''_{convection} = \frac{A_{condenser}}{h_{convection}(\eta_f \cdot A_f + A_b)} \quad (3-54)$$

where $A_{condenser}$ is the condenser total height multiplied by the total condenser width.



Figure 3-29 The hybrid heat pipe condenser fins

The resistance due to the vapor pressure drop, R_6

The pressure drop of the flowing vapour phase consists of two terms [11]:

- The pressure drop due to frictional forces, this is also called the viscous term.
- The pressure drop due to acceleration forces, this is also called the inertia or momentum term.

When the working fluid evaporates from the wick in the hybrid heat pipe the vapour has initially no “axial” velocity, only a “radial” (transverse) velocity as indicated in Figure 3-7. When the vapour is accelerated in the axial direction the static pressure decreases, which also affects the curvature of the liquid/vapour menisci in the wick. Ideally, for a uniform heat flux over the evaporator surface a linearly increasing freestream axial vapour velocity will develop in the evaporator.

The boundary layer created over the wick surface by the axial freestream will be disturbed by the radial velocity of the evaporating working fluid. The effect of the evaporating working fluid on the boundary layer is described as “blowing”, and reduces the frictional gradient in the axial direction. If the radial velocity is high enough the boundary layer can be totally blown off and the friction is then zero [83].

In the condenser, the radial velocity of the condensing vapour causes “suction”. The suction thins the boundary layer and increases the friction [83]. Analytical solutions exist for blowing and suction for laminar constant-property external boundary layers with constant free stream velocity [81], but no solution has been found for internal flow with linearly increasing/decreasing free stream velocity and constant velocity normal to the surface. The blowing or suction parameter is defined as:

$$\frac{v_v}{u_\infty} \text{Re}_x^{1/2} \quad (3-55)$$

From the analytical solutions presented in Kays, Crawford and Weigand [81] the effect of increased free stream velocity u_∞ is increased friction, both in the case of blowing and suction. Increased velocity v_s normal to the surface decreases friction in the case of blowing and increases friction in the case of suction.

A major difference between the pressure drop caused by friction and the pressure drop caused by acceleration is that the pressure drop from the acceleration can (to some extent) be recovered during deceleration. In the condenser the vapour loses its axial velocity, and the static pressure increases (i.e. static pressure recovery). For a heat pipe with sodium working fluid, 60% pressure recovery was measured for a radial Reynolds number of 10 [11].

Models for the vapour pressure drop in traditional cylindrical heat pipes were developed already from the childhood of the heat pipe technology. A comparison of some models can be found in Faghri [21]. In the earliest treatment of the pressure drop of the vapour phase Cotter [84] used two different models: One model for radial Reynolds number $\text{Re}_r \ll 1$ and one model for $\text{Re}_r \gg 1$. It followed from his models that for low radial

Reynolds numbers ($Re_r \ll 1$) the pressure drop was entirely due to frictional forces, and for high Reynolds numbers ($Re_r \gg 1$) the pressure drop was due to flow acceleration [11]. The models were developed for symmetrical, cylindrical heat pipes and would need modifications for eventual use for the rectangular hybrid heat pipe exposed for unilateral heat flux.

The radial Reynolds number is defined as [11]:

$$Re_r = \frac{\rho_v v_r r_v}{\mu_v} \quad (3-56)$$

3.8.1 Non-condensable gas

The non-condensable gas considered here is defined as one or several non-condensable gases which are not desired in the hybrid heat pipe.

The three possible sources of non-condensable gas(es):

- Residual non-condensable gas after the outgassing, filling and sealing process, due to limited vacuum achieved during evacuation. In the case of potassium working fluid argon is usually used as protective gas, so in such cases the non-condensable gas is argon.
- Reactions between the working fluid and the container and/or wick material may generate non-condensable gas(es). For surface area dependent reactions the wick is important, as the area of the wick is normally much larger than the inner area of the container.
- Leakage of air/gas from the outside of the heat pipe into the heat pipe through a defect in the heat pipe wall.

The consequences of non-condensable gas in the hybrid heat pipe are:

- Reduced heat transfer capacity if the non-condensable gas is partially or totally displacing the working fluid from a part of the heat pipe, typically in the condenser section.
- To reduce the condensation rate, because the mass transport of working fluid has to diffuse through the non-condensable gas to reach the condenser surface.
- To lower the condensation temperature, down to the temperature which corresponds to the partial pressure of the working fluid at the gas/liquid interface.
- Corrosion, if the non-condensable gas is corrosive.

In this study the volume occupied by the non-condensable gas under different working temperatures of the heat pipe was of particular interest. The following basic model was derived to estimate the volume.

A basic model for the non-condensable gas volume

The purpose of this analysis was to make a basic flat front model for the volume occupied by the non-condensable gas at temperatures ranging from room temperature (20°C) to the highest working temperature (650°C). Mass diffusion, inertia effects, radial- and axial heat conduction and transient effects have not been taken into account in the model. Models which take such effects into account have been reviewed/developed by Faghri [21]. Still, the basic flat front model has been verified by many investigators [21].

The basic flat front model developed consists of a container which is holding an non-condensable gas volume and a working fluid, as shown in Figure 3-13. The temperature is assumed to be uniform. At the bottom of the container there is a small amount of working fluid in solid or liquid form, depending on the temperature. The volume of the solid and the liquid is negligible compared to the volume occupied by the vapour and the gas. In this basic model the non-condensable gas is assumed to behave as an ideal gas.

Below the melting temperature of the working fluid the non-condensable gas occupies the entire volume above the solidified working fluid, as shown in the left part of Figure 3-13.

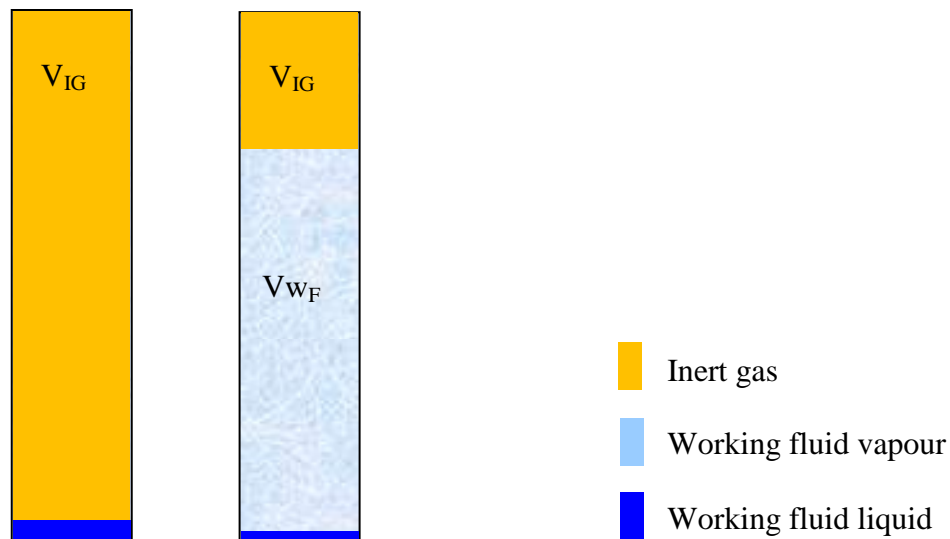


Figure 3-30 The basic flat front model

When the temperature is below the melting temperature of the working fluid, the pressure in the container is entirely given by the ideal gas law for the non-condensable gas:

$$p_{total} = \frac{n_{NCG} \cdot R_u \cdot T}{V_{total}} \quad (3-57)$$

Above the melting temperature of the working fluid the non-condensable gas has been compressed to a smaller volume by the vapour of the working fluid, as shown to the right in Figure 3-13.

In this situation the pressure in the container is the sum of the partial pressure of the non-condensable gas and the partial pressure of the vapour of the working fluid. The partial pressure of the working fluid vapour is given by its saturation curve. The volume of the non-condensable gas can be determined from Equation (3-58):

$$V_{IG} = \frac{n_{NCG} \cdot R_u \cdot T}{p_{NCG} + p_{WF}} \quad (3-58)$$

Since $V_{total} = V_{IG} + V_{WF}$ the number of moles of working fluid that is in the vapour phase at temperature T can be determined by Equation (3-59).

$$n_{WF} = \frac{(p_{NCG} + p_{WF})V_{WF}}{R_u \cdot T} \quad (3-59)$$

In Chapter 4.1 the basic model has been applied to a system consisting of potassium working fluid and argon non-condensable gas, which is relevant for the experimental part of this work.

3.8.2 A spreadsheet model of the hybrid heat pipe

A model of the hybrid heat pipe was created in a spreadsheet, utilizing thermal resistances presented in Chapter 3.8. From the overall perspective the model had to satisfy the heat balance for the hybrid heat pipe:

$$Q_{in} - Q_{loss} - Q_{N_2} = 0 \quad (3-60)$$

where Q_{in} was the power supplied to the cartridge heaters, Q_{loss} was the heat loss from the hybrid heat pipe to the surroundings, and Q_{N_2} was the power taken up by the nitrogen gas in the hybrid heat pipe condenser. Equation (3-60) was solved by iteration, for specified thermal resistances, power input, power uptake by N_2 , and surrounding temperature. The temperature at the bottom of the evaporator section was selected as starting point, and the temperature and pressure changes were calculated for 1 mm steps in the axial flow direction.

The frictional pressure drop of the potassium vapour was estimated by use of traditional pressure drop formulas for flow in a rectangular tube:

$$\Delta P_{friction} = f \frac{\rho u_m^2}{2D_h} \Delta L \quad (3-61)$$

The blowing and suction was neglected.

The pressure changes due to acceleration and retardation were calculated. The rate of retardation was determined by the rate of condensation of the potassium. The vapour velocities in the evaporator and condenser were calculated from:

$$u_v = \frac{\dot{m}_v}{\rho_v A_c} \quad (3-62)$$

The effectiveness-NTU-method [69] was applied for the modelling of the condenser. The effectiveness-NTU-method applied to each 1 mm step of the condenser:

$$q = (\dot{m} \cdot c_p)_{N_2} \cdot \varepsilon (T_{condensation, potassium} - T_{in, N_2}) \quad (3-63)$$

For a condensing fluid (here the potassium) the heat capacity rate $(\dot{m} \cdot c_p)$ is infinite, while the heat capacity rate of the nitrogen gas is finite, and in such case the ratio of the heat capacity rates is zero. For such cases the relation for the heat exchanger effectiveness becomes:

$$\varepsilon = 1 - e^{(-NTU)} \quad (3-64)$$

where

$$NTU = \frac{UA}{C_{min}} = \frac{UA}{(\dot{m} \cdot c_p)_{N_2}} \quad (3-65)$$

and

$$A = (width \cdot height)_{condenser} \quad (3-66)$$

and

$$U = \frac{1}{R''_{total, condenser}} \quad (3-67)$$

where $R''_{total, condenser}$ was calculated for each step as the sum of the thermal resistances of the potassium vapour-liquid interface, the condensate film, the condenser wall, and the fin-nitrogen gas heat transfer:

$$R''_{total,condenser} = R''_{interface} + R''_{condensate\ film} + R''_{condenser\ wall} + R''_{convection\ to\ nitrogen\ gas\ in\ channel} \quad (3-68)$$

The non-condensable gas volume on the top of the hybrid heat pipe reduced the capacity of the condenser; therefore a temperature dependent effective condenser length was implemented in the spreadsheet model utilizing the basic model for the non-condensable gas volume.

3.9 Experimental matrix

The experimental matrix is shown in Table 3-14. Periods of stable operation at lower heat fluxes were of interest, particularly at the lowest temperatures (i.e. below the lower limit of the useful range 773-1273 K for potassium indicated in literature [21]). The performance limits of the experimental/test hybrid heat pipe wick were, during a series of experiments, challenged by higher and higher heat fluxes at different working temperatures. In some experiments the heating and cooling capacity of the test rig made it possible to challenge the hybrid heat pipe further and exceed the predicted maximum heat flux.

Table 3-14 The experimental matrix

Operating temperature (inside the heat pipe)	Normal operation (stable performance)	Target q_{max}	Exceed q_{max}
[°C]			
350	v	-	
400	v	-	
430	v	-	
450	v	-	
460	v	v	
480	v	v	
500	v	v	
560	v	v	

4 Results and discussion for the hybrid heat pipe

The amount of data generated in the experiments was considerable, as the data recording was carried out from the beginning to the end of all the experiments. Selected data are reported in Table 4-1. Heat losses are taken into account. The three heat flux values reported in the “Section” columns are for the upper, mid and lower evaporator sections respectively. The heights of the upper and mid sections were 5 cm each, while the effective height of the lower section was only 1,2 cm due to the level of the potassium bath.

Table 4-1 Results

Operating temperature [°C]	Normal operation q (stable performance)		Target q_{\max}		Exceed q_{\max}	
	Section [kW/m ²]	Average [kW/m ²]	Section [kW/m ²]	Average [kW/m ²]	Section [kW/m ²]	Average [kW/m ²]
383	163	194	-	-	-	-
	163					
	451					
403	231	227	-	-	-	-
	231					
	194					
437	46	53	-	-	-	-
	46					
	114					
455	36	42	-	-	-	-
	36					
	99					
461	-	-	394	354	-	-
	-		398			
	-		0			
491	220	197	-	-	-	-
	220					
	0					
500	-	-	340	356	-	-
	-		340			
	-		486			
529	80	95	-	-	-	-
	80					
	221					
569	-	-	-	-	400	145*
	-				400	
	-				30	

*Wick problem at the top of section 2.

Data from some selected “steady state” periods (duration of at least 30 minutes) at different working conditions were selected for further analysis, and are presented here together with some special observations.

4.1 The non-condensable gas volume of the hybrid heat pipe

The volume occupied by non-condensable gas in the hybrid heat pipe at different temperatures was estimated from the theory of Chapter 3.8.1 and experimental measurements.

Experimentally, the interface between the vapour and the non-condensable gas was detected from the temperature measurements in the condenser section. The interface was expected to be associated with a sharp temperature drop from the temperature level of the working fluid vapour to that of the non-condensable gas, as described by Reay et al. [11]. The non-condensable gas of the hybrid heat pipe was assumed to be argon, based on the fact that argon was used as inert gas in the filling process. The amount of non-condensable gas in the hybrid heat pipe was estimated to $5,7 \cdot 10^{-6}$ mol from temperature measurements and interface localization made during experiments. The potassium vapour/non-condensable gas interface could be seen as a drop in temperature in the condenser section as expected.

Utilizing the basic non-condensable gas model presented in Chapter 3.8.1 the total pressure-temperature relationship for the hybrid heat pipe was estimated and plotted, see Figure 4-1. The vapour pressure data for potassium were taken from Appendix E.

The basic non-condensable gas model was also applied to estimate the volume occupied by the non-condensable gas in the hybrid heat pipe at different working temperatures, see Figure 4-2. Even at 500°C the non-condensable gas is seen to occupy about 10% of the volume. The practical implication was reduced capacity of the condenser, and thereby limited operation range for the hybrid heat pipe.

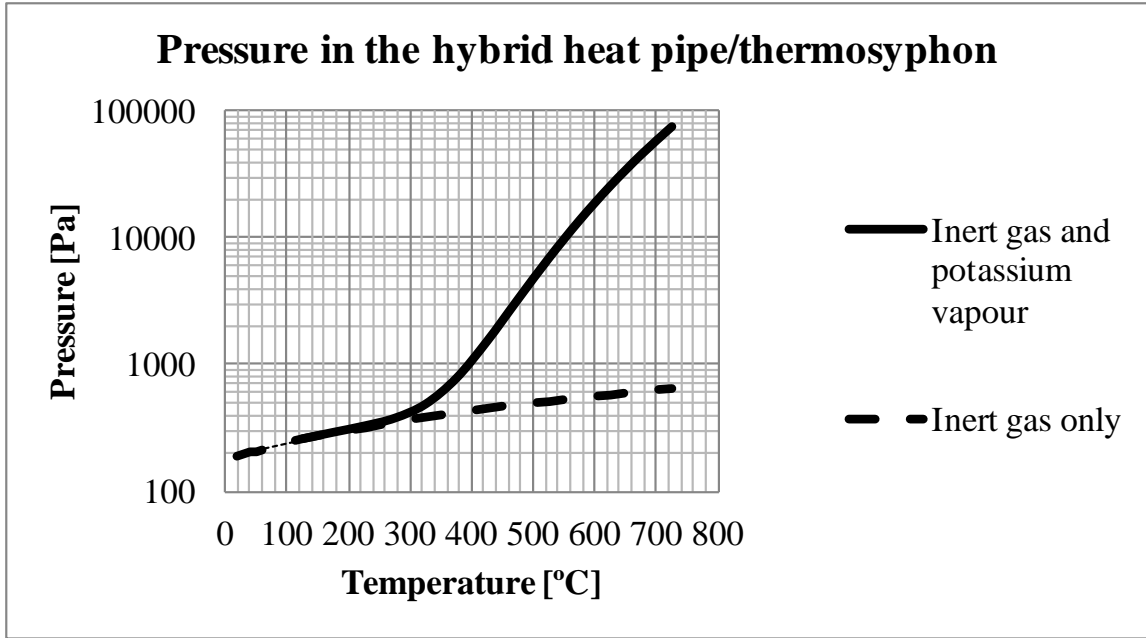


Figure 4-1 Estimated pressure in the hybrid heat pipe

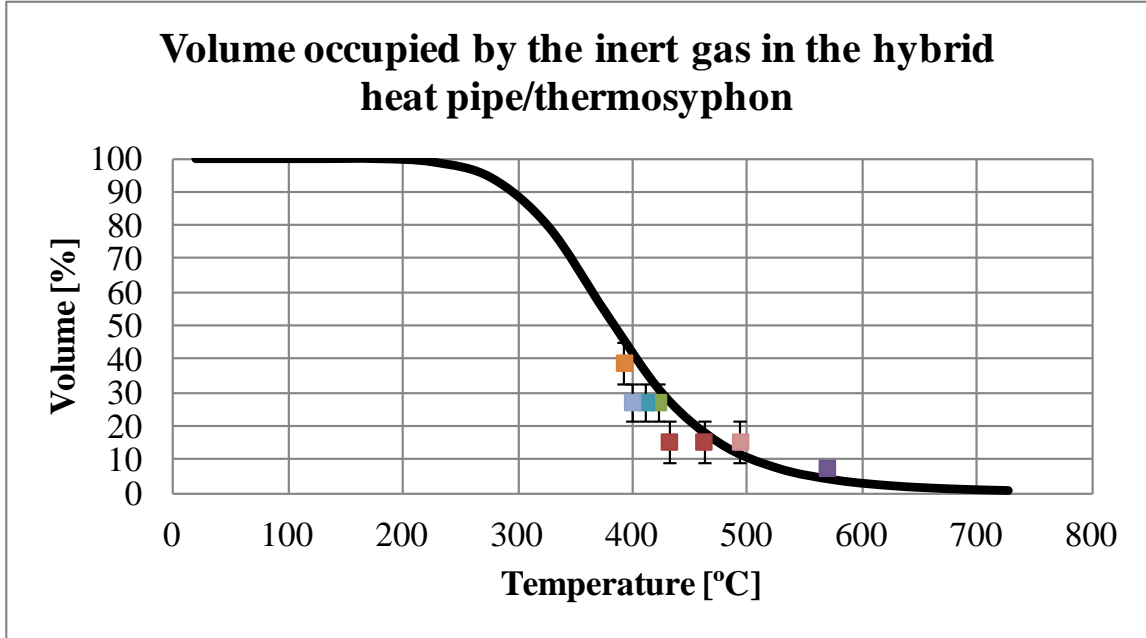


Figure 4-2 Volume of non-condensable (inert) gas at different operating temperatures. Solid line: Model prediction. Square symbols: Experimental data.

The basic model is seen to represent the experimental data quite well, even though the the model is utilizing a sharp interface assumption. The agitation of the real interface by the flowing working fluid, the limited number of thermocouples and temperature transients during the measurements constitute major uncertainties in the experimental determination of the interface. The error bars are only representing the positions of the thermocouples identified to be above and below the interface at the different operating temperatures.

4.2 The overall energy balance

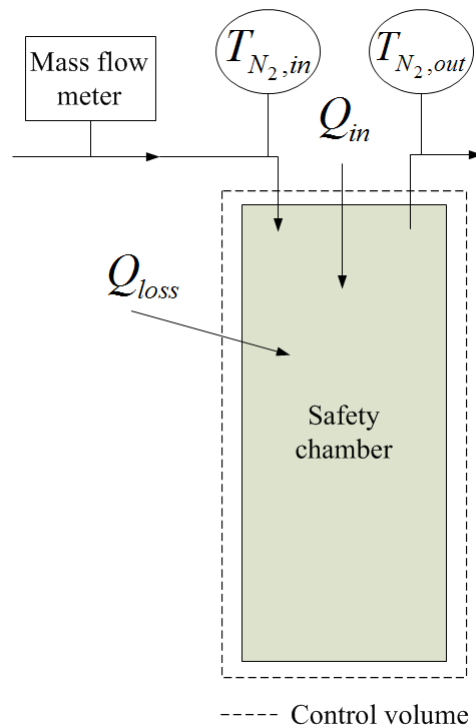


Figure 4-3 The control volume around the safety chamber

With a control volume around the safety chamber, as shown in Figure 4-3, the overall energy balance is:

$$Q_{in} - Q_{loss} - Q_{N_2} = 0 \quad (4-1)$$

The power supplied to the cartridge heaters, Q_{in} , was calculated from measurements of voltage (U) and current (I), according to Equation (4-2).

$$Q_{in} = U \cdot I \quad (4-2)$$

The heat loss to the surroundings, Q_{loss} , was estimated using a COMSOL Multiphysics 2D model, see Figure 4-4 and Figure 4-5, but also calculated from the experiments and the energy balance, Eq. (4-1).

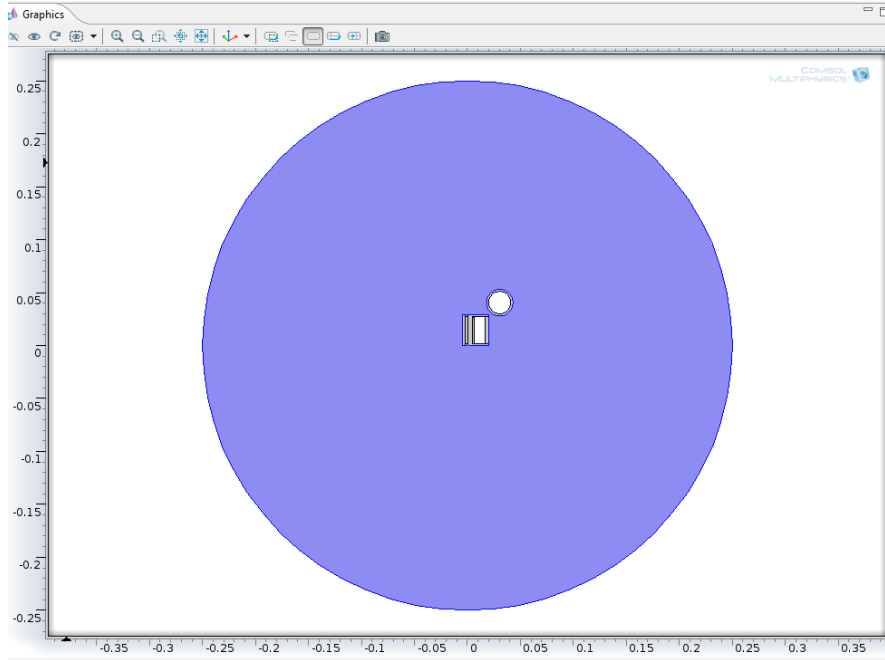


Figure 4-4 The Comsol model of the hybrid heat pipe and the N₂-tube surrounded by insulation in the safety chamber.

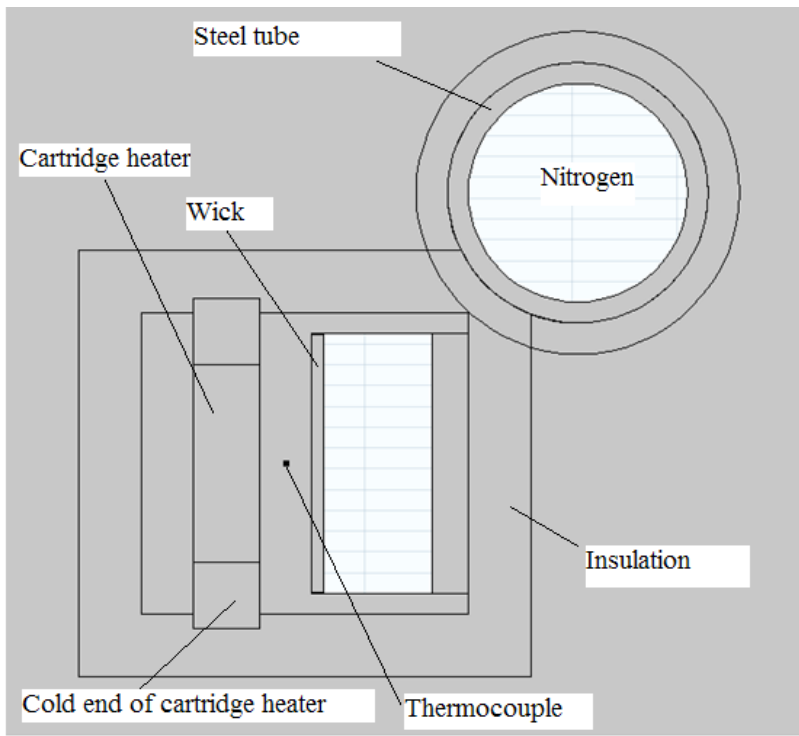


Figure 4-5 Details of the Comsol 2D model.

The heat taken up by the nitrogen cooling gas, Q_{N_2} , was calculated according to Equation (4-3), i.e. from measurements of the nitrogen temperatures in and out of the safety chamber and the measured volume flow of nitrogen converted to mass flow.

$$Q_{N_2} = \dot{m}_{N_2} \cdot c_{p,N_2} (T_{N_2,out} - T_{N_2,in}) \quad (4-3)$$

The heat taken up by the N_2 is shown in Figure 4-6. The experimental data are quite scattered, but the trendline shows clearly that the amount of heat absorbed by N_2 increases for increasing supplied power. The measured heat transfer rates could not have been achieved without evaporation and condensation of potassium inside the hybrid heat pipe. I.e. the plot shows that the hybrid heat pipe actually worked.

The heat taken up by N_2 gas was also estimated utilizing the 2D heat loss model created in Comsol Multiphysics. The fact that the heat losses predicted by the Comsol 2D model were usually smaller than the measured heat losses can partly be attributed to the limitations of the 2D model; the calculated heat losses would have been somewhat larger in a full 3D model. Also, the Comsol 2D model did not include all details as the metal-metal contact points/surfaces between the hybrid heat pipe and the rig.

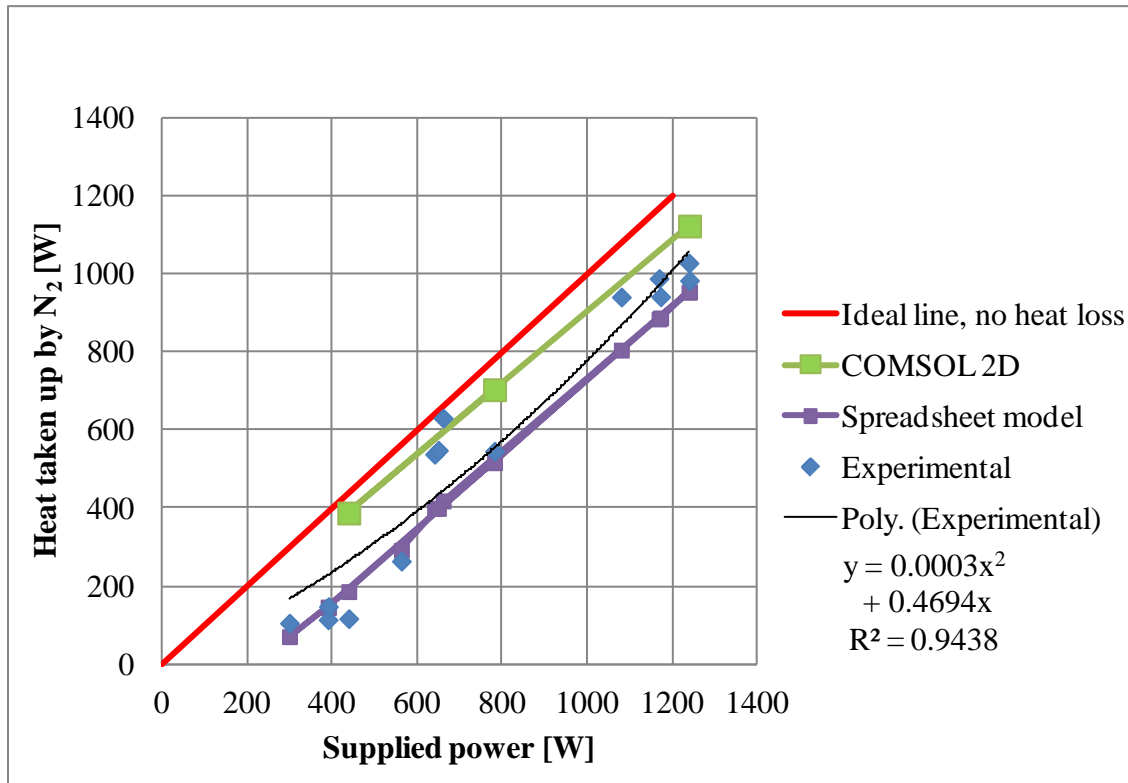


Figure 4-6 Heat taken up by N_2 gas. Temperature in heat pipe as shown in Figure 4-8

The scattering became more apparent when the data were plotted against the operating temperatures, see Figure 4-7. Ideally, one would expect the heat loss to be a linear function of operating temperature, however, it should be remembered that the experiments were run at different heat fluxes. The heat losses calculated by use of Comsol are lower than measured, while the spreadsheet model often overestimates the losses. For the points around 400-600 W supplied power the measurements were obtained 2,6 to 3 hours after startup and it may well be that there was still transient heating of the rig going on for these points. All the other points were measured longer time after startup. Transient heating of the rig would be measured as heat loss. The highest point in Figure 4-7, with a heat loss rate of 321 W, was measured 3 hours after startup.

In hindsight one may also say that the hybrid heat pipe should have been even better insulated, however, this would hardly have been possible without making changes to the design.

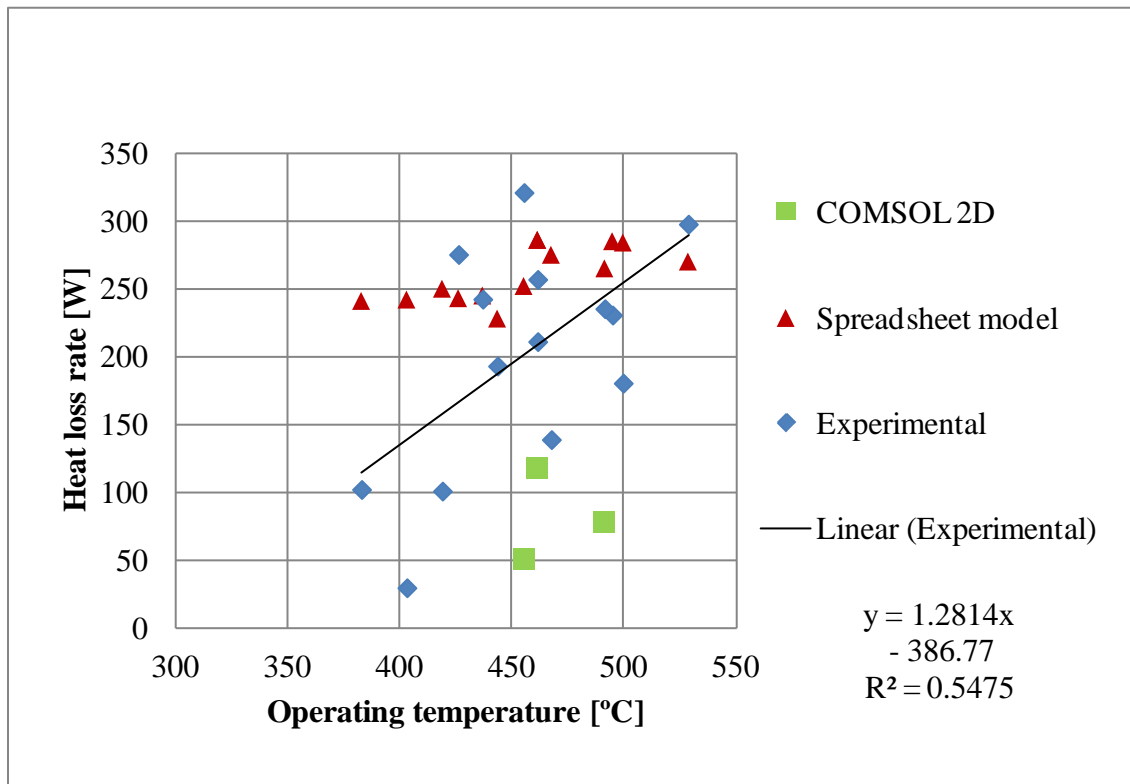


Figure 4-7 The heat loss rate

4.3 Spreadsheet model calculations

The heat transfer in the hybrid heat pipe was analysed by use of the spreadsheet model described in Chapter 3.8.2. The presented calculation results are semi-quantitative. A

precise predictive model for the whole hybrid heat pipe would require a more advanced model (for the description of blowing, suction, vapour retardation, vapour-liquid shear forces, transient effects,...) and less scattered experimental results for the verification of it. However, the plots presented here are useful for understanding trends and indicate the magnitudes of several important physical phenomena taking place inside the hybrid heat pipe. Figure 4-8 shows measured vs. calculated heat pipe operating temperatures, the ideal line which represents the perfect match between measured and calculated values is also plotted as well as a $\pm 10\%$ deviation band around it. Most of the points fall inside the $\pm 10\%$ band, indicating that the model has reasonable predictions for the operating temperature.

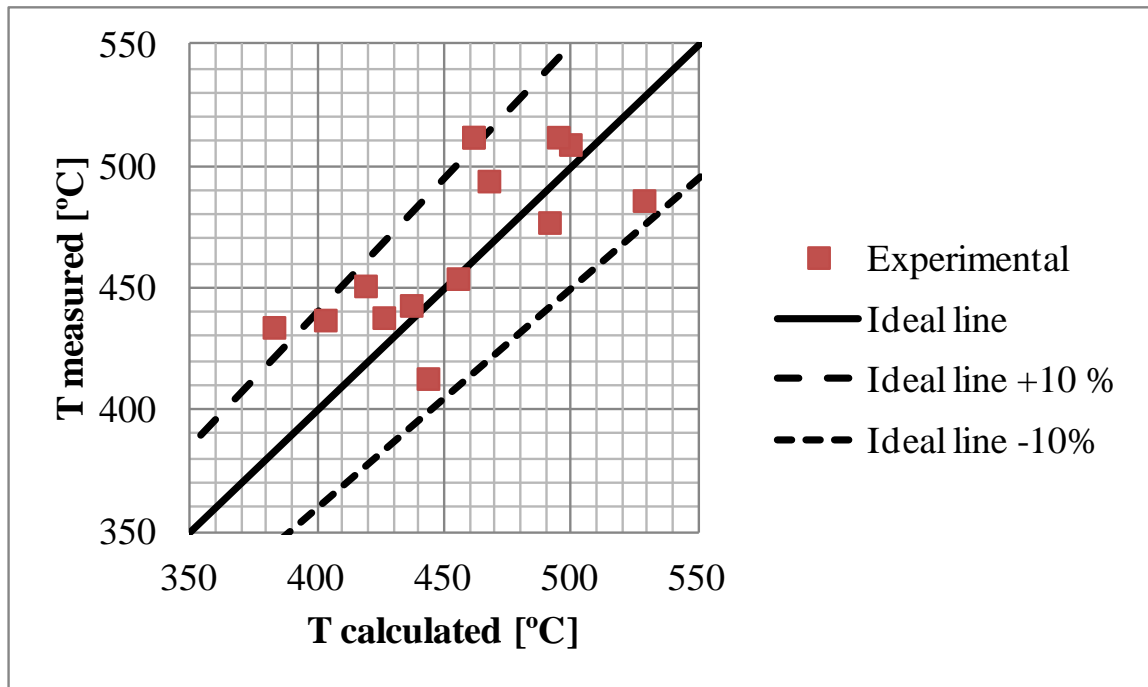


Figure 4-8 Measured and calculated heat pipe operating temperatures

Case 500°C:

A case-study was carried out by use of the spreadsheet model in order to see the magnitudes of some key parameters for the fluid flow inside the hybrid heat pipe. In this case 150W, 500W and 500W were supplied to the lower-, middle- and upper- evaporator section respectively, leading to a predicted working temperature of approximately 500°C. Under these conditions the relative magnitudes of the thermal resistances were as shown in Figure 4-9.

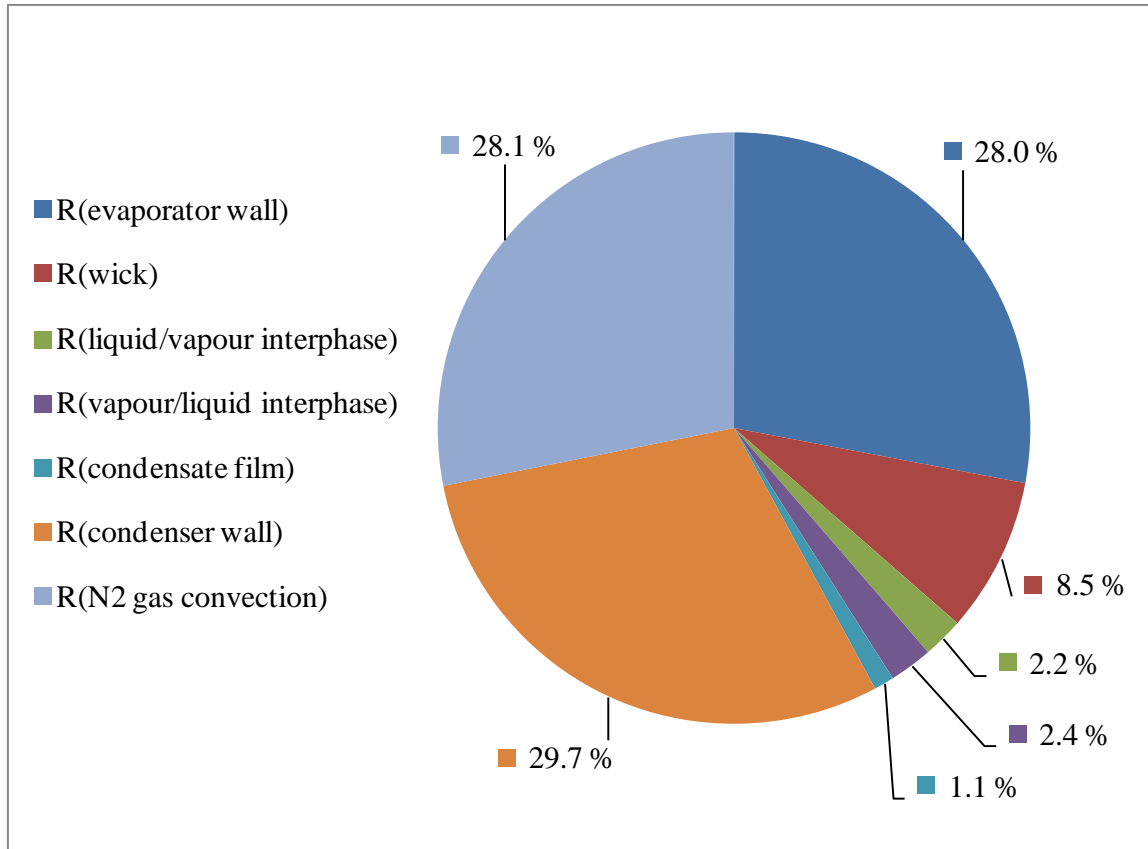


Figure 4-9 Thermal resistances [K/W] calculated for “Case 500°C”.

The thermal resistances of the heat pipe walls and the N₂ gas convection constitute the largest parts of the pie. Thereafter come the resistance of the wick, the resistance of the liquid/vapour and vapour liquid interfaces, and finally the resistance of the condensate film.

The axial Mach number, the axial Reynolds number, the momentum flux and the frictional pressure drop for the vapour flow in the “Case 500°C” are discussed below. Several plots show a jump at height 0,15 m, this is simply due to the change in the cross sectional area of the flow channel which occurs at the end of the wick.

The Mach number

The Mach number (Ma) is defined as the “ratio of velocity to speed of sound” [69]. Fluid flow is usually classified as incompressible when $Ma < 0,3$ and compressible for higher Mach numbers. The Mach number was calculated for the flow of potassium vapour in the hybrid heat pipe. The maximum Mach number was expected to occur at the end of the evaporator. During startup from room temperature the Mach number in potassium heat pipes can exceed the sonic limit ($Ma=1$) [21], due to the very low vapour density of potassium. This is, however, no serious problem because the Mach number will decrease as the temperature and potassium vapour density increases. It was therefore most interesting to consider what would be the Mach number under normal working

conditions, in particular at the lowest working temperatures. Figure 4-10 shows the axial Mach number for the 500°C case. With regard to lower temperatures calculations indicated that $Ma=0,3$ was just exceeded in the hybrid heat pipe for operating temperatures around 400°C. Consequently the assumption of incompressible flow is acceptable in the calculations.

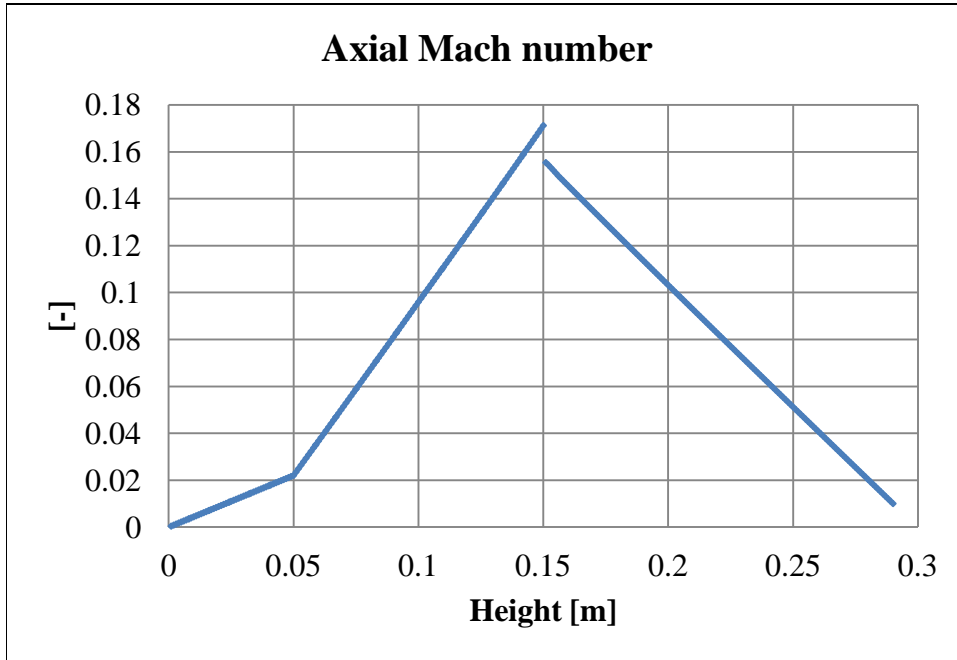


Figure 4-10 The Mach number for the 500°C case

Axial Reynolds number

Figure 4-11 shows the axial Reynolds number for the vapour, and indicates that the flow is laminar. The hydraulic diameters of the evaporator and condenser were used as characteristic lengths in the calculations.

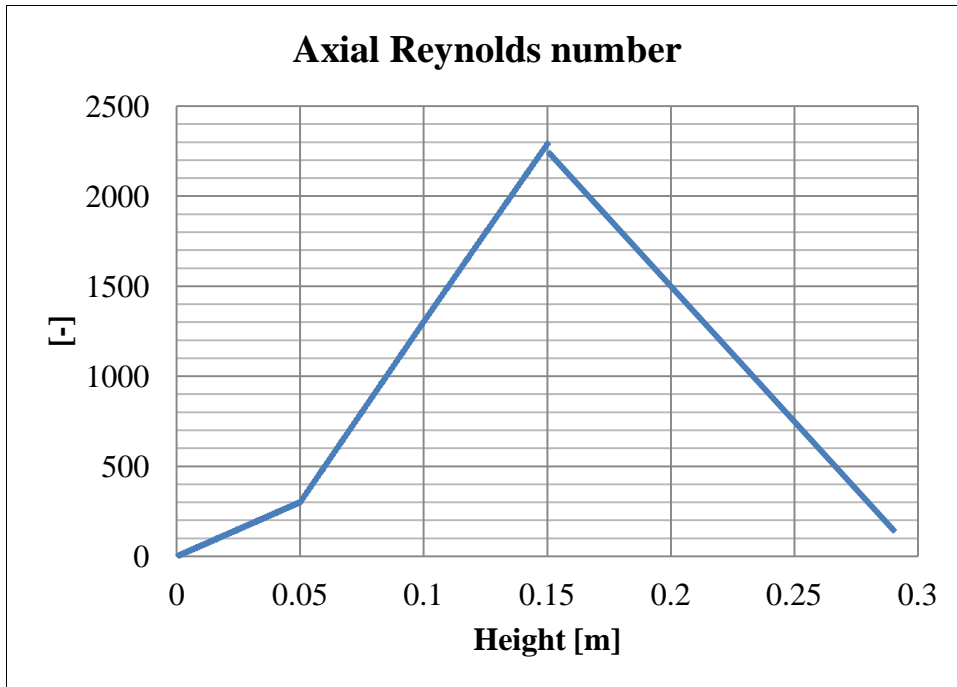


Figure 4-11 The axial Reynolds number for the 500°C case

Momentum flux

Figure 4-12 shows the momentum flux of the vapour flow in the 500°C case when 100% pressure recovery was assumed for simplicity, however, the real pressure recovery is probably less [11, 84]. The vapour static pressure of potassium is approximately 4161 Pa at 500°C, i.e. in this case the pressure variations due to the acceleration and retardation constituted about 4,3% of the vapour static pressure which corresponds to about 2,5 K variation of the saturation temperature.

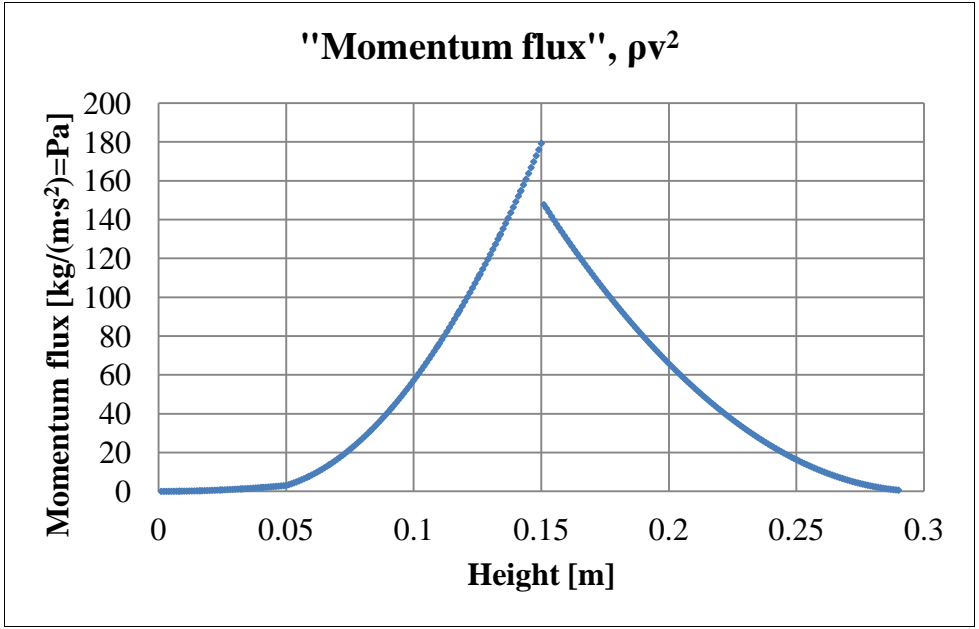


Figure 4-12 The momentum flux for the 500°C case

Frictional pressure drop of the vapour flow

Figure 4-13 shows the cumulative frictional pressure drop of the vapour flow in the 500°C case. The frictional pressure drop of 20 Pa from the saturation pressure 4161 Pa at 500°C would lower the saturation temperature about 0,3 K.

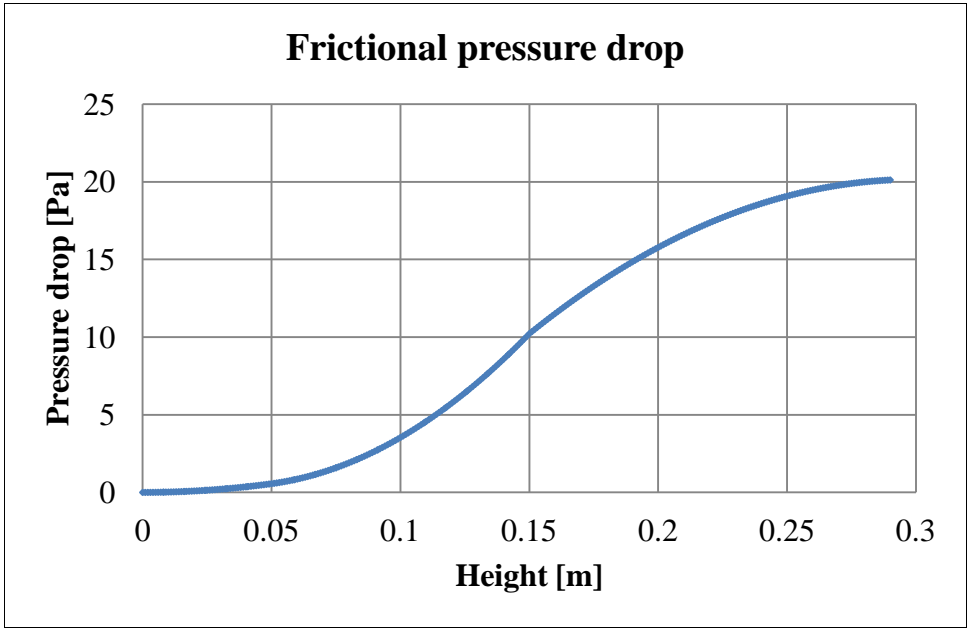


Figure 4-13 Frictional pressure drop for the 500°C case

The frictional pressure drop is small compared to the momentum flux of Figure 4-12, and both the frictional pressure drop and the momentum flux variation correspond to insignificant variations in saturation temperature for this study.

4.4 The wick performance

Successful operation of heat pipes and thermosyphons require effective wetting of the heated surface by the working fluid condensate. In the hybrid heat pipe a wick distributed the condensate over the heated surface. The main intention of the experimental program was to determine the operating limits of the wick under realistic working conditions (i.e. high temperatures and utilizing potassium working fluid). The performance of the wick under realistic working conditions was compared to performance data predicted from wick data acquired from rate-of-rise experiments at room temperature using the model fluid heptane.

4.4.1 Wick failure conditions

The maximum capacity of the wick was investigated by increasing the heat flux of the evaporator in small increments. Dryout at the top of the wick was expected to be the first sign of overload. The dryout was expected to be seen as a rapid increase in the temperature measured in the wall at the top of the wick. What actually was observed, after increasing the heat flux stepwise up to levels above the predicted limit, was a rapid increase in the temperature in the wall at the top of the middle evaporator section, i.e. not at the top of the wick. This indicated that there could be a contact problem between the wick and the evaporator surface at that point. At constant heat flux the peak in temperature was stationary. The temperatures measured in the 15 cm high wick-covered evaporator wall before and during the local dryout are shown in Figure 4-14. The stationary dryout situation was modelled in Comsol Multiphysics, and is also plotted in Figure 4-14. The peak was reproduced in the calculation when the cooling was removed from a 16 mm vertical section of the wick, from height 0.0813 m to 0.0973 m in Figure 4-14 (i.e. the top of the 16 mm unheated part was 2 mm below the top of evaporator section 2). This led to the conclusion that the loss of cooling leading to the temperature peak was a local phenomenon, occurring at about 14% of the wick total height for the applied heat flux. However, the peak extended in the vertical directions when the heat flux was increased further. The hot spot situation in Figure 4-14 occurred at an average heat flux of about 406 kW/m^2 for the 112 mm effective wick height, 17,6% heat loss to the surroundings taken into account.

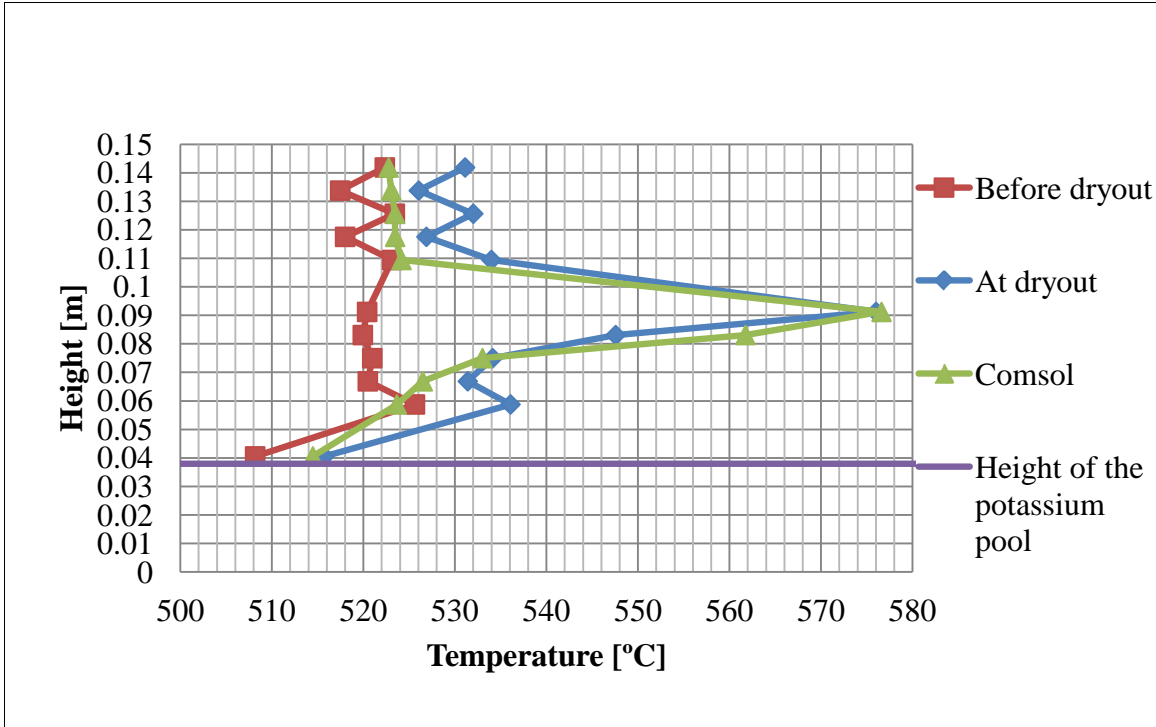


Figure 4-14 A dryout situation

The zig zag distribution of the experimental points in Figure 4-14 was due to the different positions of the thermocouples relative to the cartridge heaters, see Figure 3-18; the high temperatures were measured straight in front of the cartridge heaters.

With the power available from the cartridge heaters it was not possible to reach a dryout situation by supplying heat to the two upper sections alone, as shown in Figure 4-15; the wick problem described in Figure 4-14 occurred first when heat was added to the lower section (section 3).

For the effective wick height of 112 mm the maximum uniform heat flux obtainable by supplying heat to the two upper sections only was about 363 kW/m^2 (average for the whole wick), 17,6% heat loss to the surroundings taken into account.

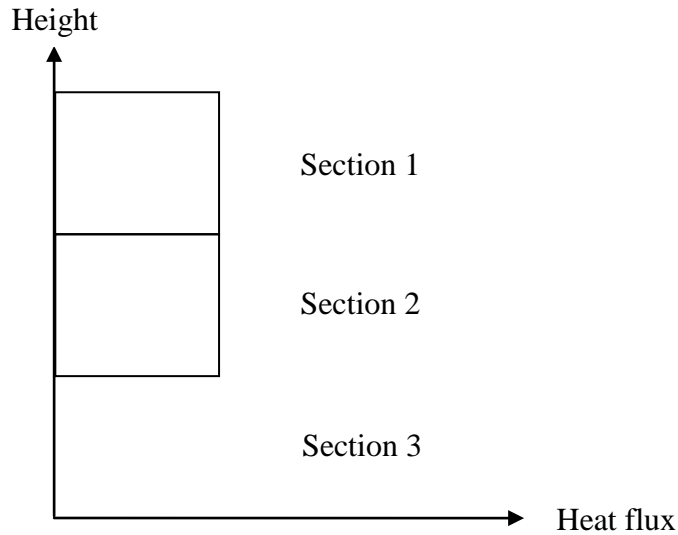


Figure 4-15 Heat supplied to the two upper sections only

4.4.2 Wick performance with potassium

For the wick of the hybrid heat pipe the permeability and effective pore radius were determined to $73 \cdot 10^{-12} \text{ m}^2$ and $50,8 \cdot 10^{-6} \text{ m}$ (for potassium) respectively.

The maximum uniform heat flux before dryout was given by Equation (2-19).

The pool of potassium covered about 38 mm of the wick, so the maximum wick height, from which evaporation occurred, was about 112 mm. The theoretical capacity for this height is shown in Figure 4-16, taking the capillary and static pressure limitations into account.

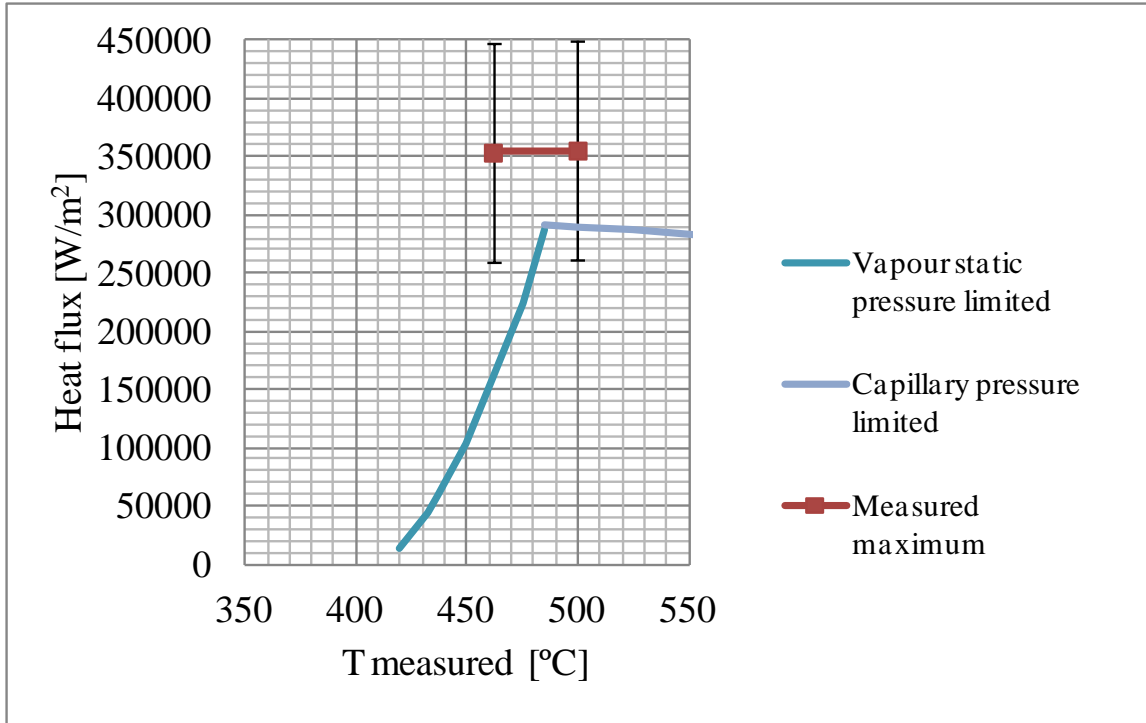


Figure 4-16 Theoretical performance and experimentally determined points

Experimental points from the measurements on the hybrid heat pipe are also shown in Figure 4-16. The wick failure reported in Chapter 4.4.1 occurred if the heat fluxes were increased above the measured maximum values. The measurements show that the hybrid heat pipe was able to operate at working conditions outside of the expected operational limit defined by the vapour static pressure limitation. The vapour static pressure limitation was expected to limit the performance of the hybrid heat pipe drastically, as shown in Figure 4-16.

If the permeability of the wick was higher than the permeability estimated from rate-of-rise experiments using heptane, the observed differences between predicted and measured capacities with potassium would be justified. The discrepancy between the theoretical and actual performance limitation is further discussed in the following.

The difference between the theoretical performance and the measured maximum for the temperature 461°C in Figure 4-16 is of most interest, because at this temperature there is a difference even when the experimental uncertainty is taken into account. In order to obtain a theoretical maximum heat flux of 258700 W/m² (which is the lower value of the error bar) the permeability would have to increase from 73·10⁻¹² m² to 124·10⁻¹² m². The increase in permeability could have been caused by a high permeability channel:

The channel hypothesis

The permeability enhancement indicated by the hybrid heat pipe experiments could have been caused by a channel/gap in the wick or between the wick and the container wall, created by thermal expansion, stress and strain. Such a channel is shown (exaggerated) in Figure 4-17, which illustrates the cross section of the hybrid heat pipe evaporator section.

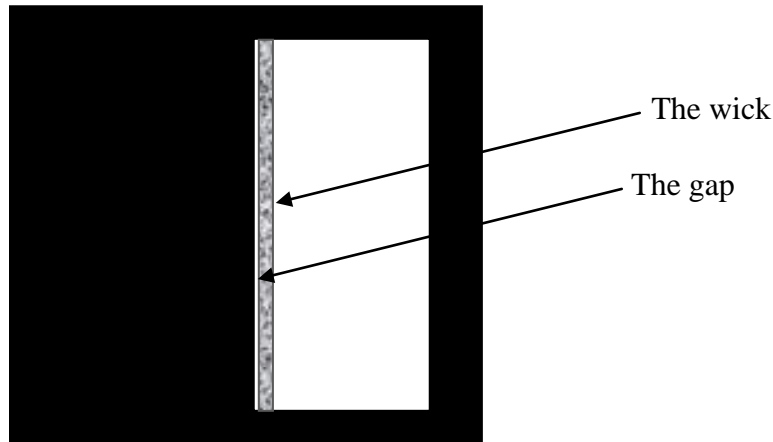


Figure 4-17 A small channel/gap between the wick and the evaporator surface

In order to have an estimate of the size of such a channel it was assumed that it was a rectangular channel of the same width as the wick. The permeability of a rectangular channel was derived from Darcy's law and the expression for the pressure drop in a rectangular tube. Assuming fully developed laminar channel flow in the gap, using a friction coefficient $f=96/Re$, the total flow resistance in the wick including the gap is:

$$\frac{1}{R_{flow,total}} = \frac{1}{R_{flow,wick}} + \frac{1}{R_{flow,channel}} \quad (4-4)$$

with:

$$R_{flow,wick} = \frac{1}{\kappa_{wick}} \quad (4-5)$$

and

$$R_{flow,channel} = \frac{1}{\kappa_{channel}} = \frac{f \cdot Re_{D_h}}{2D_h^2} \quad (4-6)$$

The thickness, a , of the channel can then be determined from for a fixed width, b , and known permeability.

It was found above that the measured heat flux at 461°C would require the total permeability to increase from $73 \cdot 10^{-12} \text{ m}^2$ to $124 \cdot 10^{-12} \text{ m}^2$. This would correspond to having a channel of approximately $25 \cdot 10^{-6} \text{ m}$ thickness in parallel to the wick, along the entire wick length. The existence of such a channel is realistic if some of the welding spots which attach the wick to the evaporator surface were damaged by thermal strain and stress.

The effect of evaporation on the effective pore radius

Shirazy and Fréchet [85] recently found that the effective pore radius decreased due to meniscus recession during evaporation. A smaller effective pore radius leads to higher theoretical capillary limit, and this may at least in part explain unexpected high performance in the temperature range where the capillary pressure is the driving pressure. Shirazy and Fréchet [85] reported 52% decrease of the effective pore radius for a sample of 82% porosity. This can not explain how the performance of the hybrid heat pipe could exceed the vapour static pressure limitation. However, there is no conflict between this proposed effect of evaporation and the channel hypothesis, so it may well be that both occurred in the hybrid heat pipe.

4.4.3 Extrapolated performance data for nickel foam wicks

The measured wick capacity using potassium as working fluid was higher than predicted from the ideal models for a similar system for temperatures up to ca. 500°C. This fact encouraged some extrapolations; what would theoretically be the performance limits of a thicker and/or longer wick? With regard to thickness, presuming the same degree of compression of the individual foam layers, the capacity is directly proportional to the wick thickness; double wick thickness means double capacity. In Figure 4-18 the capacity has been calculated for different wick heights, using the hybrid heat pipe wick properties and potassium as working fluid at an operating temperature 500°C. Increased wick thickness can increase the probability for boiling in the wick, however, this is more likely to be a problem when working fluid has low thermal conductivity. For high conductivity working fluids, like potassium, the heat will be more easily conducted through the saturated wick, and evaporation will take place at the liquid surface.

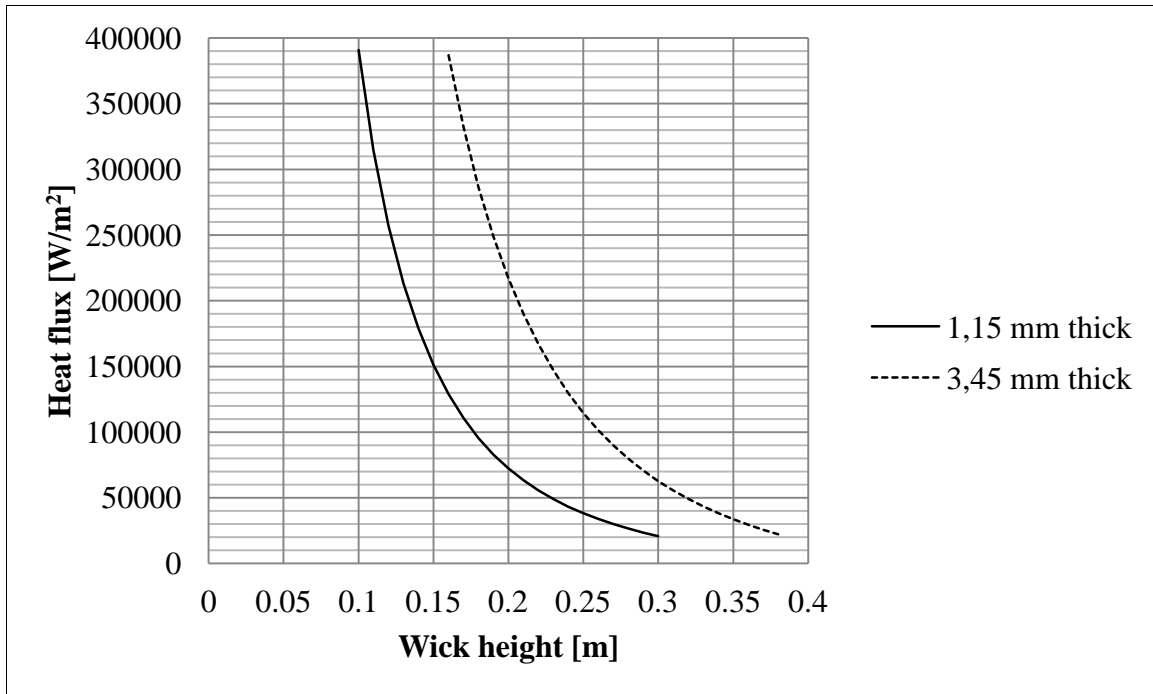


Figure 4-18 Theoretical uniform heat flux capacity as a function of height, potassium working fluid

During steady operation the heat flux from an aluminium electrolysis cell is about 20 kW/m². The 1,15 mm thick wick in the present experimental study can, according to Figure 4-18, handle such a uniform steady heat flux up to 30 cm height. However, at this maximum limit there is no capacity left to handle hot spots. If the thickness of the wick was increased to 3,45 mm the maximum height would increase up to about 38 cm, and the average capacity of a 300 mm high wick would be 60 kW/m², i.e. leaving some margin for uneven heat flux distribution and/or hot spots, as shown in Figure 4-18. Increasing the wick thickness would also increase the thermal resistance of the wick.

4.5 An evaluation of some operating limits from Chapter 3.2.2

4.5.1 The startup

Large temperature differences, up to 300 K, were measured between the evaporator and the condenser ends during startup of the hybrid heat pipe. A visualisation of the temperature distribution in the hybrid heat pipe was generated in LabView[®] from the measured temperatures, see Figure 4-19. The actual figure is a snapshot taken during startup, red colour indicates high temperature (in this case $\approx 350^{\circ}\text{C}$), and blue colour low temperature (in this case $\approx 100^{\circ}\text{C}$).

3D View

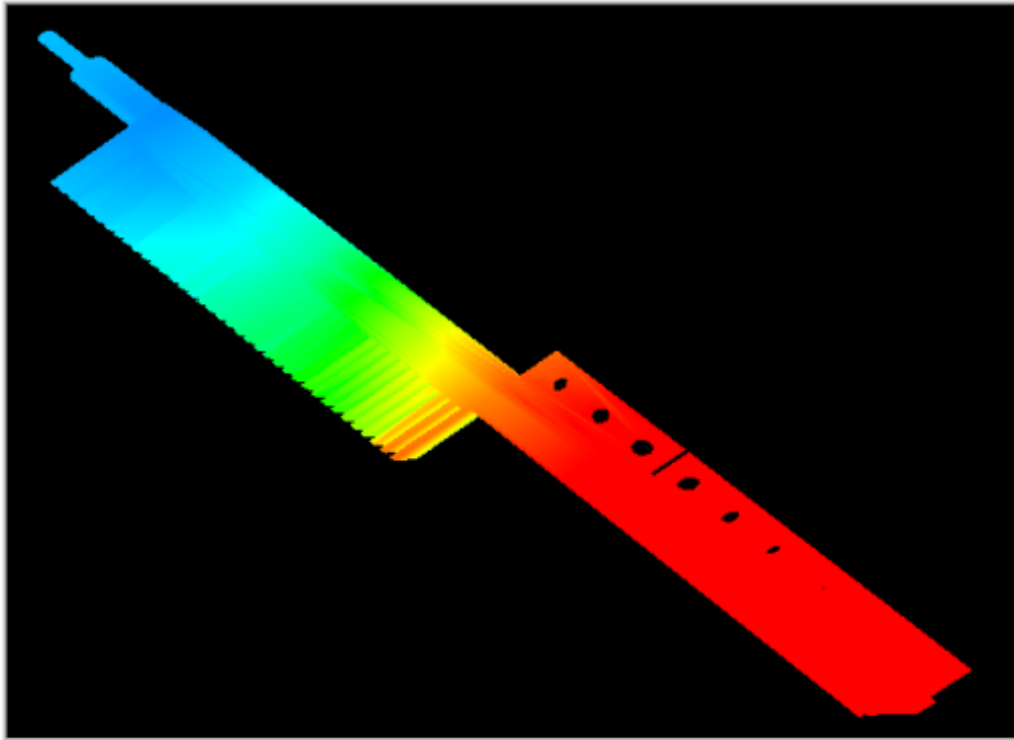


Figure 4-19 Measured startup temperature visualisation using LabView[®]. (Blue \approx 100°C Red \approx 350°C)

The considerable temperature differences during startup occurred despite of the high thermal conductivity of the nickel walls. Probable reasons were:

- The low vapour pressure of potassium reduced the heat transfer capacity at the lowest temperatures (the continuum flow limit).
- There was a cold non-condensable gas volume in the condenser region.
- The flow of vapor from the evaporator to the condenser is caused by the pressure difference, which is very small during the startup of alkali metal heat pipes. The minimum pressure at the condenser end would theoretically be zero, but with non-condensable gas present in the condenser the pressure difference between the evaporator and condenser is reduced [86]. When the pressure difference is very small it is not sufficient to overcome the flow friction (the viscous limit).
- The sonic limit would have small influence on the startup of the hybrid heat pipe because with the adopted startup procedure the evaporator heat flux (and temperature) was increased regularly, so the sonic limit would simply be overrun.

- High temperature difference between the evaporator and the condenser during startup may also indicate that the flow of condensate back to the evaporator was slowed down or prevented by the high velocity low density vapour [11].

Despite of the limitations above the startup of the hybrid heat pipe went smooth, so the influence of the limits was to slow down the startup, not to impede it. It should also be noted that the heat flux was increased slowly in small steps, in order to avoid mechanical damage from rapid thermal expansions.

The frozen startup limitation was avoided in the present study by prewarming of the condenser. The prewarming was carried out by passing hot nitrogen gas over the condenser fins until the temperature of the condenser section was around the melting point of potassium (63,7°C). The remaining heating of the hybrid heat pipe up to the desired working temperature was carried out by use of the heater cartridges.

The melting of the potassium pool was clearly observed as a temporary flattening of the temperature curves in the lower part of the evaporator; the average temperatures in the 3 evaporator sections (Figure 3-18) during the potassium melting are plotted in Figure 4-20.

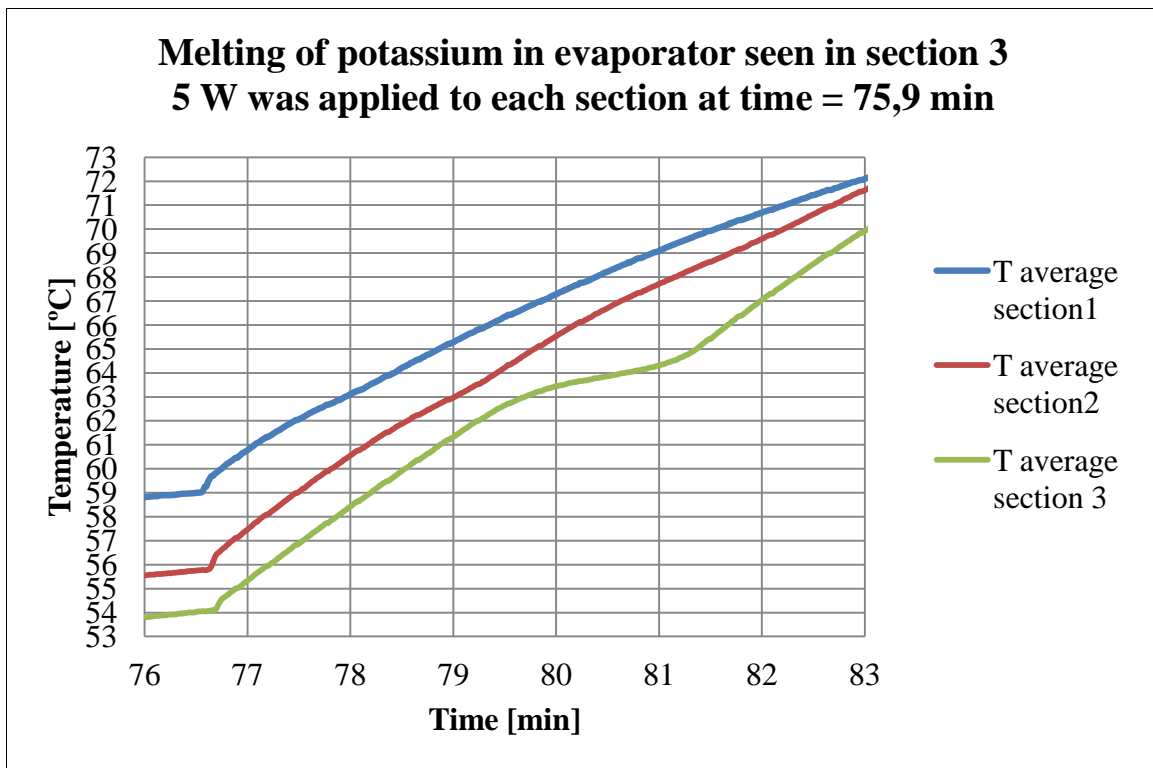


Figure 4-20 Temperatures recorded during the melting of the potassium. Section numbers refer to Figure 4-22.

The temperatures measured in the evaporator wall above the potassium pool became uniform quite quickly after the melting of the potassium, indicating that the potassium in the wick was at saturation temperature.

When uniform heat flux was applied over the three evaporator sections, the average temperature of the lower evaporator section was in general higher than the average temperature of the upper two evaporator sections. This was caused by the pool of liquid potassium; the heat transfer by potassium liquid convection in the pool, and subsequent evaporation from the pool could not compete with the heat transfer capacity of the wick.

4.5.2 Nucleate boiling

The boiling limitation

Equation (3-38) is plotted in Figure 4-21 for the wick using potassium as working fluid. The effective pore radius with potassium, $50.8 \mu\text{m}$, was used as the radius of the meniscus, r_{men} , at the wick surface.

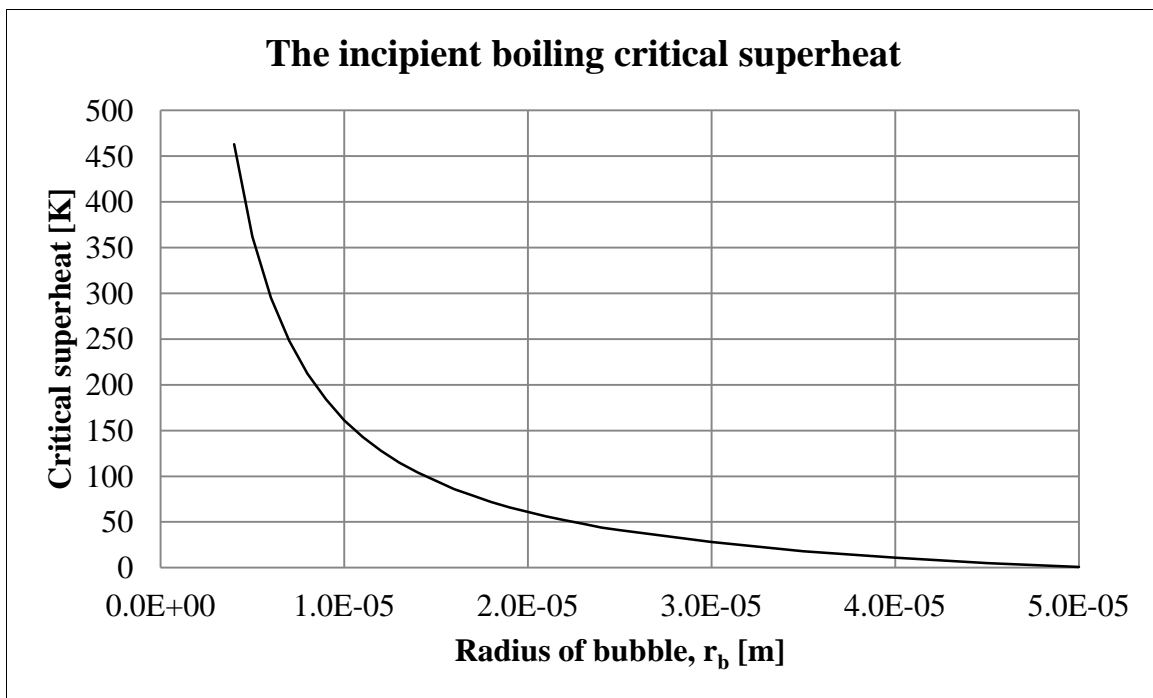


Figure 4-21 Incipient boiling critical superheat

The most difficult part of the boiling analysis is to predict the bubble radius causing boiling incipience. Alkali metals are generally associated with high incipient boiling superheats, but exceptions have been reported. With sodium as working fluid an artificial cavity having a radius as large as $200 \mu\text{m}$ was reported active [9]. The physical pore radius of the wick in the current study, estimated from the initial pore size and degree of compression, was about $49 \mu\text{m}$. The surface of the evaporator was initially machined smooth, so the only major surface roughness would be the welding spots.

Nucleate boiling in the hybrid heat pipe

Nucleate boiling was obtained in the liquid bath of potassium at the bottom of the hybrid heat pipe by supplying heat only to the lower sections (2 and 3), see Figure 4-22. Figure 4-23 shows the three temperatures (T28SK, T29SK and T30SK) measured in the evaporator wall beside the liquid bath during “stable oscillating” boiling.

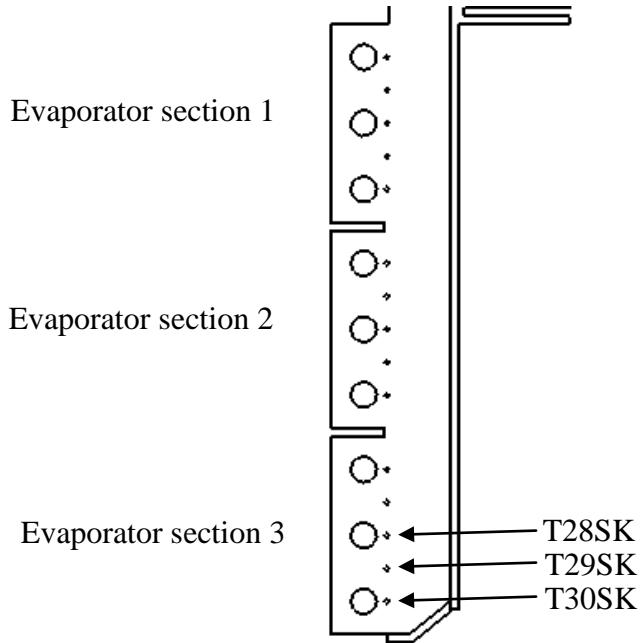


Figure 4-22 Thermocouple locations

The differences between the three temperatures can be partly explained by the fact that the lower cartridge heater was defect. Thermocouple T30SK located right in front of the lower defect cartridge heater was measuring the lowest temperatures.

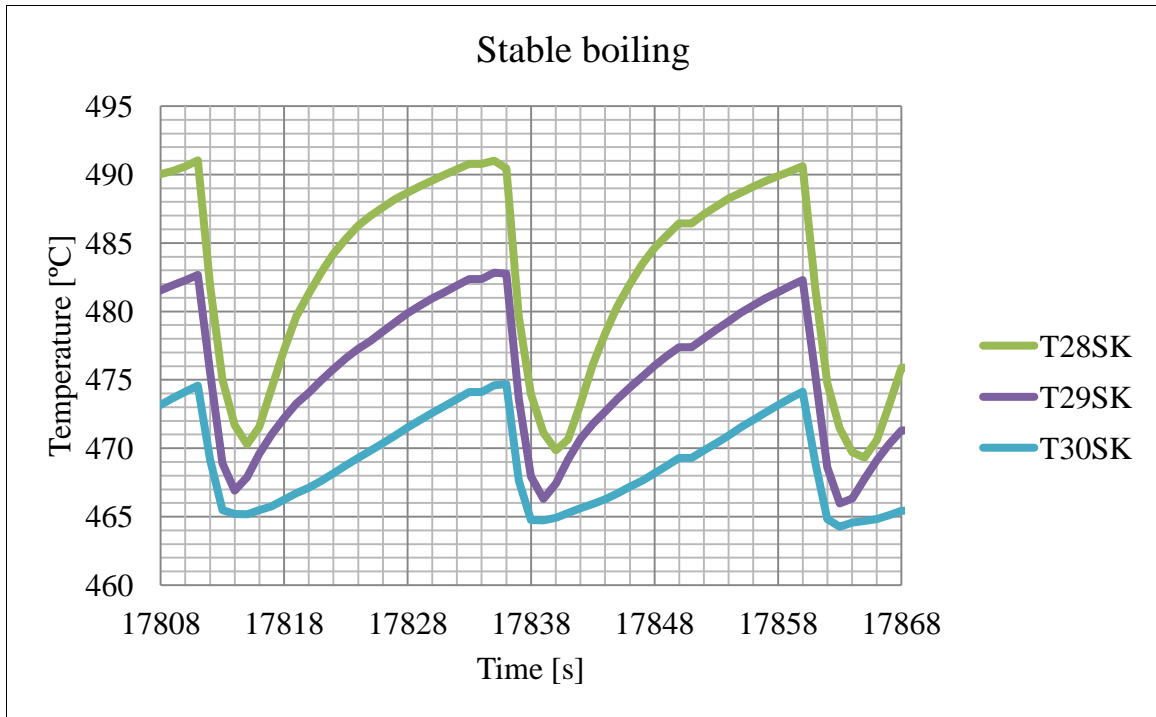


Figure 4-23 Temperatures measured during stable oscillating boiling

Basic models developed for the cyclic heating and rapid bubble growth period (Figure 2-3) are enclosed in Appendix A. In Figure 4-24 the models are plotted together with the average of the wall temperatures T28SK, T29SK and T30SK. The general trends of the models are reproducing the trends of experimental results well. The deviations between the models and the experimental results may be due to the following simplifying assumptions and non-ideal experimental conditions:

- The bath and the walls were assumed to have the same (lumped) uniform temperature.
- The supplied heat flux was assumed uniform, but was nonuniform due to a defect lower heater cartridge as seen in Figure 4-23.
- Geometrical simplifications were made related to the inclined bottom of the hybrid heat pipe.
- It was assumed that the rapid boiling took place during 1 second.

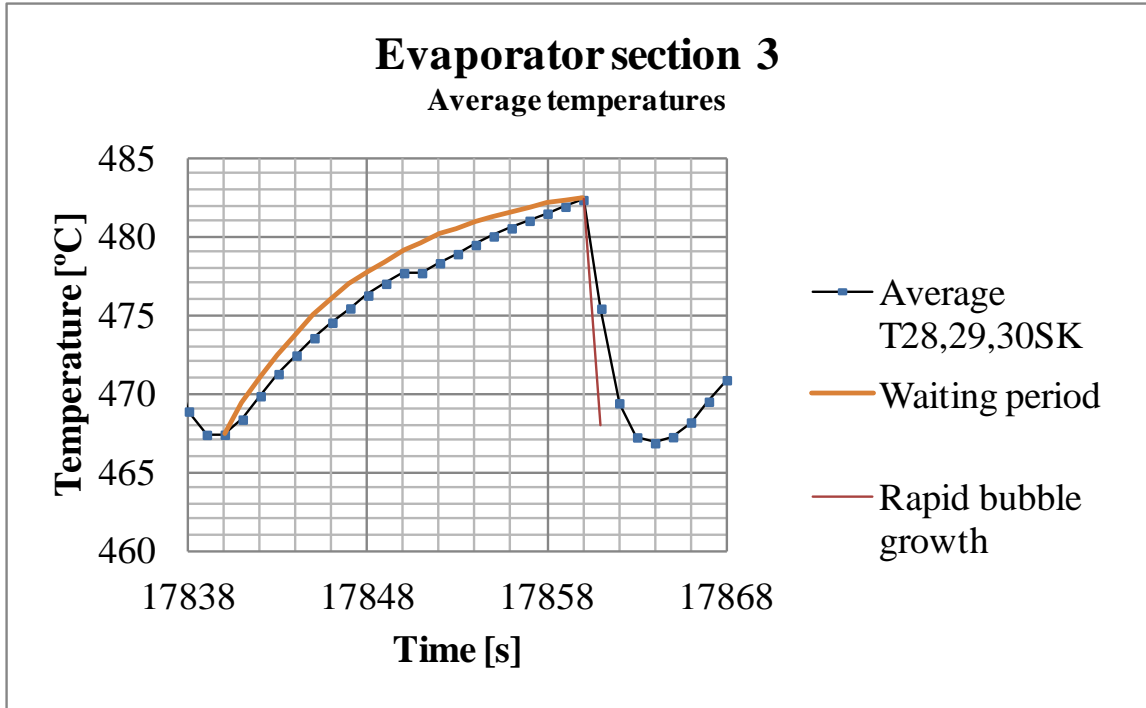


Figure 4-24 Experimental values and mathematical modelling

Incipient boiling superheat

The incipient boiling superheat (defined by Equation (2-2)) was determined from the temperature measurements of Figure 4-25, and the corresponding cavity radius was estimated by use of Equation (2-2). For comparison the incipient boiling superheat was estimated from the pore size of the wick. The physical pore radius of the wick was 49 μm (when assuming isotropic compression of the nickel foam). The interfacial tension of the potassium was taken at the saturation temperature. The results are presented in Table 4-2.

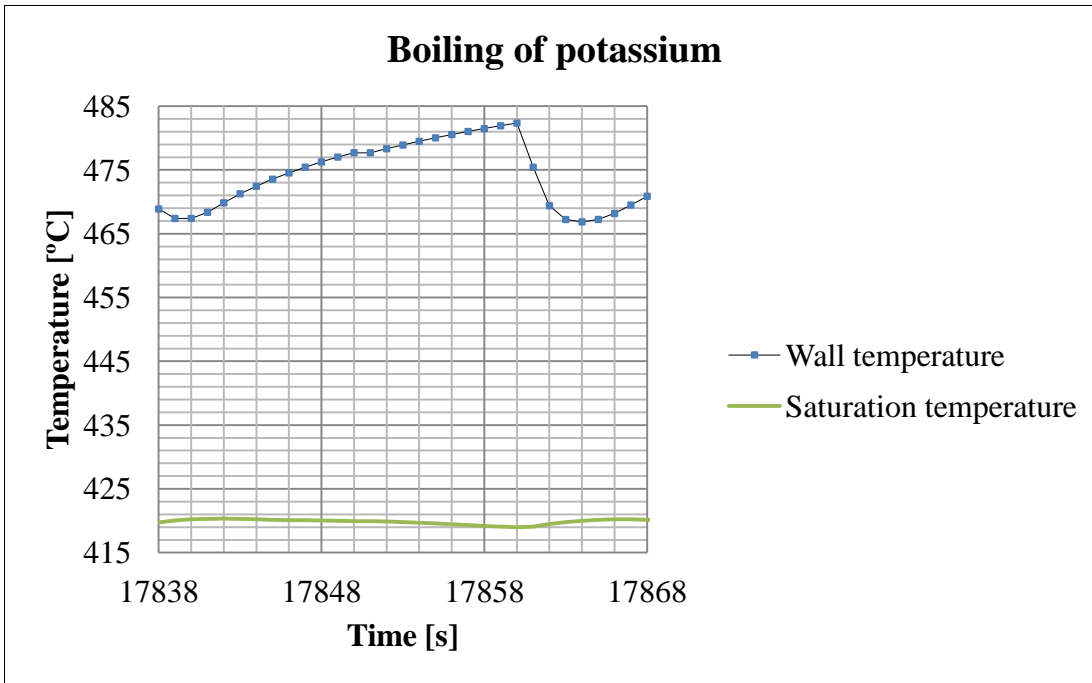


Figure 4-25

From Table 4-2 one can see that the cavity radius calculated from the data of Figure 4-25 was quite close to the radius estimated for the wick, the difference was only 16%. Similarly, of course, the incipient superheat calculated from the radius of the wick was quite close to the measured superheat. This indicates the usability of the basic models, despite assumptions and simplifications.

Table 4-2

	From Figure 4-25	From data for the wick	Difference
T_{wall}	483 °C		
T_{sat}	420 °C		
$T_{\text{wall}} - T_{\text{sat}}$	63 K	73 ± 5 K	16 %
Effective bubble radius	57 μm	49 μm	16 %

The unstable behaviour of potassium boiling predicted through pre-experimental calculations was confirmed by the experiments. The boiling of potassium was characterized by:

- Long waiting times.
- High incipient boiling superheat.
- Large fluctuations in temperature during the boiling cycle.

When stable evaporator and/or condenser temperatures are important it is far better to operate the hybrid heat pipe as a heat pipe rather than as a pool boiling cooler unit (thermosyphon).

4.6 Potassium as working fluid below 500°C

The hybrid heat pipe operated as intended (without problems) at temperatures below the useful range 500-1000°C reported in the literature. The large volume occupied by the non-condensable gas, as shown in Figure 4-2, was the only problem experienced below 500°C. The amount of non-condensable gas could be reduced by improved routines for the cleaning and filling of the hybrid heat pipe. An additional volume for the non-condensable gas, connected to top of the condenser, could also have reduced the influence of the non-condensable gas.

5 Conclusions and recommendations for future work

The hybrid heat pipe concept utilizing potassium working fluid and a wick of sintered compressed nickel foam on the evaporator surface is capable of handling the specified steady state and peak heat fluxes expected in the sidelinings of aluminium electrolysis cells, provided that the maximum wick height is not exceeded. The wick maximum height depends on the wick thickness and the peak (hot spot) heat flux criteria, and is for the system in the current study typically in the range 150-300 mm. In order to be able to cool larger heights a modular system of several wicks/heat pipes may be implemented.

Despite of the relatively high thermal conductivity of nickel, and the internally nearly isothermal conditions in the hybrid heat pipe, the unilateral heat flux causes asymmetric thermal expansion (bending) of the hybrid heat pipe. Clever design is required in order to ensure that the asymmetric thermal expansion does not cause thermal contact problems inside or outside of the hybrid heat pipe. Inside the heat pipe this means a robust method for attaching/pressing the wick to the evaporator surface.

The temperature difference between the evaporator and the condenser ends was more than 200 K during the startups of the hybrid heat pipe. From a general material/mechanical point of view such large temperature differences/gradients can cause mechanical damage, however, no damage was detected after more than 15 startups in the current study. In the test rig the hybrid heat pipe had some freedom to expand; the heat pipe would probably have been more vulnerable for mechanical damage if it was tightly fixed at both ends.

The hybrid heat pipe proved ability to operate at heat fluxes above predictions. With potassium working fluid the hybrid heat pipe offered uniform evaporator and condenser temperatures, except from a temperature drop at the top of the condenser due to the non-condensable gas. The hybrid heat pipe worked nicely also at operating temperatures below 500°C; the only problem was that the volume occupied by the non-condensable gas increased with decreasing operating temperature and reduced the capacity of the condenser. A potential future improvement is to optimize the filling process in order to minimize the amount of non-condensable gas in the heat pipe. If non-condensable gas can not be avoided, the solution may be to design the condenser so large that it can contain some non-condensable gas, however, the accompanying temperature drop in the condenser is a drawback.

The static pressure limit was estimated and expected to limit the performance of the hybrid heat pipe. However this limit was not observed in the experiments. The possible existence of a channel between the wick and the evaporator surface (container wall) having higher permeability can be the reason for this discrepancy. The high permeability channel may have been created because:

- The wick was insufficiently attached to the container wall by the spot welding.
- Thermal stress and strain created a channel.

The static pressure limit would be expected to be measurable in an even more carefully designed experiment for this purpose.

Boiling of potassium occurred in the hybrid heat pipe when only the lower parts of it were heated. During boiling the temperatures of the hybrid heat pipe were unstable (oscillating).

Potassium is an excellent heat transfer fluid for the range 400-650°C, especially in combination with a wick.

Sulfur is an interesting heat transfer fluid, but its corrosivity is a problem. A corrosion experiment with stainless steels 304 and 316L in sulfur at 550°C showed heavy corrosion. Work can be done to find/develop materials compatible with boiling sulfur. Ceramics like SiC may be compatible with pure sulfur. Alumina (Al_2O_3) has also been mentioned as a material candidate that may be compatible with sulfur [87].

Wicks made from nickel powder and compressed nickel foam cover different ranges of effective pore radius and permeability. Wicks of compressed nickel foam are best when large effective pore radius and high permeability are required.

The location of a hot spot on the wick is important; the capability to handle hot spots is at its minimum in the upper corners of the wick. The capacity and capability to handle hot spots can be improved by increasing the wick thickness, and/or decreasing the wick height.

Experimental results indicate that spot welding of the wick to the evaporator surface is not the best way to attach the wick. Contact problems between the wick and the surface may be caused by asymmetric thermal expansion of a heat pipe subject to unilateral heat flux. A better method for attaching the wick, and thereby ensuring thermal contact between the wick and the evaporator surface (container wall) under all working conditions should be developed and tested.

The accuracy of the permeability determination from the rate-of-rise experiment can be improved by use of a balance having higher maximum sampling rate, vapor concentration measurements inside the draft shield, improved mechanical mechanism for careful lifting and lowering of the wick, and an option to apply heat flux during rate-of-rise in order to investigate the possible effect of evaporation on the effective pore radius, as described by Shirazy and Fréchette [85].

Due to the uncertainty related to the permeability determination from the rate-of-rise experiment, a separate measurement of the wick permeability (for instance by use of a forced flow method) is recommended.

The final wick for the hybrid heat pipe was made and tested without back plate. However, the evaporator wall will act as “back plate” for the wick. The fact that the wick was tested without back plate does of course raise the question: What is the impact of the back plate/wall on wick performance? This may also be a topic for very careful rate-of-rise experiments.

References

- [1] E. Næss, Communication during this work., in, 2008-2015.
- [2] J.A. Aune, K. Johansen, P.O. Nos, Electrolytic cell for the production of aluminum and a method for maintaining a crust on a sidewall and for recovering electricity, in: WO/2001/94667, 2004.
- [3] K. Grjotheim, H. Kvande, Introduction to aluminium electrolysis: understanding the Hall-Héroult process, Aluminium-Verlag, Düsseldorf, 1993.
- [4] H.K. Holmen, S. Gjørven, Energy recovery and/or cooling in electrolysis cells to produce aluminum, by directing heat exchange medium to expander turbine connected with compressor supplying the medium to cells for heat exchange and cooling in self propelling manner, in: Patent US20070261826, 2006.
- [5] W. Quadackers, Corrosion of high temperature alloys in the primary circuit helium of high temperature gas cooled reactors. Part II: Experimental results, *Materials and Corrosion*, 36 (1985) 335-347.
- [6] H. Mikami, A. Shono, H. Hiroi, "Sodium leak at Monju (I)—cause and consequences—", in: Proc. Int. Working Group on Fast Reactors, Technical Committee Meeting on Evaluation of Radioactive Materials Release and Sodium Fires in Fast Reactors, O-arai, Ibaraki, Japan, Nov, Vol. 11, 1996, pp. 271.
- [7] G.A. Meyer, R.F. Coleman, Flat heat pipe cooling plate of simplified construction - has flattened copper tubing with sintered wicks, mounted in slotted plate and bonded to cover plates, in, Patent US4880052-A, 1989.
- [8] P.O. Nos, Experimental study of a rectangular evaporation cooler operating on synthetic heat transfer fluids, Norwegian Institute of Technology, Thermal Energy Division, Trondheim, 1993.
- [9] O.E. Dwyer, Boiling liquid-metal heat transfer, 1 ed., American Nuclear Society, Hinsdale, IL, USA, 1976.
- [10] J.G. Collier, J.R. Thome, Convective boiling and condensation, Clarendon Press, Oxford, 1994.
- [11] D.A. Reay, P.A. Kew, R. McGlen, P.D. Dunn, Heat pipes: theory, design, and applications, Butterworth-Heinemann, an imprint of Elsevier, Kidlington, Oxford, UK, 2014.
- [12] Y.A. Buevich, V. Mansurov, Toward a theory of shock boiling, *Journal of engineering physics*, 47 (1984) 1407-1412.
- [13] J.H. Lienhard, Correlation for the limiting liquid superheat, *Chemical Engineering Science*, 31 (1976) 847-849.
- [14] J.H. Lienhard, V.E. Schrock, Generalized displacement of the nucleate boiling heat-flux curve, with pressure change, *International Journal of Heat and Mass Transfer*, 9 (1966) 355-363.
- [15] N.B. Vargaftik, J.K. Vinogradov, V.S. Jargin, Handbook of physical properties of liquids and gases: pure substances and mixtures, Begell House, New York, 1996.
- [16] A. Devarakonda, Thermo-Physical Properties of Intermediate Temperature Heat Pipe Fluids, AIP Conference Proceedings, in, Vol. 746, 2005, pp. 179.

- [17] F. Polasek, P. Stulc, Heat pipes for the temperature range from 200°C to 600°C, in: The 2nd Int. Heat Pipe Conf., Vol. 2, ESA SP 112, Bologna, 1976, pp. 711-732.
- [18] G. Chaffey, J.C. Ralph, C.D. Wade, Development of a high temperature heat pipe heat exchanger for recovery of residual heat, in, D. Reidel Publ Co, Dordrecht, Neth, Brussels, Belg, 1983, pp. 51-65.
- [19] W.G. Anderson, Intermediate temperature fluids for heat pipes and loop heat pipes, in, Vol. 2, American Institute of Aeronautics and Astronautics Inc., Reston, VA 20191-4344, United States, St. Louis, MO, United States, 2007, pp. 1147-1164.
- [20] D.L. Timrot, M.A. Serednitskaya, A.N. Medveditskov, S.A. Traktueva, Thermophysical properties of a sulfur-iodine binary system as a promising heat transfer medium for heat pipes, *Journal of Heat Recovery Systems*, 1 (1981) 309-314.
- [21] A. Faghri, Heat pipe science and technology, Taylor & Francis, Washington, D.C., USA, 1995.
- [22] C.T. Ewing, J.P. Stone, J.R. Spann, R.R. Miller, Molecular association in sodium, potassium and cesium vapors at high temperatures, *Journal of Physical Chemistry*, 71 (1967) 473-477.
- [23] D.A. Reay, P.A. Kew, P.D. Dunn, Heat pipes, Elsevier, Amsterdam, 2006.
- [24] C.A. Tarau, William G.; Walker, Kara, NaK Variable Conductance Heat Pipe for Radioisotope Stirling Systems, in: 6th International Energy Conversion Engineering Conference (IECEC), Cleveland, Ohio, 2008, pp. 12.
- [25] I.L. Shilovich, I.E. Veneraki, V.S. Mel'nichenko, Y.N. Panov, Maximum heat flux transferable by thermosiphons operating with sulfur-iodine mixture at temperatures of 600 to 900K, *Heat Transfer - Soviet Research*, 18 (1986) 29-34.
- [26] D.M. Ernst, Sulfur/iodine heat pipes for space heat rejection, in: AIChE symposium series, Vol. 88 no 288, 1992, pp. 133-138.
- [27] R.R. Williams, D.K. Harris, The heat transfer limit of step-graded metal felt heat pipe wicks, *International Journal of Heat and Mass Transfer*, 48 (2005) 293-305.
- [28] B.D. Marcus, D.K. Edwards, Graded pore size heat pipe wick, in: Patent 4170262, USA, 1979.
- [29] P.C. Hiemenz, Principles of colloid and surface chemistry, Dekker, New York, 1986.
- [30] G. Hansen, E. Næss, Performance of compressed nickel foam wicks for flat vertical heat pipes, *Applied Thermal Engineering*, 81 (2015) 359-367.
- [31] B. Holley, A. Faghri, Permeability and effective pore radius measurements for heat pipe and fuel cell applications, *Applied Thermal Engineering*, 26 (2006) 448.
- [32] D.A. Odden, Development of heat pipes with potassium as working fluid: Performance limitations and test rig development, in: Msc-thesis, NTNU, 2012-70.
- [33] K. Kristjansson, Development of a hybrid heat pipe for high temperature applications, in: MSc-thesis, NTNU, 2011-02.
- [34] G. Hansen, E. Næss, K. Kristjansson, Analysis of a vertical flat hybrid heat pipe utilizing potassium working fluid and a wick of compressed nickel foam *Energies*, 9 (2016) 170.
- [35] D.R. Adkins, R.C. Dykhuizen, Procedures for measuring the properties of heat-pipe wick materials, in: Proceedings of the 28th Intersociety Energy Conversion Engineering Conference, vol. 2, American Chemical Society, Washington, DC, 1993, pp. 911-917.

- [36] O. Gerbaux, T. Vercueil, A. Memponteil, B. Bador, Experimental characterization of single and two-phase flow through nickel foams, *Chemical Engineering Science*, 64 (2009) 4186-4195.
- [37] K. Kristjansson, Energy recovery from the aluminium industries - Cooling of sidelinings, in: Project assignment, NTNU, 2009-32.
- [38] G. Hansen, E. Næss, K. Kristjansson, Sintered Nickel Powder Wicks for Flat Vertical Heat Pipes, *Energies*, 8 (2015) 2337-2357.
- [39] V.A. Tracey, Nickel powders into sintered structures for the alkaline battery: Porosity studies., *Industrial & Engineering Chemistry, Product Research and Development*, 25 (1986) 582-585.
- [40] K.J. Zan, C.J. Zan, Y.M. Chen, S.J. Wu, Analysis of the parameters of the sintered loop heat pipe, *Heat Transfer-Asian Research*, 33 (2004) 515-526.
- [41] S.L. Che, K. Takada, K. Takashima, O. Sakurai, K. Shinozaki, N. Mizutani, Preparation of dense spherical Ni particles and hollow NiO particles by spray pyrolysis, *Journal of Materials Science*, 34 (1999) 1313-1318.
- [42] K.J. Knutsen, *Formler og data i fysikk*, Tapir, [Trondheim], 1978.
- [43] N.N. Greenwood, A. Earnshaw, *Chemistry of the elements*, Butterworth-Heinemann, Boston, 1998.
- [44] J.N. Israelachvili, *Intermolecular and surface forces*, Academic Press, London, 1991.
- [45] R.E. Mistler, E.R. Twiname, *Tape Casting Theory and Practice*, The American Ceramic Society, Westerville, OH, 2000.
- [46] H. Lea Lein, Communication during this work, in, 2009.
- [47] Hexcel, HexTow AS7 Carbon fiber Product Data, in, 2009.
- [48] N.P. Vedvik, Communication during this work., in, 2009.
- [49] G.P. Peterson, *An introduction to heat pipes: modeling, testing, and applications*, Wiley, New York, 1994.
- [50] C.C. Silverstein, *Design and technology of heat pipes for cooling and heat exchange*, Hemisphere Pub. Corp., 1992.
- [51] L.L. Vasil'ev, S. Kaka, *Heat pipes and solid sorption transformations: fundamentals and practical applications*, 2013.
- [52] D. Reay, A. Harvey, The role of heat pipes in intensified unit operations, *Applied Thermal Engineering*, 57 (2013) 147-153.
- [53] C. Wang, D. Zhang, S. Qiu, W. Tian, Y. Wu, G. Su, Study on the characteristics of the sodium heat pipe in passive residual heat removal system of molten salt reactor, *Nuclear Engineering and Design*, 265 (2013) 691-700.
- [54] J. Rosenfeld, K. Minnerly, C. Dyson, Ten Year Operating Test Results and Post-Test Analysis of a 1/10 Segment Stirling Sodium Heat Pipe, Phase III, in, 2012.
- [55] P. Meisel, W. Lippmann, A. Hurtado, Ceramic High-Temperature Heat-Pipes, in: 22nd International Conference on Nuclear Engineering, American Society of Mechanical Engineers, 2014.
- [56] C.A. Busse, Theory of the ultimate heat transfer limit of cylindrical heat pipes, *International Journal of Heat and Mass Transfer*, 16 (1973) 169-186.
- [57] A. Hultin, Evaporation and condensation in heat pipes with potassium as working fluid, in: Msc-thesis NTNU, 2011-02.
- [58] D.A. Odden, Investigation of heat transfer and flow conditions in heat pipes using potassium as working fluid, in: Project assignment, NTNU, 2011-70.

- [59] A. Zapke, D.G. Kröger, The influence of fluid properties and inlet geometry on flooding in vertical and inclined tubes, *International Journal of Multiphase Flow*, 22 (1996) 461-472.
- [60] A. Zapke, D.G. Kröger, Countercurrent gas–liquid flow in inclined and vertical ducts — II: The validity of the Froude–Ohnesorge number correlation for flooding, *International Journal of Multiphase Flow*, 26 (2000) 1457-1468.
- [61] A. Zapke, D.G. Kröger, Countercurrent gas–liquid flow in inclined and vertical ducts — I: Flow patterns, pressure drop characteristics and flooding, *International Journal of Multiphase Flow*, 26 (2000) 1439-1455.
- [62] A.G. Cetinbudaklar, G.J. Jameson, The mechanism of flooding in vertical countercurrent two-phase flow, *Chemical Engineering Science*, 24 (1969) 1669-1680.
- [63] A. Faghri, M.M. Chen, M. Morgan, Heat transfer characteristics in two-phase closed conventional and concentric annular thermosyphons, *Journal of Heat Transfer, Transactions ASME*, 111 (1989) 611-618.
- [64] Specialmetals, *Technical Bulletin Nickel 200 & 201*, in, 2009.
- [65] D.T. Queheillalt, G. Carbajal, G.P. Peterson, H.N.G. Wadley, A multifunctional heat pipe sandwich panel structure, *International Journal of Heat and Mass Transfer*, 51 (2008) 312-326.
- [66] K. Montgomery, Type N versus type K thermocouple comparison in a brick kiln, *Temperature: its Measurement and Control in Science and Industry*, 6 (1992) 601-605.
- [67] F.P. Incropera, D.P. DeWitt, T.L. Bergman, A.S. Lavine, *Fundamentals of heat and mass transfer*, Wiley, New York, 2007.
- [68] S.J. Wilcox, W.M. Rohsenow, Film condensation of potassium using copper condensing block for precise wall-temperature measurement, *Transactions of the ASME. Series C, Journal of Heat Transfer*, 92 (1970) 359-371.
- [69] F.P. Incropera, D.P. DeWitt, T.L. Bergman, *Principles of heat and mass transfer*, Wiley, Singapore, 2013.
- [70] K. Stephan, *Wärmeübergang beim Kondensieren und beim Sieden*, Springer-Verlag, Berlin ; New York, 1992.
- [71] R.W. Schrage, *A Theoretical Study of Interphase Mass Transfer*, Columbia University Press, 1953.
- [72] V.P. Carey, *Liquid-vapor phase-change phenomena: an introduction to the thermophysics of vaporization and condensation processes in heat transfer equipment*, Hemisphere Publ., Washington, 1992.
- [73] W.M. Rohsenow, Heat transfer and temperature distribution in laminar-film condensation, *American Society of Mechanical Engineers -- Transactions*, 78 (1956) 1645-1648.
- [74] A. Bejan, *Convection heat transfer*, Wiley, New York, 1984.
- [75] A. Bejan, *Convection heat transfer*, Wiley, Hoboken, N.J., 2004.
- [76] M.M. Chen, An analytical study of laminar film condensation: part 1-flat plates, *Journal of heat transfer*, 83 (1961) 48.
- [77] E.M. Sparrow, J.L. Gregg, Boundary-layer treatment of laminar-film condensation, *American Society of Mechanical Engineers -- Transactions -- Journal of Heat Transfer*, 81, Series C (1959) 13-18.
- [78] J.C.Y. Koh, E.M. Sparrow, J.P. Hartnett, Two phase boundary layer in laminar film condensation, *International Journal of Heat and Mass Transfer*, 2 (1961) 69-82.

- [79] V.D.I. e.V., VDI Heat Atlas, Springer Berlin Heidelberg, Berlin, Heidelberg, 2010.
- [80] R. Ishiguro, K. Sugiyama, F. Terayama, Experimental study of potassium vapor condensation, in, Hemisphere Publ Corp, Washington, DC, USA, 1987, pp. 463-470.
- [81] W.M. Kays, M.E. Crawford, B. Weigand, Convective heat and mass transfer, McGraw-Hill, Boston, 2005.
- [82] Y.A. Çengel, Heat and mass transfer: a practical approach, McGraw-Hill, Boston, MA, USA, 2007.
- [83] F.M. White, Viscous fluid flow, McGraw-Hill Higher Education, Boston, 2006.
- [84] T.P. Cotter, Theory of Heat Pipes, in, United States, 1965, pp. 37p.
- [85] M.R.S. Shirazy, L.G. Fréchet, Effect of Meniscus Recession on the Effective Pore Radius and Capillary Pumping of Copper Metal Foams, Journal of Electronic Packaging, 136 (2014) 0410031-0410038.
- [86] Y. Fukuzawa, Y. Fujii-E, Performance Characteristics of Potassium Heat Pipe Loaded with Argon, Journal of Nuclear Science and Technology, 15 (1978) 109-119.
- [87] O. Paulsen, Communication during this work., in, 2009.
- [88] F.J. Lesage, S. Siedel, J.S. Cotton, A.J. Robinson, A mathematical model for predicting bubble growth for low Bond and Jakob number nucleate boiling, Chemical Engineering Science, 112 (2014) 35-46.
- [89] N.B. Vargaftik, Handbook of physical properties of liquids and gases - pure substances and mixtures. Second edition, 1975.
- [90] P.I. Bystrov, D. Kagan, G. Krechetova, E. Shpilrain, Liquid-metal coolants for heat pipes and power plants, (1990).
- [91] C.L. Yaws, Yaws handbook of thermodynamic properties for hydrocarbons and chemicals, Knovel, New York, 2009.
- [92] W.G. Breck, R.J.C. Brown, J.D. McCowan, Chemistry for science and engineering, McGraw-Hill Ryerson, Toronto, 1981.
- [93] J. Bakken, Personal communication and STANJAN calculation, in, 2011.
- [94] P. Patnaik, A comprehensive guide to the hazardous properties of chemical substances, John Wiley, Hoboken, NJ, 2007.
- [95] A.J. Wheeler, A.R. Ganji, Introduction to engineering experimentation, Pearson/Prentice Hall, Upper Saddle River, N.J., 2004.
- [96] R.J. Moffat, Describing the uncertainties in experimental results, Experimental Thermal and Fluid Science, 1 (1988) 3-17.
- [97] ISO_5017, Dense shaped refractory products -- Determination of bulk density, apparent porosity and true porosity, in, International Organization for Standardization, Geneva, Switzerland, 1998.
- [98] M.Ø. Døllner, Electrical engineer EPT, NTNU, in, 2012.
- [99] Pyrocontrol, Technical pamphlet "Termoelementer", in, www.pyrocontrol.no, 2015.

Appendix A Heterogeneous boiling

A model for the heating period ($t=0$ to $t=t_1$ in Figure 2-3):

With reference to Figure 2-3 a basic model for the surface temperature (and the liquid bath temperature) from $t=0$ to $t=t_1$ was derived. The derivation started from a heat balance for the bath, see Figure A-1.

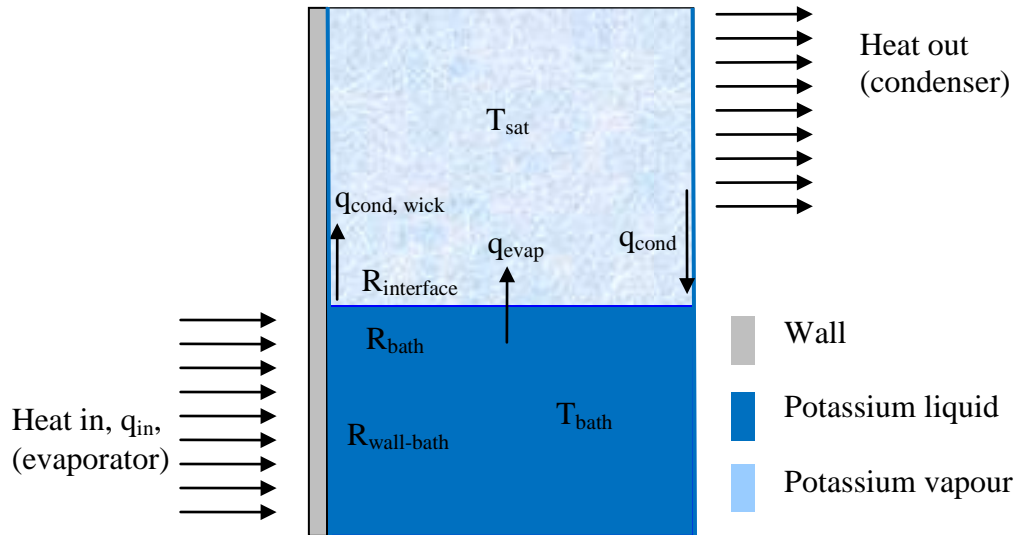


Figure A-1 A bath with evaporation and condensation

The following terms were taken into account in the heat balance:

- Heat was supplied to the bath at a constant heat flux, q_{in} , on the left side.
- Heat was supplied to the bath by the mass flow of condensate of temperature T_{sat} which returned to the bath along the right wall. The mass flow of condensate was assumed constant in order to ease the mathematical treatment. If there was a wick on the evaporator side the massflow $\dot{m}_{condensate}$ also included the mass flow leaving the bath through the wick.
- Heat left the bath in the vertical direction by evaporation. The heat transfer coefficient h_{out} in the vertical direction consisted of two series-coupled resistances:
 1. The convective resistance in the liquid bath, R_{bath} .
 2. The interfacial resistance of the evaporation, $R_{interface}$.

In some cases it may be justified to assume that also the walls of the panel which contains the bath have the same temperature as the bath. Specifically, this assumption is ok if the

thermal conductivity of the walls is high and the thermal resistance between the panel walls and the bath is low[1].

The heat balance for the bath and the panel walls (incl. the wick) surrounding the bath:

Energy stored = Energy in – Energy out

$$\left(m_{bath} \cdot c_{p,bath} + m_{panel} \cdot c_{p,panel} \right) \cdot \frac{dT_{bath+panel}}{dt} = \quad (A-1)$$

$$q_{in} \cdot A_{in} + \dot{m}_{condensate} \cdot c_{p,condensate} (T_{sat} - T_{bath}) - h_{out} A_{out} (T_{bath} - T_{sat})$$

The differential equation Eq. (A-1) was solved numerically by use of Eq. (A-2):

$$\frac{dT_{bath+panel}}{dt} \approx \frac{T_{bath+panel}(t + \Delta t) - T_{bath+panel}(t)}{\Delta t} \quad (A-2)$$

Which yielded:

$$\frac{T_{bath+panel}(t + \Delta t) - T_{bath+panel}(t)}{\Delta t} = \quad (A-3)$$

$$\frac{q_{in} \cdot A_{in} + \dot{m}_{condensate} \cdot c_{p,condensate} (T_{sat} - T_{bath+panel}(t)) - h_{out} \cdot A_{out} \cdot (T_{bath+panel}(t) - T_{sat})}{m_{bath} \cdot c_{p,bath} + m_{panel} \cdot c_{p,panel}}$$

Rewritten with a simplified notation; $T^{n+1} = T_{bath+panel}(t + \Delta t)$ and $T^n = T_{bath+panel}(t)$:

$$\frac{T^{n+1} - T^n}{\Delta t} = \frac{q_{in} \cdot A_{in} + \dot{m}_{condensate} \cdot c_{p,condensate} (T_{sat} - T^n) - h_{out} \cdot A_{out} \cdot (T^n - T_{sat})}{m_{bath} \cdot c_{p,bath} + m_{panel} \cdot c_{p,panel}} \quad (A-4)$$

Solved explicitly for T^{n+1} :

$$T^{n+1} = T^n + \left[\frac{q_{in} \cdot A_{in} + \dot{m}_{condensate} \cdot c_{p,condensate} (T_{sat} - T^n) - h_{out} \cdot A_{out} \cdot (T^n - T_{sat})}{m_{bath} \cdot c_{p,bath} + m_{panel} \cdot c_{p,panel}} \right] \Delta t \quad (A-5)$$

In Chapter 4.5.2 Equation (A-5) has been compared to experimental data.

The different parameters in Equation (A-5) affect the function $T_{bath}(\tau)$ in the following ways:

- Increasing the heat flux q_{in} leads to faster heating. If the temperature of the bath is not limited by a fixed maximum incipient boiling temperature, a higher heat flux will also lead to a higher maximum temperature of the bath.
- The returning condensate and the heat transfer by evaporation from the bath have the same impact on $T_{bath}(t)$; they both delay the warming of the bath.
- Increase in the mass of the bath and/or the panel, or increase in their specific heat capacities, would increase the time needed to reach $T_{bath}(t_1)$.

A model for the rapid bubble growth period from $t=t_1$:

From $t=t_1$ in Figure 2-3 the bubble starts growing, and the first part of the growth period has been designated as the rapid bubble growth period. The growth rates and departure diameters of bubbles have been the topics of many studies [10]. A recent model for bubble growth, as well as a review of several previous models, have been presented by Lesage et al. [88]. The model in their study was derived for a single cylindrical cavity, and compared with experimental results where n-pentane was boiling from a single artificial cylindrical cavity of radius 90 μm . The results from their model were in very good agreement with their experimental results. In real systems the growth rates and departure diameters may vary much, also over time, so statistical mean values are recommended used for experimental verifications [10].

A heat transfer model for the rapid bubble growth period (shock boiling phase) from time $t=t_1$ was developed. It was observed from plots of experimental data, presented in Chapter 4.5.2, that the temperatures measured by the termocouples in the wall were linear as function of time in a period from time $t=t_1$. A model was made to explain the linearity of the slope $\left(\frac{dT}{dt}\right)_{wall}$. The derivation started from an energy balance for the wall, see

Figure A-2. The wall was assumed to have uniform temperature and the heat transfer coefficient between the wall and the boiling fluid was assumed to be very high.

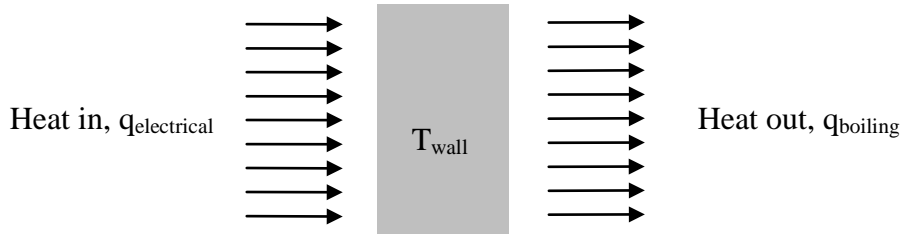


Figure A-2 The wall

Energy balance for the wall:

$$\dot{E}_{in} - \dot{E}_{out} = \dot{E}_{stored} \quad (\text{A-6})$$

$$Q_{\text{electrical}} - Q_{\text{boiling}} = \dot{E}_{\text{stored}} \quad (\text{A-7})$$

$$q_{el} A_{\text{wall},el} - \frac{dm_{\text{boiling fluid}}}{dt} h_{fg,\text{boiling fluid}} = \rho_{\text{wall}} V_{\text{wall}} c_{p,\text{wall}} \left(\frac{dT}{dt} \right)_{\text{wall}} \quad (\text{A-8})$$

Here $dm_{\text{boiling fluid}}$ designates the amount of the liquid in the bath that actually evaporates during the rapid growth period. Equation (A-8) can now be solved for $\left(\frac{dT}{dt} \right)_{\text{wall}}$:

$$\left(\frac{dT}{dt} \right)_{\text{wall}} = \frac{q_{el} A_{\text{wall},el} - \frac{dm_{\text{boiling fluid}}}{dt} h_{fg,\text{boiling fluid}}}{\rho_{\text{wall}} V_{\text{wall}} c_{p,\text{wall}}} \quad (\text{A-9})$$

Equation (A-9) is compared to experimental results in Chapter 4.5.2.

If the heat transfer coefficient between the panel walls and the bath is low the temperatures of the panel walls and the bath will no longer be the same [1].

Appendix B Corrosion experiment

Corrosion experiments with Sulfur and AISI304 and AISI316L

Materials and experimental conditions

The corrosion tests were undertaken at 550°C for a duration of 100 hours.

Metal samples:

50 mm Ø4 mm rods of AISI 304 and AISI 316L. Datasheets are found in Appendix B.

Sulfur:

Powder of 99,5% purity. Datasheet are found in Appendix B.

Procedure

The metal rod samples were ground using 600µm emery paper and rinsed in acetone.

The metal rod samples and 2,1g sulfur powder were put into ampoules of silica-glass. The ampoules were evacuated 3x5 minutes by use of a vacuum pump. Between each evacuation period the ampoules were filled with argon. While still under vacuum the ampoules were sealed by use of a hydrogen burner flame. One of the sealed ampoules with metal rod and sulfur powder inside is shown in Figure B-1.



Figure B-1 Sealed silica glass ampoule containing sulfur and metal rod

The sealed ampoules were put in a lab oven, heated up to 550°C and kept there for 100 hours, see Figure B-2. Dropwise condensation of sulfur could be seen to occur at the top of the tubes when the oven door was opened for inspection.



Figure B-2 The sealed ampoules in the lab oven at 550°C

After 100 hours the oven door was opened and the ampoules were allowed to cool down to room temperature. At room temperature the sulfur had again solidified and recovered its initial yellow colour. The ampoules were then crushed with a hammer so that close visual inspection of the metal rods was possible.

Results

The visual inspection of the stainless steel rods made it clear that both rods were heavily corroded, see Figure B-3.



AISI 304



AISI 316L

Figure B-3 The metal rods after the corrosion experiments

The corrosion products (flakes) were for the AISI304 loose, but for the AISI316L they had to be forced off. Samples of the corrosion products were analysed in a scanning electron microscope:

AISI304

For AISI304 two types of electron microscope images were generated:

BEI = Back emitting image.

SEI = Secondary electron image (shows the topography).

In addition, x-ray spectra were generated to identify the elements in the corrosion products. The BEI and SEI images and x-ray spectra are enclosed. From the x-ray spectrum for the AISI304 sample the following areas could be identified on the images, see Figure B-4.

Grey matrix = S

White spots = Ni and Fe

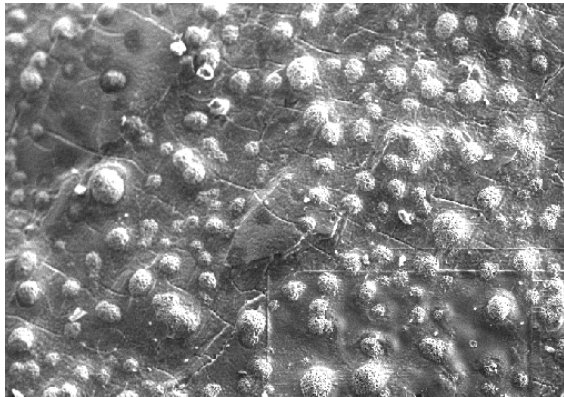


Figure B-4 Corrosion product from the AISI304 sample

AISI316L

In the corrosion product from the AISI316L sample only the matrix of sulfur was detected; other elements (like Ni and Fe) may also have been found if more time was spent on searching. Since the corrosion of the AISI316L sample was macroscopically visible it was decided not to spend more resources on further x-ray analysis.

Conclusions of the corrosion experiment

- There was significant corrosion between sulfur and AISI304/AISI316L at 550°C.
- The analysis of the corrosion products from AISI304 indicated that corrosion products of Ni and S were formed, as proposed by Timrot et al. [20].

The difference between the heavy corrosion observed here and the observation “No sign of failure“ reported by Anderson [19] may be explained by:

- The preparation of the samples. Contaminants, e.g. oxygen, may contribute to the corrosion process, i.e. it may be that higher purity of the sulfur, better cleaning of the samples and higher vacuum could have reduced the corrosion in this study.

- The higher temperature in the present study (550°C vs 350°C) may have accelerated the corrosion processes.

After the corrosion experiment no further steps were taken to study the compatibility of the stainless steels with boiling sulfur.

Without knowledge of any other suitable construction material it was decided not to spend more time investigating sulfur as working fluid.

ROLDAN, S.A. - Stainless Steels

FACTORY
 Sanjo Tomás de las Ollas, S/N
 Apdo de Correos 11
 PONFERRADA (LEÓN)
 TELEPHONE: +34 987 44 61 00
 FAX: +34 987 44 61 01
 E-MAIL: rdn_fabrica@acxgroup.com



HEAD OFFICE
 Santiago de Compostela, 100-3ª
 28035 MADRID (ESPAÑA)
 TELEPHONE: +34 913 98 52 57
 FAX: +34 913 98 51 93
 E-MAIL: roldan@acxgroup.com

INSPECTION CERTIFICATE

3.1
EN 10204



DIN EN ISO 9001:2000
 Certificado: 01 100 3143

CERTIFICATE N°	2006/018344	DATE	30/06/2006	SHEET	2	DELIVERY NOTE N°	2006/027575
GRADE	ROLDAMAX-134		AISI (302/304)				
CUSTOMER	ACERINOX SCANDINAVIA AB						
DIMENSIONS	4,00 mm.						
LENGTH	4.000 mm.			TOLERANCE	ISO h9		
PRODUCT	Round bar, cold drawn.						
REQUIREMENTS	AISI			CUSTOMER ORDER			
TENSILE TEST	EN 10002-1			Stock Malmö/E			
ACCORDING TO				EDITION			
INTERGRANULAR CORROSION	ASTM-A-262-02a PRACTICE *E* SATISFACTORY			WITHOUT OBJECTIONS			
SURFACE AND DIMENSIONS CONTROL	WITHOUT OBJECTIONS			Spektrometrical Identity Test: O.K.			
IMPACT TEST, SAMPLE DIMENSIONS							

ORDER N°	WORKS N°	MARKS/BOX	HEAT NUMBER	SAMPLE	WEIGHT	PRODUCTION PROCESS	INSPECTOR STAMP
LE54772 2	LE54772 2 4	72142 / JF36178	8VR2	8VR2	607	EAF + AOD + CC	R3
	LE54772 2 4	72143 / JF36180	8VR2		498		
	LE54772 2 4	72144 / JF36182	8VR2		204		
	LE54772 2 2	72145 / JF36183	8VR2		615		
	LE54772 2 2	72146 / JF36200	8VR2		555		
	LE54772 2 2	72147 / JF36245	8VR2		553		
	LE54772 2 2	72148 / JF36248	8VR2		575		
	LE54772 2 2	72159 / JF36324	8VR2		501		
						TRADE MARK	
						MARKING	
						HEAT NUMBER	
						GRADE (RDN 134)	
						QUALITY INSPECTOR	
						JOAQUIN DIAZ GONZALEZ	
						QUALITY CONTROL REPRESENTATIVE	
						Signature is not necessary according to EN 10204	

CAST	SAMPLE	SAMPLE DIMENSIONS	Observ.	Rm	Rp 0,2%	Rp 1%	Z %	A %	Agt %	IMPACT STRENGTH ISO-V (J)	HARDNESS KB	FATIGUE TEST	BEND TEST	CROSS SECTIONAL AREA mm²	Kg / m
8VR2				895	712	774	67	35			255				
REQUIREMENTS		EN ISO 377													


CAST	C	P	S	SI	Mn	Cr	NI	Mo	TI	N	Cu	Co
8VR2	0,0490	0,0260	0,0260	0,3720	1,4360	18,2570	8,1250	0,1790	0,0030	0,0680	0,2030	0,2050
REQUIREMENTS	0,0800	0,0450	0,0300	0,7500	2,0000	18,0000	8,0000			0,1000		

OBSERVATIONS

OTHER TEST RESULTS	REQUIREMENTS
HEAT TREATMENT	

Retorno: 430196

1968300

ROLDAN, S.A. - Stainless Steels				INSPECTION CERTIFICATE												
FACTORY Santo Tomé de las Ollas, S/N Apdo. de Correos 11 DOÑEFERRADA (2204) TEL.: +34 987 44 61 00 FAX: +34 987 44 61 01 E-MAIL: rda_fabrica@acsgroup.com				HEAD OFFICE Santiago de Compostela, 100-3° 28035 MADRID (ESPAÑA) TEL.: +34 913 98 52 57 FAX: +34 913 98 51 93 E-MAIL: roldan@acsgroup.com		3.1 EN 10204										
CERTIFICATE N° 2007/019790		DATE 28/06/2007		SHEET 1		DELIVERY NOTE N° 2007/045590										
GRADER ROLDAN-264		EN10.088:3 (1.4404.)														
CUSTOMER ACERINOX SCANDINAVIA AB (OWN STOCK)																
DIMENSIONS 4,00 mm.																
LENGTH 4.000 mm.		TOLERANCE ISO h9														
PRODUCT Round bar, annealed, pickled, cold drawn, polished																
REQUIREMENTS EN10.088:3				CUSTOMER ORDER												
TENSILE TEST EN 10002-2				316 jun1												
ACCORDING TO EDITION																
INTERGRANULAR CORROSION EN ISO 1651-2 SATISFACTORY				WITHOUT OBJECTIONS												
SURFACE AND DIMENSIONS CONTROL WITHOUT OBJECTIONS				Spectrometrical Identity Test: O.K.												
IMPACT TEST, SAMPLE DIMENSIONS																
ORDER N°	WORKS N°	MARKS / BOX	HEAT NUMBER	SAMPLE	WEIGHT	PRODUCTION PROCESS										
LK57449 1	LK57449 2 1	49005 / JF84610	C6E3	C6E3	520	EAF + AOD +CC										
						INSPECTOR STAMP										
						R3										
						QUALITY INSPECTOR										
						JOAQUIN DIEGUEZ GONZALEZ										
						QUALITY CONTROL REPRESENTATIVE <small>Signature is not necessary according to EN 10.224</small>										
MECHANICAL PROPERTIES																
CAST	SAMPLE	SAMPLE DIMENSIONS	Observ. r°.	Rm N/mm2	Rp 0,2% N/mm2	Rp 1% N/mm2	Z %	A %	Agt %	IMPACT STRENGTH ISO-V (J)	HARDNESS HB	FATIGUE TEST	BEND TEST	CROSS SECTIONAL AREA mm²	Kg / m	
C6E3				826	635	697	67	36			240					
REQUIREMENTS		EN ISO 377														
CHEMICAL COMPOSITION %																
CAST	C	P	S	SI	Mn	Cr	NI	Mo	TI	N	Cu	Co				
C6E3	0,0150	0,0110	0,0300	0,2520	1,3950	16,7570	10,6390	2,0970	0,0070	0,0510	0,4160	0,1390				
REQUIREMENTS	0,0300	0,0450	0,0300	1,0000	2,0000	16,5000	10,0000	2,0000		0,1100						
OBSERVATIONS																
OTHER TEST RESULTS																
REQUIREMENTS																
HEAT TREATMENT																

Certificate of Analysis

Material : 28260.234 SVOVEL AnalAR NORMAPUR
Batch : 08A220014 Expires end of 05/2012

CHARACTERISTICS	SPECIFICATIONS	MEASURED VALUES
Assay	Min. 99,5 %	Min. 99,5 %
Acidity or alkalinity	Max. 0,002 meq/g	Max. 0,002 meq/g
Ignition residue	Max. 0,04 %	Max. 0,04 %
Cl (Chloride)	Max. 50 ppm	Max. 50 ppm
S (Sulphide)	Max. 2 ppm	Max. 2 ppm
SO ₄ (Sulphate)	Max. 50 ppm	Max. 50 ppm
As (Arsenic)	Max. 5 ppm	Max. 5 ppm

We certify that this batch conforms to the specifications listed above.
BDL : Below detected limit.

Ingrid Dewolf Head of laboratory - Haasrode
VWR International
Document printed on 06/2008

This document has been produced electronically and is valid without a signature.

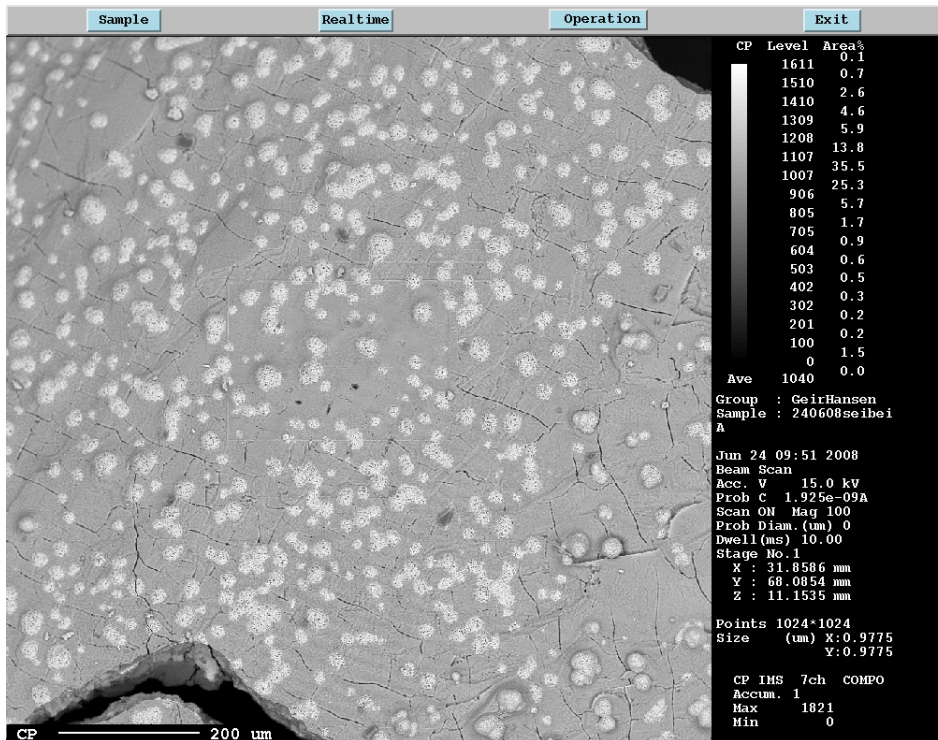


Figure B-5 BEI for the AISI304 corrosion flake sample

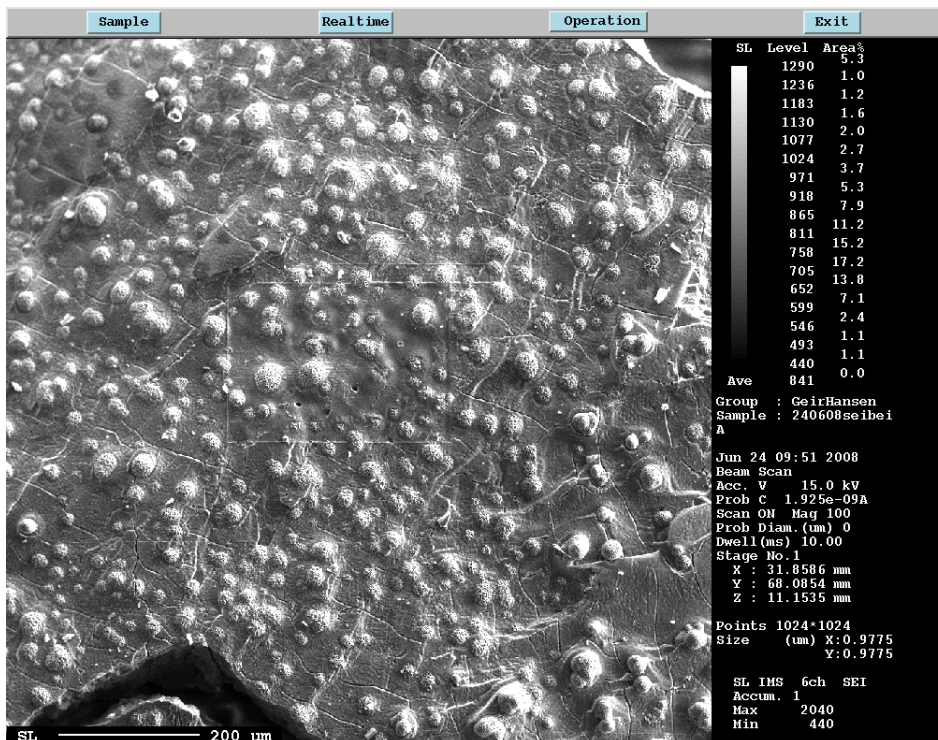


Figure B-6 SEI for the AISI304 corrosion flake example

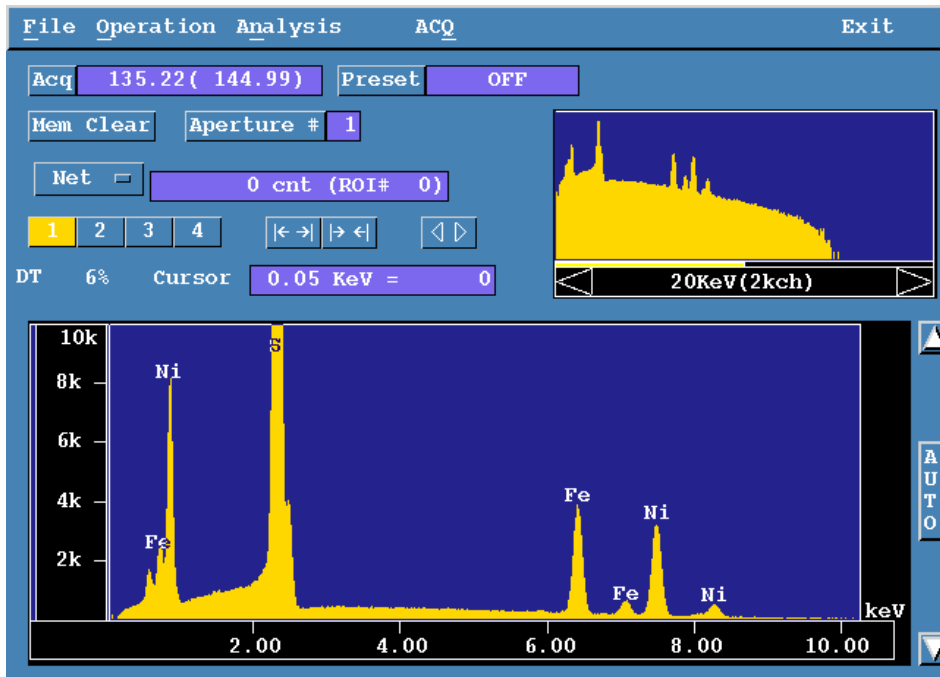


Figure B-7 X-ray spectrum of a light spot (sample AISI304)

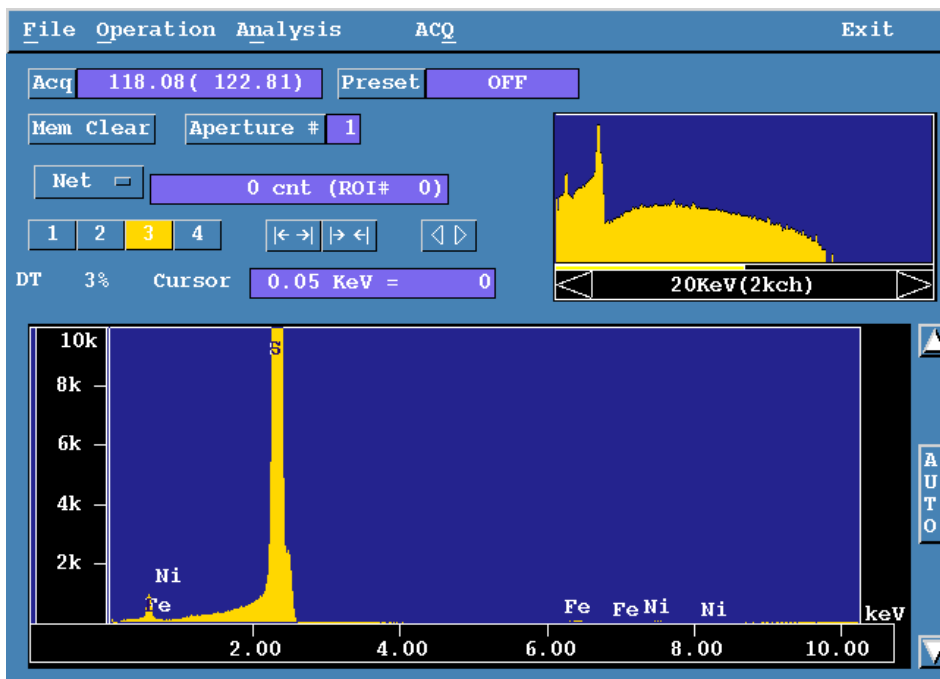


Figure B-8 X-ray spectrum of the matrix (sample AISI304)

Appendix C Rate-of-rise equations

The derivation of the close form solution of the governing equation for the rate-of-rise test.

$$m \frac{dm}{dt} = \frac{K\varepsilon(\rho A)^2}{\mu} \left(\frac{2\sigma}{r_{eff}} - \frac{g}{\varepsilon A} m \right) \quad (C-1)$$

$$-\left(\frac{2\sigma}{r_{eff}} \ln \left(1 - \frac{gr_{eff}}{2\sigma\varepsilon A} m \right) + \frac{g}{\varepsilon A} m \right) = \left(\frac{Kg^2\rho^2}{\varepsilon\mu} \right) t \quad (C-2)$$

$$\int \left(\frac{m}{\left(\frac{2\sigma}{r_{eff}} - \frac{g}{\varepsilon A} m \right)} \right) dm = \int \left(\frac{K\varepsilon(\rho A)^2}{\mu} \right) dt \quad (C-3)$$

The integral to the left can be solved by introducing a new variable u:

$$u = \left(\frac{2\sigma}{r_{eff}} - \frac{g}{\varepsilon A} m \right) \Rightarrow m = \frac{\varepsilon A}{g} \left(\frac{2\sigma}{r_{eff}} - u \right) \quad (C-4)$$

$$du = -\frac{g}{\varepsilon A} dm \Rightarrow dm = -\frac{\varepsilon A}{g} du \quad (C-5)$$

$$\int \left(\frac{\left(\frac{2\sigma}{r_{eff}} - u \right) \frac{\varepsilon A}{g} \left(-\frac{\varepsilon A}{g} \right)}{u} \right) du = \int \left(\frac{K\varepsilon(\rho A)^2}{\mu} \right) dt \quad (C-6)$$

$$-\left(\frac{\varepsilon A}{g} \right)^2 \int \left(\frac{2\sigma}{r_{eff}} \left(\frac{1}{u} \right) - 1 \right) du = \int \left(\frac{K\varepsilon(\rho A)^2}{\mu} \right) dt \quad (C-7)$$

$$-\left(\frac{\varepsilon A}{g} \right)^2 \left(\frac{2\sigma}{r_{eff}} \ln(u) - u + c_1 \right) = \left(\frac{K\varepsilon(\rho A)^2}{\mu} \right) t + c_2 \quad (C-8)$$

$$-\left(\frac{\varepsilon A}{g}\right)^2 \left(\frac{2\sigma}{r_{eff}} \ln \left(\frac{2\sigma}{r_{eff}} - \frac{g}{\varepsilon A} m \right) - \left(\frac{2\sigma}{r_{eff}} - \frac{g}{\varepsilon A} m \right) + c_1 \right) = \left(\frac{K\varepsilon(\rho A)^2}{\mu} \right) t + c_2 \quad (\text{C-9})$$

Let $c=(c_1+c_2)$:

$$-\left(\frac{2\sigma}{r_{eff}} \ln \left(\frac{2\sigma}{r_{eff}} - \frac{g}{\varepsilon A} m \right) - \left(\frac{2\sigma}{r_{eff}} - \frac{g}{\varepsilon A} m \right) + c \right) = \left(\frac{Kg^2\rho^2}{\varepsilon\mu} \right) t \quad (\text{C-10})$$

$$-\left(\frac{2\sigma}{r_{eff}} \ln \left(1 - \frac{gr_{eff}}{2\sigma\varepsilon A} m \right) - \left(\frac{2\sigma}{r_{eff}} - \frac{g}{\varepsilon A} m \right) + c \right) = \left(\frac{Kg^2\rho^2}{\varepsilon\mu} \right) t \quad (\text{C-11})$$

Boundary condition:

$$(t=0 \Rightarrow m=0) \Rightarrow c = \frac{2\sigma}{r_{eff}}$$

gives:

$$-\left(\frac{2\sigma}{r_{eff}} \ln \left(1 - \frac{gr_{eff}}{2\sigma\varepsilon A} m \right) + \frac{g}{\varepsilon A} m \right) = \left(\frac{Kg^2\rho^2}{\varepsilon\mu} \right) t \quad (\text{C-12})$$

From Equation (3-13) to Equation (3-14).

$$\Delta P_f = -\frac{\mu}{K\rho A} \int_0^x \left(\rho A \varepsilon \frac{dx}{dt} + \Gamma(x - \xi) \right) d\xi \quad (\text{C-13})$$

$$\Delta P_f = -\frac{\mu}{K\rho A} \left[\rho A \varepsilon \frac{dx}{dt} \xi + \Gamma \left(x\xi - \frac{1}{2} \xi^2 \right) \right]_0^x \quad (\text{C-14})$$

$$\Delta P_f = -\frac{\mu}{K\rho A} \left(\rho A \varepsilon \frac{dx}{dt} x + \Gamma \left(x^2 - \frac{1}{2} x^2 \right) \right) \quad (\text{C-15})$$

$$\Delta P_f = -\frac{\mu}{K\rho A} \left(\rho A \varepsilon \frac{dx}{dt} x + \Gamma \left(\frac{1}{2} x^2 \right) \right) \quad (\text{C-16})$$

$$\Delta P_f = -\frac{\mu}{K} \left(\varepsilon x \frac{dx}{dt} + \frac{\Gamma x^2}{2\rho A} \right) \quad (\text{C-17})$$

From Equation (3-15) to Equation (3-16).

$$\Delta P_{cap} - \Delta P_{hs} - \Delta P_f = 0 \quad (\text{C-18})$$

$$\frac{2\sigma}{r_{eff}} - \rho g x - \frac{\mu}{K} \left(\varepsilon x \frac{dx}{dt} + \frac{\Gamma x^2}{2\rho A} \right) = 0 \quad (\text{C-19})$$

$$\frac{2\sigma}{r_{eff}} \frac{K}{\mu} - \rho g x \frac{K}{\mu} = \varepsilon x \frac{dx}{dt} + \frac{\Gamma x^2}{2\rho A} \quad (\text{C-20})$$

$$\frac{2\sigma K}{r_{eff} \mu} - \frac{\rho g x K}{\mu} - \frac{\Gamma x^2}{2\rho A} = \varepsilon x \frac{dx}{dt} \quad (\text{C-21})$$

$$\frac{2\sigma K}{r_{eff} \mu \varepsilon} - \frac{\rho g x K}{\mu \varepsilon} - \frac{\Gamma x^2}{2\rho A \varepsilon} = x \frac{dx}{dt} \quad (\text{C-22})$$

$$x \frac{dx}{dt} = -\frac{\Gamma}{2\rho A\varepsilon} \left(x^2 - \frac{4\sigma\rho AK}{r_{eff}\mu\Gamma} + \frac{2\rho^2 AKgx}{\mu\Gamma} \right) \quad (C-23)$$

$$\frac{x \frac{dx}{dt}}{x^2 + \frac{2\rho^2 gAK}{\mu\Gamma} - \frac{4\sigma\rho AK}{r_{eff}\mu\Gamma}} = -\frac{\Gamma}{2\rho A\varepsilon} \quad (C-24)$$

From Equation (3-16) to Equation (3-17) and (3-18) [37].

$$\frac{x \frac{dx}{dt}}{x^2 + \frac{2\rho^2 gAK}{\mu\Gamma} - \frac{4\sigma\rho AK}{r_{eff}\mu\Gamma}} = -\frac{\Gamma}{2\rho A\varepsilon} \quad (C-25)$$

$$-\frac{\Gamma}{2\rho A\varepsilon} dt = \frac{x}{x^2 + \frac{2\rho^2 gAK}{\mu\Gamma} - \frac{4\sigma\rho AK}{r_{eff}\mu\Gamma}} dx \quad (C-26)$$

Defining:

$$b = \frac{2\rho^2 gAK}{\mu\Gamma} \quad c = -\frac{4\sigma\rho AK}{r_{eff}\mu\Gamma} \quad (C27)$$

So that:

$$-\frac{\Gamma}{2\rho A\varepsilon} dt = \frac{x}{x^2 + bx + c} dx \quad (C-28)$$

Integrating:

$$-\frac{\Gamma}{2\rho A\varepsilon} \int dt = \int \frac{x}{x^2 + bx + c} dx \quad (C-29)$$

From mathematics:

$$\int \frac{x}{x^2 + bx + c} dx = \frac{1}{2} \ln(x^2 + bx + c) - \frac{b}{2} \int \frac{x}{x^2 + bx + c} dx + IC_1 \quad (C-30)$$

IC = Integration Constant

From mathematics the solution of the second integral above is:

$$\int \frac{x}{x^2 + bx + c} dx = \frac{1}{\sqrt{b^2 - 4c}} \ln \left[\frac{2x + b - \sqrt{b^2 - 4c}}{2x + b + \sqrt{b^2 - 4c}} \right] + IC_2 \quad (C-31)$$

$$-\frac{\Gamma}{2\rho A \varepsilon} \int dt = \frac{1}{2} \ln(x^2 + bx + c) - \frac{b}{2\sqrt{b^2 - 4c}} \ln \left[\frac{2x + b - \sqrt{b^2 - 4c}}{2x + b + \sqrt{b^2 - 4c}} \right] + IC_3 \quad (C-32)$$

Here $IC_3 = IC_1 + IC_2$.

$$-\frac{\Gamma}{2\rho A \varepsilon} t = \frac{1}{2} \ln(x^2 + bx + c) - \frac{b}{2\sqrt{b^2 - 4c}} \ln \left[\frac{2x + b - \sqrt{b^2 - 4c}}{2x + b + \sqrt{b^2 - 4c}} \right] + IC \quad (C-33)$$

Then using that:

$$x^2 + bx + c = (x - C_1)(x - C_2) \quad , \quad C_1 = -\frac{b + \sqrt{b^2 - 4c}}{2} \quad \text{and} \quad C_2 = -\frac{b - \sqrt{b^2 - 4c}}{2} \quad (C-34)$$

$$-\frac{\Gamma}{2\rho A \varepsilon} t = \frac{1}{2} \ln[(x - C_1)(x - C_2)] - \frac{C_1 + C_2}{2(C_1 - C_2)} \ln \left[\frac{x - C_2}{x - C_1} \right] + IC \quad (C-35)$$

Rewriting the ln-terms:

$$-\frac{\Gamma}{2\rho A \varepsilon} t = \frac{1}{2} [\ln(x - C_1) + \ln(x - C_2)] - \frac{C_1 + C_2}{2(C_1 - C_2)} [\ln(x - C_2) - \ln(x - C_1)] + IC \quad (C-36)$$

$$-\frac{\Gamma}{2\rho A \varepsilon} t = \frac{1}{2} \ln(x - C_1) + \frac{1}{2} \ln(x - C_2) - \frac{C_1 + C_2}{2(C_1 - C_2)} \ln(x - C_2) + \frac{C_1 + C_2}{2(C_1 - C_2)} \ln(x - C_1) + IC \quad (C-37)$$

$$-\frac{\Gamma}{2\rho A\varepsilon}t = \left[\frac{1}{2} + \frac{C_1 + C_2}{2(C_1 - C_2)} \right] \ln(x - C_1) + \left[\frac{1}{2} - \frac{C_1 + C_2}{2(C_1 - C_2)} \right] \ln(x - C_2) + IC \quad (C-38)$$

$$-\frac{\Gamma}{2\rho A\varepsilon}t = \left[\frac{(C_1 - C_2) + (C_1 + C_2)}{2(C_1 - C_2)} \right] \ln(x - C_1) + \left[\frac{(C_1 - C_2) - (C_1 + C_2)}{2(C_1 - C_2)} \right] \ln(x - C_2) + IC \quad (C-39)$$

$$-\frac{\Gamma}{2\rho A\varepsilon}t = \left[\frac{C_1}{(C_1 - C_2)} \right] \ln(x - C_1) - \left[\frac{C_2}{(C_1 - C_2)} \right] \ln(x - C_2) + IC \quad (C-40)$$

$$-\frac{\Gamma(C_1 - C_2)}{2\rho A\varepsilon}t = C_1 \ln(x - C_1) - C_2 \ln(x - C_2) + IC(C_1 - C_2) \quad (C-41)$$

$$-\frac{\Gamma(C_1 - C_2)}{2\rho A\varepsilon}t = C_1 \ln\left(1 - \frac{x}{C_1}\right) - C_2 \ln\left(1 - \frac{x}{C_2}\right) + C_1 \ln C_1 - C_2 \ln C_2 + IC(C_1 - C_2) \quad (C-42)$$

Boundary condition:

$$x = 0 \quad \text{for} \quad t = 0 \quad \text{and} \quad C_1 \neq 0, C_2 \neq 0 \quad (C-43)$$

$$-IC(C_1 - C_2) = C_1 \ln(C_1) - C_2 \ln(C_2) \quad (C-44)$$

$$IC = \frac{-C_1 \ln(C_1) + C_2 \ln(C_2)}{(C_1 - C_2)} \quad (C-45)$$

IC inserted:

$$-\frac{\Gamma(C_1 - C_2)}{2\rho A\varepsilon}t = C_1 \ln\left(1 - \frac{x}{C_1}\right) - C_2 \ln\left(1 - \frac{x}{C_2}\right) + C_1 \ln C_1 - C_2 \ln C_2 + \frac{-C_1 \ln C_1 + C_2 \ln C_2}{(C_1 - C_2)}(C_1 - C_2) \quad (C-46)$$

Finally this leads to Equation (3-18):

$$-\frac{\Gamma(C_1 - C_2)}{2\rho A\varepsilon}t = C_1 \ln\left(1 - \frac{x}{C_1}\right) - C_2 \ln\left(1 - \frac{x}{C_2}\right) \quad (\text{C-47})$$

Appendix D The nickel powder

Inco special products

Inco Type 255

Nickel Powder

Inco Type 255

Inco Type 255 nickel powder is a fine filamentary, high purity, particle developed and produced by Vale Inco carbonyl technology.

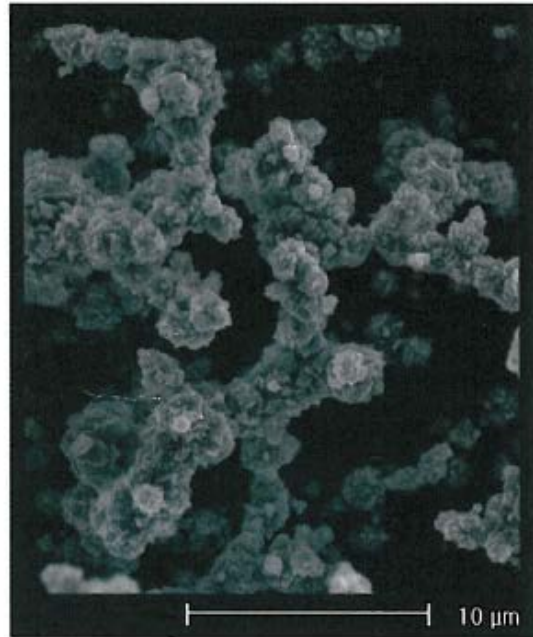
The powder is ideally suited to the production of porous structures by sintering or for the formation of conductive networks.

Applications

Inco Type 255 is recognized by the battery and fuel cell industry as the worldwide standard for the production of porous electrodes by sintering

Inco Type 255 is used as a conductive additive in a variety of media including battery and fuel cell active materials, and as a conductive pigment in coatings, especially for EMI shielding applications

Inco Type 255 is used to produce sintered steels and as a binder metal in tungsten heavy alloys, diamond tools and hard metals.



Advantages

- Tight control of the particle size and bulk density of Type 255 provides well controlled porosity in battery and fuel cell sintered electrodes and other porous structures.
- The relationship between Type 255 properties and the porosity and strength of sintered structures is well understood, enabling appropriate tailoring of porous structure properties.
- Provides a ferromagnetic component to shielding paints.
- Provides enhanced corrosion resistance in conductive coatings.
- Fine primary particle size can be advantageous in PM processing utilising aggressive mixing to break down the chainlike structure.
- High green strength due to the irregular powder shape.
- Enhances the ductility and corrosion resistance in heavy metal, diamond and hard metal binder applications.

Features

Benefits

Shape

Fine three-dimensional filamentary structure

Creation of 3-D Structure:
Allows production of uniformly porous sintered structures and conductive networks

Size Uniformity

Reproducible distribution of fine filamentary particles

Consistent Performance:
With uniform, repeatable performance

Experience

Decades as a reliable supplier to the nickel battery industry worldwide

Continued Commitment:
To meeting exacting customer specifications

Traceability

Each batch is tested and recorded from refinery to customer delivery

Confidence in Sourcing:
Complete tracking paper trail from refinery to finished product

ISO-9001

All powders are produced in ISO 9001 qualified refineries

Conformance: *To stringent requirements that demand ISO 9001 standards*

Inco special products
COPPER, NICKEL AND COBALT TECHNOLOGIES

CANADA
2101 Finchway Road
Mississauga, Ontario, Canada L5M 3L0
TEL: 905-403-2100 FAX: 905-403-8190

USA
601 Lawrence Road
Windsor, New Jersey 07091, USA
TEL: 1-201-948-1612 FAX: 1-201-948-1025

EUROPE
1st Floor, Division House
15 Grosvenor Place, London, SW1P 3HH, England
TEL: 44 20 7592 3525 FAX: 44 20 7591 7700

ASIA
237, Raaga-Gilgan-Hills Main Tower
P.O. Box, Kowloon, Kowloon
Hong Kong, 999, 001, Japan
TEL: 81 3 5422 8201 FAX: 81 3 5422 8281

ASIA (Singapore)
23-27, Avenue Tower
80 Via Changi Road
Singapore, 398128, 911, China
TEL: 65 2 1 0000 FAX: 65 2 1 0000 6706

ASIA (Hong Kong)
15th Floor, Wilson House
16-17, Robinson Street, Central, Hong Kong
TEL: 852 2421 0353 FAX: 852 2616 1046

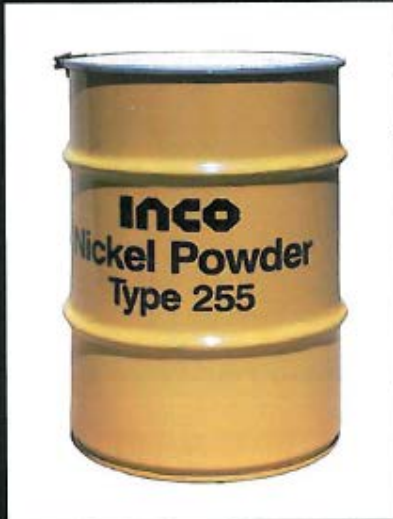
ASIA (Taiwan)
40 Hsinchu 3rd Street
104-A Industrial District
Kunming Road, Taipei
TEL: 886 2 287 0000 FAX: 886 2 287 7921

Steel drum internally coated with protective, inert resin

Approximate Dimensions

Diameter: 410 mm
 Height: 640 mm
 Net Weight: 75 kg
 Gross Weight: 84 kg

Multiples can be palletised and shrink-wrapped



UN Approved Packaging

Typical Chemical Composition

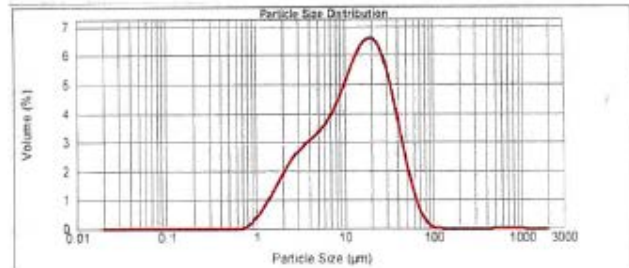
	Typical Wt %	Maximum Wt %
Carbon	0.2	0.3
Sulphur	0.0002	0.001
Oxygen	0.05	0.15
Nitrogen	0.003	n.d.
Iron	0.004	0.01
Cobalt	<0.00002	n.d.
Nickel	balance	--
Total Other Elements	<0.001	--

Scott Volumeter Method

Typical Physical Characteristics

Fisher Sub-Sieve Size: (Air Permeability Method)	2.2 - 2.8 microns
Bulk Density:	0.50 - 0.65 g/cm ³
Typical Specific Surface Area:	0.7 m ² /g (BET)

Typical Particle Size Distribution



This product is part of a complete range of Inco Special Nickel Products. The range includes: fine and extra fine nickel powders of many different morphologies, nickel coated graphite particles, INCOFOAM™ high porosity nickel foam, nickel oxides and nickel flakes.

Appendix E Thermophysical data

Thermophysical data for Ni 201 [64]

Temperature	Density	Specific heat	Thermal conductivity
[K]	[kg/m ³]	[kJ/(kg·K)]	[W/(m·K)]
173,15	8890	0,456	88,3
293,15	8890	0,456	79,3
373,15	8890	0,456	73,4
473,15	8890	0,456	66,3
573,15	8890	0,456	59,9
673,15	8890	0,456	56,1
773,15	8890	0,456	58,2
873,15	8890	0,456	60,6
973,15	8890	0,456	62,8
1073,15	8890	0,456	65,1
1173,15	8890	0,456	67,7
1273,15	8890	0,456	69,9

Thermophysical data for heptane

The thermophysical data of heptane were taken from Faghri [21], which used Vargaftik [89] as source for the data. Unfortunately, there was no information about the uncertainty for the data in Faghri [21] or in Vargaftik [89].

Thermophysical data for potassium

A table of thermophysical properties of saturated potassium from 600K to 1500K was presented in Faghri [21] based on data from the 1975 edition of the “Handbook of Physical Properties of Liquids and Gases” by Vargaftik et al. [89]. In 1996 a new edition of the handbook by Vargaftik et al. [15] was released, in which the data for potassium were slightly changed. Presuming that the data of the new edition of the handbook are more correct than the data of the previous edition, the data of the new edition were adopted here. For some of the properties the data of Vargaftik et al. [15] did not cover the whole temperature range of interest. For temperatures where data were lacking, one of the following two solutions was applied:

- The existing data of Vargaftik [15] were extrapolated by use of functions developed by curve fitting of existing data in TableCurve[®].

- Data were supplied from the table of Faghri [21].
Data above 1100K were not of interest in this study.

The melting temperature of potassium is $336,76 \pm 0,01$ K [15].

Saturation vapour pressure [15]

From Vargaftik et al. 1996 [15]		
T_{sat}	P_{sat}	Uncertainty
[K]	[MPa]	[%]
400	$1,972 \cdot 10^{-8}$	± 5
500	$3,349 \cdot 10^{-6}$	± 5
600	$9,872 \cdot 10^{-5}$	± 5
700	$1,080 \cdot 10^{-3}$	$\pm 4,5$
800	$6,407 \cdot 10^{-3}$	$\pm 4,5$
900	$2,536 \cdot 10^{-2}$	$\pm 4,5$
1000	$7,583 \cdot 10^{-2}$	$\pm 4,5$
1100	$1,852 \cdot 10^{-1}$	$\pm 4,5$

Latent heat of evaporation

From Vargaftik et al. 1996 [15]			From Faghri [21]
T_{sat}	h_{fg}	Uncertainty	h_{fg}
[K]	[J/kg]	[%]	[J/kg]
400	$2,208 \cdot 10^6$ *		
500	$2,165 \cdot 10^6$ *		
600	$2,120 \cdot 10^6$ *		$2,143 \cdot 10^6$
700	$2,073 \cdot 10^6$ *		$2,108 \cdot 10^6$
800	$2,024 \cdot 10^6$		$2,068 \cdot 10^6$
900	$1,973 \cdot 10^6$		$2,023 \cdot 10^6$
1000	$1,920 \cdot 10^6$		$1,970 \cdot 10^6$
1100	$1,865 \cdot 10^6$		$1,924 \cdot 10^6$

*Extrapolated values.

Liquid density [15, 90]

From Vargaftik et al. 1996 [15]		
T_{sat}	ρ_l	Uncertainty
[K]	[kg/m ³]	[%]
400	814,3	±0,25
500	790,6	±0,25
600	767,3	±0,25
700	744,1	±0,25
800	720,9	±0,25
900	697,4	±0,25
1000	673,6	±0,25
1100	649,1	±0,25

Vapour density [15, 90]

From Vargaftik et al. 1996 [15]		From Faghri [21]	
T_{sat}	ρ_v	Uncertainty	ρ_v
[K]	[kg/m ³]	[%]	[kg/m ³]
400	2,23·10 ⁻⁶ *		
500	3,17·10 ⁻⁵ *		
600	0,00069**		0,00069
700	0,00668**		0,00668
800	0,03947		0,03644
900	0,1417		0,13480
1000	0,3893		0,38020
1100	0,8822		0,87190

*Extrapolated values. **From Faghri [21]

Liquid dynamic viscosity [15]

From Vargaftik et al. 1996 [15]		
T_{sat}	μ_l	Uncertainty
[K]	[N·s/m ²]	[%]
400	3,930·10 ⁻⁴	±5
500	2,802·10 ⁻⁴	±5
600	2,204·10 ⁻⁴	±5
700	1,838·10 ⁻⁴	±5
800	1,591·10 ⁻⁴	±5
900	1,414·10 ⁻⁴	±5
1000	1,281·10 ⁻⁴	±5
1100	1,176·10 ⁻⁴	±5

Vapour dynamic viscosity [15]

From Vargaftik et al. 1996 [15]		
T_{sat}	μ_v	Uncertainty
[K]	[N·s/m ²]	[%]
400	$7,30 \cdot 10^{-6}$ *	
500	$9,55 \cdot 10^{-6}$ *	
600	$1,14 \cdot 10^{-5}$ *	
700	$1,289 \cdot 10^{-5}$	±0,25
800	$1,412 \cdot 10^{-5}$	±0,25
900	$1,515 \cdot 10^{-5}$	±0,25
1000	$1,605 \cdot 10^{-5}$	±0,25
1100	$1,689 \cdot 10^{-5}$	±0,25

*Extrapolated values.

Liquid thermal conductivity [15, 90]

From Vargaftik et al. 1996 [15]		
T_{sat}	k_l	Uncertainty
[K]	[W/(m·K)]	[%]
400	50,2	±5
500	47,6	±5
600	45,0	±5
700	42,4	±5
800	39,9	±5
900	37,3	±5
1000	34,7	±5
1100	32,1	±5

Vapour thermal conductivity [15]

From Vargaftik et al. 1996 [15]		
T_{sat}	k_v	Uncertainty
[K]	[W/(m·K)]	[%]
400	0,00497*	
500	0,00763*	
600	0,01043*	
700	0,0132	±4
800	0,01574	±4
900	0,01793	±4
1000	0,01969	±4
1100	0,02109	±4

*Extrapolated values.

Liquid surface tension [15, 90]

From Vargaftik et al. 1996 [15]		
T_{sat}	σ	Uncertainty
[K]	[N/m]	[%]
400	$108 \cdot 10^{-3}$	± 5
500	$101 \cdot 10^{-3}$	± 5
600	$94 \cdot 10^{-3}$	± 5
700	$87 \cdot 10^{-3}$	± 5
800	$79 \cdot 10^{-3}$	± 5
900	$72 \cdot 10^{-3}$	± 5
1000	$64 \cdot 10^{-3}$	± 5
1100	$57 \cdot 10^{-3}$	± 5

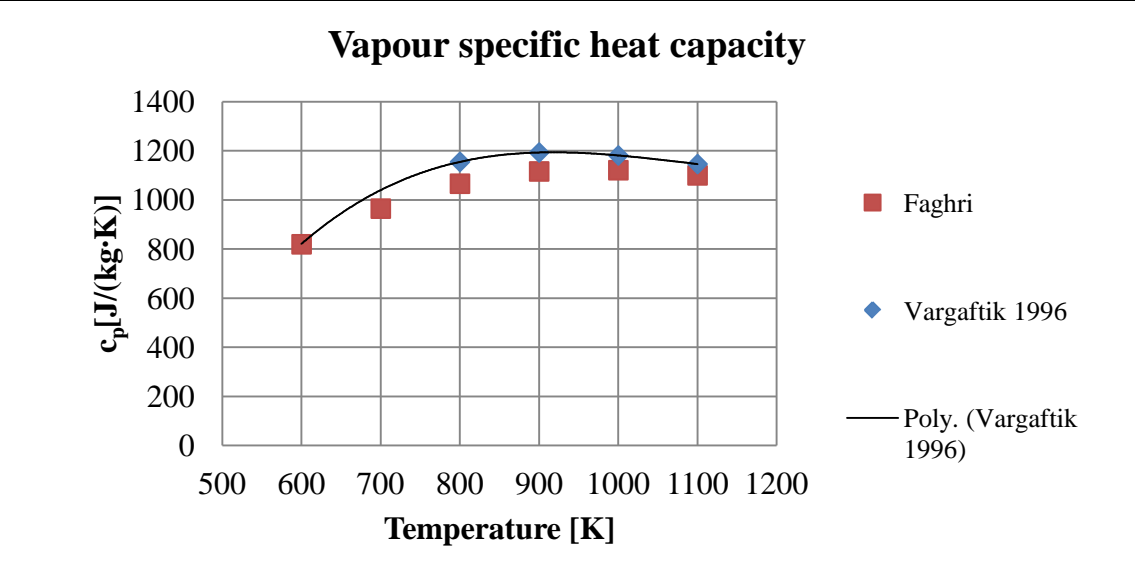
Liquid specific heat capacity [15]

From Vargaftik et al. 1996 [15]		
T_{sat}	$c_{p,l}$	Uncertainty
[K]	[kJ/kg·K]	[%]
400	0,8069	± 14
500	0,7862	± 14
600	0,7714	± 14
700	0,7634	± 14
800	0,7632	± 14
900	0,7706	± 14
1000	0,7859	± 14
1100	0,8092	± 14

Vapour specific heat capacity [15, 90]

From Vargaftik et al. 1996 [15]			From Faghri [21]
T_{sat}	$c_{p,v}$	Uncertainty	
[K]	[J/kg·K]	[%]	
400			
500			
600	821*		819,4
700	1040*		964,6
800	1155		1066
900	1193		1116
1000	1181		1121
1100	1146		1100

*Extrapolated values, see figure below.



Appendix F The filling and sealing rig

The rig designed for evacuation, outgassing, filling and sealing of the hybrid heat pipe

The rig described here was designed but not used for the final filling and sealing process, due to problems related to the high reactivity and stickiness of potassium.

Evacuation and outgassing

Ideally there should be only pure working fluid in the hybrid heat pipe. In the real case there will be some other components present. The components may be divided into two groups:

1. Non-condensable components. Non-condensable gases are most undesirable; they will accumulate in the condenser section and hamper the condensation of the working fluid.
2. Reacting components. Here oxygen is probably the most important reacting component, depending on the concentration and temperature it can form various compounds with potassium and nickel [Barker, Barker].

Since both non-condensable and reacting components are undesirable it was important to minimize their concentrations in the hybrid heat pipe. This required evacuation and outgassing of the hybrid heat pipe before filling and sealing.

In this work evacuation was defined as the removal of air from the hybrid heat pipe interior, by use of vacuum pumps. Outgassing was defined as the process of simultaneous evacuation and heating, with the goal to desorb and remove as much undesired elements from the hybrid heat pipe interior as possible. After the evacuation and outgassing the hybrid heat pipe was going to be filled with potassium and sealed.

Sealing of the heat pipe

In principle sealing could be done in two ways:

1. By use of a valve.
2. By making a permanent seal, for instance by welding.

Important factors for the choice of sealing method:

1. Nickel reacts with oxygen, the rate is very high at temperatures above ca. 300°C.
2. Potassium reacts with air and humidity.
3. The working temperature range is 400-650°C.
4. The vapour pressure of potassium is very low in the working temperature range.

A gas tight weld was considered as the safest seal. An approach based on induction welding under vacuum was used at Reading University [Reay]. Unfortunately the alkali metal heat pipe research activity at Reading University ended years ago, and the setup does no longer exist. With no detailed information available about the setup at Reading University this method required an experimental study to determine the parameters for the sealing by induction welding.

Induction welding under controlled gas atmosphere

The real heat pipe filling and sealing had to be carried out under vacuum. However, a setup for induction welding under controlled gas atmosphere was available in our laboratories. In order to gain experience on induction welding it was decided to do two tests with this setup. A special feature of the setup was that the axial pressure on the sample could be measured during the induction welding. The tests were carried out by the owners of the setup, AMR Engineering AS.

The test chamber was evacuated and filled with a gas mixture of 10% H₂ and 90 % N₂ in which the welding took place

Test 1:

The tube was mounted in the lower chuck and the plug in the upper chuck. The coil, which was just 3 mm thick (high), was adjusted to surround the welding zone. The temperature was measured by use of a thermocouple (type K) welded to the surface of the tube a couple of millimeters below the tube/plug interface. The temperature measurement was considered as an indicative measurement rather than a high precision measurement, due to the unknown magnitude of the error caused by the effect of the magnetic field on the thermocouple. A careful stepwise approach was chosen to see the response of the sample to the induction heating. A total of 5 heating periods of 8-11 seconds were run. The maximum temperature measured was 1300°C. The melting range of nickel 200/201 is 1335-1446°C [Specialmetals]. No sign of melting could be seen on the sample, but the plug was mechanically attached to the tube. (The plug could not be removed by hand). No leak could be detected in a simple test where the welded part of the sample was immersed in water.

Because of the fixing of the tube and the plug in the chucks the thermal expansion during the induction heating caused an axial force of around 2000N. From experience such a force could have contributed to the successful welding of the parts [Salberg]. Without having the possibility to impose such an axial force in the real filling setup it was decided to do a second test, this time with the plug loosely fixed in the chuck.

Test 2:

With the plug loosely fixed in the upper chuck the axial force due to thermal expansion was almost eliminated. The welding without visible melting did also this time attach the plug to the tube. On the other side this weld was not water tight, big leaks were detected in the water immersion test.

After the completion of the second test the setup was no longer available for further testing. It was therefore necessary to build a new setup to establish the correct parameters for successful sealing by induction welding. By replacing the active gas atmosphere with vacuum the new setup was made more relevant for the real application.

Induction welding in vacuum

A new induction welding setup was made in order to develop a detailed robust procedure for the sealing of the filling tube under vacuum. The chamber and coil are shown in Figure F-1 below. The picture was taken during one of the welding experiments so the tube and plug are glowing.



Figure F-1 The induction welding test setup

The chamber was connected to a vacuum pump, Pfeiffer Type DUO 004 A having 4 m³/h pumping speed. The pressure was measured by use of an Edwards Pirani Gauge Head M50-2 connected to a Speedivac Model 8/2 analogue display, also from Edwards High Vacuum LTD, England. Since the equipment had not been used for some time it was calibrated against a newer gauge, in order to have more reliable pressure level indications.

The frequency generator was an EFD Minac 50, the specifications can be found below. The Minac 50 had an external control option which was connected to a thermocouple temperature measurement. This made it possible to cut the power to the induction coil when the temperature read by the thermocouple reached a preset temperature limit.

The induction coil was made of copper tube with 6,35 mm outer diameter and wall thickness 1 mm. The inner diameter of the single loop coil was 20 mm

Experiments on induction welding in vacuum

In all the experiments the nominal output power of the Minac 50 was set to 18,5 kW. The heating period was in all experiments controlled by a temperature measurement on the surface of the sample. The working range of the type K thermocouples was from -250°C to 1372°C [Wheeler]. The melting temperature range of the Nickel 201 was 1435-1446°C [Specialmetals]. By attaching the thermocouple some millimeters away from the tube/plug interface it was possible to have melting at the interface without exceeding the temperature limit of the thermocouple. The external control function was set to cut the power to the induction coil when the thermocouple temperature reached 1350°C. The thermocouple was best attached to the nickel tube by spot welding.

For effective welding it was crucial that the two parts (i.e. the end of the tube and the plug) were heated equally, and this was best achieved if the material thicknesses of the two parts were equal.

Ni201 tubes of outer diameter $\varnothing_o=13,5$ mm and inner diameter $\varnothing_i=9,5$ mm were used.

Before all the experiments the plug, the tube and the ring (if used) were cleaned with soap and water, and then rinsed with acetone.

In the previous induction welding tests under controlled gas atmosphere it was observed that the plug was lifted up from the tube when the induction power was applied. It was therefore decided to make a holder for the plug in the vacuum setup. The holder made of a ceramic material, was mounted on a spring attached to the plexiglass cover of the vacuum chamber. The force from the spring was measured by pushing it against a balance. The maximum weight measured at maximum compression was 660 gram. I.e. the force from the holder on the plug never exceeded 6,5 N.

After the experiments the welds were leakage tested by use of a "Varian 936-40 contra-flow helium leak detector". The leak detector was operated by lab engineer Reidar Tellebon.

A total of 8 induction welding experiments were carried out. Experimental details and results are reported in the Table F-1 below.

Table F-1 Induction welding experiments with the test setup

No.	Description	Distance TC-top of the tube [mm]	Max. temp. [°C]	Results		Leak
				Heating period [s]	Comments	
1	A first test of the setup.	1-2	1000	11	It was observed that: The tube was heated much faster than the plug. The chamber was heated up at the feethrough of the coil, especially at one place where the distance between the coil and the chamber was only about 10 mm.	Yes
2	In this experiment a modified plug was used. The coil was modified to increase the distance from the chamber.	2-2,5	1350	16	No melting could be seen. The plug could be removed by hand. The tube was heated up faster than the plug. The heating of the chamber was reduced by the increased distance to the coil.	Yes
3	In this experiment the distance TC-top of tube was increased. The sample was mounted lower compared to the coil.	3	1350	21	The tube and plug were heated at a quite uniform rate. The plug was partly welded to the tube.	Yes
4	This time a ring was placed between the plug and the tube.	5	1350	34	Melting and boiling of the lower flange of the plug were observed. The plug was partly forced into the tube by the force from the spring. The coil became black of soot that was easily wiped off.	No

5	This experiment was an attempt to reproduce experiment 4.	5	1350	30	The experiment was a successful reproduction of experiment 4.	No
6	This experiment was carried out without ring.	5	1350	35	Some melted nickel had run down inside the tube.	No
7	This experiment was with ring but without spring and holder.	5	1350	25	The heating seemed this time to start lower on the tube. Without the spring to force the plug down the result looked somewhat different than in the last experiments.	No
8	Without ring and without spring and holder.	4	1350	22	Nice weld.	No

The frequency of the induction generator changed automatically from 11 to 12 kHz from experiment 1 to experiment 2. This was probably due to a modification of the coil made after experiment 1. The modification increased the distance to the chamber at the coil feedthrough, and eliminated undesired induction heating of the chamber at the feedthrough. The modification implied that the tubes of the coil were partly bent closer together and this probably caused a higher frequency.

The picture in Figure F-2 shows a tube and plug successfully weld together, as well as the thermocouple which was attached just below the welding zone.



Figure F-2 Tube and plug weld together

Conclusions:

The results showed that leak tight welds could be achieved both with and without ring and with and without holder. The vertical position of the coil was important for correct heating of the welding zone. The length of the heating period could be adjusted by changing the distance from the welding zone to the thermocouple.

Evacuation, outgassing, filling and sealing of the heat pipe

The purpose of the rig and experiments described above was to determine the parameters and procedures for the sealing the heat pipe by induction welding. While the vacuum in that rig was sufficient to avoid visible nickel oxide formation during induction welding it was not sufficient for evacuation and outgassing of the the hybrid heat pipe. It was therefore necessary to construct a high vacuum rig for the real case. The rig was designed by stud. tech. Kolbeinn Kristjansson as one part of his master thesis, in close cooperation with an expert on vacuum systems and Geir Hansen. Several lab engineers also contributed to the design.

General overview of the high vacuum rig

The rig was mostly built up of standard high vacuum components. Flanges of CF (ConFlat) type were used throughout the rig, only the connection to the vacuum pump station was of KF type. CF gaskets of nickel were used where there could be direct contact between liquid potassium and the gaskets. All the other CF gaskets were made of copper. The CF flanges were rated to $1 \cdot 10^{-13}$ mbar [Caburn].

The main chamber was a tailor-made six-way cross. Through the bottom port of the six-way cross came the filling tube of the heat pipe. The side ports were used for:

- Viewport
- Vacuum gauge
- RF induction coil
- Vacuum pump

Through the top of the six-way cross came the tube from the filling bottle and the multi-motion manipulator.

The mutual interaction between the induction coil and the inlet port was one of the important issues in the design of the main chamber. Two arguments for increasing the port diameter were:

1. A small diameter port would be heated by induction.
2. A small diameter port may reduce the frequency of the induction currents.

One argument for decreasing the port diameter:

3. Decreased port diameter would decrease the length of the filling tube and thereby increase the conductance. Reduced conductance would increase the time needed to reach desired vacuum.

Point 1 and 2 were considered as more important than point 3.

The filling bottle was simply the open space in an all metal valve. In order to avoid contact with copper the all metal valve had a special valve seat of nickel plated copper. The gaskets were of nickel. The all metal valve was attached to a multi-mini flange and another valve, and together these three components formed a “bottle” for the potassium.

A photo of the high vacuum rig is shown in Figure F-3.



Figure F-3 The high vacuum rig

Testing of the high vacuum rig

The welding knowledge acquired during the previous induction welding experiments made it possible to carry out successful induction welding in the high vacuum rig without the use of a thermocouple attached below the welding zone.

The high vacuum and sealing by induction welding capabilities of the high vacuum rig were tested with success in experiments not involving potassium. However, the attempts to carry out the real filling and sealing process failed because:

- Potassium was very difficult to get out of the glass ampoules.
- Potassium oxidized even in the glove box.
- Potassium was sticking to the wall of the filling rig (“bottle” and tubes).

A modified procedure was developed, where the potassium was planned to be filled directly into the hybrid heat pipe in the glove box (instead of filling it into the “bottle”). The hybrid heat pipe containing potassium and argon was then planned to be transferred to the high vacuum rig for evacuation and sealing. One attempt was made to carry out this approach, but it failed already at the first stage in the glove box. The stickiness of the potassium, and the fact that it solidifies at $63,7^{\circ}\text{C}$, were again causing problems.

A better glove box, and unlimited access to it, would probably have solved these problems. A successful procedure for the potassium transfer in the glove box could then have been developed. The procedure may have utilized a heated syringe to get the potassium out of the glass ampoules.

Taken into account the time and resources needed to solve these problems it was decided to get potassium filled into the hybrid heat pipe at an external laboratory, which was utilizing the heated syringe technique.



1 TECHNICAL SPECIFICATION

1.1 Minac 50 Induction Heating System

SUPPLY

Supply voltage range	: 400–480 V \pm 10 %
Frequency	: 50/60 Hz
Nominal line current (RMS)	: 91 A
Maximum line current (RMS)	: 142 A
Nominal apparent power	: 60 kVA
Maximum apparent power	: 93 kVA
Power factor (cos ϕ)	: 0.95
Recommended fuse	: 100 A
Mains cable length	: 5 m

OUTPUT

Nominal output power	: 50 kW
Output power, intermittent duty	: 80 kW at 400 VAC
Duty factor/Cycle time	: 0.5/10 min
Output power regulation range	: 10–100 %
Frequency range	: 10–25 kHz
Efficiency	: 0.93
Flexible HHT power cable length	: 5 m

COOLING

Cooling water consumption, min.	: 20 l/min
Cooling water inlet temperature, max.	: 35 °C
Cooling water pressure, min./max.	: 4/6 bar
Ambient operating temperature	: +5 °C - +50 °C

ENCLOSURE

Outer dimensions, mobile cabinet (WxDxH)	: 610 x 1218 x 1060 mm
Outer dimensions, stationary cabinet (WxDxH)	: 548 x 678 x 883 mm
Weight with mobile cabinet	: approx. 230 kg
Weight with stationary cabinet	: approx. 195 kg
Enclosure protection	: IP 54
Color	: RAL 7032 Gray
Outer dimensions HHT without handle (LxOD)	: 190 x 77 mm
Weight HHT without handle	: 7.5 kg

NOTE.

To obtain the given enclosure protection, IP 54, the glass cover over the operating panel and the electronics rack must be kept closed.

Appendix G Safety, health and environment

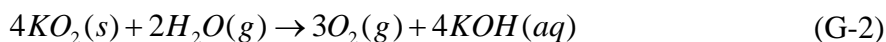
Potassium and oxygen

When potassium reacts with oxygen there can be formed both potassium peroxide (K_2O_2), potassium oxide (K_2O) and potassium superoxide (KO_2).

Potassium superoxide (KO_2) is known for its reactivity and can be formed when potassium reacts with oxygen (or air) even at room temperature [21].

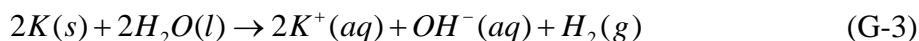


The heat of formation of KO_2 is $-284,5\text{kJ/mol}$ [91]. In contact with water/moisture the potassium superoxide will react according to Equation (G-2). Oxygen gas and an alkaline aqueous solution are formed.



Potassium and water

Hydrogen gas is produced when potassium and water/moisture react according to Equation (G-3):

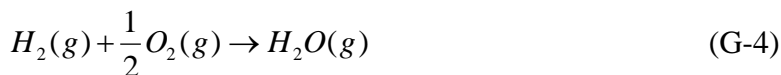


Hydrogen gas together with oxygen forms an explosive mixture. An explosion is a fast exothermic reaction from which there is formed a shock wave [92]. The shock wave can be caused by [92]:

1. Sudden release of a large amount of gas in the reaction.
2. Sudden release of energy which heats up gases in the vicinity of the reaction.

Without a powerful ignition source a deflagration (rapid burning) is likely to take place. A deflagration will produce a subsonic wave. With a powerful ignition source a detonation can take place [93]. The detonation produces a supersonic wave.

The explosive nature of the reaction between hydrogen gas and oxygen gas is caused by the heat released [92].

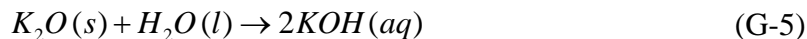


The enthalpy change in the reaction (Equation (G-4)) is $\Delta H = -241,8\text{kJ}$ [92].

The amount of potassium used in the experimental hybrid heat pipe was approximately 10g, which corresponds to 0,256 mol. From Equation (G-3) there will be formed 0,5 mol of H₂ for each mole of potassium. The maximum amount of hydrogen gas (H₂) formed from 10 g of potassium reacting with water is therefore about 0,128 mol ≈ 0,26 g. If this amount of hydrogen gas is allowed to react according to Equation (G-4) there will be released about 0,128·241,8 ≈ 31 kJ.

Potassium oxide and water

When potassium oxide reacts with water there is not produced any hydrogen gas. The only product is a alkaline aqueous solution, according to Equation (G-5).



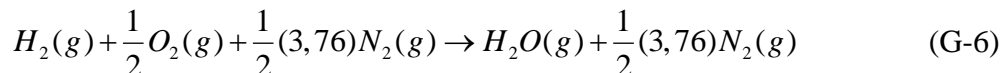
The high vacuum rig

In a situation of equipment breakdown there can be produced hydrogen from contact between potassium and water. For an explosion to occur it is necessary to have:

1. Hydrogen gas
2. Oxygen gas or air
3. An ignition source, i.e a spark/flame or something holding a higher temperature than the autoignition temperature of hydrogen in air (500°C).

The maximum amount of hydrogen gas produced from the 10g potassium is 0,128 mol, which corresponds to about 3,1 liters at a pressure of 1 bara and a temperature of 25°C. The volume of the main chamber of the high vacuum rig is approximately 5 liters.

In the experimental system there is no pure oxygen gas, oxygen will only be present as a component of air if air leaks into the system. For each mole of oxygen in air there is 3,76 moles of nitrogen, i.e. for stoichiometric combustion of hydrogen in air the reaction is:



For 0,128 mol of hydrogen gas the total volume of the reactants in Equation (G-6) is about 10,6 liter (from the ideal gas equation of state). In other words, the total volume required for complete combustion of 0,128 mol hydrogen in air at 1 bara and 25°C is about 2 times the volume of the main chamber of the rig. Complete deflagration of 0,128 mole of H₂ is therefore not possible in the chamber unless the pressure of the hydrogen air mixture is increased above 1 bara.

A constant volume deflagration of an uncompressed hydrogen air mixture at 1 bara would increase the pressure in the chamber to about 8 bara [93].

In the case of a water leak from the induction coil into the main chamber of the high vacuum rig (after filling the heat pipe with potassium and before it is sealed) there may be produced hydrogen gas according to Equation (G-3). The hydrogen gas will fill the upper part of the main chamber as well as the vacuum pipes above. In such case the hydrogen can be diluted by nitrogen to a concentration of 4% through a valve system and vented.

If there is air present the energy released in the reaction (Equation (G-3)) will probably increase the temperature enough to cause autoignition of the hydrogen, causing fire. Hydrogen air mixtures are explosive in the concentration range 4-74% H₂ by volume [94]. The autoignition temperature of such mixtures is 500°C [94].

Appendix H The nitrogen/water heat exchanger

AlfaNovaPlate Heat Exchanger



Technical Specification

Model : AlfaNova 14-10H(32870 5066 1)
 ItemName : Date : 15.07.2010
 Units : 1

		Hot Side	Cold side
		Secondary side	Primary
side(S4)		Nitrogen	Water
Fluid		Nitrogen	Water
Mass flow rate	kg/s	0.004931	0.02147
Fluid Condensed/Vapourized	kg/s	0.000	0.000
Inlet temperature	°C	200.0	15.0
Dew p.	°C		
Outlet temperature(vapor/liquid)	°C	25.0	25.0
Operating pressure(In/Out)	bara	2.00/ 1.96	
Pressure drop	kPa	4.28	0.305
Velocity connection(In/Out)	m/s	17.2/11.1	0.107/0.107
Heat Exchanged	kW	0.9000	
Heat transfer area	m²	0.10	
O.H.T.C clean conditions	W/(m²K)	264.4	
O.H.T.C service	W/(m²K)	153.9	
Fouling resistance*10000	m²K/W	0.0	
Margin	%	71.8	
Mean Temperature Difference	K	56.2	
Relative directions of fluids		Countercurrent	
Number of passes		1	1
Materialplate/ bonding		Alloy 316 / SS	
ConnectionS1 (Hot-In)		Threaded (External)/ 3/4" ISO 228/1-G (A21)	
Alloy 316			
ConnectionS2 (Hot-Out)		Threaded (External)/ 3/4" ISO 228/1-G (A21)	
Alloy 316			
ConnectionS3 (Cold-In)		Threaded (External)/ 3/4" ISO 228/1-G (A21)	
Alloy 316			
ConnectionS4 (Cold-Out)		Threaded (External)/ 3/4" ISO 228/1-G (A21)	
Alloy 316			
Pressure vessel code		PED	
Design pressure at 75.0 Celsius	Bar	23.0	23.0
Design pressure at 225.0 Celsius	Bar	20.0	20.0
Design temperature	°C	-196.0/225.0	
Overall length x width x height	mm	57 x 77 x 207	
Net weight, empty / operating	kg	1.20 / 1.20	
Package length x width x height	mm	190 x 93 x 233	
Package weight	kg	0.000	

Performance is conditioned on the accuracy of customers data and customers ability to supply equipment and products in conformity therewith.

Program version – 5.36, Rating 2-Phase

/15.07.2010/13:31:25

Physical Properties

(inlet/outlet)	Hot Side Liquid	Vapour	Cold side Liquid	Vapour
Dens	1.425/2.215		998.8/996.0	
Sp.heat	1.047/1.039		4.197/4.186	
Visc	0.0247/0.0177		1.14/0.895	
Th.Cond	0.0370/0.0258		0.595/0.610	

Appendix I Theory of uncertainty analysis

The uncertainty analysis in this work follows the book of Wheeler and Ganji [95] and the paper of Moffat [96]. Experimental results are reported in the form $X \pm \omega_p$ where ω_p is the uncertainty. All estimated uncertainties are at 95% confidence level, which means that the actual error is smaller than the estimated uncertainty in 95 of 100 cases.

Uncertainties are summarized by use of the *root of the sum of the squares* (RSS). The *root of the sum of squares* is a best-estimate of the uncertainty; it is not the maximum uncertainty which would occur if all errors occurred at their maximum values simultaneously. For the general case where the result R is a function of n independent variables x_1, x_2, \dots, x_n the *root of the sum of squares* (RSS) uncertainty ω_R becomes [95]:

$$\omega_R = \left(\sum_{i=1}^n \left[\omega_{x_i} \frac{\partial R}{\partial x_i} \right]^2 \right)^{1/2} \quad (\text{I-1})$$

where ω_{x_i} is the uncertainty in the variable x_i . The term $\frac{\partial R}{\partial x_i}$ is the sensitivity of the result R to a change in x_i . When uncertainties are “added” by use of RSS the larger uncertainties get much more weight than the smaller uncertainties. According to Moffat [96] it is usually acceptable to ignore terms which are smaller than 1/3 of the largest term.

Sometimes it is convenient to express the uncertainty as a fraction or percentage of the reading or result. The relative uncertainty $\frac{\delta R}{R}$ can be calculated directly for cases where the result R is calculated from an equation on “product form” [96]:

$$R = X_1^a X_2^b X_3^c \dots X_M^m \quad (\text{I-2})$$

$$\frac{\delta R}{R} = \left[\left(a \frac{\delta X_1}{X_1} \right)^2 + \left(b \frac{\delta X_2}{X_2} \right)^2 + \dots + \left(m \frac{\delta X_m}{X_m} \right)^2 \right]^{1/2} \quad (\text{I-3})$$

When the result is not obtained from a simple equation on product form, and the sensitivity coefficients can not be obtained, the impact of the uncertainty of each variable can be found by varying the variables one by one and calculating the response in R . The $\Delta R_i = (R_i - \text{new } R_i)$ caused by the different variables are then finally added by RSS to give the total uncertainty in R . This method has been widely applied in this study.

For many measuring devices the uncertainties are specified as “accuracy”, so also for devices in this study. The accuracy is defined as “the closeness of agreement between

measured value and the true value” [95]. A paradox pointed out by Wheeler and Ganji [95] is that it is the inaccuracy that is specified rather than the accuracy.

The method of sequential perturbations

The uncertainty terms of the inner brackets of the RSS-equation can also be determined directly from the experiment by perturbing the inputs. The procedure was described in detail by Moffat [96]. The method of sequential perturbations is a suitable approach when the mathematical relationship between the result R and the variables x_i is unknown or complex.

The uncertainty in the rate-of-rise and contact angle determination

The physical dimensions of the wick

The radius of the uncompressed foam was specified on the data sheet from the manufacturer, but without giving any information about the uncertainty. The pore radius was therefore considered as an average value, with unknown uncertainty. The effect of a 10% error in the pore radius was investigated.

The foam thicknesses were measured by use of vernier calipers that had an uncertainty of $\pm 0,03$ mm. The thickness of the uncompressed Foam 2 was 1,7 mm (according to the data sheet for the foam), and after the compression the thickness was 0,31 mm. In the uncertainty analysis the effect of a 10% error in the thickness ratio was investigated.

The porosity

The determination of the porosity was based on mass measurements and followed the ISO-standard [97]. When the standard is followed the porosity can be reported to the nearest 0,1% (V/V). In other words, the accuracy of the porosity measurements is very good if the standard is followed. For the porosity experiments in this study the accuracy of the mass and temperature measurements were better than specified by the standard. The only deviation from the standard in this work was the sample sizes, which were smaller than specified by the standard. This was believed to have only minor effect on the porosity results. Porosity variations within the uncertainty claimed by the porosity standard would have negligible impact on the effective pore radius and permeability.

The rate-of-rise experiment

The effective pore radius was determined together with the permeability from the rate-of-rise experiment. The variables of the rate-of-rise experiment were:

$$\kappa, r_{eff} = f(m, \dot{m}, \dot{m}_{evap}, T, A_c, \varepsilon, \rho, H, \mu, \sigma, g) \quad (\text{I-4})$$

The mass of liquid, m , was measured by use of the electronic balance, a Mettler AT261 which had 0,01 mg resolution. The uncertainty related to the mass measurements was probably more related to disturbances of the liquid surface, which more or less

unavoidably occurred when the wick tip was immersed, rather than to the accuracy of the balance.

In the rate-of-rise experiment the evaporation of the fluid had a cooling effect, both on the liquid pool of the petri dish, but also on the wick. The liquid properties were therefore evaluated at the arithmetic average temperature of the start and end temperatures of the liquid in the petri dish. The temperatures were measured by use of a thermocouple type N, which had an uncertainty of $\pm 0,3\text{K}$ at room temperature according to the calibration certificate. The thermocouple logging module, NI9211 from National Instruments, had an uncertainty of $\pm 1,2\text{K}$ at the room temperature. The overall root-sum-square (RSS) uncertainty [95] of the temperature measurements was calculated to $\pm 1,24\text{K}$. This error in fluid temperature would lead to very small, negligible, changes in the properties of the model fluid, liquid heptane.

The errors due to the numerical conversion of mass data to height data were presumed minor and neglected.

Specific estimates of the uncertainties were made for wick 12 of paper 2 [30]. The analysis did also clarify in which direction the independent variables affected the dependent variables. The results are summarized in the table below.

Table I-1 Results of the uncertainty analysis for wick 12 [30].

	Uncertainty estimate
Porosity	$\pm 0,1\%$
The contact angle	$\pm 8,9\%$
Permeability, κ	$\pm 26\%$
Effective pore radius, r_{eff}	$\pm 2\%$
Heat transfer capacity, \dot{Q}	$\pm 26,7\%$

From the calculations it was noted that:

- An increase in liquid viscosity had to be accompanied by an increase in the permeability in order to leave the capacity of the wick unchanged.
- An increase in the liquid surface tension had to be accompanied by an increase in the effective pore radius in order to leave the capacity of the wick unchanged.

- An increase in the liquid density had to be accompanied by a decrease in the permeability in order to leave the capacity of the wick unchanged.
- An increase in the wick thickness had to be accompanied by a decrease in the permeability and by an increase in the effective pore radius in order to leave the capacity of the wick unchanged.

It may also be of interest to consider some statistics from repeated experiments. For the wicks 9-12 in Paper 2, which were expected to have the same results for the effective pore radius and permeability, the average effective radius was $105 \cdot 10^{-6}$ m with a standard deviation of $1,2 \cdot 10^{-6}$ m. The average permeability was $117,5 \cdot 10^{-12}$ m² with a standard deviation of $9,0 \cdot 10^{-12}$ m². Assuming students distribution and a confidence level of 95% this corresponds to:

$$r_{eff} = 105 \cdot 10^{-6} \pm 1,7 \cdot 10^{-6} \text{ m} \quad (\text{i.e. } \pm 2 \%)$$

$$\kappa = 117 \cdot 10^{-12} \pm 12,5 \cdot 10^{-12} \text{ m}^2 \quad (\text{i.e. } \pm 11 \%).$$

Higher uncertainty for the permeability than for the effective pore radius is in accordance with the results of the uncertainty analysis.

The heat transfer capacity

The uncertainties in the effective pore radius and the permeability propagates further to the wick heat transfer capacity through the following equation

$$\dot{Q} = \dot{m}_{y=0} h_{fg} = \frac{2\kappa A_c \rho}{H \mu} \left(\frac{2\sigma}{r_{eff}} - \rho g H \right) h_{fg} \quad (\text{I-5})$$

I.e. the heat transfer capacity depends on the following variables:

$$\dot{Q} = f(\kappa, r_{eff}, A_c, H, \mu, \sigma, \rho, h_{fg}, g, T)$$

The contact angle

The contact angle of heptane on the wicks was estimated from

$$\theta = \cos^{-1} \left(\left(\frac{r}{2\sigma} \right) \left(\rho_l g H + \frac{\mu}{\kappa \rho_l A_c} \dot{m}_{\max} \left(\frac{H}{2} \right) \right) \right) \quad (\text{I-6})$$

where

$$r = r_0 \frac{\delta}{\delta_0} \quad (\text{I-7})$$

I.e.

$$\theta = f \left(r_0, \frac{\delta}{\delta_0}, r_{eff}, \kappa, A_c, \dot{m}_{max}, \sigma, \rho_l, \mu \right) \quad (\text{I-8})$$

where the height H was a function of the other variables listed. The uncertainty related to the use of the capillary tube model as a model for the wick structure was not taken into consideration.

Uncertainty analysis for the hybrid heat pipe testrig.

Uncertainty estimation for the electrical power measurements

The wiring diagrams for the heat pipe test rig are enclosed in Appendix J. The correctness of the determination of the supplied power was confirmed by several tests carried out by electrical engineers.

The electrical power was calculated from measurements of voltage and current. Modules from National Instruments® were used for the voltage and current measurements. The accuracies of the modules are shown in the table below, as reported in their specifications.

Table I-2 Accuracy for modules from National Instruments®

	Accuracy	Measurement conditions
NI 9225 (voltage)	±0,084% of reading and ±0,016% of range (425 V)	25°C±15°C
NI 9227 (current)	±0,011 mA	-40°C to 70°C

The best-estimate of the uncertainty (ω_p) of a power measurement is then given by:

$$\omega_p = \left(\left(\omega_U \frac{\partial P}{\partial U} \right)^2 + \left(\omega_I \frac{\partial P}{\partial I} \right)^2 \right)^{1/2} \quad (\text{I-9})$$

Example:

The NI-modules report voltage $U=229V$ and current $I=4A$. What is the power $P \pm \omega_p$?

The uncertainty in the voltage measurement is

$$\omega_U = \pm \sqrt{(0,00084 \cdot 229)^2 + (0,00016 \cdot 425)^2} = \pm 0,204V$$

and the uncertainty in the current measurement is $\pm 0,000011A$.

The uncertainty in the computation of the power is then:

$$\omega_P = \pm \left((0,204 \cdot 4)^2 + (0,000011 \cdot 229)^2 \right)^{1/2} = \pm 0,8W$$

Finally: $P = 916 \pm 0,8W$

I.e. for the real experiments where the maximum power was about 620 W per section the uncertainty in the power determination was less than 1 %.

Two experimental test series were carried out before the NI-modules were implemented for power measurements in the real system. The tests were carried out by electrical engineer Marius Østnor Døllner [98]:

Test 1: Instrument vs. Instrument

The intention was to compare the power measured by use of the National Instruments modules (NI 9225 and NI 9227) to the power measured with a Fluke 43 Power Quality Analyzer. Both were measuring the thyristor output to a 1000 W (nominal) cartridge heater element.

Conclusions from Test 1: There was good agreement between the measurements; the difference was never more than 5%. The differences could be due to different sampling rates, and the fact that the National Instruments modules were brand new while the Fluke 43 was some years old and not calibrated. The two Ni modules were sampling at a rate of 10000 samples per second. A high sampling rate is necessary to record the shape and variations of the output of a phase angle firing thyristor.

Test 2: Estimation vs. Instrument vs. Instrument

In test 2 the resistance of a 1000 W (nominal) cartridge heater was first measured to 53 ohm at room temperature, by use of a multimeter (Fluke 117). The voltage from the thyristor at 20 mA signal (100%) was measured with the NI 9225 to 228,1 V. From this a maximum power of 981,7 W was estimated for the cartridge heater. A series of measurements were then carried out to compare estimated power, power measured by use of the NI-modules and power measured by use of the Fluke 43. The comparison was carried out for 0%, 25%, 50%, 75%, and 100% of the estimated maximum power 981,7 W. The temperature dependence of the resistance was not taken into account in the estimates. The results are shown in Table I-3.

Table I-3

Signal to the thyristor	[mA]	20,000	4,000	8,000	12,000	16,000	20,000
Temperature of element	[°C]	524,7	97,5	125,4	172,9	414,5	546,0
Current from NI 9227	[Arms]	4,241	0,001	2,124	3,010	3,667	4,257
Voltage from NI 9225	[Vrms]	229,617	0,0041	113,479	161,894	199,354	229,895
Current from Fluke 43	[Arms]	4,270	0,005	2,158	3,055	3,693	4,288
Voltage from Fluke 43	[Vrms]	229,800	0,033	113,700	161,900	199,600	229,500
Estimated power	[W]	981,7	0	245,3	490,9	736,3	981,7
Power from NI-modules	[W]	973,8	0	241,0	487,3	731,0	978,7
Power from Fluke 43	[W]	981,2	0	245,4	494,6	737,1	984,1

Conclusions from Test 2:

The three different methods to determine the power gave quite similar results. Taken into account the uncertainties of the power estimate and the Fluke 43 they can not be considered to give more correct results than the NI-modules.

Conclusion from Test 1 and 2:

There is no reason to suspect larger errors for the power measurements than what follows from the inherent accuracies of the NI-modules.

Uncertainty estimation for the temperature measurements

The uncertainties of the temperature measurements of this study are related to:

- The uncertainty related to the non-ideality of the thermocouple.
- The uncertainty of the thermocouple logging modules.
- The uncertainty related to the position of the thermocouple; this was addressed in Chapter 3.6.

In this study 50 mineral insulated metal sheathed thermocouples of type N were used. They all were of length 1 meter and had a diameter of 1mm. They were all from the same production batch. The first and the last thermocouple in the batch were calibrated by a professional calibration laboratory. The calibration certificates are enclosed, but they were replaced by calibration results obtained by use of brand new JOFRA 65-RTC-

700 C calibrator, which became available during this study. The uncertainty of thermocouples calibrated by use of the JOFRA calibrator is $\pm 0,11^{\circ}\text{C}$. During the calibration and use the thermocouples were connected by extension wires for type N thermocouples to 3 high-accuracy thermocouple modules type NI 9214 from National Instruments. Each module had 16 channels and were connected to a PC running LabView®. The recommended warm up time for the modules was 15 minutes. They were mounted in a corner of a cabinet equipped with a thermostat and a cooling fan. The cabinet also contained the other measurement modules, thyristors and electronic equipments for the test rig. For high measurement accuracy it is recommended that the compensation cables are mounted more than 0,3 meter from powerlines, in order to avoid disturbance by induction [99]. The calibrations and integration of the results into LabView were carried out by electrical engineer Odin Hoff Gardå. Each thermocouple was calibrated at the temperatures 50, 150, 300, 450, 600, 700, 600, 450, 300, 150, 50°C , using a stability criterion of $\pm 0,1\text{K}$ over 5 minutes. Average values were calculated from 100 samples, corresponding to 50 s for the sampling rate 2 Samples/s. The averages of the temperatures measured on the way up and down were used. Linear interpolation was utilized for temperatures between the calibration temperatures.

Uncertainty estimation for the nitrogen flow measurement

The nitrogen flow in the testrig is measured by use of a mass flow meter from Sierra Instruments.

Accuracy	Calibration temperature	Calibration pressure
$\pm 1\%$ of full scale and $\pm 0,5\%$ of reading	$50,00^{\circ}\text{C}$	1,20 Bara

Full scale is $23,45\text{ m}^3/\text{h}$ at reference pressure 1 atm and reference temperature 15°C . From the ideal gas law the density of nitrogen at the reference conditions ($P=101325\text{ Pa}$, $T=15^{\circ}\text{C}$) is $1,19\text{ kg}/\text{m}^3$. At full scale the mass flow is $(23,45 \cdot 1,19) = 27,9055\text{ kg}/\text{h} = 0,00775\text{ kg}/\text{s}$.

CALIBRATION CERTIFICATE

CERTIFICATE NUMBER	5532872115
--------------------	-------------------

PAGE 1 OF 1

Applicant/Customer
Name
Customer Address
City, State, Zip Code
Country
Sales Order 120253
Purchase Order
Instrument
Model 620S-L04-M1-EN2-V4-NR-10
Serial number 136685
Tag #: N/A
Input Power 18-30 Volt DC
Factory F/S 29.3125 **units** NM3/H
User Full Scale 23.45 **units** NM3/H
Output signal 4 20 **units** 4-20 mA
Display N/A
Totalizer N/A **Units per pulse:** N/A
Alarm settings 0 **Low** 23.45 **High**
Customer line size 40.5mm
Accuracy DUT (+/-) 1.0% F/S

Calibration method
Calibration Station/Cal Due Date Flobot Asset # 0479 January 17, 2011
Calibration Procedure 6440 Rev. D
Software release Flobot Calibration System, Rev. 1.01.13
Repeatability +/- 0.2% of full scale
Temperature coefficient +/- 0.02% of reading per °F within +/- 50°F of customer specified conditions
Pressure coefficient 0.02% per psi for air, consult factory for other gases
System ERROR maximum systematic ERROR = 0.2%
DMM Asset / Cal Due Date 1373 January 19, 2011

Calibration details
Date of calibration October 28, 2010
Suggested recal date October 28, 2011

Calibration data
Ambient pressure 29.72 In Hg a.
Ambient temperature 69.00 °F
Gas Nitrogen
Calibration gas Nitrogen
K-Factor 1.000
Reference temperature 15.0 °C
Reference pressure 1 ATM
Calibration pressure 1.20 Bar a.
Calibration temperature 50.00 °C

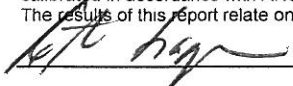
Other
 Special Calibration Information

Calibration results


Bridge	Output	Indicated Flow	Actual Flow	Difference	Difference
Voltage	4-20 mA	NM3/H	NM3/H	Allowable	Actual
3.383	4.000	0.000	0.0000	0.293	0.000
4.499	7.923	5.750	5.7120	0.293	0.038
4.895	12.000	11.725	11.6850	0.293	0.040
5.161	15.980	17.558	17.4910	0.293	0.067
5.367	19.980	23.421	23.3700	0.293	0.051

Traceability

Calibration of Sierra products is performed with equipment containing components which are tested and calibrated in accordance with ANSI/NCCL Z540 and/or ISO 17025 and are traceable to NIST. The results of this report relate only to the item calibrated or tested.

Calibration technician


Q.C. Technician



This calibration certificate shall not be reproduced, except in full, without the written approval of Sierra Instruments, Inc.



TC Ltd, Units 1-6, Brimington Rd North, Chesterfield, S41 9BE, United Kingdom
 Email: callab@tc.co.uk - Web: www.tc.co.uk
 Tel: 01895 252222 - Fax: 01895 273540

CERTIFICATE OF CALIBRATION

Date of Issue: 21st December 2010
Customer: Max Sievert A/S
Address: Hausmannsgt 6, N-0186 Oslo, Norway
Order Number: 84763
Our Reference: 22992M/1
Date Received: 2nd December 2010
Type: N 1.0mm dia x 1000mm long
Serial Number: 22992M/1/1A
Product Code: 12-N-1000-114-1.0-2I-3P6M
 Mineral Insulated Metal Sheathed Thermocouple
Ambient Temp: 20°C +/- 2°C

Page 1 of 1
Approved Signatory
 L R Walker
 K M Donaldson

K Donaldson

Certificate
Number : 18663 - 1A

Calibration Procedure: The thermocouple was calibrated by comparison with two reference resistance thermometers and two reference type R thermocouples. The calibration took place in a Venus dry block, a Neptune parallel tube liquid bath, a Ayrles fluidised alumina bath and a Lenton triple zone furnace. All measurements are traceable to recognised national standards. The thermocouple wires were referenced to 0 Degrees Celsius with the cold junction of the unit under test at ambient. The resistance and voltage outputs were measured on a precision digital multimeter. All tests were carried out in a controlled environment using devices having known and traceable values. The temperature measurements are traceable to ITS-90. The thermocouple voltages were converted using IEC584-1:1995.

REFERENCE TEMPERATURE (°C)	MEASURED VOLTAGE (µV)	EQUIVALENT IEC VALUE (°C)	ERROR (°C)	UNCERTAINTY (+/- °C)
0.16	3.8	0.15	-0.01	0.3
150.15	4320.5	150.60	0.45	0.3
299.82	9369.7	300.80	0.98	0.6
449.65	14892.7	451.23	1.58	0.6
600.52	20662.3	601.26	0.74	1.3
750.40	26520.3	750.76	0.36	1.3
900.76	32399.8	900.73	-0.03	1.3
750.18	26519.8	750.75	0.57	1.3
599.49	20630.3	600.44	0.95	1.3
450.89	14884.7	451.02	0.13	0.6
300.34	9354.2	300.36	0.02	0.6
150.09	4310.8	150.29	0.20	0.3
0.08	3.5	0.14	0.06	0.3

The depth of immersion of the test thermocouple was a minimum of 125mm

Calibrated by: T Heath

Calibration date: 21st December 2010

The reported expanded uncertainty is based on a standard uncertainty multiplied by a coverage factor of $k = 2$, providing a level of confidence of approximately 95%. The uncertainty evaluation has been carried out in accordance with UKAS requirements.

Note: It is the user's responsibility to determine the long-term drift and the uncertainty under the conditions of use

This certificate is issued in accordance with the laboratory accreditation requirements of the United Kingdom Accreditation Service. It provides traceability of measurement to recognised national standards, and to units of measurement realised at the National Physical Laboratory or other recognised national standards laboratories. This certificate may not be reproduced other than in full, except with the prior written approval of the issuing laboratory.

Issue 02/01



TC Ltd, Units 1-6, Brimington Rd North, Chesterfield, S41 9BE, United Kingdom
 Email: callab@tc.co.uk - Web: www.tc.co.uk
 Tel: 01895 252222 - Fax: 01895 273540

CERTIFICATE OF CALIBRATION

Date of Issue: 21st December 2010
Customer: Max Sievert A/S
Address: Hausmannsgt 6, N-0186 Oslo, Norway
Order Number: 84763
Our Reference: 22992M/1
Date Received: 2nd December 2010
Type: N 1.0mm dia x 1000mm long
Serial Number: 22992M/1/50A
Product Code: 12-N-1000-114-1.0-2I-3P6M
 Mineral Insulated Metal Sheathed Thermocouple
Ambient Temp: 20°C +/- 2°C

Page 1 of 1
Approved Signatory
 L R Walker
 K M Donaldson

K Donaldson

Certificate
Number : 18663 - 50A

Calibration Procedure: The thermocouple was calibrated by comparison with two reference resistance thermometers and two reference type R thermocouples. The calibration took place in a Venus dry block, a Neptune parallel tube liquid bath, a Ayries fluidised alumina bath and a Lenton triple zone furnace. All measurements are traceable to recognised national standards. The thermocouple wires were referenced to 0 Degrees Celsius with the cold junction of the unit under test at ambient. The resistance and voltage outputs were measured on a precision digital multimeter. All tests were carried out in a controlled environment using devices having known and traceable values. The temperature measurements are traceable to ITS-90. The thermocouple voltages were converted using IEC584-1:1995.

REFERENCE TEMPERATURE (°C)	MEASURED VOLTAGE (µV)	EQUIVALENT IEC VALUE (°C)	ERROR (°C)	UNCERTAINTY (+/- °C)
0.12	3.8	0.15	0.03	0.3
150.16	4315.3	150.43	0.27	0.3
299.83	9363.5	300.62	0.79	0.6
449.65	14886.0	451.05	1.40	0.6
600.46	20640.3	600.70	0.24	1.3
750.51	26500.3	750.25	-0.26	1.3
900.67	32372.3	900.02	-0.65	1.3
749.61	26466.8	749.40	-0.21	1.3
599.43	20602.0	599.70	0.27	1.3
450.81	14872.0	450.68	-0.13	0.6
300.36	9345.5	300.11	-0.25	0.6
150.09	4305.8	150.13	0.04	0.3
0.09	3.0	0.12	0.03	0.3

The depth of immersion of the test thermocouple was a minimum of 125mm

Calibrated by: T Heath

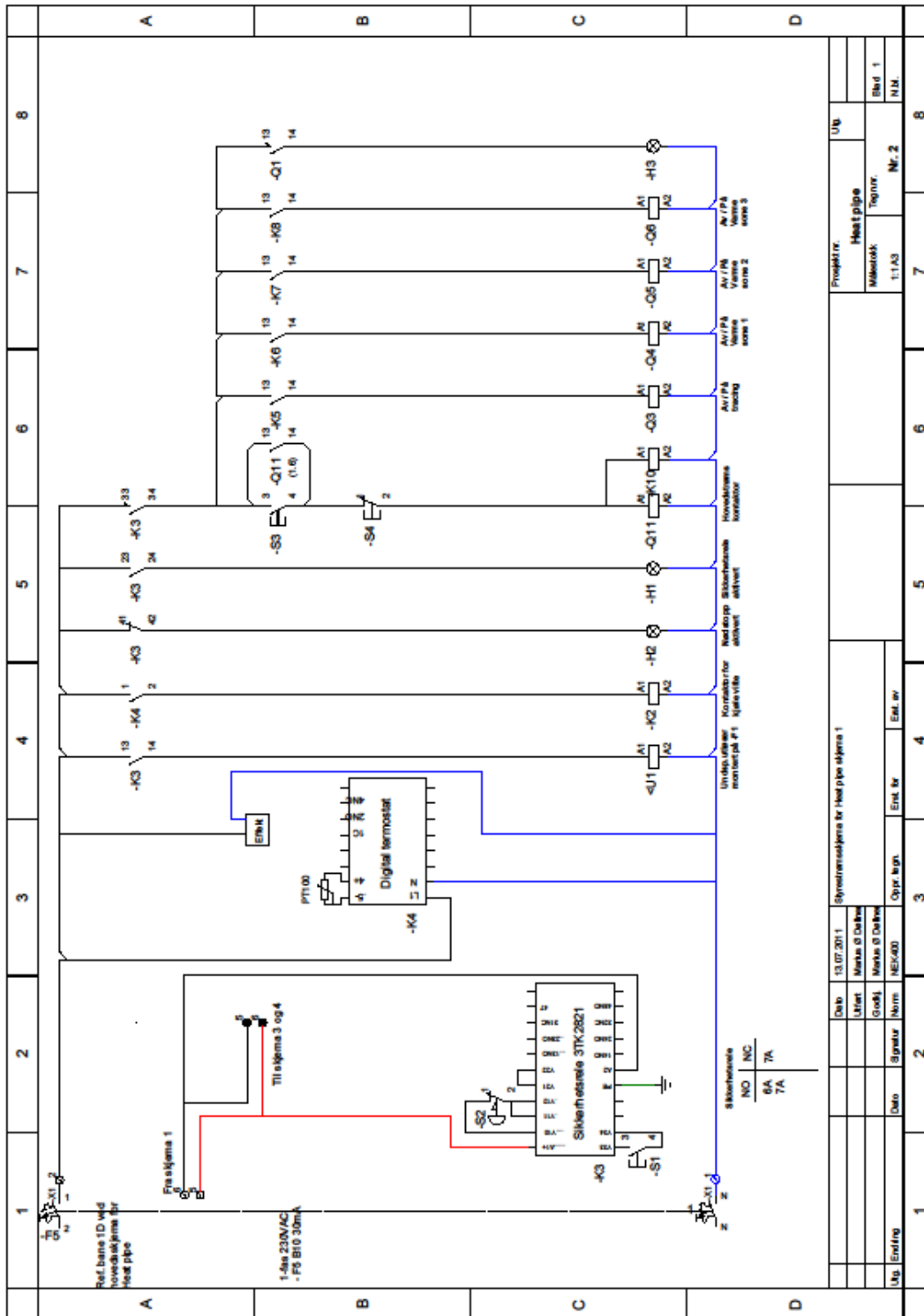
Calibration date: 21st December 2010

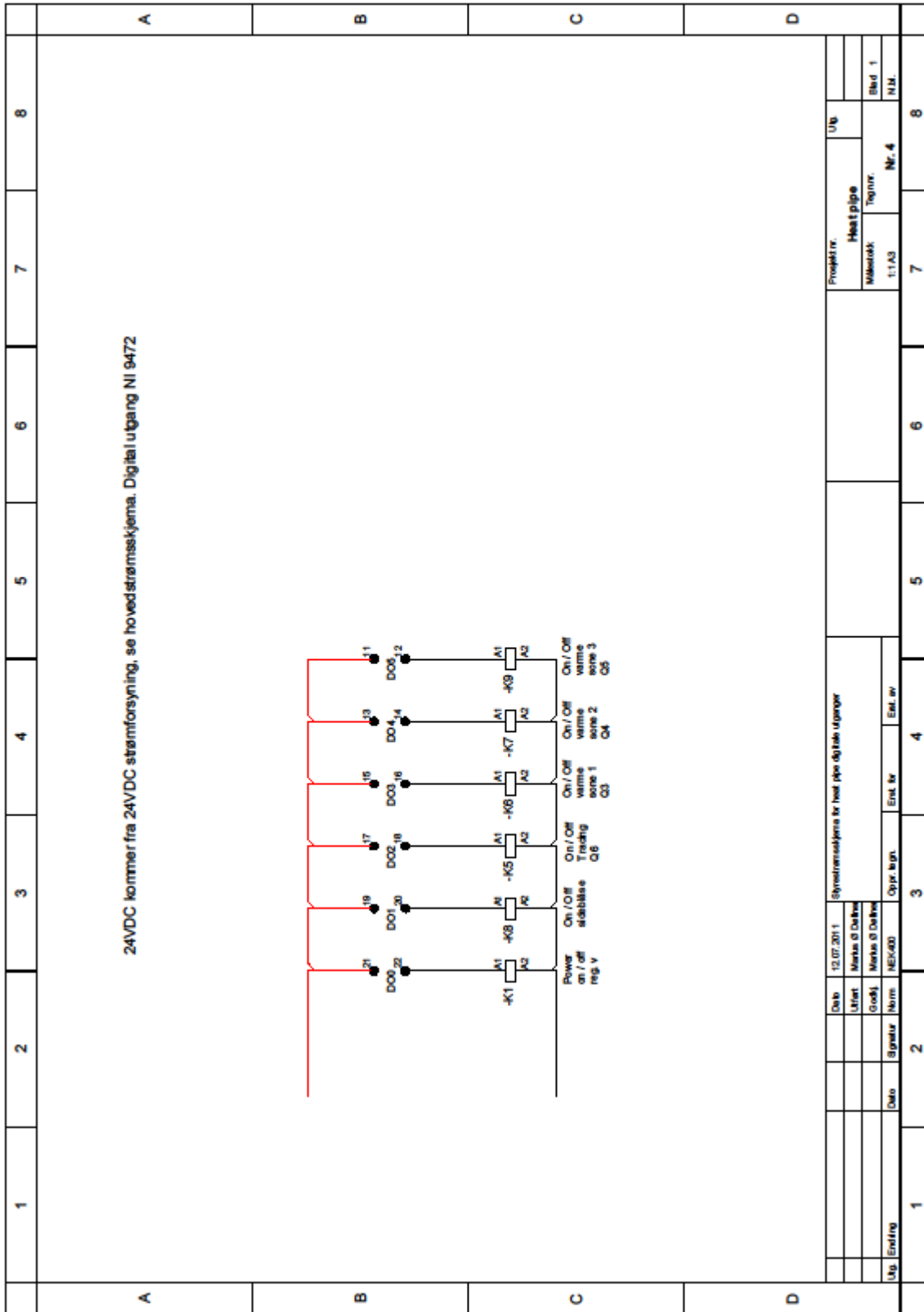
The reported expanded uncertainty is based on a standard uncertainty multiplied by a coverage factor of $k = 2$, providing a level of confidence of approximately 95%. The uncertainty evaluation has been carried out in accordance with UKAS requirements.

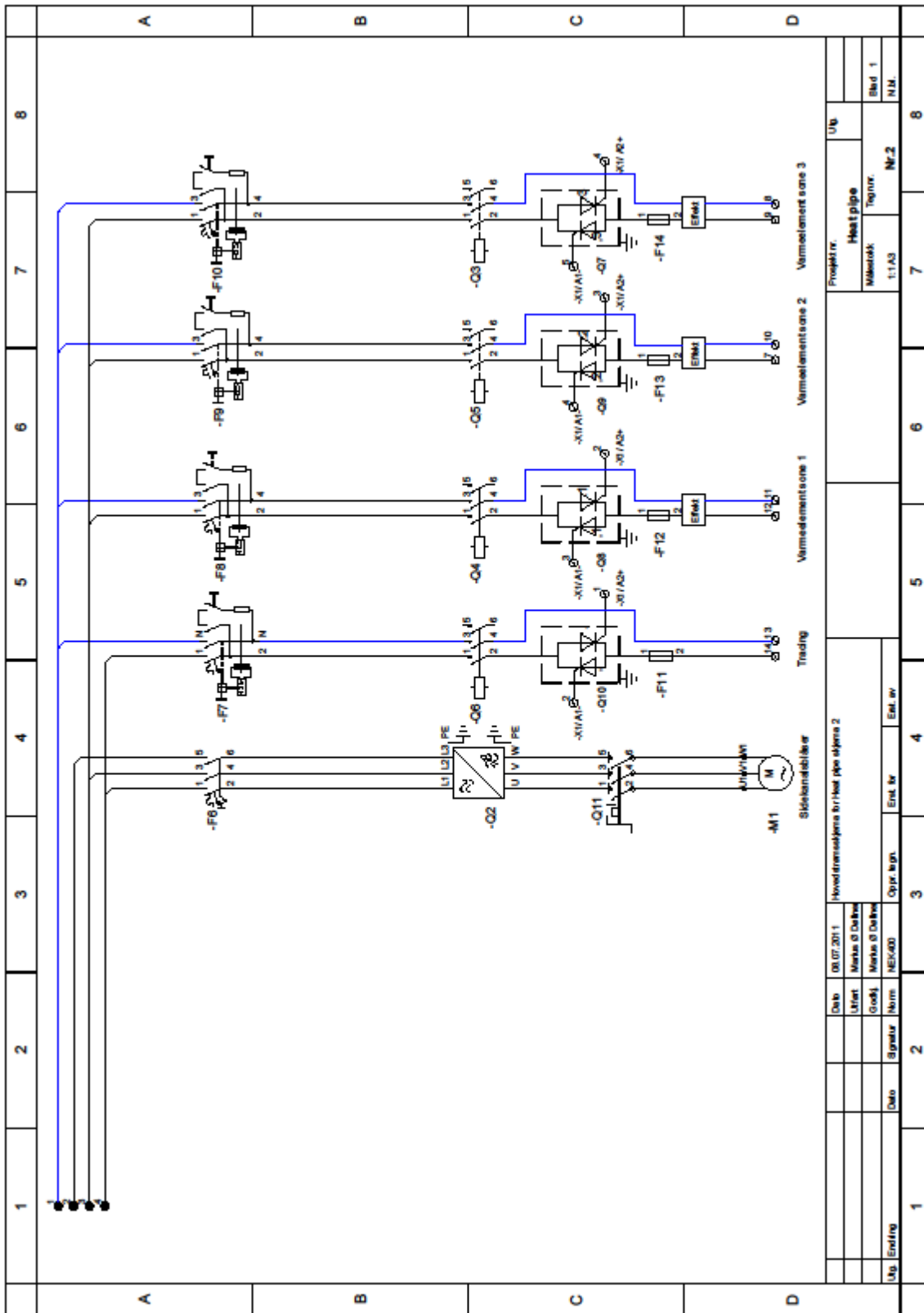
Note: It is the user's responsibility to determine the long-term drift and the uncertainty under the conditions of use

This certificate is issued in accordance with the laboratory accreditation requirements of the United Kingdom Accreditation Service. It provides traceability of measurement to recognised national standards, and to units of measurement realised at the National Physical Laboratory or other recognised national standards laboratories. This certificate may not be reproduced other than in full, except with the prior written approval of the issuing laboratory.

Appendix J Electrical systems for the test rig







Date		08.07.2011		Project nr.		U/6	
U.rett.		Marius Ø Dalen		Heat pipe			
Grokkj.		Marius Ø Dalen		Målestokk		1:1A3	
Norm		NEI/400		Tegn.nr.		Nr.2	
Oppr. tegn.		Ent. nr.		Ent. nr.		Ent. nr.	
Blad 1		Blad 1		Blad 1		Blad 1	
N.M.		N.M.		N.M.		N.M.	

**Appendix K Paper: Analysis of a vertical flat heat pipe
using potassium working fluid and a wick of
compressed nickel foam**

Article

Analysis of a Vertical Flat Heat Pipe Using Potassium Working Fluid and a Wick of Compressed Nickel Foam

Geir Hansen *, Erling Næss † and Kolbeinn Kristjansson †

Department of Energy and Process Engineering, Norwegian University of Science and Technology, Kolbjørn Hejes vei 1a, Trondheim 7491, Norway; erling.nass@ntnu.no (E.N.); kolbeinn.j.kristjansson@ntnu.no (K.K.)

* Correspondence: g.hansen@ntnu.no; Tel.: +47-7359-3938; Fax: +47-7359-3580

† These authors contributed equally to this work.

Academic Editor: George Kosmadakis

Received: 30 December 2015; Accepted: 1 March 2016; Published: 7 March 2016

Abstract: Heat at high temperatures, in this work 400–650 °C, can be recovered by use of cooling panels/heat pipes in the walls of aluminum electrolysis cells. For this application a flat vertical heat pipe for heat transfer from a unilateral heat source was analyzed theoretically and in the laboratory, with special emphasis on the performance of the wick. In this heat pipe a wick of compressed nickel foam covered only the evaporator surface, and potassium was used as the working fluid. The magnitudes of key thermal resistances were estimated analytically and compared. Operating temperatures and wick performance limits obtained experimentally were compared to predictions. Thermal deformation due to unilateral heat flux was analyzed by the use of COMSOL Multiphysics®. The consequences of hot spots at different locations on the wick were analyzed by use of a numerical 2D model. A vertical rectangular wick was shown to be most vulnerable to hot spots at the upper corners.

Keywords: aluminum electrolysis cell; heat pipe; compressed nickel foam wick; potassium; hot spot analysis

1. Introduction

The current study originated from an industrial demand for heat recovery from electrolysis cell side-linings at temperatures in the range 400–650 °C. In aluminum electrolysis, about 50% of the total supplied energy is currently lost as heat to the surroundings. About 35% of the total heat loss is through the walls of the electrolysis cells [1], which corresponds to *ca.* 2.4 kWh/kg of produced aluminum. Cooling panels in the side walls of the electrolysis cells were proposed by Aune *et al.* [2] for improved process control, as well as for high temperature heat recovery. The panels were specified to utilize evaporation and condensation of a working fluid and the recovered heat can be used for, for instance, electricity production. The temperature of the recovered heat depends on the position of the cooling panels in the side-linings of the cells; in the current study, a position corresponding to a temperature range 400–650 °C was specified. The main components of the electrolyte bath are cryolite (Na₃AlF₆) and alumina (Al₂O₃) [1]. The melting point of aluminum is 660 °C, but the cryolite (in which the alumina is dissolved) requires a temperature of 1010 °C for melting [1]. The electrolyte bath is very corrosive, but with a working temperature of 400–650 °C in the cooling panels it is possible to create and maintain a protective frozen ledge on the inside of the cell walls. Figure 1 shows a sketch of the cross section of an electrolysis cell equipped with a wall cooling panel [2] (only a part of the cell is shown). The captions in Figure 1 are listed in Table 1. The protective frozen side ledge (24) is formed on the cooling panel. The panel can be exposed to hot spots if the protective frozen side ledge breaks

down. In such cases, the hot molten electrolyte (12) can come directly in contact with the cooling panel evaporator (8), through cracks in the frozen side ledge. The cooling panel represents the first stage in a heat recovery system, in which heat is transferred from the cooling panel evaporator (8) via the condenser (9) to a cooling circuit (10C) by evaporation and condensation of a working fluid.

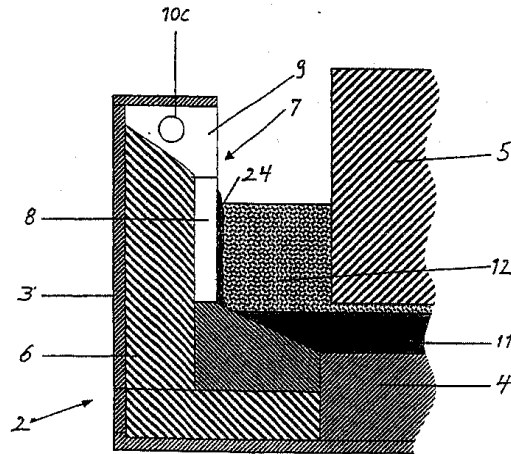


Figure 1. A cross-section of an electrolysis cell with cooling panel [2].

Table 1. Captions in Figure 1.

Number	Explanation
2	Electrolysis cell
3	Steel shell
4	Cathode
5	Anode
6	Insulation
7	Cooling panel
8	Cooling panel evaporator
9	Cooling panel condenser
10C	Cooling circuit
11	Aluminum
12	Electrolyte bath of alumina (Al_2O_3) and cryolite (Na_3AlF_6)
24	Solid electrolyte (frozen side ledge)

The current paper reports:

- A vertical flat heat pipe considered for use as cooling panel;
- Experimental results obtained for the built heat pipe, in a laboratory test rig;
- A thermal resistance network for the built heat pipe;
- Results from an analytical spreadsheet model of the built heat pipe;
- A numerical study of the thermal expansion of the heat pipe, using finite-element (FEM) analysis; and
- A numerical hot spot analysis, undertaken to determine the most vulnerable position(s) of hot spots on a vertical flat heat pipe wick.

Heat pipes of many forms and for many applications have been proposed and are analyzed in textbooks (for instance, [3–6]); a review including recent advances was given recently by Faghri [7]. In some areas, for instance computer cooling, heat pipe technology is well established; however, due to new areas of application for heat pipes the components, materials, and physical processes of heat pipes are still receiving considerable attention. Reay and Harvey [8] recently reviewed the role of heat pipes in intensified unit operations, and pointed specifically at chemical reactors as highly relevant

application areas. Heat pipe technology is in the current study considered for the cooling panels of the aluminum electrolysis cells.

In traditional “capillary heat pipes” the inner surfaces of the evaporator, the condenser, and the adiabatic section are all covered by a wick material, or have grooves serving as capillary pumps, wetting the surface. The capillary pressure is the driving force for the flow and distribution of the working fluid in the wick/groove, and in many cases the performance of the wick/groove will be the main limiting factor of the heat pipe. Wicks are still being developed and improved in order to best fit the application requirements. For instance, advanced bimodal wicks have been designed by sintering fine wick structures to coarse wick structures [9]. Another advanced wick has a graded structure which reflects the pressure gradient inside the heat pipe [10]. Several references on wicks of sintered, groove and mesh type were listed in a recent review by Chan *et al.* [11]. Faghri [3] divided wicks into two groups; homogeneous and composite, and stated that homogeneous wicks are usually chosen due to simple design, manufacture, and installation (*i.e.*, lower costs), even though the composite wicks usually have better performance. Wicks can be made of compressed nickel foam, and the development and testing of such wicks were reported in an earlier paper [12]. This type of wick has the advantage that the wick properties can be selected within a wide range by choosing the degree of compression [13].

Heat pipe wicks are characterized by their porosity, permeability, thermal conductivity, and effective pore radius with regard to a specific fluid. The wick porosity and permeability are properties of the pore structure only [14], independent of the fluid applied. The effective pore radius depends on the contact angle between the wick structure and the fluid applied and is, therefore, not fluid independent. The porosity is usually determined according to a standardized procedure [15]. Various methods exist for the determination of the permeability and the effective pore radius, and in most cases these properties are determined by use of a model fluid and without exposing the wick to a heat flux, for instance as in [16]. Shirazy and Fr chet te [17] recently questioned the validity of the effective pore radius determined this way for the calculation of the wick heat transfer capacity (the capillary limit). They had experienced that wicks made of copper foam performed much better in heat pipes than predicted from existing correlations for the capillary limit. Their explanation was that the effective pore radius will decrease during evaporation due to meniscus recession, and thereby increase the wick heat transfer capacity (compared to the value calculated from an effective pore radius determined from an experiment in which the wick was not exposed to heat). More studies of this hypothesis and comparative studies between the different methods for the determination of the permeability and the effective pore radius will increase the reliability of wick heat transfer capacity predictions.

With regard to working fluid, attention is here given to the alkali metal potassium, which is a commonly-used working fluid in traditional heat pipes for the temperature range 500–1000 °C [4,7]. Alkali metals are very reactive, but excellent working fluids in heat pipes when treated correctly. Potassium has to be handled in a high-quality glove box filled with inert gas (such as Ar), or under vacuum, due to the reactivity with oxygen and water (moisture). Hydrogen gas will be produced in the reaction between potassium and water. Potassium will also tend to remove oxide from the surface of steel [18]. Chemical compatibility between the envelope material and the working fluid is essential in order to avoid corrosion and/or inert gas generation. Ten years of successful operation was reported for a heat pipe made of stainless steel 718 envelope and 316L wick material, utilizing sodium as a working fluid at 750 °C operating temperature [19]. In industry, lifetimes of years are usually needed and expected for heat pipes, often with harsh thermal, chemical, and mechanical loads. Compatibility between the heat pipe and its surroundings is, therefore, equally important to the internal compatibility between the envelope, wick, and working fluid. Metals are the dominating envelope and wick materials, but high temperature wickless heat pipes (thermosyphons) of ceramic material are also being developed; results from promising experiments with sodium and zinc as working fluids were reported recently [20]. Nickel is compatible with potassium [4], but starts oxidizing rapidly at about 350 °C [21] and a protective/reducing gas atmosphere of 5 %(v) H₂, 95 %(v) Ar is therefore often used

during the heat treatments and preparations of the nickel wicks and heat pipe envelopes. Stainless steel 304 is also reported to be compatible with potassium [4], and may be a more economical choice than nickel for heat pipes for industrial applications.

Panels/heat pipes in the side lining of the aluminum electrolysis cells should be as slim as possible. Attention must, therefore, be given to the sonic limit for the vapor flow, especially when alkali metal working fluids are applied, due to their low vapor densities [22]. The entrainment and flooding limits will also be important if the vapor and condensate are in direct contact and flowing in opposite directions in a heat pipe/thermosyphon.

2. Experimental Characterization

An experimental study was carried out to investigate the performance of a flat vertical heat pipe under temperature and heat flux conditions expected in the walls of aluminum electrolysis cells (including hot spot heat fluxes). The hypothesis was that a wick in the evaporator section would be a robust solution for the distribution of working fluid over the evaporator surface under varying temperature and heat flux conditions.

The Heat Pipe

An experimental heat pipe was made specifically for this study. The built experimental heat pipe is shown in Figure 2, to the left fully assembled, to the right split in two.

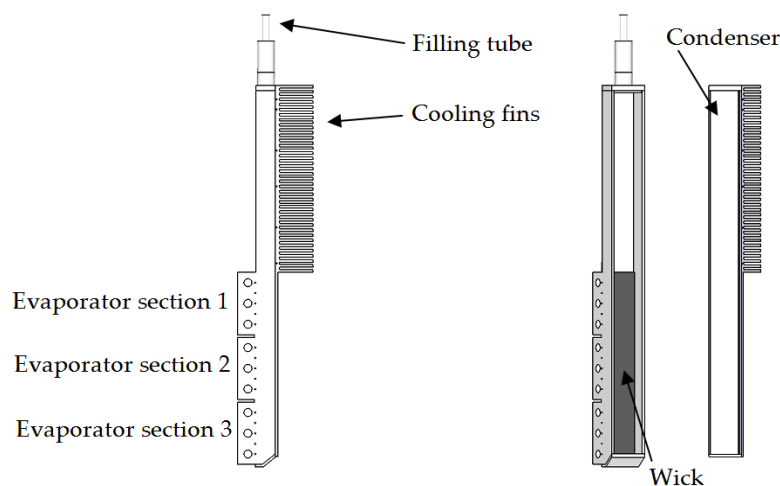


Figure 2. The experimental heat pipe fully assembled (left) and split in two (right).

For the current experimental study, nickel was selected both for the envelope and the wick, due to its relatively high thermal conductivity and reported compatibility with potassium. The heat pipe was designed “as slim as possible”, according to the requirements for the cooling panel for electrolysis cell walls. However, the dimensions of the flow channel were chosen such that the sonic limit, the entrainment limit, and the flooding limit were unlikely to cause problems. Correlations available in reference [3,4] for predicting these limits were used in the design process. The flow channel width was chosen so large that the sidewalls of the heat pipe would likely not cause significant disturbance of the fluid flow.

The experimental heat pipe had no adiabatic section, due to manufacturing limitations. The total height of the evaporator was 150 mm. The inner height of the condenser section was 142 mm. The inner width of the flow channel was 25 mm and the depth 11.55 mm. A wick, 25 mm × 150 mm × 1.15 mm, consisting of four layers of compressed and sintered nickel foam was attached to the evaporator surface by use of electron beam spot welding. The evaporator was divided in three sections where each had three cartridge heaters. The motivation for having multiple sections was to be able to

impose a non-uniform heat flux distributions over the evaporator surface. The cartridge heaters were mounted into the heat pipe having force fit tolerances, hence no thermal paste was necessary. The supplied power to each evaporator section was controlled by phase angle firing thyristors. Each cartridge heater was rated 225 W at 240 V, and had a maximum work temperature of 760 °C. For an ideal case without heat losses the nine cartridge heaters could, from their specifications, provide a maximum uniform heat flux of 540 kW/m². The temperatures in the evaporator wall were measured by 3 × 5 type N thermocouples, Ø1 mm, installed in pockets in each section of the evaporator wall. Similar thermocouples were also installed in pockets in the condenser wall and on the outside of the heat pipe adiabatic walls (the walls opposite of the evaporator, respective condenser surfaces). LabView[®] together with modules NI 9214, NI 9219, NI 9225, and NI 9227 from National Instruments[®] were used for data recording and parameter control. The uncertainty of the measurement of the power supplied to the cartridge heaters was less than 1%. The thermocouples attached to the logging system were calibrated by use of a JOFRA RTC-700 calibrator (accuracy ± 0.11 K). The amount of potassium filled into the heat pipe was 10.2 g, which was estimated to be sufficient for full wetting of the wick, with a good safety margin, for all planned experimental operating conditions.

The outside of the condenser section was equipped with fins and was cooled by nitrogen gas. The heat taken up by the nitrogen gas was calculated from the measured nitrogen flow rate and the temperature increase of the nitrogen over the condenser ($Q_{N_2} = \dot{m}_{N_2} \cdot c_{p,N_2} \cdot \Delta T_{N_2}$). The inlet temperature of the nitrogen was kept at 50 °C. The nitrogen flow rate was determined from the volume flow rate measured by use of a Sierra 620S insertion flow meter in the cooling circuit. The range of the Sierra flow meter was 0–23.45 Nm³/h and the uncertainty ± 0.28% = 0.066 Nm³/h, where N in this particular case was defined as 15 °C and 1 atm. The heat loss to the surroundings was the difference between the heat supplied to the heat pipe by the cartridge heaters and the heat taken up by the nitrogen gas. For safety reasons, the heat pipe was in a container filled with nitrogen gas during the experiments.

3. Theoretical Analysis

3.1. Wick Performance

The limitation that directly addresses the performance of the wick alone is defined by the pressure balance [3]:

$$\Delta P_{cap,max} \geq \Delta P_{hs} + \Delta P_f \quad (1)$$

The pressure loss of the vapor flow in the heat pipe is not taken into account here, as attention is given to the wick only. Inertia effects in the wick and the pressure losses associated with the interfacial thermal resistances are also omitted because these terms are small compared to the terms of Equation (1) in the current case.

If the tortuous flow paths in the wick are represented by a capillary tube model then the capillary pressure can be expressed from the Young–Laplace equation as:

$$\Delta P_{cap,max} = \frac{2\sigma}{r_{eff}} \quad (2)$$

The hydrostatic pressure of the working fluid in the wick relative to the vapor pressure outside the wick is:

$$\Delta P_{hs} = \rho_l g H \quad (3)$$

The frictional pressure loss due to the flow of working fluid in the wick is calculated by use of Darcy's law:

$$\Delta P_f = \frac{\mu_l}{\kappa A_c \rho_l} \int_0^H \dot{m}_l dy \quad (4)$$

The total heat transfer capacity (in Watts) of a vertical flat wick exposed to a uniform heat flux is obtained by inserting Equations (2)–(4) into Equation (1) [12]:

$$Q = \dot{m}_{l,\max} \cdot h_{fg} = \frac{2\kappa A_c \rho_l}{H\mu_l} \left(\frac{2\sigma}{r_{eff}} - \rho_l g H \right) h_{fg} \quad (5)$$

Equation (5) has been applied to predict the heat transfer capacity of the wick in the capillary pressure-limited range. In the vapor static pressure-limited range the capillary pressure term ($2\sigma/r_{eff}$) in Equation (5) is replaced by the vapor pressure of the working fluid [21].

3.2. The Numerical Hot Spot Analysis

A numerical 2D hot spot analysis for a flat vertical wick was carried out, considering the combined effect of frictional and static pressure losses due to localized regions of high heat flux. The method is quite similar to the method described in [23]. The relevant equations were discretized and solved numerically using MatLab®.

Starting with the continuity equation:

$$\frac{\partial u}{\partial x} + \frac{\partial v}{\partial y} = \frac{\alpha}{\rho} \quad (6)$$

where $\alpha = f(x,y)$ is a mass flux source/sink function, and expressing the velocity components u and v respectively using Darcy's law:

$$u = -\frac{\kappa}{\mu} \frac{\partial P}{\partial x} \quad ; \quad v = -\frac{\kappa}{\mu} \frac{\partial P}{\partial y} \quad (7)$$

Equation (7), inserted into the continuity equation, Equation (6), yields Equation (8) which describes the pressure field due to flow friction in the wick:

$$\frac{\partial^2 P}{\partial x^2} + \frac{\partial^2 P}{\partial y^2} = -\frac{\mu\alpha}{\rho\kappa} \quad (8)$$

Appropriate boundary conditions are:

Through the left and right boundaries there is no flow, *i.e.*:

$$\left(\frac{\partial P}{\partial x} \right)_{\text{right, left boundary}} = 0 \quad (9)$$

No flow through the top boundary, *i.e.*:

$$\left(\frac{\partial P}{\partial y} \right)_{\text{top boundary}} = 0 \quad (10)$$

At the bottom of the wick the following boundary condition applies:

$$P_{\text{bottom}} = P_{\text{sat}} - \rho g H \quad (11)$$

where the hydrostatic pressure as a function of height from the liquid bath, y , is:

$$P_{\text{hydrostatic}} = \rho g y \quad (12)$$

H is the height of the wick. It should be emphasized that this definition of P_{bottom} is a fictive pressure, created as an intermediate step in the calculation, the real pressure at the bottom of the wick is P_{sat} . The boundary condition P_{bottom} as defined by Equation (11) may be seen as the pressure available to overcome flow friction.

The total pressure field in the vertical wick is:

$$P_{total}(x, y) = P_{flow\ friction}(x, y) + P_{hydrostatic}(y) \quad (13)$$

The total pressure is compared to a critical pressure, which may be seen as the “pressure remaining in the wick” and has minimum values defined by Equations (14) and (15):

$$P_{critical} = \left(P_{sat} - \frac{2\sigma}{r_{eff}} \right) \text{ when } P_{sat} > \frac{2\sigma}{r_{eff}} \quad (14)$$

$$P_{critical} = 0 \text{ when } P_{sat} < \frac{2\sigma}{r_{eff}} \quad (15)$$

The calculation procedure is as follows:

1. The pressure field in the wick is calculated from Equation (8) and the boundary conditions, *i.e.*, the pressure field is determined entirely by the flow friction, starting from the saturation pressure minus the hydrostatic pressure at the bottom of the wick.
2. The total pressure field in the wick is then calculated by adding the hydrostatic pressure, as a function of height y , to the pressure field generated in point 1, according to Equation (13).
3. For the selected heat fluxes and hot spot the minimum pressure in the total pressure field is compared to the critical pressure defined by Equation (14) or Equation (15). The wick works well if the minimum total pressure is higher than the critical pressure. The capacity of the wick has been exceeded if the minimum total pressure is lower than the critical pressure.

3.3. Thermal Resistance Model for the Whole Heat Pipe

The thermal resistance network for the heat pipe is shown in Figure 3. Heat is supplied from the cartridge heaters at the lower left of the resistance network. The heat leaves the network with the nitrogen gas to the right or as heat loss to the left.

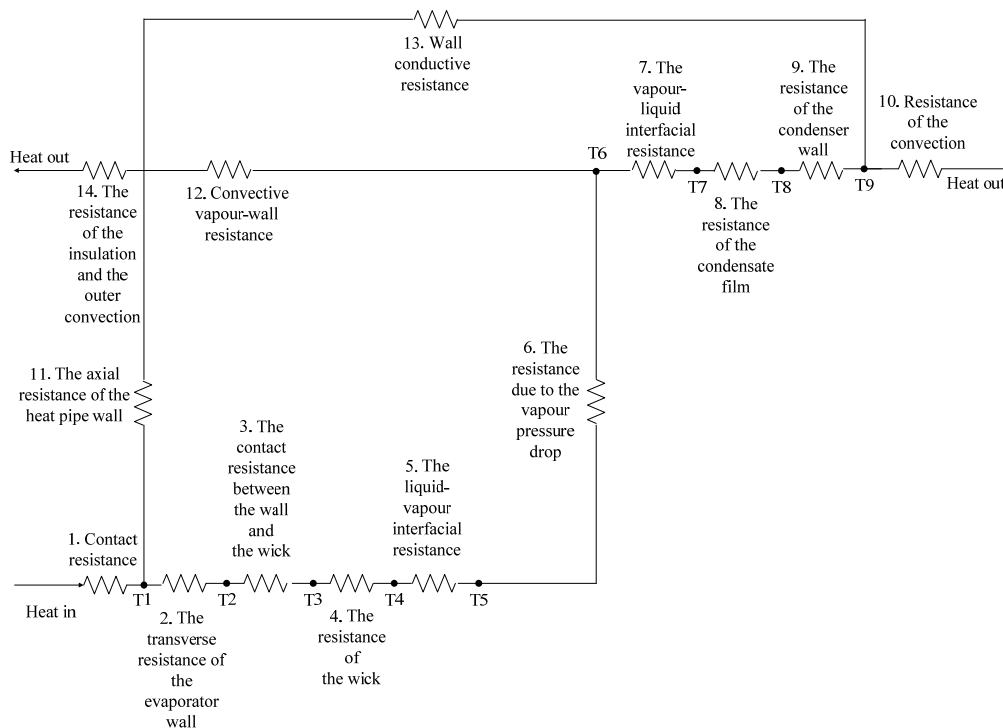


Figure 3. The thermal resistance network of the heat pipe.

A simplified model of the heat pipe based on major heat transfer resistances was developed and implemented in a spreadsheet. With known dimensions and boundary conditions, the individual resistances in Table 2 were calculated. This process was iterative, as the operating condition in the heat pipe had to be determined. For simplicity, metal/metal thermal contact resistances were neglected, as were axial conduction in the heat pipe wall, resistance due to vapor pressure loss, and blowing and suction effects in the evaporator and condenser. The heat transfer coefficient for the nitrogen convective gas cooling, $h_{convection}$, was calculated for flow in a rectangular channel because, when mounted in the test rig, the flow areas between the heat pipe fins became rectangular channels. Fully developed flow was assumed, which gave a conservative estimate for $h_{convection}$. A fin efficiency was calculated to account for the temperature gradient in the fins. The magnitudes of the thermal resistances listed in Table 2 are compared in the Results and Discussion section. The spreadsheet model was also used to estimate the operating temperature (T_5 in Figure 3) of the heat pipe for the following input parameters: heat input, nitrogen gas flow rate, and inlet temperature. Operating temperatures calculated by use of the spreadsheet model have been compared to measured operating temperatures in the Results and Discussion section. With regard to uncertainty, the input parameters are based on the measurements and have the same uncertainties as them. The output parameters have, in addition, the uncertainties from the different resistances in the network plus the uncertainty of the simplifications, which are not quantified.

Table 2. Thermal resistances taken into account.

Thermal Resistance	Expression for R'' ($\text{m}^2 \cdot \text{K}/\text{W}$)	Reference
2. The transverse resistance of the evaporator wall.	$\frac{L}{k_{Ni201}}$	[24]
4. The resistance of the wick.	$\frac{2L}{\left[(1 - \varepsilon)k_{solid} + \varepsilon k_{fluid} \right] + \left[\frac{k_{fluid} \cdot k_{solid}}{\varepsilon k_{solid} + k_{fluid} (1 - \varepsilon)} \right]}$	The average of parallel and serial wick resistances [3] was assumed.
5. and 7. The liquid-vapor and vapor-liquid interfacial resistance.	$\frac{1}{\left(\frac{2\alpha}{2 - \alpha} \right) \left(\frac{h_{fg}^2}{T_v v_{fg}} \right) \sqrt{\frac{M_v}{2\pi R_u T_v}} \left(1 - \frac{p_v v_{fg}}{2h_{fg}} \right)}$	[3]
8. The resistance of the condensate film.	$\frac{\left(\frac{3\mu_l \Gamma}{g\rho_l (\rho_l - \rho_v)} \right) \left(\frac{1}{3} \right)}{k_l}$	[24]
9. The resistance of the condenser wall.	$\frac{L_{wall}}{k_{Ni201}}$	[24]
10. Resistance of the nitrogen gas convective cooling.	$\frac{1}{h_{convection}}$	[24]

4. Results and Discussion

4.1. Thermal Resistance Model

Using the developed model, the magnitudes of the heat pipe related thermal resistances were calculated and are compared in Figure 4 for an operating temperature of about 500 °C. The thermal resistance on the coolant side has been omitted in Figure 4 as this resistance depends on the cooling fluid (in this case N₂-gas) and is not related to the heat pipe characteristics (for the experimental heat pipe setup, the coolant-side resistance represented 85% of the total resistance due to the poor heat transfer characteristics of the nitrogen gas). Figure 4 shows the relative magnitudes of the resistances associated with the heat pipe, for 2 mm envelope wall thickness overall. The thermal resistances associated with the conduction through the evaporator and condenser walls were the largest, followed by the thermal resistance of the wick, the interfacial resistances, and finally the thermal resistance of

the condensate film. The interfacial thermal resistance at the vapor/liquid interface was about twice the thermal resistance of the condensate film, which emphasizes that interfacial thermal resistances can be important in studies of metal vapor condensation [25]. The magnitude and relative importance of the interphase thermal resistances increase with decreasing temperature; however, at an operating temperature of 500 °C the thermal resistances associated with the condensation of the potassium constitute only a small part of the total thermal resistance. The total thermal resistance between the evaporator and condenser external surfaces is 0.031 K/W, representing an effective axial thermal conductivity of the heat pipe of 10,560 W/(m·K) for an effective length of 14.6 cm and an outer axial cross-sectional area of $451 \times 10^{-6} \text{ m}^2$. For comparison, this represents a thermal conductivity of 26.4 times the thermal conductivity of copper (400 W/(m·K) [24]).

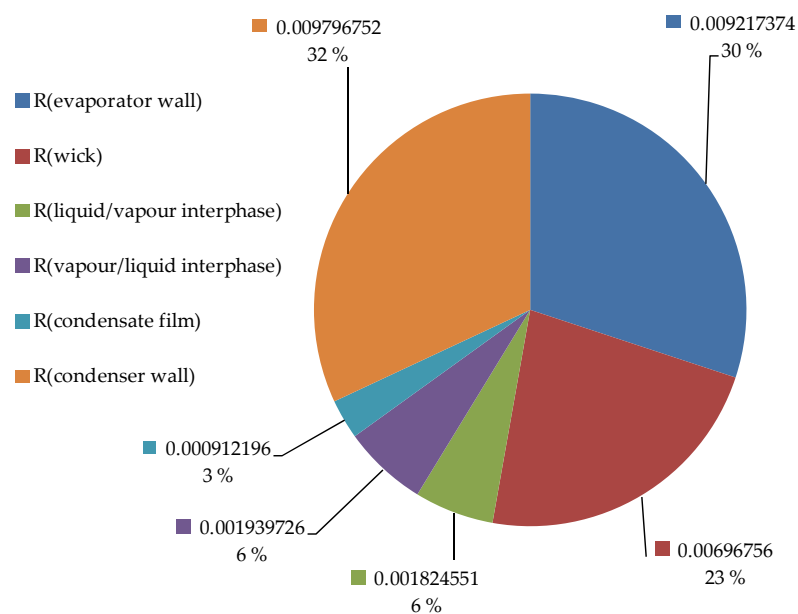


Figure 4. The importance of the considered thermal resistances [K/W] at $T_5 \approx 500 \text{ °C}$.

In Figure 5 the heat pipe operating temperatures calculated by use of the spreadsheet model are compared to measured operating temperatures.

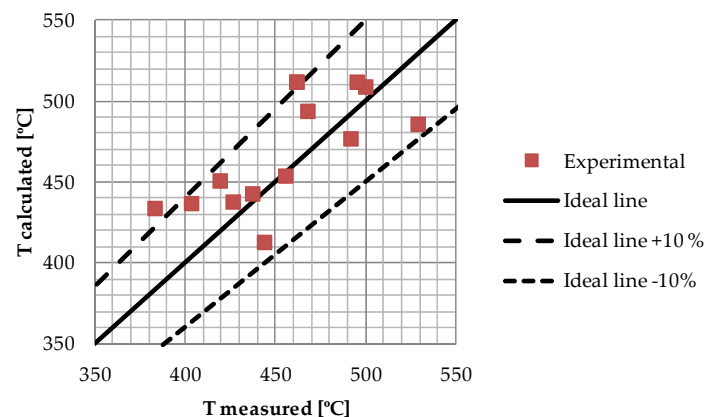


Figure 5. Calculated *vs.* measured operating temperatures, at position T_5 (Figure 3).

For the limited set of data comparisons the simplified thermal resistance model seems to reproduce the experiments to within $\pm 10\%$. The points in Figure 5 were obtained at a wide range of experimental conditions; heat fluxes were in the range from 38 kW/m² to 360 kW/m² and N₂ flow rates between

2.3 Nm³/h and 17.2 Nm³/h. The main reason for the prediction deviation is related to transient heat losses to the insulation and safety chamber not fully accounted for in the spreadsheet model.

4.2. Performance Limitations of the Wick, Analytical, and Experimental Results

The capillary pressure in a heat pipe wick can never be higher than the vapor pressure of the working fluid. This will limit the performance of the heat pipe wick, as it is the capillary pressure (or the vapor static pressure) that will be the “driving force” in Equation (5).

The active height of the heat pipe wick was 11.2 cm, and the wick capacity limitations are shown in Figure 6.

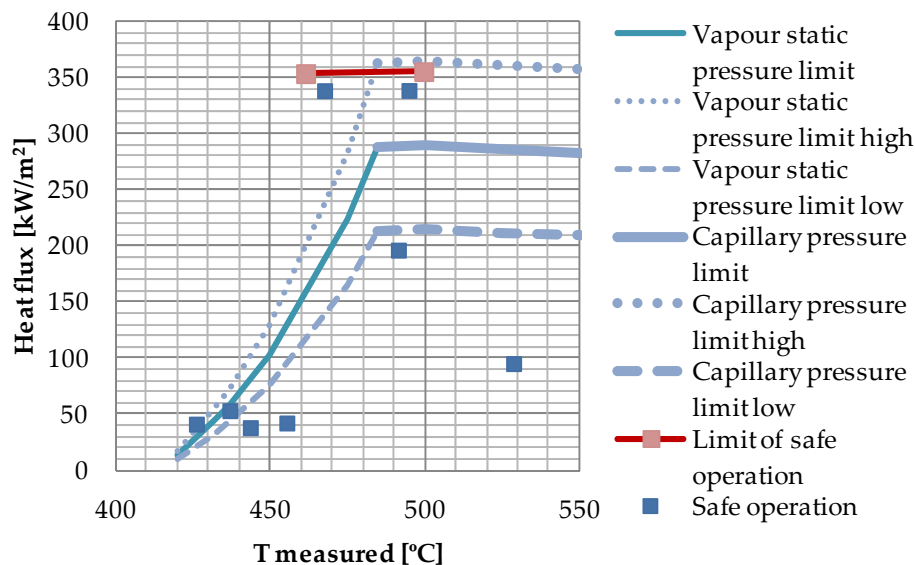


Figure 6. Wick performance data for wick height 11.2 cm. Dots represent experimental data. Red dots—at maximum performance limit; blue dots—safe operation.

For a uniform heat flux the dryout at the exceedance of the wick maximum capacity would be expected to occur at the top of the wick, *i.e.*, an accompanying temperature peak would be registered at the top of evaporator Section 1 in Figure 2. For the experiments reported in Figure 6 the heat flux was increased in small steps, and the temperatures in the evaporator were monitored graphically on the computer screen. For heat fluxes above the reported measured limits the rapid increase in temperature did not occur at the top of the wick, but at the top of evaporator Section 2. This could indicate that the evaporator surface dryout and the accompanying temperature peak were caused by a local contact problem between the wick and the evaporator surface at the top of evaporator Section 2, rather than by the exceedance of the “pumping” capacity of the wick. In such case, the maximum capacity of the wick could be even higher than shown by the experimental points in Figure 6. The most likely scenario is that such a contact problem was caused by thermal expansions, which are largest at the maximum heat flux. In the following discussion it is assumed that the measured maximum reported in Figure 6 represents the maximum capacity of the 11.2 cm wick, even though the dryout did not occur at the top.

From Figure 6 it is observed that the heat pipe was able to operate above the vapor static pressure limitation calculated for the whole effective wick height (11.2 cm), while in the capillary pressure limited range the performance overlapped the calculated limit when the experimental uncertainty was taken into account. The large uncertainty indicated in Figure 6 by the high and low vapor static pressure limit curves and the high and low capillary pressure limit curves is a result of the uncertainty of the permeability of the compressed wick, which was calculated to $\pm 26\%$ [12]. In general, from Equation (5), the heat transfer capacity will increase by decreased effective pore radius and/or increased permeability. Increased effective pore radius due to a heat flux, as described by Shirazy and

Fréchette [17], will only have effect in the capillary pressure limited region. The experimental point above the vapor static pressure limit line can, therefore, only be explained if the real permeability of the wick was higher than the value ($73 \times 10^{-12} \text{ m}^2$) used in the calculation of the corresponding limit. However, the calculated limits are extremely sensitive to the permeability. Estimates have shown that a small channel in the wick, or between the heated wall and the wick, in the order of $34 \mu\text{m}$, will increase the permeability sufficiently to explain the deviation between experiments and predictions. It is not unlikely that such a channel can have been created between the compressed foam layers of the wick due to the mechanical handling of the heat pipe, or due to thermal expansion, as discussed in the following.

4.3. Thermal Expansion

A heat transfer panel/heat pipe located in the side lining of an aluminum electrolysis cell will be exposed to unilateral heat fluxes. The temperature gradients caused by the unilateral heat flux will cause some thermal deformation for any real structure of finite thermal conductivity, such as the heat pipe envelope. The thermal deformation of the heat pipe was analyzed by use of Comsol Multiphysics®. Figure 7 shows the results from one of the most extreme cases, where about 480 kW/m^2 were applied to each of the upper two evaporator sections and about 160 kW/m^2 was applied to the lower evaporator section.

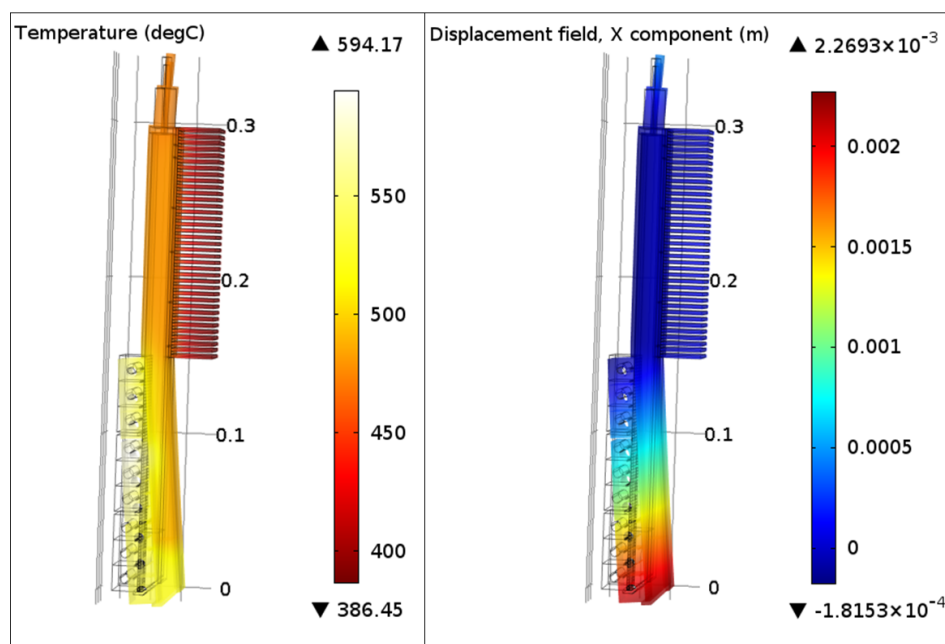


Figure 7. Temperature distribution [°C] and corresponding thermal deformation [m] of the heat pipe.

The heat pipe was fixed at the fin base. The results shown in Figure 7 indicate that the heat pipe bends more than 2 millimeters due to the unilateral heat flux, despite the relatively high thermal conductivity of the envelope material (Ni201). Under the current conditions the temperature at the cartridge heaters was about 90 K above the operating temperature of the heat pipe. Awareness about thermal deformation is important in future design processes in order to implement solutions which can prevent potential thermal contact problems on the outside of the heat pipe, as well as between the wick and the evaporator surface.

4.4. Numerical 2D Hot Spot Analysis

In this section the results of the numerical study of hot spots on vertical flat wicks are reported. Different scenarios were considered, exemplified here by analysis of the consequences of hot spots in the different positions, 1 to 9, of the wick in Figure 8. The maximum uniform heat flux for the whole wick is used as reference in the discussion. Dryout will occur at the top of the wick if the maximum uniform heat flux is exceeded.

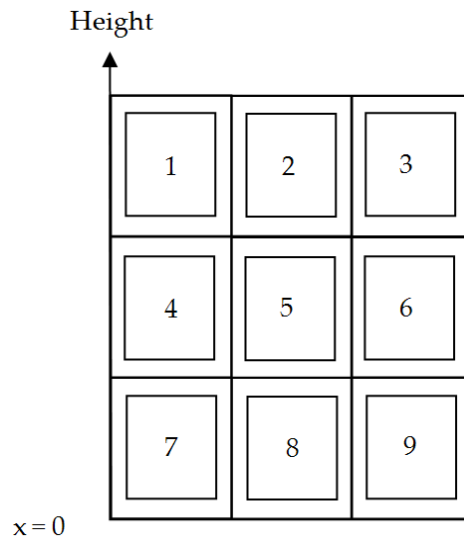


Figure 8. A vertical rectangular wick with nine potential hot spot positions.

The experimental heat pipe wick (0.025 m wide) represented just a slice of a larger wick for a cooling panel. The width of the wick in the numerical study was set to 0.112 m, giving a quadratic wick for this analysis. The size of the hot spot was 0.0112 m \times 0.0112 m, *i.e.*, it occupied 1% of the wick area. The wick properties and thickness were the same as for the experimental wick.

In Figure 9 the pressure field obtained from one of the numerical calculations is shown. A hot spot of 15 times the normal heat flux has been imposed in position 2, Figure 8, where the normal heat flux is defined as the maximum uniform heat flux outside of the hot spot. The temperature for this case was 773 K, the working fluid potassium, the wick permeability $73 \times 10^{-12} \text{ m}^2$ and the effective pore radius $50.8 \times 10^{-6} \text{ m}$. The pressure isolines in the upper part of the wick are clearly affected by the presence of the hot spot. The distance between the 2000 Pa line and the 1500 Pa line is smallest at the horizontal position of the hot spot due to the high flow friction pressure drop around the hot spot. In general the vertical distance between the pressure isolines is increasing from the bottom of the wick and up; this is because the mass flow rate in the wick is decreasing upwards due to the evaporation. The minimum pressure ($P_{\text{critical}} = 1283 \text{ Pa}$, Equation (14)) is marked with a small circle on the top of the wick, *i.e.*, in this case the dryout occurs at the top of the wick and not in the hot spot.

Figure 10 shows the maximum average heat flux, *i.e.*, $q_{\text{max,average}} = (0.99 + 0.01 \cdot q_{\text{hotspot}}/q_{\text{normal}})q_{\text{normal}}$, for the case $q_{\text{hotspot}}/q_{\text{normal}} = 15$ as a function of the position of the hot spot. For a hot spot positioned below the vertical mid-position the average heat flux increases above the nominal value of 301.5 kW/m^2 , whereas for positions above the middle the heat flux is lower than the nominal value.

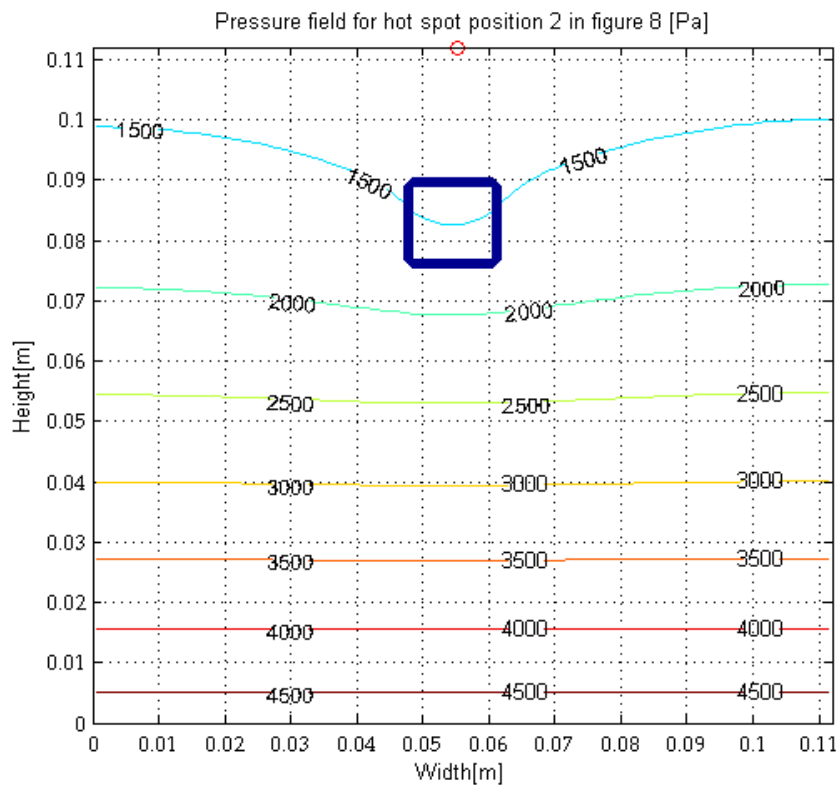


Figure 9. The pressure field for a 0.112 wide and 0.112 m high wick with a hot spot ($q_{hotspot}/q_{normal} = 15$).

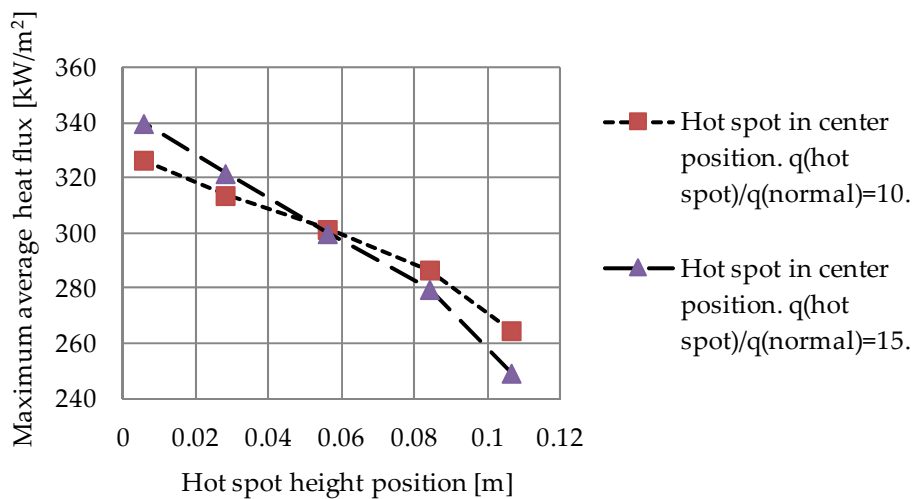


Figure 10. Maximum average heat flux as a function of hot spot vertical position.

Compared to the nominal case 301.5 kW/m^2 (without hot spot) a high flux hot spot above the mid-position will be more detrimental than a weaker hot spot. For a hot spot below the mid-position the reduced flow distance for the supply to the hot spot will be increasingly important with increasing hot spot heat flux.

In Figure 11 the wick maximum average heat flux, $q_{max,average}$, has been plotted for cases with hot spots $q_{hotspot}/q_{normal} = 10$ and $q_{hotspot}/q_{normal} = 15$ for different horizontal positions at the hot spot center vertical position $(0.112 - 0.0112/2) = 0.1064 \text{ m}$.

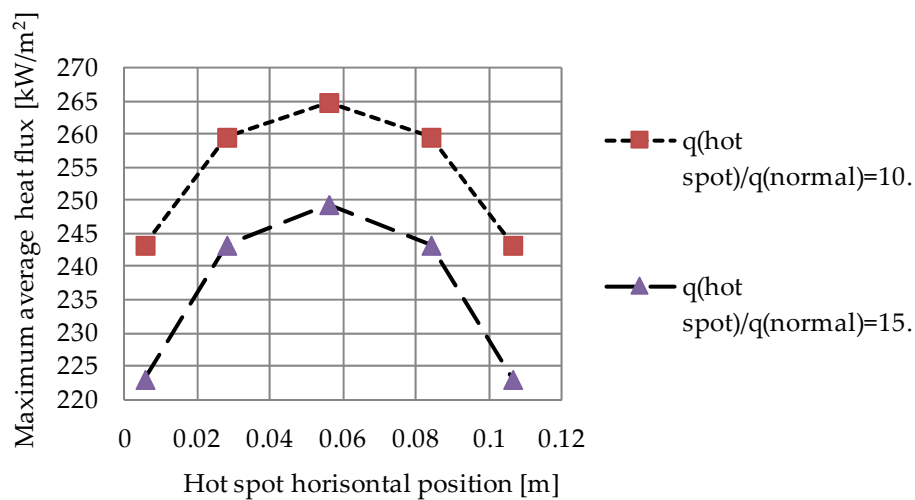


Figure 11. Maximum average heat flux for hot spots at different horizontal positions, all at top height level.

In Figure 11 the least detrimental hot spot positions are at the vertical centerline (*i.e.*, for 0.056 m horizontal position), where the hot spots can receive liquid symmetrically from both sides. The flow resistance increases with distance from the centerline, and accordingly the maximum average heat flux decreases.

Figures 10 and 11 show that the impact of the hot spot increases with its heat flux and that the vertical position of the hot spot is more important than the horizontal position for the analyzed cases.

Important observations from the analysis are:

- Positions 1 and 3 in Figure 8 are the two most detrimental hot spot areas for a vertical wick. The upper corner hot spot positions are critical because they are associated with the longest average flow distances for the liquid from the pool at the bottom of the wick and a higher local mass flow rate at the hot spot border. The hot spot positions 1 and 3 will lead to the lowest maximum average heat flux for the whole wick.
- Position 2 is less detrimental than position 1 and position 3 because a hot spot in position 2 will receive liquid from both sides, with a lower average flow resistance than the corner hot spots 1 and 3.
- A hot spot in position 7, 8, or 9 will lead to the highest maximum average heat fluxes because the average flow resistance is reduced compared to the uniform heat flux case. A hot spot in position 7, 8, or 9, which may not be sufficient to cause dryout there, can still cause dryout at the top of the wick.

A dryout situation caused by a hot spot will lead to a sharp increase in the temperature at the dryout position. Mechanical damage to the wick can occur due to the thermal expansion which accompanies the dryout. An undamaged wick will normally be rewetted at the dryout position if the heat flux at the hot spot is decreased below the dryout value.

One way to reduce the risk for hot spots is to increase the thickness of the wick, because the capacity of a wick is directly proportional to its thickness. Increased thickness will, however, increase the thermal resistance of the wick.

Reduced wick height will also increase the ability of the wick to handle hot spots, and lead to increased maximum average uniform heat flux.

The conclusions of the hot spot analysis are also considered valid for wicks exposed to non-uniform heat fluxes, in general.

Special design is required when the application requires cooling over a larger height than a single wick can handle. This may be a system consisting of several heat pipes, or a single heat pipe in which condensate is supplied to the wick at several vertical positions.

5. Conclusions

- From the analytical model:

For the heat pipe at an operating temperature of 500 °C the thermal resistances related to the evaporation and condensation of the working fluid were small compared to the thermal resistances of the heat pipe walls.

- From the analytical model and the experimental results:

A simplified thermal resistance spreadsheet model of the heat pipe produced operating temperatures which correlated within a $\pm 10\%$ error band within a wide range of operating parameters. The limited amount of experiments of this study indicated that the heat transfer capacity of the heat pipe utilizing potassium working fluid was higher than predicted from theory in the vapor static pressure-limited region, in the capillary pressure-limited region the capacity was in accordance with theory when the experimental uncertainty was taken into account. In general, the wick performance may be higher than predicted due to:

- A The theory of Shirazy and Fr chet te [17], which says that the effective pore radius is decreasing when the wick is exposed to a heat flux, *i.e.*, use of an effective pore radius obtained from an experiment without heat flux will underestimate the wick capacity.
 - B The permeability of the wick is larger than measured in experiments with the model fluid. Point A can be excluded as explanation for the high wick capacity measured in the vapor static pressure limited region, only increased permeability can lead to increased performance in that part.
- From analysis of the thermal expansion by use of COMSOL Multiphysics[®]:
The unilateral heat flux caused about 2 mm horizontal deformation (bending) of the experimental heat pipe. Asymmetrical thermal expansion caused by unilateral heat flux can cause thermal contact problems even for heat pipes of made of materials of relatively high thermal conductivity, like nickel, and can have created a high permeability channel in the wick in the current case.
 - From the numerical 2D wick hot spot analysis:
A rectangular, vertical wick is most vulnerable to hot spots located at the upper corners, which are associated with the highest flow resistances. Heat pipe technology is promising for an aluminum electrolysis cell wall cooling system due to high effective thermal conductivity and ability to handle hot spots.

Acknowledgments: The authors would like to thank Elkem and the Research Council of Norway for funding this work.

Author Contributions: Geir Hansen carried out the experimental work, data reduction, and prepared the first draft of the paper. The hot spot analysis was done by Kolbeinn Kristjansson. Geir Hansen and Erling N ess have equally contributed to the analysis and paper preparation.

Conflicts of Interest: The authors declare no conflict of interest.

Symbols

- A area, m^2
- A_c wick cross sectional area, m^2
- c_p specific heat capacity, $J/(kg \cdot K)$

g	gravity constant, $g = 9.81 \text{ m/s}^2$
h	heat transfer coefficient, $\text{W}/(\text{m}^2 \cdot \text{K})$
H	wick total height, m
h_{fg}	latent heat of evaporation, J/kg
k	thermal conductivity, $\text{W}/(\text{m} \cdot \text{K})$
L	length, m
\dot{m}	mass flow rate, kg/s
P	pressure, Pa
\dot{Q}	heat flow rate, W
R	radius, m
r_{eff}	effective pore radius, m
R	thermal resistance, (K/W)
R''	specific thermal resistance, $(\text{m}^2 \cdot \text{K}/\text{W})$
R_u	the universal gas constant, $\text{J}/(\text{mol} \cdot \text{K})$
T	temperature, K
u	velocity in x-direction, m/s
v	velocity in y-direction, m/s
v_{fg}	change in specific volume from liquid to vapour, m^3/kg
x	length, m
y	height, m

Greek Symbols

α	accommodation coefficient (dimensionless), or source/sink function, $\text{kg}/(\text{m}^2 \cdot \text{s})$
Γ	evaporation rate per unit height of wetted wick, $\text{kg}/(\text{m} \cdot \text{s})$
ε	porosity
κ	permeability, m^2
μ	dynamic viscosity, $\text{kg}/(\text{m} \cdot \text{s})$
ρ	density, kg/m^3
σ	surface tension, N/m

Subscripts

c	cross-section
cap	capillary
eff	effective (pore radius)
f	friction
g	gravity
hs	hydrostatic
l	liquid
max	maximum
sat	saturated
v	vapour

References

1. Grjotheim, K.; Kvande, H. *Introduction to Aluminium Electrolysis: Understanding the Hall-Héroult Process*; Aluminium-Verlag: Düsseldorf, Germany, 1993.
2. Aune, J.A.; Johansen, K.; Nos, P.O. Electrolytic Cell for the Production of Aluminum and a Method for Maintaining a Crust on a Sidewall and for Recovering Electricity. U.S. Patent 6811677B2, 2 November 2004.

3. Faghri, A. *Heat Pipe Science and Technology*; Taylor & Francis: Washington, DC, USA, 1995.
4. Reay, D.A.; Kew, P.A.; McGlen, R.; Dunn, P.D. *Heat Pipes: Theory, Design, and Applications*; Butterworth-Heinemann, an Imprint of Elsevier: Oxford, UK, 2014.
5. Silverstein, C.C. *Design and Technology of Heat Pipes for Cooling and Heat Exchange*; Hemisphere Pub. Corp.: Washington, DC, USA, 1992.
6. Peterson, G.P. *An Introduction to Heat Pipes: Modeling, Testing, and Applications*; Wiley: New York, NY, USA, 1994.
7. Faghri, A. Review and advances in heat pipe science and technology. *J. Heat Transf.* **2012**, *134*. [[CrossRef](#)]
8. Reay, D.; Harvey, A. The role of heat pipes in intensified unit operations. *Appl. Therm. Eng.* **2013**, *57*, 147–153. [[CrossRef](#)]
9. Huang, X.; Franchi, G. Design and fabrication of hybrid bi-modal wick structure for heat pipe application. *J. Porous Mater.* **2008**, *15*, 635–642. [[CrossRef](#)]
10. Marcus, B.D.; Edwards, D.K. Graded Pore Size Heat Pipe Wick. U.S. Patent 4,170,262, 9 October 1979.
11. Chan, C.W.; Siqueiros, E.; Ling-Chin, J.; Royapoor, M.; Roskilly, A.P. Heat utilisation technologies: A critical review of heat pipes. *Renew. Sustain. Energy Rev.* **2015**, *50*, 615–627. [[CrossRef](#)]
12. Hansen, G.; Næss, E. Performance of compressed nickel foam wicks for flat vertical heat pipes. *Appl. Therm. Eng.* **2015**, *81*, 359–367. [[CrossRef](#)]
13. Queheillalt, D.T.; Carbajal, G.; Peterson, G.P.; Wadley, H.N.G. A multifunctional heat pipe sandwich panel structure. *Int. J. Heat Mass Transf.* **2008**, *51*, 312–326. [[CrossRef](#)]
14. Dullien, F.A. *Porous Media: Fluid Transport and Pore Structure*; Academic Press: San Diego, CA, USA, 2012.
15. International Organization for Standardization. *Dense Shaped Refractory Products—Determination of Bulk Density, Apparent Porosity and True Porosity*; ISO_5017; International Organization for Standardization: Geneva, Switzerland, 1998.
16. Holley, B.; Faghri, A. Permeability and effective pore radius measurements for heat pipe and fuel cell applications. *Appl. Therm. Eng.* **2006**, *26*, 448–462. [[CrossRef](#)]
17. Shirazy, M.R.S.; Fréchette, L.G. Effect of meniscus recession on the effective pore radius and capillary pumping of copper metal foams. *J. Electron. Packag.* **2014**, *136*, 041003. [[CrossRef](#)]
18. Dwyer, O.E. *Boiling Liquid-Metal Heat Transfer*, 1st ed.; American Nuclear Society: Hinsdale, IL, USA, 1976.
19. Rosenfeld, J.; Minnerly, K.; Dyson, C. *Ten Year Operating Test Results and Post-Test Analysis of a 1/10 Segment Stirling Sodium Heat Pipe, Phase III*; NASA/CR-2012-217430; National Aeronautics and Space Administration, Glenn Research Center: Cleveland, OH, USA, 2012.
20. Meisel, P.; Lippmann, W.; Hurtado, A. Ceramic high-temperature heat-pipes. In Proceedings of the 22nd International Conference on Nuclear Engineering, American Society of Mechanical Engineers, Prague, Czech Republic, 7–11 July 2014.
21. Hansen, G.; Næss, E.; Kristjansson, K. Sintered nickel powder wicks for flat vertical heat pipes. *Energies* **2015**, *8*, 2337–2357. [[CrossRef](#)]
22. Vargaftik, N.B.; Vinogradov, J.K.; Jargin, V.S. *Handbook of Physical Properties of Liquids and Gases: Pure Substances and Mixtures*; Begell House: New York, NY, USA, 1996.
23. Huang, X.Y.; Liu, C.Y. The pressure and velocity fields in the wick structure of a localized heated flat plate heat pipe. *Int. J. Heat Mass Transf.* **1996**, *39*, 1325–1330. [[CrossRef](#)]
24. Incropera, F.P.; DeWitt, D.P.; Bergman, T.L. *Principles of Heat and Mass Transfer*; Wiley: Singapore, Singapore, 2013.
25. Stephan, K.; Green, C.V. *Heat Transfer in Condensation and Boiling*; Springer: Berlin, Germany, 1992.

